Large-scale Imaging of Endothelial Calcium from Inside Intact Arteries

A thesis submitted to

The Department of Bioengineering

University of Strathclyde

for the degree of

Doctor of Engineering

by

Calum Wilson

2014

“Too little knowing or too much brings grief, for each is equidistant from the mean.”

- Lorenzo d’Medici, *A Wood of Love II*

Declaration of Author's Rights

This thesis is the result of the author's original research. It has been composed by the author and has not been previously submitted for examination which has led to the award of a degree.

Signed: 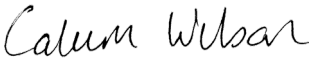

Date: 05/12/2014

Acknowledgements

The work presented in this thesis is the result of three years of work, the completion of which would most probably have not have occurred without help, guidance, and constant encouragement from a number of people. I would hope that those who have contributed to my progress know both who they are and the extent to which I am indebted to them. Without them, there would be nothing to write.

First and foremost, I wish to express my immense gratitude to, respect for, and admiration towards my first supervisor, John McCarron. Not only did John accept me into his research group and give me the chance to work on a particularly interesting topic, he did so knowing that I had zero knowledge of biology. John's knowledge, encouragement, patience, and humour have made the process of completing this work not only interesting, but also fun.

Secondly, I must thank the members of John's lab both past and present who have helped me throughout my EngD. Susan Chalmers, Mairi Sandison, Manuel Sanchez Santos, and Marnie Olson: thanks for teaching me, answering all my questions, providing many useful suggestions, and for always letting me eat more than my fair share of biscuits and cake.

I also wish to extend my deepest gratitude to my second supervisor, John Girkin, and to Chris Saunter, both from the University of Durham. I am truly grateful for their help: from their initial concept of the work presented in this thesis, to their invaluable suggestions and guidance that has improved my work. A special thank you must go to Chris, who wrote the Python scripts that automatically analysed my results and saved me countless hours using my archaic, mostly manual analysis procedure. Additionally, Chris performed the computational modelling that beautifully compliments the experimental results presented in this thesis.

I also wish to thank members of the technical services at the Strathclyde Institute of Pharmacy and Biomedical Sciences (SIPBS). Specifically, Margaret MacDonald and Graeme McKenzie, who helped with experimental preparation and Dennis McLoughlin, for advice on the correct use of fixatives, and for processing and staining my fixed samples.

This work would not have been possible without financial support from the following sources: the EPSRC, who funded my doctoral studies; SIPBS, who generously donated equipment funds; the British Heart Foundation; and the Wellcome Trust.

Finally, thanks to my friends and to my family.

Abstract

A complete understanding of endothelial calcium (Ca^{2+}) signalling has been hampered by the inability to directly image the endothelium in arteries exposed to physiological conditions. To date, most studies have been performed in cultured cell models, or in preparations where arteries have been sliced open and flattened out to expose the endothelium to microscopic investigation. Such techniques have provided much useful information, but cannot fully replicate *in vivo* responses because of the unphysiological arrangements. The focus of the work presented in this thesis is the investigation of endothelial Ca^{2+} signalling in a physiologically relevant model.

This thesis describes a novel microscopic imaging system that enables direct visualisation of the endothelium from within the lumen of intact and pressurised arteries. The system incorporates a custom-built, side-viewing imaging probe (consisting of a gradient-index relay lens and an aluminium-coated micro-optical prism), and permits direct visualisation of an area of the endothelium encompassing ~200 cells with subcellular resolution. The system allows arteries to be pressurised within a normal physiological range, and cytosolic Ca^{2+} concentration ($[Ca^{2+}]_i$) to be measured in endothelial cells labelled with fluorescent chemical Ca^{2+} indicators.

Using this system, the endothelial Ca^{2+} response to haemodynamic stimuli (chemical and mechanical) and its alterations in ageing were investigated. The data indicate that coordinated Ca^{2+} signalling contributes to the physiological endothelial response, and that sustained mechanical stimulation dramatically alters endothelial Ca^{2+} signals. Moreover, endothelial Ca^{2+} signalling is significantly altered in ageing. Histological analysis and computational modelling provide evidence that changes in cell geometry may regulate endothelial Ca^{2+} signalling, and highlight the importance of studying the endothelium in a physiologically relevant model. Furthermore, gradient-index imaging provides parallel access to hundreds of endothelial cells in intact arteries, permitting examination of macroscopic endothelial regulatory functions that are inaccessible by traditional microscopic approaches.

Contents

List of Figures

List of Abbreviations and Symbols

$[Ca^{2+}]_{ER}$: endoplasmic reticulum calcium concentration
$[Ca^{2+}]_i$: cytoplasmic calcium concentration
18β-GA: 18β -glycyrrhetinic acid
2-APB: 2-aminoethoxydiphenyl borate
ACh: acetylcholine
ADV: adventitia
ANOVA: analysis of variance
ATP: adenosine triphosphate
Ca^{2+}: calcium
Ca_v: voltage-operated calcium channel
cAMP: cyclic adenosine monophosphate
CBX: carbenoxolone
CCD: charge-coupled device
cGMP: cyclic guanosine monophosphate
CPA: cyclopiazonic acid
DOF: depth of field
ECs: endothelial cells
EC_{50}: half maximal effective concentration
EDHF: endothelium-derived hyperpolarising factor
EDRF: endothelium-derived relaxing factor
EGTA: ethylene glycol tetraacetic acid
eNOS: endothelial nitric oxide synthase
ER: endoplasmic reticulum
ET: endothelin
F: fluorescence intensity
F/F_0: baseline-corrected fluorescence intensity
F_0: baseline fluorescence
FOV: field of view
FWHM: full width at half maximum
G protein: guanine nucleotide-binding protein
GPCR: guanine nucleotide-binding protein-coupled receptor
GRIN: gradient-index
GTP: Guanosine-5'-triphosphate
ICAM-1: intercellular adhesion molecule-1
IP_3: inositol 1,4,5-triphosphate
IP_3R: inositol 1,4,5,-triphosphate receptor
K^+: potassium
L-NAME: L-N^G-Nitroarginine methyl ester

L-NMMA: L-N^G-monomethyl Arginine citrate
MEGJ: myoendothelial gap junction
$MgCl_2$: magnesium chloride
MLC: myosin light chain
MLCK: myosin light chain kinase
MLCP: myosin light chain phosphatase
mmHg: millimetres of mercury
NA: numerical aperture
Na^+: sodium
nAChR: nicotinic acetylcholine receptor
NCX: Na^+/Ca^{2+} exchanger
NO: nitric oxide
OGB-1/AM: Oregon green BAPTA-1 acetoxymethyl ester
P: gradient-index lens pitch
PGI_2: prostaglandin I_2/prostacyclin
PIP_2: phosphatidylinositol 4,5-biphosphate
PKA: protein kinase A
PMCA: plasma membrane calcium ATPase
PSS: physiological saline solution
ROC: receptor-operated ion channel
ROI: region of interest
RyR: ryanodine receptor
s: second
SELFOC: self-focussing
SEM: standard error of the mean
SERCA: sarco/endoplasmic reticulum calcium ATPase
SM: smooth muscle
SMC: smooth muscle cell
SMOC: second messenger-operated ion channel
SOC: store-operated ion channel
SOCE: store-operated calcium channel entry
SR: sarcoplasmic reticulum
STDev: standard deviation
TRPV4: transient receptor potential cation channel, subfamily V, member 4
VCAM-1: vascular adhesion molecule-1
VOC: voltage-operated ion channel
VOCC: voltage-operated calcium channel
$\Delta F/F_0$: change in baseline-corrected fluorescence intensity

Chapter 1. General Introduction

1.1 Adaptive Properties of Arterial Wall

To satisfy metabolic demand, the vasculature carries blood through a closed-loop system, away from the heart to local tissues, where nutrients and metabolites are exchanged in the capillary networks (1). Once this has occurred, blood is returned back to the heart to be pumped through the pulmonary circulation. The metabolic demand of local tissues is dynamic and dependent on cell type and location, as well as local environmental parameters such as pH and temperature (2). As such, the vascular tree is composed of a diverse system of blood vessels (1) that modulate the cyclical flow of blood exiting the heart so that region-specific, optimal exchange can occur at the capillary level.

Despite changes in function throughout the vasculature, all blood vessels (arteries and veins), with the exception of the capillaries, are composed of four basic building blocks: 1) smooth muscle cells, 2) endothelial cells, 3) elastin, and 4) collagen. These components form a series of three morphologically and functionally distinct layers that make up the arterial wall (Figure 1.1): the tunica adventitia, an outer layer of fibrous collagen that protects the vessels and anchors them to surrounding structures; the tunica media, composed of a varying number of layers of circumferentially arranged smooth muscle cells, that control vessel diameter, and sheets of elastin that provide tensile strength; and the tunica intima, or endothelium, that is composed of a monolayer of endothelial cells and a thin basement membrane, and is separated from the media by a layer of elastin that is of the order of 1 μm thick (internal elastic lamina) (3). As arteries become smaller, the thickness of the constituent layers decreases. For example, endothelial cells are between 0.1 μm thick, in rat capillaries (4), and 2.5 μm thick in rat aorta (5). Similarly the medial layer ranges from approximately 10 μm thick in rat arterioles (6) to 90 μm thick in rat aorta, and the adventitia ranges from approximately 20 μm in rat arterioles (6) to 60 μm, in rat aorta (5).

1.1.1 Vascular Smooth Muscle Tone

The primary role of blood vessels is to control blood flow and blood pressure. This occurs through the contraction and relaxation of vascular smooth muscle (vascular tone). Several mechanisms may contribute to contraction. For example, contraction is elicited in response to activation of surface receptors on smooth muscle cells, which leads to changes in membrane potential via activation of ion channels in the plasma membrane (7). Regardless of the initiating mechanism, contraction occurs as a result of calcium (Ca^{2+}) signalling cascades (8,9) that activate the contractile machinery required to generate force in a Ca^{2+}-dependent manner (10). The sensitivity of the Ca^{2+} dependence may also be altered by additional signalling pathways such as that of Rho/Rho kinase (11).

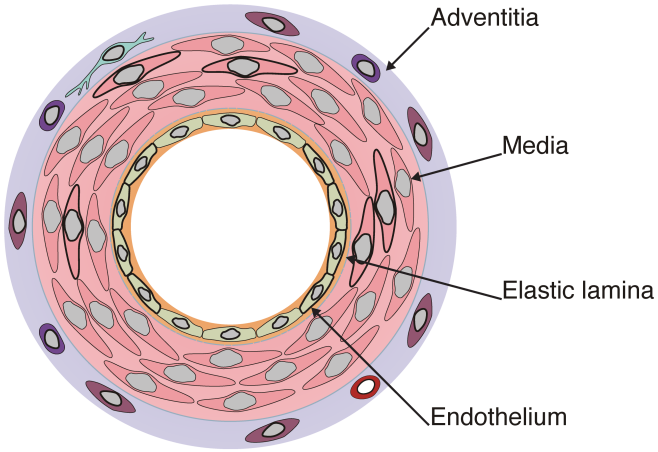

Figure 1.1 – Cartoon illustrating the structure of the blood vessel wall. Blood vessels are composed of three main layers: 1) the outermost adventitia, which is predominantly composed of collagen and fibroblasts; 2) the medial layer, composed of circumferentially arranged smooth muscle cells and sheets of elastin; and 3) the innermost endothelium, a single layer of endothelial cells that is separated from the media by the internal elastic lamina.

Contraction is principally regulated by contractile actin and myosin filaments and, to a smaller extent, by other actin binding proteins such as calponin and caldesmon (12). To enable the interaction of myosin and actin, Ca^{2+} binds to calmodulin. The resulting Ca^{2+}-calmodulin complex activates myosin light chain (MLC) kinase (MLCK), which phosphorylates MLC. By a process not fully resolved, this causes myosin ATPase to release energy from ATP, which subsequently results in cross-bridge cycling and smooth muscle contraction (8). The contraction causes a

reduction of vessel diameter due to the circumferential alignment of smooth muscle cells in blood vessels (Figure 1.1). The phosphate group attached to myosin is covalently bound such that the maintenance of tone depends on the transient nature of the contractile stimuli and on the phosphorylation state of MLC. As such smooth muscle contractility is also governed by the action of myosin light chain phosphatase (MLCP), which dephosphorylates MLC, as well as specific inhibitors of the smooth muscle cell contractile mechanisms due to the action of Rho kinase. Alterations in the rate of dephosphorylation changes the rate of contraction.

1.1.2 Control of Vascular Smooth Muscle Tone

Smooth muscle cells throughout the vascular system may exhibit a certain degree of basal vascular tone. This basal tone provides a means for blood vessels to maintain constant blood flow, in spite of fluctuations in arterial blood pressure. The extent of this tone is dependent on a balance of factors, both extrinsic (neurohormonal) and intrinsic (local) to the vascular bed, that act to induce vasoconstriction or vasodilation. Extrinsic factors governing vascular tone include circulating vasoactive catecholamines (e.g. noradrenaline, dopamine), amines (e.g. serotonin), peptides (e.g. angiotensin II), and the action of neurotransmitters released from sympathetic nerve terminals innervating the vasculature. These extrinsic factors preferentially act to increase smooth muscle cytoplasmic Ca^{2+} concentration ($[Ca^{2+}]_i$), causing vasoconstriction and thus increase vascular tone. In contrast, intrinsic influences, released from cells within the vessel wall, can act to either increase or decrease smooth muscle $[Ca^{2+}]_i$, and thus increase or decrease vascular tone. Such mechanisms include myogenic regulation, conducted vasomotor responses, metabolic regulation, mechanical regulation, and autocrine and paracrine signalling.

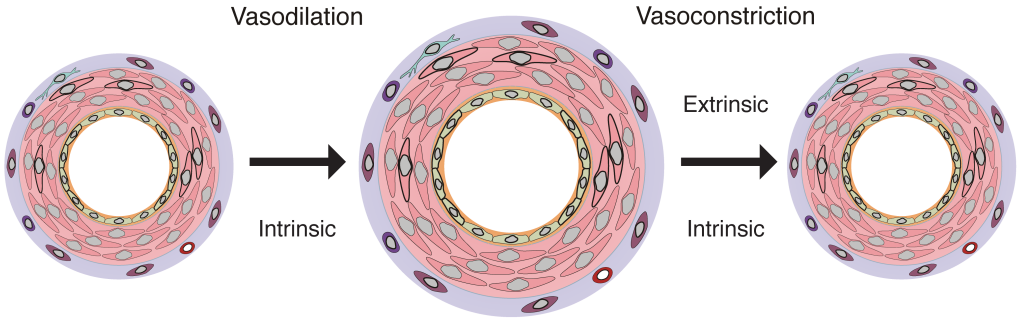

Figure 1.2 – Intrinsic and extrinsic factors affect vascular tone. Vascular tone is controlled by a myriad of vasoactive factors that may be either local (intrinsic) to the vascular wall or may result from signalling mechanisms that initiate outwith the vascular wall (extrinsic). Whilst intrinsic factors may contribute to either vasodilation or vasoconstriction, extrinsic factors almost exclusively lead to vasoconstriction.

Regardless of origin, all vasoactive factors act on smooth muscle by either: 1) modifying smooth muscle $[Ca^{2+}]_i$ due to influx/efflux across the plasma membrane or Ca^{2+} release/reuptake from intracellular stores (sarcoplasmic reticulum; SR); or 2) altering the sensitivity of the contractile elements to Ca^{2+} (7–9,11). There are at least 7 classifications of ion channels/transporters, present on the plasma membrane, that directly or indirectly modulate smooth muscle $[Ca^{2+}]_i$ (13). These may be subdivided into ≥ 12 different subtypes of plasmalemmal $[Ca^{2+}]_i$ modulators: voltage-gated Ca^{2+} channels (L-type and T-type), store-operated Ca^{2+} channels (SOCs), ligand-gated (non-selective) cation channels, potassium (K^+) channels, chloride channels, the plasma membrane Ca^{2+} ATPase (PMCA), and the Na^+/Ca^{2+} exchanger (NCX). However, these plasmalemmal sources of Ca^{2+} do not act independently of each other. For example, the influx/efflux of Ca^{2+}, and other ions, determines the plasma membrane potential (14) which modulates further influx and release of Ca^{2+}.

Further increasing the complexity of the control of smooth muscle contractility, Ca^{2+} release from the internal SR store occurs via both the inositol 1,4,5-trisphosphate (IP_3) receptor (IP_3R) and the ryanodine receptor (RyR) (15). Together with the aforementioned plasmalemmal modulators of $[Ca^{2+}]_i$, these sources of Ca^{2+} form a feedback loop in the smooth muscle $[Ca^{2+}]_i$ control system, and interact not only with each other but also with the SR Ca^{2+} ATPase (SERCA). For example, SOC activation occurs as a result of depleting the SR of Ca^{2+} - both of which can also alter

the plasma membrane potential and Ca^{2+} entry via voltage-dependent Ca^{2+} channels (15).

1.1.3 The Endothelium

The endothelium is ubiquitous throughout the cardiovascular system. Made up of millions of cells, pieced together in a single layer mosaic, it forms the interface between the blood and the tissues of the body. The arterial endothelium also expresses many receptors and channels that are activated by vasoactive stimuli and, with close apposition of endothelial cells and smooth muscle cells and the presence of heterocellular contact through holes in the internal elastic lamina (myoendothelial gap junctions, MEGJs), the endothelium is predisposed to significantly modulate smooth muscle function.

Though the general composition of blood vessels was well established by the middle of the 19th century, the importance of this special lining in was not truly appreciated until 1977, when Ross formulated his response to injury hypothesis (16). The endothelium itself was first alluded to in Theodore Schwan's description of tadpole capillaries in 1839 (17). A few decades later, in 1860, von Recklinghausen published an 8-line memo on the use of silver nitrate as a histological stain (18), and using this technique went on to show that lymphatic vessels were lined with cells (19). By 1865 and 1866 the silver nitrate technique had been applied by several German investigators to the linings of capillary blood vessels and the existence of the vascular endothelium was definitively proven (20).

Once the existence of the endothelium was established, function was soon ascribed. Detailed investigation into its purpose began with close microscopic scrutiny, leading to an astonishing tempo of insights into endothelial complexity. The importance of the endothelium to the governance of blood flow and the passage of solutes through the artery wall was soon feverously debated (21,22), and by the mid 20th century electron microscopy was providing detailed insight into endothelial ultrastructure (23,24). A major result of these early electron micrograph studies was the discovery of localised differences in the structure of endothelial cells from different vascular beds and organs (25), and differences in cells even from the same vessel (26).

1.2 Endothelial Control of Vascular Tone

Henry Dale first showed that acetylcholine (ACh) was a vasodilator *in vivo* in 1914 (27). However, subsequent *ex vivo* experiments established a paradox as, almost universally, ACh stimulation of isolated blood vessel strips resulted in vasoconstriction (28). The role of the endothelium in these contradictory results was established in 1980 when Furchgott and Zawadzki published their discovery that the vasodilator effect of ACh is dependent on an intact endothelial layer (29). Since then, the endothelium has been shown to produce a large number of vasodilators and vasoconstrictors that are released in response to activation of receptors present on the endothelium (Figure 1.3) (30–32). These signalling molecules can diffuse through the internal elastic lamina, or can pass through MEGJ, to act directly on smooth muscle cells and alter vascular tone.

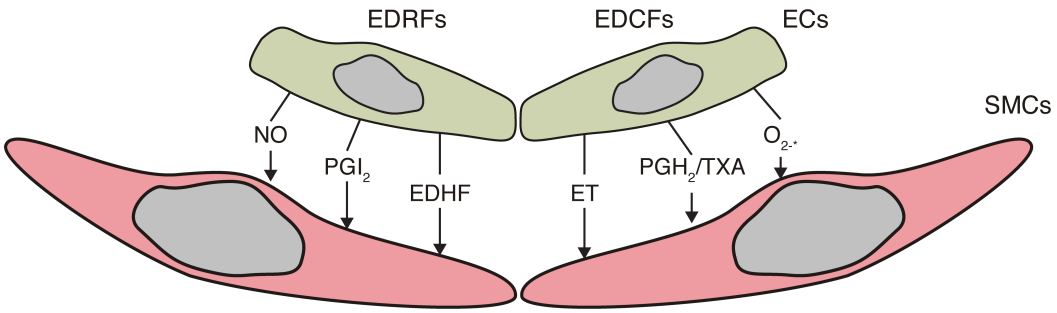

Figure 1.3 – Vasoactive control of smooth muscle cells by the endothelium. Vascular endothelial cells (ECs) release various vasoactive factors that can diffuse to smooth muscle cells (SMCs) and modulate arterial tone. Endothelium-derived relaxation factors (EDRFs) include: the gaseous signalling molecule, nitric oxide (NO); the prostanoid, prostaglandin I_2 (PGI_2); and endothelial derived hyperpolarisation factor (EDHF), a subset of various pathways resulting in sequential hyperpolarisation of endothelial cells and smooth muscle cells. Endothelium-derived contracting factors (EDCFs) include: the potent peptide, endothelin (ET); various prostanoids, such as prostaglandin H_2 (PGH_2) and thromboxane A_2 (TXA_2); as well as reactive oxygen species (O_{2-*}).

1.2.1 Endothelial Vasodilators

As illustrated in Figure 1.3, endothelial vasodilators (endothelium-derived relaxing factors; EDRFs) include nitric oxide (NO), C-type Prostaglandin I_2 (PGI_2, prostacyclin) and endothelium-derived hyperpolarising factors (EDHF).

1.2.1.1 Nitric Oxide

Seven years after the discovery of EDRF (29), NO was identified as the bioactive molecule, synthesised in the endothelium, that resulted in smooth muscle relaxation (30). Subsequently the mechanism of NO production was determined (33), enabling the development of inhibitors of the NO generation including L-N^G-Nitroarginine methyl ester (L-NAME) and L-N^G-monomethyl arginine citrate (L-NMMA) (34) – two of the most commonly used tools for excluding the role of NO release in experiments examining alternative mechanisms of blood vessel function.

Several bioactive substances (e.g. ACh, bradykinin, or substance P) cause NO production after ligating their respective receptors (muscarinic M1-3, bradykinin B1 & B2, neurokinin 1). The link between extracellular receptor activation and NO production is an increase in endothelial $[Ca^{2+}]_i$. Intracellular Ca^{2+} binds to calmodulin, forming a Ca^{2+}-calmodulin complex that activates endothelial nitric oxide synthase (eNOS) (35). Activated eNOS converts L-arginine to citrulline plus NO, in the presence of oxygen and NADPH. Diffusion of NO from the endothelium to smooth muscle cells, where it converts the soluble guanylate cyclase enzyme to its activated form, results in the conversion of guanosine-5'-triphosphate (GTP) to cyclic guanosine monophosphate (cGMP) (36). cGMP then reduces smooth muscle $[Ca^{2+}]_i$ to cause vascular relaxation (37).

NO is the dominant endothelial vasodilator and exhibits continuous and significant physiological, as well pathophysiological, control of blood pressure. Indeed, inhibition of eNOS *in vivo* results in an immediate increase in arterial blood pressure that is reversed by the substrate L-arginine (38) and genetic mice lacking eNOS have chronically elevated blood pressure (39). Furthermore, disruption to the NO pathway plays a key role in the development of atherosclerosis, particularly by its inhibitory effects on smooth muscle cell proliferation and migration (40,41), and by reducing platelet and leukocyte adhesion (42,43).

1.2.1.2 Prostaglandin I_2

In addition to inhibiting platelet adhesion and aggregation, PGI_2 (prostacyclin) is a potent vasodilator. It is derived from arachidonic acid, following the sequential

activation of phospholipase A_2, cyclooxygenase, and prostacyclin synthase (for review, see refs 37 & 38). Once synthesised in the endothelium, PGI_2 translocates to smooth muscle cells, via facilitated diffusion, where it binds to specific G (guanine nucleotide-binding) protein-coupled receptors that transduce the signal by activating andenylate cyclase. Adenylate cyclase activation results in production of the second messenger cyclic adenosine monophosphate (cAMP), which in turn, activates protein kinase A (PKA). The cAMP-PKA signalling pathway governs the phosphorylation of MLC, and hence vascular tone, via a number of downstream effects including (for review, see refs 39 & 40): 1) increased SERCA activity; 2) increased efflux of Ca^{2+} by PMCA; 3) inhibition of Ca^{2+} influx through voltage-operated Ca^{2+} channels (VOCCs) due to K^+-channel activation; and 4) decreased Ca^{2+} sensitivity due to inhibition of MLCK.

Like NO, the physiological significance of PGI_2 extends beyond direct control of vascular tone. For example, genetic manipulation of PGI_2 G protein coupled receptors leads to accelerated atherosclerosis (48) and atherothrombosis (49). Indeed, prostacyclin is currently used clinically for the treatment of pulmonary hypertension (50,51) and peripheral arterial disease (52).

1.2.1.3 Endothelium-derived Hyperpolarisation Factor

Another endothelium-derived vasodilatory pathway, first described in 1984 (31), involves the hyperpolarisation of both endothelial cells and smooth muscle cells in a manner distinct from the actions of NO and prostacyclin. Such hyperpolarisation is termed endothelium-derived hyperpolarisation factor (EDHF) (53), and has been demonstrated in a number of resistance artery preparations, including the mesenteric and coronary arteries of various species (e.g. 31,54,55), as well as larger conduit arteries such as the rabbit iliac artery (56), the guinea-pig carotid artery (57), and the rat aorta (58). The origins and transmission of this hyperpolarisation are still not fully understood and continue to be a matter of intense debate. However, current evidence favours three proposals: 1) Ca^{2+}-dependent production of epoxyeicosatrienoic acids (cytochrome P450) in endothelial cells that play a key role in vascular homeostasis (59); 2) Ca^{2+}-dependent release of K^+ ions by endothelial K^+ channels, that results in smooth muscle cell hyperpolarisation through Na^+/K^+ ATPase and inward rectifier

K^+ channels (60); 3) transmittance of endothelial cell hyperpolarisation to smooth muscle cells via heterocellular gap junctions (61). The precise contribution of each of these pathways is unresolved. For example, whilst some evidence suggests that epoxyeicosatrienoic acids are a prerequisite for EDHF-mediated responses there is little direct evidence that they can be released in large enough quantities from endothelial cells to elicit smooth muscle cell relaxation *in vivo* (62). Similarly, although the opening of endothelial K^+ channels results in smooth muscle cell hyperpolarization in many vascular beds, K^+-induced hyperpolarisations have been absent from many others. Gap junctions have long been recognised as providing a low-resistance electrical pathway from endothelial cells to endothelial cells and smooth muscle cells to smooth muscle cells, but whilst homocellular coupling is well characterised and the presence of heterocellular connections (MEGJs) is established (63), conclusions regarding the role of these junctions in EDHF are still contradictory (64).

1.2.2 Endothelial Vasoconstrictors

Not long after the initial description of endothelial dependent PGI_2 induced vasodilation (65), it was noticed that PGI_2 may also evoke an endothelium-dependent vasoconstriction (66). Since then, various prostanoids, such as thromboxane A_2 and prostaglandin H_2, oxygen free radicals and angiotensin II (summarised in Figure 1.3) have all been shown to be significant contributors to EDCF (67). However, one of the most potent vasoconstrictors known is the peptide endothelin (ET; 62).

Endothelin, first isolated from the supernatant of cultured endothelial cells (32), is secreted abluminally by endothelial cells and binds to specific ET receptors present on smooth muscle cells. As a vasoconstrictor, ET has the opposite effect to NO on smooth muscle cells, causing an increase in smooth muscle $[Ca^{2+}]_i$ due to SR Ca^{2+} release (68,69) and increased Ca^{2+} influx across the plasma membrane (70,71). However, the control of ET and NO release and the ways these molecules act on smooth muscle are not complimentary. For example, endothelin knockout mice have elevated blood pressure rather than reduced blood pressure (72), as would be expected. This finding suggests there is a complicated array of second messenger effects regulating endothelin control of blood pressure. Indeed, although the

pharmacology of endothelin has been well elucidated, clinical application of ET receptor blockers in the treatment of various vascular disease conditions has been largely unsuccessful (73).

1.2.3 Mechanical Forces

In addition to the aforementioned biochemical stimuli, it has become clear that mechanical forces generated by the pulsatile flow of blood also continuously influence endothelial function, particularly by influencing the expression of genes that are fundamental to vascular homeostasis. Under normal conditions, these mechanical forces combine with chemical forces to affect a balanced biological response that maintains vascular homeostasis (74). Excessive or deficient forces disrupt the balance, with the cellular response inducing alterations in the intracellular signalling mechanisms that control vascular tone (75,76), arterial wall permeability (77), and genes regulating vascular remodelling (78,79), finally leading to pathophysiological disease. Indeed, the long-standing observations that atherosclerotic lesions commonly develop in a particular pattern, the geometry of which correlates with regions of altered blood flow (80,81), provide the conceptual rationale behind the hypothesis of a dynamic, regulatory association between mechanical forces and endothelial function.

1.2.3.1 Shear Stress

In the most general of approximations (see ref. 82 for more general concepts of fluid mechanics), blood can be considered to flow through arteries with a parabolic velocity distribution. Such a flow, where velocity is maximal in the centre of the vessel and decreases with radius, is termed laminar flow. This is best understood by considering a uniform, constant flow of blood entering a hollow, rigid-walled vessel. In this scenario, the initial velocity profile is constant with radius. However to conserve the constant rate of flow under a “no-slip” boundary condition, where an infinitesimally small layer of fluid at the wall has zero velocity, the flow in the centre of the vessel is accelerated. Such a flow is also known as Poiseuille flow, and is governed by the following equation:

$$Q = \frac{\Delta P \pi r^4}{8 \eta L} \quad \textbf{(1.1)}$$

where Q is volumetric flow rate of a fluid of viscosity, η, in a tube of length, L, radius, r, over which there is a drop in pressure, ΔP.

Shear stress is the force that acts parallel to the wall due to the velocity profile of blood. It reaches a maximum value at the wall where it is defined as the tangential force per unit area exerted on the wall, τ_w, and expressed as:

$$\tau_w = \frac{\Delta P}{2L} r \quad \textbf{(1.2)}$$

Equations (1.1) and (1.2) may be combined to express shear stress at the wall in terms of the volumetric flow rate. Namely, for laminar flow:

$$\tau_w = \frac{4 \eta Q}{\pi r^3} \quad \textbf{(1.3)}$$

This equation is known as the Hagen-Poiseuille formula, and is often used to estimate shear stress in *in vitro* and *in vivo* experiments from measured values of flow rate, lumen radius and blood viscosity. However, equation (1.3) provides only an estimation of shear stress at the vascular wall because, in the case of whole blood, flow deviates from the parabolic velocity profile. Such deviations arise from the fact that blood is a non-Newtonian fluid, mainly due to the aggregation of red blood cells at low flow/shear rates (83), and streamlining and deformation of red blood cells (84).

1.2.3.2 Circumferential Stretch

Circumferential stretch refers to the stress experienced by the vessel wall as a consequence of transmural pressure. Thus, it is the perpendicular, or tangential, force transferred through all layers of the blood vessel. The term cyclic strain is applied to the dynamic deformation of the vascular wall as it rhythmically distends and relaxes in response to the cardiac cycle. Laplace's Law gives the relationship between transmural pressure, P_t, and tension, T (force per unit length):

$$T = P_t r \tag{1.4}$$

Thus, the circumferential stress (σ_c, force/area) may be expressed as:

$$\sigma_c = \frac{P_t r}{h} \tag{1.5}$$

where h is the thickness of the wall. Note, that for any given transmural pressure the circumferential stress increases as the radius increases.

1.2.3.3 Mechanical Forces in Vascular Disease

Shear stress can activate a number of mechanosensitive components present in endothelial cells. These include G proteins and G protein-coupled receptors (85), integrins (86), ion channels (87,88), membrane proteins (89), membrane lipids (90), and the endothelial glycocalyx (91). Physiological fluctuations in shear stress, due to alterations in flow, activate endothelium-dependent vasodilation. The primary chemical that mediates this response in cell cultures (92), animals (93,94), and humans (95,96) is NO, and is synthesised to maintain a consistent flow of blood. Indeed, shear stress results in an increase in NO production that can be maintained at levels two- to four-fold above basal production (97). The transduction of physiological levels of steady laminar shear stress is also associated with upregulation of numerous genes with direct relevance to atherogenesis, whilst turbulent shear stresses result in their downregulation (72,78,96,97). Such genes, including those encoding the enzymes eNOS and cyclooxygenase-2, have known anti-thrombotic and anti-inflammatory effects within the endothelium and smooth muscle cells, as well as with other interacting cells such as leukocytes and platelets (99–101). Thus, steady laminar flow is associated with quiescent endothelial cells that present a non-adhesive surface to passing blood cells, and imparts an atheroprotective effect on blood vessels (99–101). In contrast, there is an increased occurrence of atherosclerotic lesions at branch points and bifurcations in the vasculature (80,81). Due to the partition of flow, these regions are exposed to turbulent flow patterns as well as vortexes (102). Such alterations in flow lead to

altered levels of shear stress (compared to that resulting from laminar flow, (99)), and contribute to the initiation and progression of atherosclerotic lesions (103).

Circumferential stretch and shear stress act cooperatively in the regulation of vascular homeostasis. Nevertheless, it is customary to isolate one from the other, in order to elucidate underlying mechanotransduction pathways (104). Due to the positioning of the endothelium, at the interface of the vessel wall and passing blood, this has led to a strong focus on the role of frictional forces that act almost exclusively on endothelial cells. This has established a strong body of evidence regarding the role of disturbed flow in the progression of various vascular diseases, whilst the influence of transluminal pressure has been largely overlooked.

The importance of circumferential stretch to the maintenance of vascular homeostasis is, however, exemplified in the myogenic response of vascular smooth muscle (105–107). When exposed to a step-wise increase in transmural pressure and a resultant increase in vessel calibre, smooth muscle cells respond by contracting thus reducing blood vessel diameter to maintain a constant flow of blood. Upon a decrease in transmural pressure, smooth muscle cells respond by relaxing, thus increasing luminal diameter. This phenomenon is dependent on the ability of smooth muscle cell to maintain a level of vascular tone that allows constriction or relaxation of vessels in response to specific contractile or relaxatory stimuli (107).

There are several pathological conditions that result in increased hydrostatic (transmural) pressure, for example, atherosclerosis and heart disease. However, elevated pressure is both an affecter and an effector of vascular disease: raised pressure not only results from vascular disease, but also acts to further disease progression. For example, it has been reported that chronic application of high arterial pressures induces endothelial cell proliferation and morphological changes (108–110), which are both etiological components of vascular disease and are similar to those seen in cells exposed to turbulent shear stresses. Interestingly, exposure of cultured endothelial cells to sustained high pressure levels does not alter basal levels of intercellular adhesion molecule-1 (ICAM-1), vascular adhesion molecule-1 (VCAM-1) or E-selectin (111), in contrast to the differential regulation of ICAM-1,

VCAM-1, and E-selectin with shear stresses (98,112). Hypertension is also associated with decreased agonist-evoked vasodilation to ACh, and other endothelium-dependent vasoactive stimuli (113), most likely due to impaired NO production (114). Such data indicates that the pressure-dependent response of the artery is significantly modulated by the endothelium, and that physiological hydrostatic pressures may protect endothelial cell functions *in vivo*. To date, a variety of endothelial components have been identified as mechanotransducers, however uncertainty with regards to the exact role and the physiological relevance of each has ensured that mechanotransduction remains a central topic of vascular biology. To elucidate further, a fuller understanding of the behaviour of the endothelium under physiological and pathophysiological pressures is required.

1.2.4 Endothelial Ca^{2+}

In the 1970s, methods for the successful culture of endothelial cells provided the means to obtain a large bank of empirical details regarding the function of the endothelium (115,116). Studies of endothelial cells in culture have revealed that the endothelium does not just influence the regulation of vascular tone, but produces numerous messengers that control several vascular functions (117). Furthermore, cell culture studies have revealed that Ca^{2+} signalling is the coupling between environmental input and cellular output (118,119), and controls the mechanisms by which the endothelial cells receives and interprets multiple hemodynamic stimuli, to orchestrate a physiological response. For example endothelial $[Ca^{2+}]_i$ regulates the formation of new blood vessels during angiogenesis (120), and the regulation of leukocyte adhesion and extravasation during inflammation (121,122). However, the exact mechanisms by which the Ca^{2+} ion exerts such far-reaching control lie beyond current understanding.

Cultured cells have provided the majority of results on endothelial Ca^{2+} control. However, cultured cells differ significantly from native cells. The phenotype and the structural and functional characteristics of endothelial cells depend heavily on their environment (cell-cell contacts, hormones, nutrients, mechanical forces, etc.), and as such substantial differences between the behaviour of endothelial cells in culture and those *in situ* are recognised (123). For example, in contrast to the response in native

endothelial cells, muscarinic agonists often fail to increase endothelial $[Ca^{2+}]_i$ (124) or release any EDRFs (125) in cultured endothelial cells. The cell culture process also selectively maintains only the fastest growing subset of the initial population (123).

Nevertheless, cell culture has revealed that the initial response of endothelial cells to chemical, hormonal, or mechanical stimuli, such as changes in shear stress leading to NO production, is an elevation in $[Ca^{2+}]_i$ (117). Furthermore, endothelial cell culture studies have shown that the Ca^{2+}-calmodulin complex tightly regulates NO production, demonstrating that, despite inadequacies, endothelial cell culture remains a powerful and important system for elucidating biological mechanisms. The use of freshly isolated cells overcomes some of the shortcomings of cell culture: native cells respond to ACh with a transient increase in $[Ca^{2+}]_i$, although usually at concentrations greatly exceeding those required to produce elevation in isolated vessels (29,126). The reason for this is rapid loss of cell surface receptors, such as M3 receptors (127), mostly likely due to enzymatic digestion (128,129).

1.2.5 Sources of Endothelial Ca^{2+}

Although cultured endothelial cells have been shown to express voltage-gated sodium channels on their membranes (130–133), endothelial cells are generally considered to be a non-excitable cell-type (134), as they do not produce regenerative events such as action potentials. Nevertheless, $[Ca^{2+}]_i$ is a key regulator of cell function and, like in smooth muscle cells, there are two main routes of entry for Ca^{2+} into the cytosolic space: 1) release from the intracellular store (endoplasmic reticulum, ER); and 2) influx across the plasma membrane from the extracellular space. The two routes of Ca^{2+} entry appear to generate different types of Ca^{2+} signal. Indeed, two main types of Ca^{2+} signals can be distinguished in the endothelium: repetitive oscillations in $[Ca^{2+}]_i$, and biphasic increases in $[Ca^{2+}]_i$ (135). Each of these signals is generated by the interplay of Ca^{2+} release/uptake from the ER and Ca^{2+} entry into the cell. For example, flow-mediated biphasic increases in $[Ca^{2+}]_i$, consist of an initial transient increase in intracellular Ca^{2+} due to release from the ER, followed by a sustained elevation of $[Ca^{2+}]_i$ caused by influx from the extracellular space (117).

1.2.5.1 Intracellular Stores

The ER contains considerable quantities of Ca^{2+} binding proteins. As such, the ER Ca^{2+} concentration ($[Ca^{2+}]_{ER}$) can reach millimolar values (117), although most reports suggest it is in the hundreds of micromolar range. The major Ca^{2+} uptake mechanism on the individual stores is the SERCA pump (Figure 1.4) and, in permeabilised endothelial cells, the ER accounts for approximately 75% of the Ca^{2+} availability (136,137). This imparts an obligatory role of ER Ca^{2+} channels on the control of $[Ca^{2+}]_{i.}$ Many endothelial activators induce an initial transient increase in cytosolic Ca^{2+}. Such agonists, including bradykinin, angiotensin II, serotonin and ACh, induce Ca^{2+} release from the ER in the same manner as SR release in smooth muscle cells. These agonists activate G protein-coupled receptors that, in turn, activate phospholipase C causing hydrolysis of phosphatidylinositol 4,5-biphosphate (PIP_2) into IP_3 and diaglycerol (Figure 1.4)). Subsequent binding of IP_3 molecules to the IP_3 receptor (IP_3R) activates Ca^{2+} channels on the ER, releasing Ca^{2+} into the cytoplasm. Additionally, many studies have presented evidence suggesting a role of RyRs in endothelial Ca^{2+} signalling (e.g. 138,139). However, evidence is not universally supportive and many studies suggest a minor contribution of RyR in agonist-evoked Ca^{2+} signalling, due to the dominant action of IP_3Rs (117).

1.2.5.2 Ca^{2+} Entry

Ca^{2+} entry from the extracellular space serves to sustain chemically- and mechanically-induced endothelial Ca^{2+} responses (140). Several pathways may contribute to Ca^{2+} entry, and subsequent ER store refilling (via SERCA) in endothelial cells (95,114,117; Figure 1.4). These may be classified, according to their ion selectivity, as either highly selective Ca^{2+} ion channels or non-selective Ca^{2+} permeable cation channels. Another classification system is based on the mode of activation of the ion channel. For example, ion channels may be activated by depolarisation of the plasma membrane (voltage-operated channels), agonists (agonist-operated channels), or mechanical stimuli (mechanosensitive ion channels).

Although generally considered a non-excitable cell type, the endothelium may express highly selective voltage-operated Ca^{2+} (Ca_V) channels (141,142). However, these voltage-operated channels are generally thought to be of little functional

importance, as depolarisation of the plasma membrane (with high K^+ solutions) drastically reduces agonist-mediated Ca^{2+} entry instead of increasing it (143), as would be expected for voltage-dependent Ca^{2+} entry. However, recent reports have demonstrated the existence of Ca_V channels in the mesenteric (144) and cerebral (145) vasculature, suggesting that Ca_V channels may indeed have a physiological role in the control of endothelial function.

Agonist-operated channels comprises ion channels that are activated by at least three distinct signalling mechanisms (140): receptor-operated channels, which are activated following the binding of their associated ligand; second-messenger operated channels, which open in response to cytosolic messengers generated by intracellular mechanisms; and store-operated channels, which are activated following the release of Ca^{2+} from the ER by IP_3 or other mechanisms (store-operated Ca^{2+} entry; SOCE). Two distinct receptor-operated channels (non-selective Ca^{2+} channels) have been reported in endothelial cells: the nicotinic ACh receptor (nAChR) and the purinergic P_{2X} receptor. Like Ca_V channels, nAChRs are found mostly in excitable cells, but have also been reported in the endothelium (146) where their function remains unclear. In contrast, the P_{2X} receptor, classically considered as a smooth muscle receptor (147) well associated with the vasoconstrictor properties of ATP, is a known mediator of endothelium-dependent vasodilation (148) and injury-evoked Ca^{2+} signalling in the intact vascular wall (149).

Store-operate channels are perhaps the most prevalent Ca^{2+} entry pathway in endothelial cells. First proposed by Putney in 1986 (150), SOCE is based on the concept that the relationship between current through a Ca^{2+} entry channel, and emptying/refilling of the ER is analogous to that of current through a resistor (channel) and charging/discharging of a capacitor (ER) connected in series. Under physiological conditions, any stimuli that increase IP_3 can deplete the ER of Ca^{2+} and activate SOCE. However, the molecular identity of endothelial store-operated channels is still a matter of debate (140).

In endothelial cells, it is generally considered that SOCE-independent pathways are activated by second messengers or mechanical forces. Many such channels have

been reported. Most, but not all, are members of the transient receptor potential family of nonselective cation channels (140), and may function as both second messenger-operated channels and store-operated channels. For example, mechanical forces activate the non-selective transient receptor potential cation channel, subfamily V, member 4 (TRPV4) directly and indirectly (151). However, in eukaryotic cells no ion channel so far identified as a mechanosensitive channel meets all the criteria required to be considered a transducer of mechanical signals, and may only play a role in the regulation of the response to mechanical stimuli (152).

1.2.5.3 Ca^{2+} Extrusion

Following stimulation of Ca^{2+} release from the ER, a number of mechanisms operate to remove Ca^{2+} from the cytosol (Figure 1.4). These include SERCA on the ER membrane, and the plasmalemmal Na^{+}/Ca^{2+} exchanger and PMCA. The interplay of these extrusion mechanisms and Ca^{2+} release from the ER governs the type of Ca^{2+} response elicited by the endothelium.

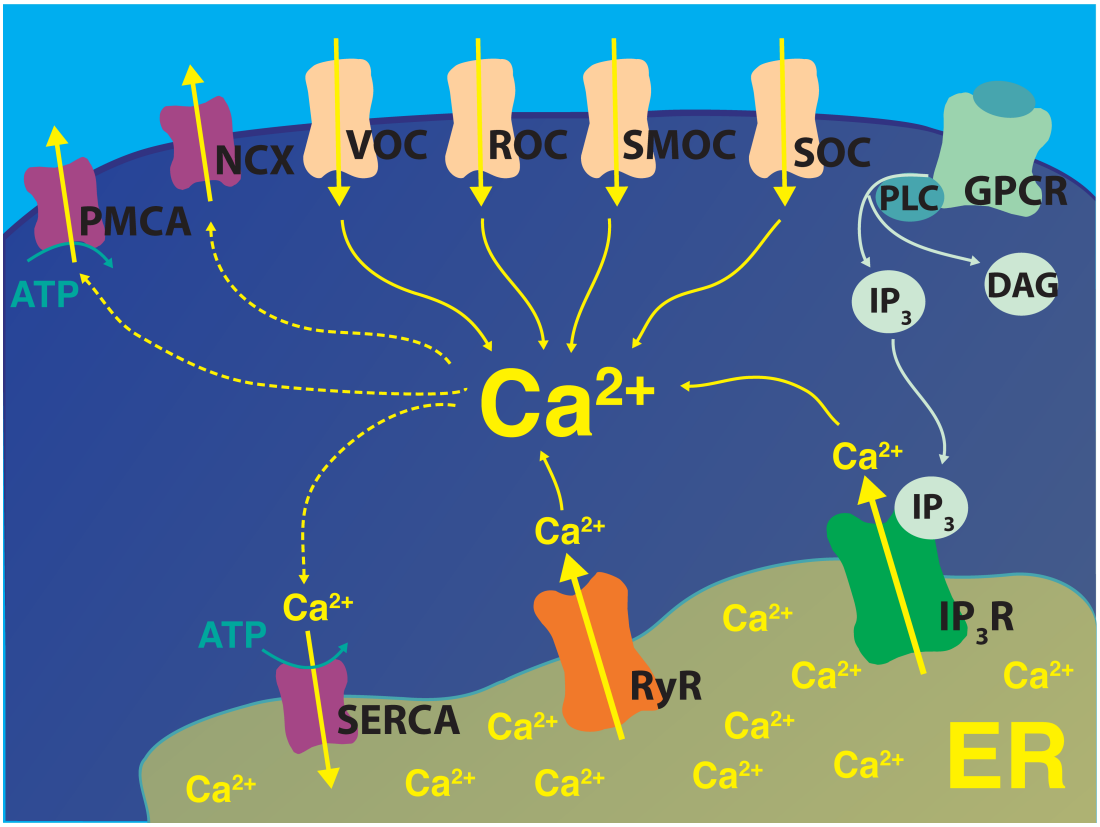

Figure 1.4 – Regulation of endothelial intracellular Ca^{2+} concentration. Endothelial $[Ca^{2+}]_i$ may be regulated by the influx of the ion across the plasma membrane through numerous classifications of ion channels, voltage-operated channels (VOCs), receptor-operated channels (ROCs), second messenger-operated channels (SMOCs) and store-operated ion channels (SOCs). Additionally, Ca^{2+} may be released from the ER by IP_3Rs following, in sequence, activation of G protein-coupled receptors (GPCRs), activation of phospholipase C (PLC), generation of IP_3 and binding of IP_3 to IP_3Rs. Pathways that act to increase $[Ca^{2+}]_i$ are indicated by the solid yellow arrows. The ER also contains ryanodine receptors (RyR), which may be activated by caffeine. Ca^{2+} may be sequestered back into the ER by the sarco/endoplasmic reticulum ATPase (SERCA). Additionally, Ca^{2+} may be pumped back into the extracellular space by the plasma membrane Ca^{2+} ATPase (PMCA) or the Na^+/Ca^{2+} exchanger (NCX). The dashed yellow arrows indicate Ca^{2+} removal pathways (Adapted from (15)).

1.3 Techniques for Assessing Endothelial Function

An abundance of techniques exist to study the function and interactions of endothelial cells. Most assess endothelial cell function indirectly, by relying on a change in smooth muscle performance as a measure of endothelial cell function. Many early studies utilised intravital videomicroscopy as a particularly successful means of assessing endothelium-dependent responses *in vivo*. In different studies, endothelial cell monolayers have been used to evaluate the response of the vasculature to physiological stimuli and pathological stresses, as well as to elucidate the mechanisms that coordinate intercellular action. More recently, enthusiasm for *in vitro* models has grown as recent cell culture advances have enabled endothelial cells and smooth muscle cells to be grown in co-culture models that more accurately mimic *in vivo* conditions compared to single cell-type monolayers or cell suspensions (153,154). Such techniques are widely used as a model for studying systemic arterial endothelial cell and smooth muscle cell behaviour, particularly the study of heterocellular electrical communication as they allow for the formation of MEGJs (155). Despite the large shift towards the use of *in vitro* models of vascular regulation, it is particularly difficult to extend meaningful conclusions to the *in vivo* environment. Explanted vessel preparations, such as arterial strips, ring preparations, and intact arteries are perhaps the most physiologically relevant models to elucidate mechanisms of vascular reactivity in the vessel wall. The discussion below presents the most widely used of such techniques.

1.3.1 Indirect Assessment of Endothelial Function

The isometric ring protocol was first developed by Bevan and Osher in 1972 (156) and further developed by Mulvany and Halpern to include force transducers (157). Vessel segments, cut transversely with a double-bladed scalpel such that they form a ring, are threaded onto stainless steel wires that are subsequently clamped in place. One of the wires is connected to a micrometer to allow precise control of stretch, the other to a force transducer. In this configuration the artery is stretched such that opposing walls are parallel, leading to unphysiological geometry and loading (uniaxial and planar, under zero axial tension). Moreover, the attachment of vessels to the wires may cause significant endothelial injury. However, this preparation

allows arteries to be examined under isometric (constant length) conditions and the sensitivity of tension measurements is exceptional.

To mimic the physiological condition more closely than the wire myograph, the pressure myograph was developed (158). The pressure myograph employs two axially aligned and opposing cannulae, onto which opposite ends of an intact vessel segment can be mounted and secured (with suture thread). This permits *in vivo* loading conditions, such as circumferential stretch and axial tension, to be applied. As opposed to isometric conditions, where tension is recorded, vessel diameter is the measurement variable as it is free to vary under isobaric (constant pressure) conditions. The diameter can be measured using video callipers (158), or online with a number of automated tracking algorithms (159,160).

Both the wire and pressure myographs provide measures of vascular reactivity in physiologically relevant preparations. The choice of technique is usually based on vessel size because percentage diameter changes diminish with vessel size, rendering the pressure myograph most suitable for smaller vessels that exhibit substantial changes in vessel calibre (161). Other reasons for choosing the wire myograph may include the ease and speed with which data may be obtained from multiple preparations and the standardisation of normalisation protocols, whilst the more realistic loading and ability to study the effects of flow may impart a preference for the pressure myograph. It should be noted that both approaches rely on indirect measures to assess endothelial function, i.e. both rely on an ability to measure changes induced by the contractile state of vascular smooth muscle cells, and as such, neither approach adequately captures the intricacies and subtleties of endothelial control of the vascular system.

1.3.2 Direct Assessment of Endothelial Ca^{2+} Signalling

There are two main tools used to image Ca^{2+} signalling in living cells: fluorescent Ca^{2+} indicators (162), and bioluminescent protein-based genetically encoded Ca^{2+} indicators (163). The use of fluorescent Ca^{2+} indicators is particularly widespread due to the ease-of-use of these indicators, which are the results of hybridisation of highly sensitive calcium chelators (e.g. BAPTA and EGTA) with versatile

fluorophores. Upon binding to freely diffusible Ca^{2+}, these indicators undergo intramolecular conformational changes that lead to a change in their spectral properties (164). Depending on the specific fluorophores, these changes may include: shifts in the absorption spectra, shifts in the emission spectra, or increases/decreases in the intensity of fluorescence emission (quantum yield). The choice of fluorophores depends on the specific biological question.

Early studies utilised fluorescent Ca^{2+} indicators to enable fluorometric monitoring of global Ca^{2+} mobilization in the arterial wall. Whilst such studies highlighted the importance of assessing *in situ* Ca^{2+} signalling and provided the first evidence for the presence of two endothelin receptor subtypes in the intact aortic endothelium (165,166), the contribution of single cells is lost. High-resolution charge-coupled device (CCD; widefield) and photomultiplier based (point-scanning) imaging approaches (129) permitted single cell analyses. However, due to the inherently slow rate of two-dimensional image acquisition, localised Ca^{2+} signals and waves are generally analysed using user-defined ROIs from linescan confocal microscopy images, to optimise temporal resolution. Recent technological advances in electron-multiplied CCD cameras and the advent of spinning-disk confocal microscopy have enabled rapid acquisition of two-dimensional images of endothelium yet, to date, there have been few studies directly imaging endothelial Ca^{2+} in pressurised arteries.

Whilst slower and more difficult to implement than indirect approaches, direct measurement of endothelial Ca^{2+} signals have provided a more detailed understanding of endothelial function. Endothelial Ca^{2+} signals are both subtle and complex, and endothelial cells exhibit multiple signalling modalities dependent on the agonist and the level of physiological stimuli (167). Spatiotemporally distinct signals have been identified. These include subcellular transient signals (119,168–170), cell-wide waves (126,167,171) and whole-cell oscillations (123,135). Furthermore, endothelial cells form direct contacts with neighbouring endothelial cells and smooth muscle cells (though homo- and heterocellular gap junction channels, respectively), allowing cells to influence or dictate the response of their neighbours. Indeed, it is proposed that endothelial cells can initiate increases in $[Ca^{2+}]_i$ localised to intimate sites of contact with smooth muscle cells (MEGJs) via

two distinct pathways (119,170). Both result in activation of K^+ channels and endothelial hyperpolarisation that subsequently spreads to smooth muscle cells causing smooth muscle relaxation and have been demonstrated in intact, pressurised arteries (170). Such complexity renders Ca^{2+} signalling a particularly challenging area of endothelial research, and highlights the need to relate complex inter- and intra-cellular Ca^{2+} regulation in intact networks back to, for example, the regulation of vascular tone, as has been done for global measures (172,173). Underlying anatomical information can then be obtained *post hoc* using complementary histological, immunohistochemical, or ultrastructural methods.

The first study of endothelial Ca^{2+} in intact arteries (Figure 1.5) utilised widefield fluorescence microscopy to reveal that endothelial cells respond to ACh with a biphasic $[Ca^{2+}]_i$ response and that shear stress (flow) increased endothelial Ca^{2+} (135). Since then, pressurised artery techniques have expanded to allow the endothelial $[Ca^{2+}]_i$ to be measured concurrently with vessel diameter (174). However, these experiments are technically problematic and have been successful in few cases. To enable dual acquisition of both diameter and endothelial $[Ca^{2+}]_i$ data, the microscope focus is constrained to the mid-plane of the artery such that only a very thin, transverse region of endothelial cells are in focus and Ca^{2+} measurements are usually integrated over the whole field of view. Whilst this approach has provided important systems-level information regarding the biological function, the exact contribution of single cells and intercellular communication are lost, as only a section through a single line of endothelial cells is imaged (167). To enable visualization of multiple, easily distinguishable endothelial cells in a pressurised artery, the plane of focus must be lowered to the bottom of the artery (top when using an upright microscope) (135,175,176,168,169). This approach provides subcellular resolution but, because of light scattering in the artery wall, high excitation powers (that limit acquisition times due to photobleaching) are required. Additionally, the curvature of the artery and the need to use confocal or two-photon imaging to avoid contamination of endothelial $[Ca^{2+}]_i$ signals with those arising from neighbouring smooth muscle cells, constrains the study of endothelial cells to thin-walled, small-

calibre, arteries where the number of cells that can be visualised in a single optical plane is limited (typically fewer than 20 cells (168,169,e.g. 170)).

To combat non-specific dye loading of smooth muscle cells, researchers are increasingly utilising transgenic mice that express the fluorescent Ca^{2+} indicator protein GCaMP2 specifically in endothelial cells (119,170,171,177–179). The distinct lack of fluorescence arising from erroneously labelled smooth muscle cells in the GCaMP2 mouse preparation facilitated specific endothelial Ca^{2+} investigation and permitted the discovery of endothelial Ca^{2+} "sparklets". However, GCaMP2 fluorescence is relatively weak fluorescence when compared to fluorescent chemical Ca^{2+} indicators. This limits signal-to-noise ratios and requires higher laser excitation powers to achieve adequate signals (178).

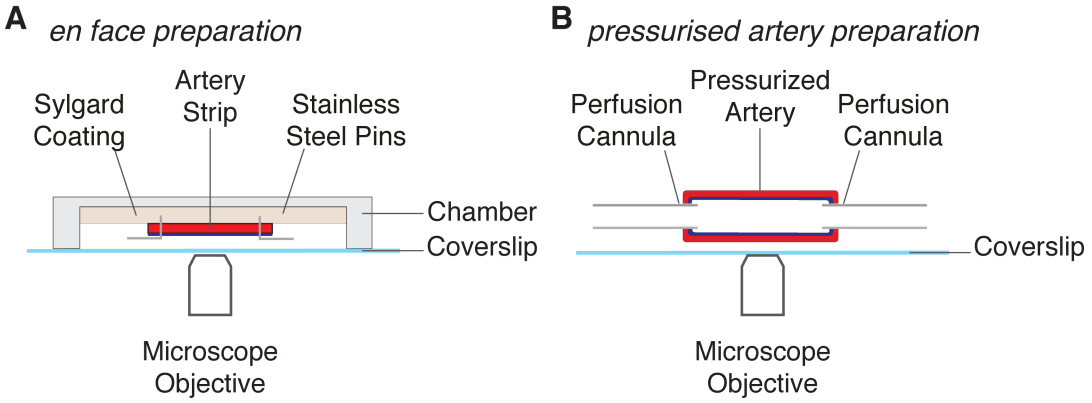

Figure 1.5 – Methods for visualising fluorescently labelled endothelial cells *in situ*. (A) Schematic diagram illustrating the *en face* artery preparation for visualising the endothelium on an inverted microscope. An artery is cut open along the long axis and pinned out in a Sylgard coated chamber, which can be sealed with a coverslip, inverted, and placed on the stage of the microscope. (B) Schematic diagram illustrating the pressurised artery preparation for visualising the endothelium on an inverted microscope. A small-calibre artery is double cannulated and pressurised in a bath chamber that is placed on the microscope stage. By focussing through the arterial wall, the endothelium may be visualised.

In an alternate approach which is compatible with fluorescent Ca^{2+} indicators, the cut open (*en face*) (123,129,173,180,181) artery preparation (Figure 1.5) allows the functional interactions of whole endothelial cell networks (hundreds of cells) to be visualised at high enough spatial and temporal resolutions to relate the signals back to, for example, the regulation of vascular tone (172). This preparation also has the

advantage of enabling concurrent measurement of endothelial membrane potential via patch clamp techniques, revealing the variable extent to which changes in endothelial membrane potential correlate with endothelial $[Ca^{2+}]_i$ (172). The *en face* technique has revealed the heterogeneity of $[Ca^{2+}]_i$ signalling in the endothelium, the differential response of the endothelium to various vasoactive substances (182), and it has revealed that endothelial Ca^{2+} signalling adapts to the hypercholesterolemic environment in the aorta of $ApoE^{-/-}$ mice (183). Whilst the *en face* preparation highlights the complexity of Ca^{2+} signalling in large networks of endothelial cells and revealed their orchestrating influence, the unphysiological configuration of an opened and flattened artery necessitates caution in extrapolating experimental results to the *in vivo* case.

Indeed, arteries configured in their natural pressurised state reproduce *in vivo* responses more faithfully than other *ex vivo* models (184,185). This conclusion is supported by the observation that in cultured cells, higher concentrations of ACh are required to induce rises in endothelial $[Ca^{2+}]_i$ (62), than are required to produce endothelial-induced relaxation in isolated vessels (29). Furthermore, resting $[Ca^{2+}]_i$ in isolated smooth muscle cells are half the value found in the same preparations when measurements are taken from intact pressurised arteries (186), and differences in ACh-induced endothelial Ca^{2+} activity have been reported between intact arteries and freshly isolated sheets of endothelial cells (126). These results further highlight the role of heterocellular communication via functional coupling of smooth muscle/endothelial cells through MEGJs (126,176).

It is also generally agreed that the pressurised artery technique reiterates *in vivo* responses more faithfully than ring preparations (187), where smooth muscle cells are not permitted to shorten. Experiments using isolated cells, cultured cells, and *en face* arterial strips all indicate that mechanosensitive mechanisms contribute to the endothelial response, but the nature of any mechanosensor, and any integrated response, is unresolved. This is partly because neither methodology reproduces the output of a complex, cylindrical network of endothelial cells. This places the onus on studying the endothelium in its natural state – a cylindrical network of cells in an

intact tubular artery where interactions with other cell types, physiological mechanical forces and native receptor expression are all maintained. However, the aforementioned limitations of current optical techniques for assessing endothelial Ca^{2+} signalling in intact arteries prevent imaging of the endothelium in large arteries, thus precluding assessment of endothelial changes in $[Ca^{2+}]_i$ in large networks in physiological conditions.

1.4 Summary

Studies of endothelial cells in culture have now linked the endothelium to the production and the regulation of a myriad of messengers controlling vascular tone (117). There is universal agreement that almost all aspects of cardiovascular homeostasis are intimately linked to endothelial Ca^{2+} signalling: the formation of new blood vessels during angiogenesis (120), the clotting of blood in thrombosis (188), the control of blood pressure due to vascular tone (92), and the regulation of leukocyte adhesion and extravasation during inflammation (189). However, the isolation of individual endothelial cells and their subsequent culture provides a model that is far removed from the complex and distributed topology of the intact endothelium that appears necessary for function. As a result, our appreciation of the normal behaviour of the endothelium, specifically the dynamic interactions that occur among endothelial cells and the interplay between endothelial cells and smooth muscle cells, is lacking. Significantly, the endothelium is acknowledged to be a spatially heterogeneous system that acts as a functional syncytium (190,191), and the tacit assumption that a homogeneous layer of cultured cells, grown on a plastic substrate, can approximate the properties of an *in vivo* cell network is unwarranted.

Two techniques have emerged to study inter- and intra-cellular endothelial Ca^{2+} signalling in intact arteries: the *en face* artery preparation, where arteries are surgically opened and laid out flat for microscopic examination; and the isolated pressurised artery preparation, where the endothelium is monitored by focussing through the wall of arteries that have been pressurised between two cannula. These complementary approaches to visualising endothelial Ca^{2+} have separately

contributed a number of important insights into endothelial Ca^{2+} control. However the respective advantage - either maintenance of physiological forces or visualisation of large networks – are exclusive and come at the expense of the other. For example, high-speed fluorescence imaging (wide-field and confocal) of open artery preparations permits large fields of endothelial networks to be visualised with high-resolution, but the influence of the physiological structure of the artery is lost due to the artificial mechanical forces imposed. Similarly, fluorescence imaging of endothelial cells in pressurised arteries permits subcellular Ca^{2+} measurements under the influence of physiological mechanical forces and of neighbouring tissues, however optical penetration depths limit this technique to the study of arteries with thin walls and, consequentially, the number of cells visible/size of endothelial network visible is limited to around 10-20 individual endothelial cells. A complete understanding of endothelial Ca^{2+} signalling, and its effects of vascular function, requires methods to study the endothelium as a whole functional network in large arteries under physiological mechanical forces.

Recently, cylindrically shaped gradient-index (GRIN) lens microprobes have been established as a valuable tool for imaging physiological processes *in vivo*. For example, GRIN lenses have been used to visualise neuronal Ca^{2+} activity in freely moving mice (192), image the rapid infiltration of circulating monocytes in the infarcted heart (193), and map the vasculature of the colon in three dimensions (194). However, despite their cylindrical shape rendering them almost perfect for the insertion into blood vessels, these lenses have never been used to provide an unobstructed view of the endothelium.

In this regard, this thesis first presents a summary of the most relevant knowledge of Ca^{2+}-dependent regulation of vascular homeostasis, with a specific focus on the role of the endothelium and the techniques currently used to study endothelial Ca^{2+} signalling. Chapter 2 describes novel instrumentation employing single-photon fluorescence microscopy and GRIN lenses designed to image large areas of endothelium in intact and pressurised arteries subject to physiological pressures and mechanical forces. Chapter 3 presents a novel image processing procedure and algorithm for extracting cellular Ca^{2+} signals from the data obtained from functional

imaging experiments. Chapter 4 describes experiments performed to characterise the Ca^{2+} response of endothelial cells in intact and pressurised artery upon chemical activation. Chapter 5 describes experiments performed to characterise how mechanical forces, resulting from transmural pressure, modulate the endothelial Ca^{2+} response in large, intact and pressurised arteries. Chapter 6 presents experiments performed to elucidate the effects of ageing on endothelial Ca^{2+} signalling in large, intact and pressurised arteries. Finally, Chapter 7 presents a brief summary of the work contained within the preceding chapters and suggests areas for future work.

Chapter 2. Gradient-index System for Luminal Imaging of the Endothelium of Intact, Pressurised Arteries

2.1 Introduction

Scientific theory and technological development display a synchronicity whereby the evolution of one is mirrored and impacted upon by the other. This is all too evident in the history of endothelial research. Prior to 1973, successful endothelial cell culture techniques did not exist and an integrated approach to vascular biology prevailed – one in which the ultrastructure and physiology of the endothelium were studied in the context of the intact blood vessel or of whole animals (195). Reliable endothelial cell culture is widely held to mark the beginnings of modern vascular biology (196). However, the arterial wall exhibits properties that are specific to individual native microenvironments and, as a result of endothelial plasticity and heterogeneity, conflicting conclusions regarding biological mechanisms have arisen from cell culture models (197). As such, the usefulness of endothelial culture models - *in isolation* - is diminishing, and an appreciation of studying cells in their physiological environment has begun anew. New and powerful techniques have been developed so that endothelial function can be assessed in whole artery preparations and in whole animals. These techniques include molecular imaging of specific endothelial disease markers (198) and functional assessment of the endothelium using ultrasound (199).

Of the techniques developed, fluorescence microscopy is now one of the most commonly used tools in biomedical research, particularly due to its ease of use, and the specificity and robustness of the many fluorescent probes available. A range of Ca^{2+} indicators and optical techniques now exist that permit the study of native endothelial $[Ca^{2+}]_i$ in preparations ranging from isolated endothelial cells (126) and endothelial tubes (167) to explanted (135,168,174) and *in vivo* (171,200) vessels. These methods have illustrated the significance of Ca^{2+} in the control of endothelial function. Numerous studies have demonstrated the cross-level interdependence and integrated nature of Ca^{2+} signals, initiated at the cellular level, in multicellular endothelial networks (e.g. 167,171,201). Of particular relevance to the collective endothelial response is the complexity of dynamic signalling that is dependent upon the interconnected arrangement of endothelial cells (169,202). However, this dependence has so far only been open to investigation in limited cell populations

experiencing true mechanical forces, or in large cell populations under artificial conditions. Central to this problem, both the curvature of intact arteries and light scattering by the artery wall limit the study of endothelial cells in intact arteries to thin-walled, small-calibre vessels where the number of cells that can be visualised in a single optical plane is limited. Previous two-photon studies of fluorescently labelled endothelial cells (non Ca^{2+}) in large arteries have been limited to acquisition speeds of 0.1 Hz (203–205). In these investigations the maximum field of view (FOV) was 309 × 309 μm with a theoretical depth of field (DOF) of 0.9 μm. Even in rapid scanning, optically-sectioning systems (206), imaging rates are too slow (typically 0.375 s for 30 planes at 80 Hz) to adequately record Ca^{2+} activity in large populations of endothelial cells in a large, intact, cylindrical artery with sufficient spatial resolution. Thus, only a small number of cells can be imaged at adequate speed and resolution with conventional approaches. To overcome this, alternative imaging strategies are required.

2.1.1 Application of GRIN Lenses to Biological Imaging

Recent strides in confocal and two-photon imaging have enabled imaging of neuronal Ca^{2+} activity in head-restrained, awake animals (207), and of the *in vivo* structure of the full vessel wall of large arteries (208). However, the scattering of light by biological tissue restricts imaging to superficial tissues, or prevents examination of fast physiological processes. Recently, a range of innovative optical methods for increasing the functionality of optical microscopy has been developed (209–212). Of these, optical microendoscopy using GRIN lenses provides more minimally-invasive and deeper access to tissue than any other current technique (213).

The seeds of development for GRIN lenses in *in vivo* fluorescence imaging were planted by early uses of GRIN lenses for fundoscopy (214) and the study of intrinsic electrical signals in the rodent brain (215,216). Nowadays, numerous GRIN microendoscope designs exist and have collectively provided a wealth of information from tissues that were previously inaccessible. For example, front-viewing single-photon probes have been used to visualise neuronal activity using voltage sensitive fluorescent dyes (217) and provide high speed imaging of cerebral microcirculation

and dendritic Ca^{2+} spiking in freely-moving mice (192). These probes enable imaging of a plane parallel to the front face of the cylindrically shaped GRIN lens. Two-photon approaches are perhaps more widespread, due to their optical sectioning capabilities, and have enabled deep *in vivo* imaging of many tissues (e.g. brain, spleen, kidney and liver (218)). GRIN lenses can also be used for studying disease progression, as has been demonstrated by time-lapse imaging of glioma angiogenesis (219). This study was facilitated by the chronic implantation of guide tubes that allowed repeatable measurements to be taken from multiple animals using a single lens. Side-viewing GRIN microprobes have also been reported, where the viewing direction is changed by attaching a prism to the front surface of the GRIN lens. Side-view probes have been used for enabling single photon imaging of Ca^{2+} activity in Layer 5 apical dendrites (220,221), and large-area 360 degree imaging of tubular organs (194,218,222). The latter has enabled the vascularization of the descending colon of anaesthetised mice/rats to be mapped in three dimensions (194). Side-viewing GRIN microprobes have also been applied to the study of murine respiratory tract regeneration following injury (222), and have been used clinically to image breast cancer tumours in humans *in vivo* (223).

Here we extend the application of GRIN lenses to provide unobstructed fluorescence imaging of the endothelium, from within the lumen of large, intact, pressurised arteries.

2.2 Methods

2.2.1 GRIN Optics

Although a relatively recent technology (GRIN lenses are in essence the precursor to optical fibres), many eye lenses, including in humans, are of a GRIN construct (224). The term gradient-index applies to optical materials that have a varying refractive index profile. As a consequence of this, optical rays travelling within GRIN media follow curved trajectories. Conventional optical components utilise discrete changes of refractive index to refract light according to Snell's law. Thus, traditional lens fabrication requires precise control of curved surfaces to achieve specific control of light. In contrast, GRIN lenses can be fabricated with planar faces. With careful control of the material properties of the GRIN substrate, these lenses can be fabricated with equivalent performance to traditional lenses. Most commonly, GRIN lenses are formed from glass cylinders whose refractive index varies with radial position from the optical axis in accordance with a continuous function ***n(r)***. A special case of such a lens, the cylindrically shaped self-focussing (SELFOC®) lens (225–227), has a refractive index that falls approximately quadratically with radial distance, r, from the optical axis (Figure 2.1A), governed by the following equation:

$$n(r) = n_0(1 - \frac{A}{2}r^2) \qquad \textbf{(2.1)}$$

where n_0 is the refractive index along the optical axis, and A is the squared refractive index gradient constant. Under the paraxial approximation (i.e. $\sin(\theta) \approx \theta$), the imaging properties of a GRIN lens may be analysed using ray propagation matrices. For a GRIN media of length, z, the ABCD matrix of a grin lens may be shown to be:

$$\begin{pmatrix} \cos\left(\sqrt{A}z\right) & \frac{1}{\sqrt{A}}\sin\left(\sqrt{A}z\right) \\ -\sqrt{A}\sin\left(\sqrt{A}z\right) & \cos\left(\sqrt{A}z\right) \end{pmatrix} \qquad \textbf{(2.2)}$$

It follows that light rays travelling in a SELFOC® GRIN lens follows a sinusoidal path. The fraction of a full sinusoidal cycle that a ray traverses in a lens is known as the pitch length, P, and is governed by:

$$2\pi P = z\sqrt{A} \tag{2.3}$$

Thus, SELFOC® lenses of various diameters and lengths can be tuned to achieve specific optical behaviour Figure 2.1B. For example, a quarter pitch lens focuses a collimated beam to a point on the distal surface of the lens, whilst the focus of a lens slightly shorter than $P = 0.25$ will be slightly beyond the distal surface, and a single pitch lens acts as a simple relay lens.

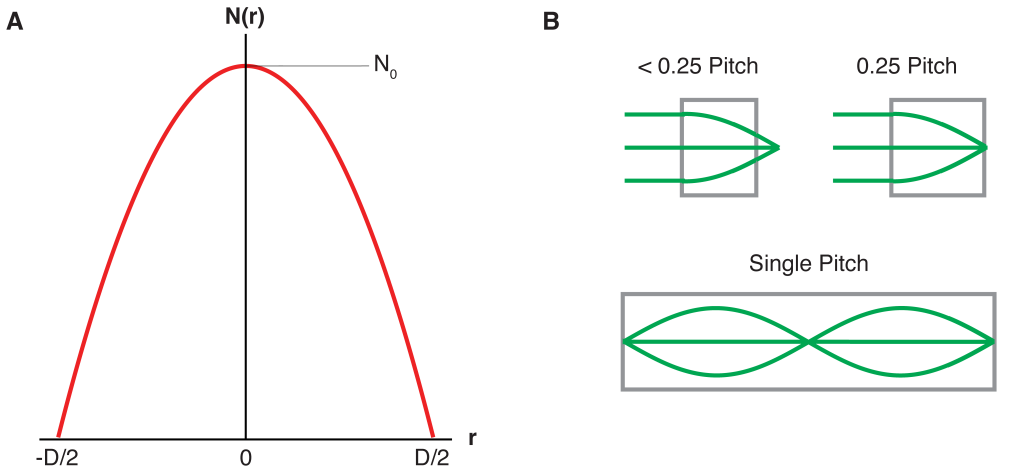

Figure 2.1 – Imaging properties of gradient-index (GRIN) lenses. (A) Refractive index profile of a cylindrically shaped GRIN (SELFOC®) lens. The refractive index is highest along the central (optical) axis of the lens and decreases approximately quadratically with radial distance. (B) Ray diagrams for GRIN lenses of various pitch lengths. Dependent on the length of the lens and gradient constant, lenses can be used as collimating (top left and right), imaging lenses, or relay lenses (bottom). Combining various lenses into doublet, or even triplet, probes further increases the range of applications.

The versatility of GRIN lenses permits a wide variety of probe designs. Previously, GRIN microendoscopes have been used in a wide variety of *in vivo* imaging applications, for example to permit *in vivo* imaging of the brain (212). Such probes typically utilise high (~0.5) NA GRIN lenses for high-resolution imaging. Due to manufacturing constrains, these high NA lenses are short in length (typically less than 5 mm (213)). However, optimal design depends on a range of interdependent factors: probe dimensions, image resolution, imaging speed, FOV, DOF, and viewing direction. Thus, although a high numerical aperture (NA) is preferred to maximise resolution, the delivery of excitation light, and the collection of the fluorescence

emission, long probes may be required to meet mechanical constraints posed by the depth of tissue under examination.

In conventional fluorescence microscopy, microscope objectives with NA > 0.8 are typically used; however the NA of a GRIN lens is limited by the refractive index gradient achievable without huge optical distortion, and typically does not exceed 0.5. Thus, where a long probe is required, high NA imaging lenses are attached in series to a weaker GRIN lens of lower NA (Figure 2.2). The GRIN probes are then coupled to a conventional microscope system. Depending on the imaging modality and, where necessary, the illumination/scanning strategy, the relay lens is chosen to be either a quarter or half pitch (212). Additional length may be achieved by adding integer half-pitch lengths to the relay lens. Thus, high NA microendoscopic imaging is achievable, however the combination of lenses results in a FOV that is a fraction of the cross-sectional area of the lens itself. A number of microprobes have been designed which can be easily integrated into standard wide-field epi-fluorescence, confocal, or two-microscopes. In terms of construction, these probes can be classified according to the number of GRIN lens elements used (singlet, doublet, triplet; Figure 2.2A), and according to the viewing direction (front-view or side-view).

A

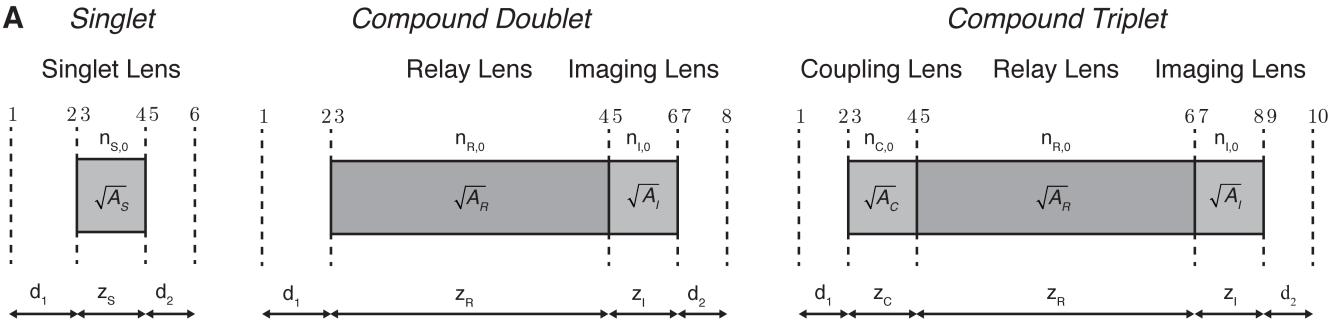

B

$$\begin{pmatrix} A & B \\ C & D \end{pmatrix}_{Singlet} = M_{56}M_{45}M_{34}M_{23}M_{12}$$

$$\begin{pmatrix} A & B \\ C & D \end{pmatrix}_{Singlet} = \begin{pmatrix} 1 & d_2 \\ 0 & 1 \end{pmatrix}\cdot\begin{pmatrix} 1 & 0 \\ 0 & \frac{n_{S,0}}{n_2} \end{pmatrix}\cdot\begin{pmatrix} \cos\left(\sqrt{A_S}z_S\right) & \frac{1}{\sqrt{A_R}}\sin\left(\sqrt{A_S}z_S\right) \\ -\sqrt{A_S}\sin\left(\sqrt{A_S}z_S\right) & \cos\left(\sqrt{A_S}z_S\right) \end{pmatrix}\cdot\begin{pmatrix} 1 & 0 \\ 0 & \frac{n_1}{n_{S,0}} \end{pmatrix}\cdot\begin{pmatrix} 1 & d_1 \\ 0 & 1 \end{pmatrix}$$

$$\begin{pmatrix} A & B \\ C & D \end{pmatrix}_{Doublet} = M_{78}M_{67}M_{56}M_{45}M_{34}M_{23}M_{12}$$

$$\begin{pmatrix} A & B \\ C & D \end{pmatrix}_{Doublet} = \begin{pmatrix} 1 & d_2 \\ 0 & 1 \end{pmatrix}\cdot\begin{pmatrix} 1 & 0 \\ 0 & \frac{n_{I,0}}{n_2} \end{pmatrix}\cdot\begin{pmatrix} \cos\left(\sqrt{A_I}z_I\right) & \frac{1}{\sqrt{A_I}}\sin\left(\sqrt{A_I}z_I\right) \\ -\sqrt{A_I}\sin\left(\sqrt{A_I}z_I\right) & \cos\left(\sqrt{A_I}z_I\right) \end{pmatrix}\cdot\begin{pmatrix} 1 & 0 \\ 0 & \frac{n_{R,0}}{n_{I,0}} \end{pmatrix}\cdot\begin{pmatrix} \cos\left(\sqrt{A_R}z_R\right) & \frac{1}{\sqrt{A_R}}\sin\left(\sqrt{A_R}z_R\right) \\ -\sqrt{A_R}\sin\left(\sqrt{A_R}z_R\right) & \cos\left(\sqrt{A_R}z_R\right) \end{pmatrix}\cdot\begin{pmatrix} 1 & 0 \\ 0 & \frac{n_1}{n_{R,0}} \end{pmatrix}\cdot\begin{pmatrix} 1 & d_1 \\ 0 & 1 \end{pmatrix}$$

$$\begin{pmatrix} A & B \\ C & D \end{pmatrix}_{Triplet} = M_{910}M_{89}M_{78}M_{67}M_{56}M_{45}M_{34}M_{23}M_{12}$$

$$\begin{pmatrix} A & B \\ C & D \end{pmatrix}_{Triplet} = \begin{pmatrix} 1 & d_2 \\ 0 & 1 \end{pmatrix}\cdot\begin{pmatrix} 1 & 0 \\ 0 & \frac{n_{I,0}}{n_2} \end{pmatrix}\cdot\begin{pmatrix} \cos\left(\sqrt{A_I}z_I\right) & \frac{1}{\sqrt{A_I}}\sin\left(\sqrt{A_I}z_I\right) \\ -\sqrt{A_I}\sin\left(\sqrt{A_I}z_I\right) & \cos\left(\sqrt{A_I}z_I\right) \end{pmatrix}\cdot\begin{pmatrix} 1 & 0 \\ 0 & \frac{n_{R,0}}{n_{I,0}} \end{pmatrix}\cdot\begin{pmatrix} \cos\left(\sqrt{A_R}z_R\right) & \frac{1}{\sqrt{A_2}}\sin\left(\sqrt{A_R}z_R\right) \\ -\sqrt{A_2}\sin\left(\sqrt{A_R}z_R\right) & \cos\left(\sqrt{A_R}z_R\right) \end{pmatrix}\cdot\begin{pmatrix} 1 & 0 \\ 0 & \frac{n_{C,0}}{n_{R,0}} \end{pmatrix}$$
$$\cdot\begin{pmatrix} \cos\left(\sqrt{A_C}z_C\right) & \frac{1}{\sqrt{A_C}}\sin\left(\sqrt{A_C}z_C\right) \\ -\sqrt{A_C}\sin\left(\sqrt{A_C}z_C\right) & \cos\left(\sqrt{A_C}z_C\right) \end{pmatrix}\cdot\begin{pmatrix} 1 & 0 \\ 0 & \frac{n_1}{n_{C,0}} \end{pmatrix}\cdot\begin{pmatrix} 1 & d_1 \\ 0 & 1 \end{pmatrix}$$

C

$$M_{Singlet} = \cos\left(\sqrt{A_S}z_S\right) - \frac{d_2 n_{S,0}\sqrt{A_S}\sin\left(\sqrt{A_S}z_S\right)}{n_2}$$

$$M_{Doublet} = \left(\cos\left(\sqrt{A_I}z_I\right) - \frac{d_2 n_{I,0}\sqrt{A_I}\sin\left(\sqrt{A_I}z_I\right)}{n_2}\right)\cos\left(\sqrt{A_R}z_R\right) - \frac{1}{n_{I,0}}\left(\frac{\sin\left(\sqrt{A_I}z_I\right)}{\sqrt{A_I}} + \frac{d_2 n_{I,0}\cos\left(\sqrt{A_I}z_I\right)}{n_2}\right)n_{R,0}\sqrt{A_R}\sin\left(\sqrt{A_R}z_R\right)$$

$$M_{Triplet} = \left(\left(\cos\left(\sqrt{A_I}z_I\right) - \frac{d_2 n_{I,0}\sqrt{A_I}\sin\left(\sqrt{A_I}z_I\right)}{n_2}\right)\cos\left(\sqrt{A_R}z_R\right) - \frac{1}{n_{I,0}}\left(\frac{\sin\left(\sqrt{A_I}z_I\right)}{\sqrt{A_I}} + \frac{d_2 n_{I,0}\cos\left(\sqrt{A_I}z_I\right)}{n_2}\right)n_{R,0}\sqrt{A_R}\sin\left(\sqrt{A_R}z_R\right)\right)\cos\left(\sqrt{A_C}z_C\right)$$
$$-\frac{1}{n_{R,0}}\left(\frac{1}{\sqrt{A_R}}\left(\cos\left(\sqrt{A_I}z_I\right) - \frac{d_2 n_{I,0}\sqrt{A_I}\sin\left(\sqrt{A_I}z_I\right)}{n_2}\right)\sin\left(\sqrt{A_R}z_R\right) + \frac{1}{n_{I,0}}\left(\frac{\sin\left(\sqrt{A_I}z_I\right)}{\sqrt{A_I}} + \frac{d_2 n_{I,0}\cos\left(\sqrt{A_I}z_I\right)}{n_2}\right)n_{R,0}\cos\left(\sqrt{A_R}z_R\right)\right)n_{C,0}\sqrt{A_C}\sin\left(\sqrt{A_C}z_C\right)$$

Figure 2.2 – Numerical analysis of various GRIN probe designs. (A) Schematic diagram of a singlet (left), doublet (middle), and triplet (right) microprobe. (B) ABCD ray transfer matrices for corresponding microprobes. (C) Magnification equations calculated from ABCD ray transfer matrices presented in B. In all equations subscripts R, C and I indicate the constants for the relay, coupling or imaging lens, respectively.

2.2.1.1 GRIN Probe Design

To calculate the properties of possible probe designs, we computed the ABCD matrices for front viewing singlet, doublet, and triplet probes (Figure 2.2B) with refractive indices governed by equation 2.1. Previous examples of this analysis have calculated matrices for probes immersed in a homogenous medium (212) or air (228). We extend the analysis to distinct media at either end of the probe – as is the case in most GRIN imaging applications. To calculate the transverse magnification, M_T, of the various probes we apply the definition, $M_T = d_2/d_1$, which implies that, for each probe matrix, M_T = A. Equations for magnification for three variations of probe (singlet, doublet, and triplet) are given in Figure 2.2C. From these equations, and equation 2.3 it can be shown that there are only a few cases in which the magnification is invariant of the object-lens spacing.

For a singlet lens, the magnification is equal to unity for all lenses of length equal to any integer multiple of 1/2*P*. However, for other lens lengths magnification is a function of focal distance (d_2). In the case of a doublet probe, the relay lens is usually chosen to be of a length that is 1/4*P* modulo 1/2*P* (i.e. 1/4*P*, 3/4*P*, 5/4*P*...), such that light focussed on the proximal face of the relay lens is refocused at the front surface of the imaging lens (imaging lens pitch, $P_I = 0.25$) or slightly beyond (imaging lens pitch, $P_I < 0.25$). Such a design facilitates integration of the probe into the optical path of a conventional microscope (widefield, confocal, or two-photon). In this use, the distal face of the probe may be placed at the focal point of a traditional microscope, allowing the focal plane (projected onto the sample by the GRIN probe) to be adjusted without moving the probe or the sample, and the magnification simplifies to:

$$\left|Mag_{Doublet}\right| \coloneqq \frac{n_{R,0}\sqrt{A_R}\left(d_2 n_{I,0}\cos\left(\sqrt{A_I}z_I\right)\sqrt{A_I}+\sin\left(\sqrt{A_I}z_I\right)n_2\right)}{n_{I,0}\sqrt{A_I}n_2} \qquad \textbf{(2.4)}$$

which is constant only for $P_I = 0.25$, in which case:

$$\left|Mag_{Doublet,P_I=0.25}\right| = \frac{n_{R,0}\sqrt{A_R}}{n_{I,0}\sqrt{A_I}} \tag{2.5}$$

In the triplet configuration, the relay lens is chosen to be of length that is 1/2*P* modulo 1/2*P* and the coupling lens is chosen to be of quarter pitch length (P_C = 0.25) such that light focussed on the proximal face of the coupling lens is refocused at the front surface of the imaging lens (imaging lens pitch, P_I = 0.25) or slightly beyond (imaging lens pitch, P_I < 0.25). In this case, the magnification is constant only if the imaging lens length is equal to that of the coupling lens (P_I = 0.25). This magnification is given by:

$$\left|Mag_{Triplet=0.5,C=0.25,I=0.25}\right| \coloneqq \frac{n_{C,0}\sqrt{A_C}}{\sqrt{A_I}\,n_{I,0}} \tag{2.6}$$

which is unity for imaging and coupling lenses made of the same GRIN substrate.

It follows that most GRIN microprobes are designed to operate at fixed object-lens spacing, and with a specific magnification and FOV. For the doublet probes, this FOV is approximately proportional to the diameter of the probe multiplied by the ratio of the imaging lens pitch length to the objective pitch length (229). The same is true for the triplet probe, as the relay lens acts as an aperture for both the imaging and coupling lenses. Thus, such probes trade a reduction in FOV for a gain in resolution (NA) at a specific focal depth.

In our goal of imaging Ca^{2+} activity of large areas of endothelium in large, pressurised arteries there are numerous requirements:

1. The probe must be side viewing.
2. The imaging system must have an adjustable focus mechanism such that focus can be adjusted according to changing artery dimensions, in order to image the endothelium of arteries of various diameter (i.e. a vessel at various physiological pressures),
3. The probe must possess a large FOV, and a DOF that is sufficient to image a large curved surface (i.e. a large number of endothelial cells in an intact artery).

4. The magnification must be invariant of focal depth, such that a constant FOV is achieved regardless of vessel diameter.
5. The outer probe dimensions must be slightly smaller than the lumen diameter of the artery of interest.
6. The probe must be long enough to be accommodated through a port in the wall of the chamber, in which the artery is held, and into the lumen of a vessel.

As doublet and triplet probes fail to meet our requirements, we instead employ a single pitch GRIN relay lens (NA = 0.084, M_T = 1), with a micro-prism to facilitate side-view imaging, to reconjugate the image plane of detection optics through the length of the cylinder. To provide adequate length, we chose a 0.5 mm diameter (FOV = 0.5 mm), 30.2 mm lens (SRL-050; GoFoton!, USA), and to facilitate side-viewing we chose a 0.5 mm x 0.5 mm x 0.5 mm aluminium coated micro-prism (66-771; Edmund Optics, USA). By focusing to a sufficient depth inside the single pitch GRIN relay lens with traditional detection optics, the image plane can be extended beyond the front surface of the probe (216), as shown in Figure 2.3A, without a change in magnification. The use of a low NA GRIN relay lens imposes two constraints on the delivery of excitation light through our system. First, to maximise the delivery of excitation light through the GRIN rod, the NA of the excitation light should not be greater than the NA of the GRIN lens. Secondly, to maximise the fluorescence detection, the NA of the collection lens should be higher than that of the GRIN rod. Additionally, excitation illumination of the endothelium should be independent of the distance between the microprobe and the endothelium, for proper illumination of vessels at various pressures (i.e. diameters). The solution to these opposing constraints is to illuminate the proximal end of the GRIN lens with collimated light, which is re-collimated at the output towards the object plane (Figure 2.3B) illuminating the entire FOV (230).

2.2.2 Microprobe Construction

In preliminary experiments, we obtained GRIN lenses, enclosed in stainless steel sheaths, direct from the manufacturer. However, the adhesive used to secure the lenses emitted severe fluorescence when illuminated at 488 nm, which significantly reduced the performance of our system. Thus we abandoned the use of pre-fabricated lens assemblies and opted to construct our own. For mechanical protection, a 30.2 mm long GRIN relay lens (SRL-050; GoFoton!, USA) was fixed in a surgical stainless steel tube (0.51 inner diameter, 0.71 mm outer diameter, 27 mm length; Cooper Needle Works, Ltd, UK). The sheath was secured to the GRIN lens with ultraviolet (UV) curing optical epoxy (NAO 63; Norland Products, USA), with the distal face of the lens flush with the end of the sheath. This operation was facilitated by the use of a three-axis stage equipped with optical fibre holders. Three millimetres of the lens was left protruding from the proximal end of the protective sheath, to ensure that the conjugate plane of detection optics was not placed near the face of the protective sheath or any epoxy. This eliminated detection of unwanted fluorescence and or backscattered excitation light, due to possible misalignments in the optical system. To complete the probe construction, the sheathed lens was mounted vertically under a dissection microscope, a small bead of epoxy was placed on the surface of the GRIN lens, and the micro-prism was positioned using fine surgical forceps before curing of the epoxy. The epoxy was applied by dipping the point of a needle into epoxy, and then gently bringing the epoxy on the needle into contact with the GRIN lens. Epoxy and micro-prism placement were facilitated by the use of two orthogonally mounted dissection microscopes. The ultraviolet epoxy was cured using a portable UV light gun for 5 minutes. The assembled microprobe is pictured in Figure 2.3F.

2.2.3 Vessel Bath

The assembled GRIN microprobe was introduced into a custom-designed, 10 ml volume imaging bath (Figure 2.3G) through a port in the side wall, and held in place using a Super Flangeless fitting (M-644-03 Nut, M650 Ferrule, F232 0.786 mm OD tubing; IDEX Health and Science LLC, USA). A custom, blunted 22G cannula was mounted in the bath using an arm connected to a miniature, 3-axis translation stage

(DT12XYZ; Thorlabs, UK) that was mounted on the opposite end of the bath from the microprobe. An optical rail, fixed along the length of the bath permitted a second cannula to be introduced to the chamber. Both cannulae were connected, via Tygon tubing, to individual three-way vales. The total volume of the bath was 10 ml. A cover slip fixed in a viewing hole in the bottom of the chamber, permitted direct conventional imaging on an inverted microscope.

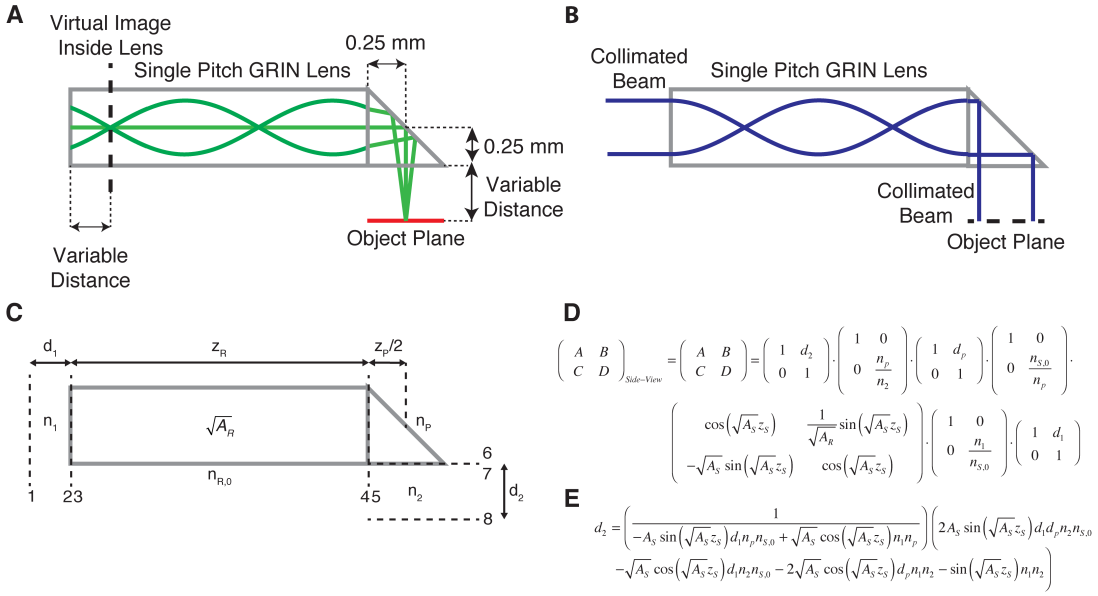

Figure 2.3 – Optical configuration of GRIN microprobe. (A) Simplified optical ray diagram illustrating imaging capabilities of a side-viewing single-pitch GRIN lens microprobe. (B) Simplified optical ray diagram illustrating the delivery of collimated laser excitation by our side viewing single-pitch GRIN lens microprobe. (C) Schematic diagram of the side viewing single-pitch GRIN microprobe with labels illustrating parameters used for ABCD matrix analysis. (D) ABCD ray transfer matrix for the side-viewing single-pitch GRIN lens microprobe. (E) Equation relating the distance beyond the proximal face, d_1, that a virtual image of a surface a distance, d_2, beyond the distal prism surface, is formed. (F) Image of the distal end of the GRIN microprobe. (G) 3-dimensional rendering of the custom-imaging bath designed to permit endothelial imaging. (H) 3-dimensional rendering illustrating how the side viewing microprobe enables endothelial imaging. Note the outer dimension of the GRIN probe is 0.71 mm.

2.2.4 Imaging System

The fluorescence excitation/delivery system was constructed using a cage system (30 *mm*; Thorlabs, UK) mounted on a 3-axis, micrometer driven translation stage (DT12XYZ; Thorlabs, UK). The system was fixed to the stage of an inverted microscope (TE300, Nikon), permitting coupling of the GRIN microprobe to the imaging system by mounting the imaging bath on the stage using custom fixation blocks. This design permitted standard imaging through the viewing hole, and allowed movement of the microscope stage or GRIN imaging system (for focussing) without decoupling the optics. In detail, 6% (3 mW) of the available power from a remote diode pumped solid-state laser operating at 488 nm (50 mW Vortran Stradus; Vortran Laser Technology Inc., USA) was coupled into a single mode fiber (P1-405A-FC-2; Thorlabs, UK) using a fixed-focus fibre-coupling lens (F230FC-A; Thorlabs, UK). The other end of the fibre was connected to the microscope-mounted optical system. Light exiting the fibre was collimated (L2; Figure 2.4A) before being focused by another lens (L3; Figure 2.4A) and guided to the back of a 20X 0.5NA infinity-corrected microscope objective (Plan Fluor; Nikon, UK) via a dichroic mirror (FF499-Di01; Semrock, USA). The focal lengths of L1 and L2 were chosen such that the beam emerged from the microscope objective collimated to 0.5mm diameter. Additionally, the objective lens was chosen for its long (2 mm) working distance - permitting imaging up to 1.5 mm past the distal face of micro-prism and necessary to image past the distal face or the microprobe. The microscope objective and a 65 mm focal length tube lens imaged fluorescence emission, returning through the probe, through an emission filter (FF01-530/43; Semrock, USA) and onto an sCMOS camera (Zyla 3-Tap; Andor, UK). The deviation in tube lens focal length from the manufacturer's reference length of 200 mm resulted in an effective magnification of 6.5X and an effective pixel size of 1 μm at the object plane.

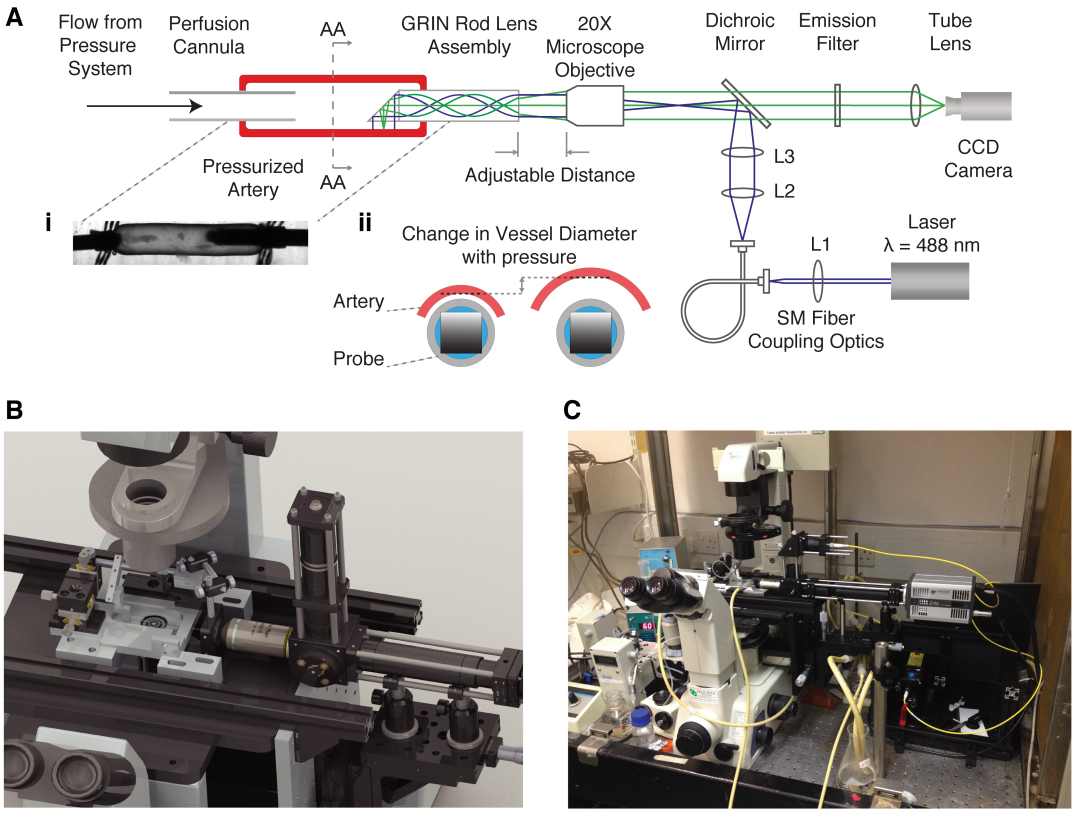

Figure 2.4 – GRIN microprobe imaging system. (A) A simplified schematic diagram of the optical system used for fluorescence imaging of the endothelium of intact and pressurised arteries with: (i) an image of a cannulated artery taken in transmission, the probe is visible on the right hand side; and (ii) cross sectional views of AA-AA, shown in A, illustrating the change in focal plane required to visualise the endothelium at different arterial diameters. (B) 3-dimensional rendering illustrating the full GRIN imaging system coupled to the stage of an inverted microscope. This permits visualisation of the artery as shown in Ai. (C) Photograph of the GRIN imaging system.

2.2.5 Animals and Tissue Preparation

The outer diameter of our probe (0.71 mm) determines the range of arteries amenable to study, i.e. those with unpressurised lumen diameters greater than 0.71 mm. In initial investigations, several arteries were obtained (aorta, common carotid, illiac, femoral, superior mesenteric, tail) from adult male Sprague-Dawley rats and Dunkin-Hartley guinea pigs and assessed for suitability on the following parameters (in descending order of importance): 1, lumenal diameter; 2, available length; 3, frequency of branch points; 4, ease of dissection. Based on these parameters, the common carotid arteries of the rat were identified as the most appropriate and used for all subsequent studies.

Approximately 12 week old, male Sprague-Dawley rats (250-350 *g*) were killed by overdose of pentobarbital sodium (intraperitoneal injection, ≥200 mg/kg; Schedule 1 procedure; Animal (Scientific Procedures) Act 1986, UK). Subsequently, the neck was opened by surgical incision and the left and right common carotid arteries were exposed by blunt dissection. During dissection, the arteries were continually irrigated with physiological saline solution. To prevent damage to the endothelium, from collapse of the artery, the rostral and caudal ends of both carotid arteries were ligated with 8-0-suture thread prior to removal. After ligation, arteries were cut at the rostral end (distal to the ligature), whilst being held at their *in situ* length by a pair of surgical forceps (Dumont #5; Fine Science Tools Inc., USA), and then gently allowed to shorten. The caudal ends of the arteries were subsequently cut and the ligated segments were quickly removed and placed in chilled physiological saline solution (PSS). Arteries were transferred to a Sylgard (Dow-Corning Corp., USA) coated Petri dish, also filled with chilled PSS, and pinned using 0.1 mm stainless steel pins (26002-10, Fine Science Tools Inc., USA). Using a stereomicroscope (Nikon, UK), fine Vannas micro-scissors and surgical forceps, the arteries were carefully cleaned of any adipose and connective tissue attached to the adventitia. Following preparation, arteries were immediately mounted onto two blunted and deburred 22-gauge cannula, using two lengths of 8-0-suture thread, in our custom-imaging bath. Arteries were flushed with PSS for 10 minutes (150 µl/min), to remove blood, and then pressurised to 60 mmHg. The temperature was slowly

brought up to 37°*C* and the artery allowed to equilibrate (30 min). Perfusion was accomplished by a pressure servo and peristaltic pump (PS-200, Living Systems, USA) connected to the proximal cannula. Arteries were mounted such that fluid flow matched that *in vivo.*

2.2.6 Preferential Loading of Endothelial Cells with Fluorescent Indicators

In preliminary experiments, we attempted to load endothelial cells with the fluorescent Ca^{2+} indicator, fluo-4 (10 μM), at room temperature and at 37°C. Regardless of loading temperature or incubation time (30 – 120 minutes), we were unable to visualise basal fluo-4 fluorescence. Instead, endothelial cells were loaded with the higher fluorescence quantum (ion-free and ion-bound) yield Ca^{2+} indicator, Oregon Green BAPTA-1/AM (OGB-1/AM, 20 μM) using a modification of the procedure of Kansui *et al*. (168). Briefly, after an equilibration period (30 min), the intraluminal pressure was decreased to 0 mmHg and ~2 ml of filtered endothelial cell loading solution was perfused through the lumen. When the lumen was filled with loading solution, flow was stopped to allow endothelial cells to load (30 min). Excess dye was then flushed from the lumen (10 min; 150 μl/min) before cessation of luminal flow. An inline, three-way valve permitted exchange of the luminal perfusion solution without the introduction of air bubbles. Throughout the loading procedure the artery was continuously superfused with PSS that was warmed to 37°C by a heat-exchange coil before entering the bath.

Following removal of excess dye, the distal end of the artery was freed from the cannula and the cannula itself was removed from the imaging bath. The distal end of the artery was positioned such that the artery was axially aligned with the imaging probe and the mouth of the artery was coincident with the apex of the side-viewing prism on the imaging probe. The artery was then advanced until it enveloped the imaging probe and could be secured using two lengths of 8-0 suture thread. Cutting the end of the artery at a 45-degree angle and using the z-translation, to ensure that no part of the endothelial layer came into contact with the imaging side of the prism, facilitated this procedure. Once secured onto the probe, the artery was slightly pressurised and moved incrementally up the GRIN microprobe by axially translating

the cannula and gently sliding the artery further onto the microprobe, until the probe was approximately coincident with the midpoint of the artery. This procedure minimised damage to the endothelial layer. The transmural pressure was then incrementally increased to 160 mmHg, whilst stretching the artery to remove buckle. Following this procedure, the pressure was decreased to 60 mmHg and the artery left for a further 30 minutes to equilibrate, and to provide adequate time for de-esterification of the Ca^{2+} indicator.

2.2.7 Endothelial Imaging

Following equilibration, endothelial fluorescence was measured using the GRIN imaging system. During imaging, the superfusion pump was switched off during acquisitions (limited usually to 90 s) to avoid movement artefacts. The bath temperature did not drop more than $2^{o}C$ during this time. The rat carotid artery preparation exhibits no spontaneous tone. In Ca^{2+} experiments, the plane of focus was set to the endothelial layer and arteries were stimulated with ACh from resting diameter, to achieve continuous observation of the endothelium. To assess endothelial function, arteries were stimulated, at 60 mmHg, by application of ACh (100 μM) delivered directly into the arteriography with a handheld pipette. This concentration of ACh was used as, in preliminary experiments, it was found to activate the majority of endothelial cells across the field of view. Following each acquisition period, the bath solution was immediately exchanged and the arteries were left for at least 20 min to re-equilibrate. Laser illumination and camera operation were synchronised, and images captured using the open-source microscopy software μManager (231). Images were acquired at a rate of 5 Hz and stored for subsequent analysis.

2.2.8 Solutions and Drugs

The PSS consisted of (mM): NaCl (145), KCl (4.7), 3-[N-morpholino]propane-sulphonic acid (MOPS, 2.0), NaH_2PO_4 (1.2) glucose (5.0), ethylenediamine-tetraacetic acid (EDTA, 0.02), sodium pyruvate (2.0) $MgCl_2$ (1.17), $CaCl_2$ (2.0), (pH adjusted to 7.4 with NaOH). The endothelial loading solution consisted of the cell permeant acetoxymethyl ester form of OGB-1/AM (20 μM), with a final concentration of 0.04% Pluronic F-127 and of 0.96% dimethyl sulfoxide (DMSO).

To ensure full dissolution of the OGB-1 AM ester, a 2 mM stock solution was made by dissolving the contents of a 50 µg vial in 16 µl DMSO and 4 µl 20% Pluronic F-127 solution. The stock solution was gently vortexed for 15 min and then placed in a shaker bath at 37°C for 15 min. 10 µl stock solution was added to 1 ml PSS, for a working solution of 20 µM. Drugs were all obtained from Sigma except for the following OGB-1/AM and Pluronic F-127 which were obtained from Invitrogen.

2.2.9 Statistics

Summarised data are expressed as mean ± standard error of the mean (SEM). One-way analysis of variance (ANOVA; with Tukey's post-hoc test as appropriate) was used for comparisons between two groups and among more than two groups. A p-value less than 0.05 was considered significant and n = number of animals.

2.3 Results

2.3.1 System Performance

Due to our focussing mechanism (translation stage), we could not easily measure the change of focal depth (distance from distal prism surface to focus; d_2 in Figure 2.3C) as a function of the objective-microprobe spacing (d_1 in Figure 2.3C). However, we calculated the ABCD matrix for our microprobe (Figure 2.3D), from which we derived the theoretical relationship (Figure 2.3E). This relationship is plotted for our side-viewing GRIN microprobe, imaging in water, (n_2 = 1.33; Figure 2.5). Negative d_1 values indicate that the objective is focused inside the GRIN lens, whilst negative d_2 values indicate the image plane does not reach beyond the distal prism surface.

From Figure 2.5 it can be seen that by focussing 2 mm (working distance of our microscope objective) inside our microprobe, we can image a distance 2 mm past the distal surface of the probe and thus image the endothelium of vessels up to 4.5 mm in lumen diameter. To determine if we would be able to image across the full curvature of arteries mounted on our probe, we calculated the DOF of our imaging system from (232):

$$DOF = \frac{\lambda_0 n}{NA^2} + \frac{n}{M \cdot NA} e \qquad \textbf{(2.7)}$$

where λ_0 is the wavelength of illuminating light, n is the refractive index of the medium, e is the smallest distance that can be resolved by a detector in the image plane (i.e. 2× CCD pixel size) of the microscope objective of magnification, M, and numerical aperture, NA. From this equation, the DOF of our microprobe (in water) is 141 μm. Thus, the minimum size of artery from which we can image the endothelium across the entirety of our FOV (500 μm diameter) has a diameter of 584 μm. As this is smaller than the 710 μm diameter outer dimension of our probe, it follows that our system can image a full 500 μm diameter field of endothelium in any artery of lumen diameter 710 μm < 4500 μm.

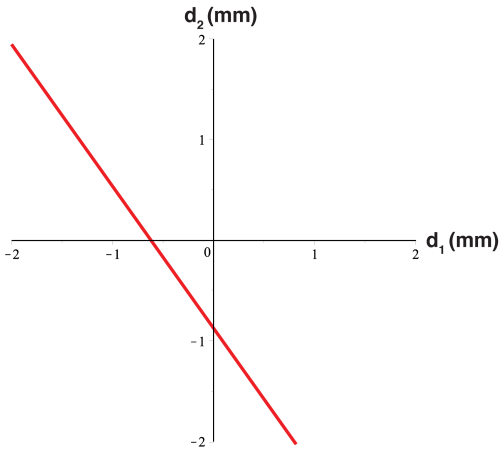

Figure 2.5 – Relationship between probe-object and objective-microprobe distances. The plotted line indicates that to image beyond the distal surface of the micro-prism on our probe, the objective focus must be set > 0.6 mm beyond the proximal surface of the GRIN probe. As the working distance of our microscope objective is limited to 2 mm, we are theoretically limited to imaging vessels of a maximal 4.5 mm diameter.

To measure resolution, we imaged 1.0 μm diameter fluorescent micro-beads (Figure 2.6A) (F8820; Invitrogen, UK). The microspheres were diluted by a factor of 1×10^6 in water and a droplet placed on the distal prism surface. Gaussian fits of the line intensity profiles of individual beads (Figure 2.6B) yielded a lateral resolution of 4.51 ± 0.04 μm (n = 6 beads). This measured value may be considered to be the actual resolution of our system because it is much larger than the actual size of the beads. The efficiency of our GRIN microprobe system was measured by illuminating a thin film of fluorescent plastic placed just beyond the end of the probe. Figure 2.6C shows a radial cross section of the detected fluorescence intensity, normalised by the maximal intensity at the centre. Due to vignetting of the illumination light and the fluorescence excitation by the GRIN lens, the efficiency drops to 50% at a radius of approximately 175 μm. This effect is demonstrated in our images of large (15 μm diameter, Dragon Green; Figure 2.6D), where beads at the periphery of the circular FOV are significantly dimmer than those in the centre.

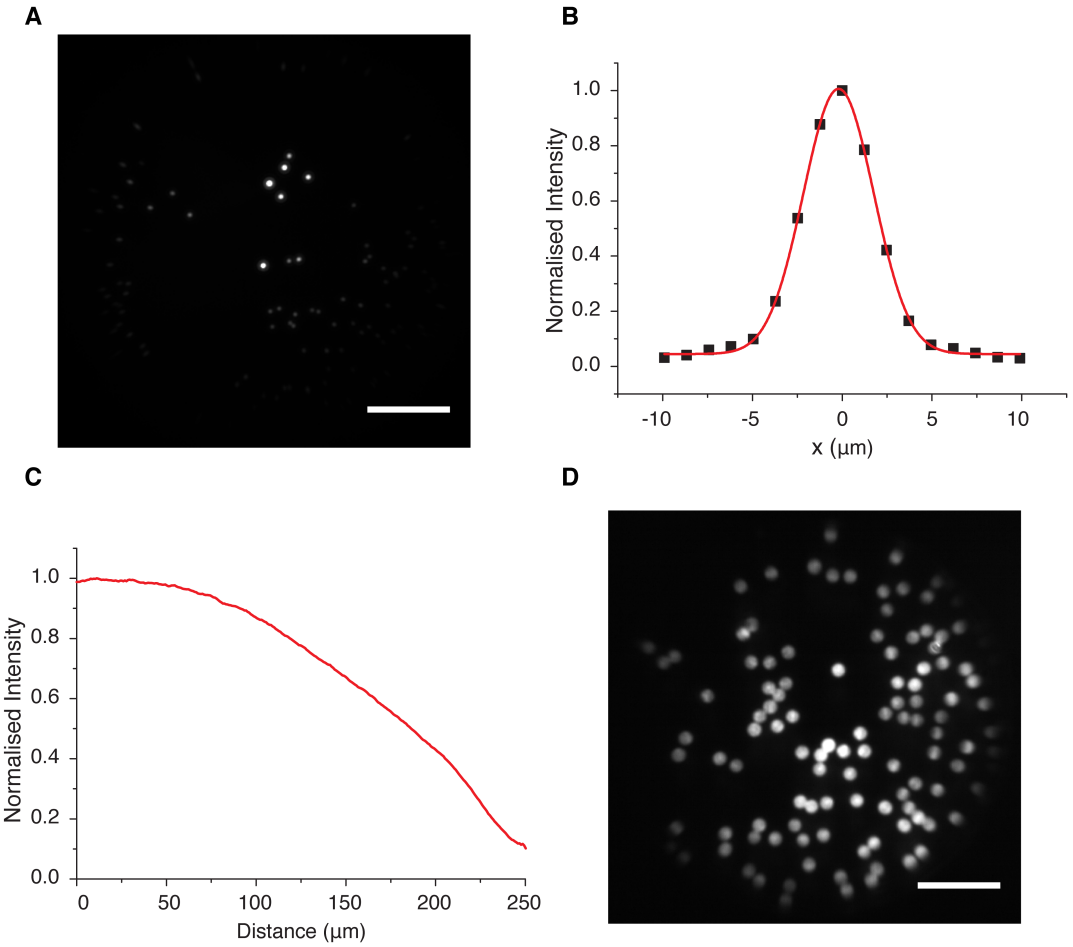

Figure 2.6 – Optical characterisation of the side-viewing GRIN imaging system. (A) Images of sub-resolution (1.0 µm) fluorescent beads. (B) Representative fluorescence intensity profile of a single bead imaged in A, from which we calculated the optical resolution of our system to be 4.51 ± 0.04 µm (n = 6 beads). (C) Normalised intensity profile, plotted as a function of radius from the centre of the FOV, of a thin strip of fluorescent plastic placed at the distal end of the probe. (D) Fluorescence image of 15 µm fluorescent spheres. Scale bars: 100 µm.

2.3.2 Ca^{2+} Imaging of Endothelial Cells in an Intact and Pressurised Artery

2.3.2.1 Endothelial Morphology

In intact rat carotid arteries pressurised to 60 mmHg, up to ~200 individual endothelial cells selectively labelled with the fluorescent chemical Ca^{2+} indicator, OGB-1/AM, were visualised (Supplementary Video 1). Cells were in focus across the entire 500 μm FOV provided by our side-view GRIN microprobe, although cells at the periphery were dimmer than those in the centre, due to vignetting (Figure 2.6C). Using OGB-1/AM we could visualise endothelial cells at regular intervals for periods in excess of three hours. Over this time basal fluorescence stayed relatively constant, suggesting little bleaching or dye extrusion occurred. However, with continuous illumination, baseline fluorescence intensity decayed approximately mono-exponentially, most likely due to photobleaching. After periods of time in excess of three hours, baseline fluorescence began to decay until individual endothelial cells could no longer be distinguished, presumably due to loss of the Ca^{2+} indicator.

Dissection of rat carotid arteries caused significant longitudinal shortening of the vessel. Figure 2.7 illustrates the geometric deformation of the endothelium, caused by dissection, in an artery pressurised to 60 mmHg. Visualised using our GRIN microprobe imaging system, individual endothelial cells in pressurised arteries were elongated but appeared to follow an undulating path along the long axis of the vessel (Figure 2.7A). In contrast, when arteries were first unbuckled at 160 mmHg, endothelial cells visualised at 60 mmHg were elongated along a straight path that followed the longitudinal axis of the artery (Figure 2.7B; Supplementary Video 1). Whether or not arteries were straightened at 160 mmHg, endothelial cell fluorescence was brightest in the perinuclear region of the cell, and significantly dimmer towards the peripheral processes. This is because the perinuclear region is thicker than the rest of the cell, thus the microprobe samples more Ca^{2+} indicator per unit volume in this area. Smooth muscle cells were not loaded with OGB-1/AM in any of our preparations, as indicated by an absence of fluorescence staining orthogonal to the longitudinal vessel axis.

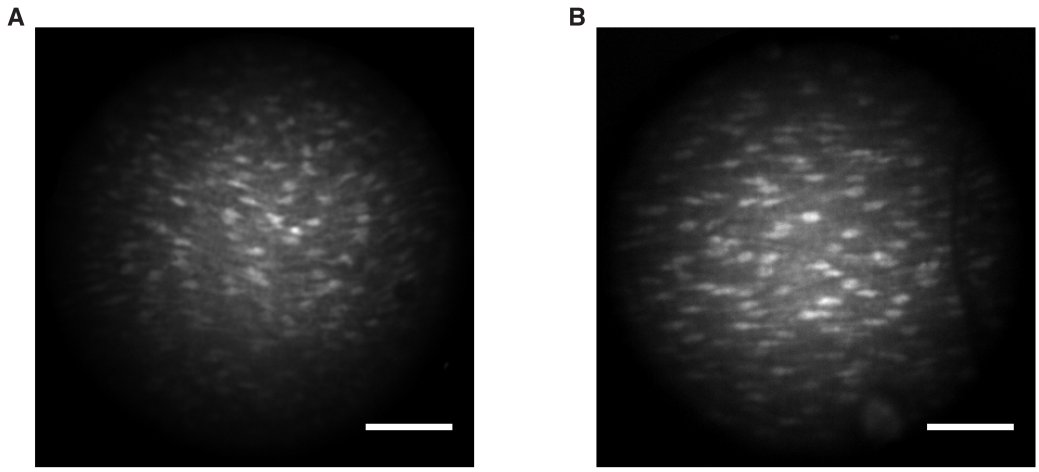

Figure 2.7 – Fluorescence images of rat carotid artery endothelial cells. Images of endothelial cells labelled with OGB-1/AM were obtained using our GRIN microprobe-imaging system, from within the lumen of arteries pressurised to 60 mmHg without (A) and with (B) length adjustment. Cells in (A) can be seen to follow a curved path along the longitudinal axis of the vessel (left-to-right in images), whilst the orientation of cells in arteries that have been unbuckled at 160 mmHg is parallel to the longitudinal axis of the vessel. Images are a single frame of a temporally smoothed (5-frame running average) raw image series, obtained post ACh-activation (100 μM). Scale bar: 100 μm.

2.3.2.2 ACh-evoked Ca^{2+} Signalling

Whole-field Ca^{2+} Measurement

We activated the endothelium of a pressurised artery with 100 μM ACh, applied extraluminally – a concentration found to activate the majority of cells across the FOV (Supplementary Video 1). As illustrated in Figure 2.8Bi, 100 μM ACh caused a significant increase in global Ca^{2+}, measured as the mean baseline-corrected fluorescence intensity of OGB-1/AM (F/F_0) in a circular region of interest (ROI) encompassing the entire 500 μm diameter FOV (Figure 2.8Ai). The global Ca^{2+} response was biphasic in nature, with an initial transient increase that plateaued at a stable level, well above baseline, for the remaining duration of our recording (60 seconds post-activation).

Cellular Ca^{2+} Measurements

To determine if the whole-field Ca^{2+} measurement (Figure 2.8Bi) was influenced by heterogeneity in Ca^{2+} signals of individual cells, we analysed changes in Ca^{2+} of individual cells. Cellular Ca^{2+} signals (Figure 2.8Bii) were extracted from raw

images series by placing circular regions of interest (ROIs) over the central portion of all individual cells (Figure 2.8Aii) that we could identify in temporally smoothed (5-frame rolling averaged) image series. For clarity, Ca^{2+} signals from only 6 individual ROIs corresponding to individual cells are shown (Figure 2.8Aiii,Biii). In this experiment, 100 μM ACh induced an increase in $[Ca^{2+}]_i$ in all 147 identified cells. The averaged response of all individual cells was similar in nature and in magnitude to the global measure. However, increases in $[Ca^{2+}]_i$ did not occur simultaneously in all cells and there was striking heterogeneity in Ca^{2+} signals among individual cells. Whilst some endothelial cells exhibited a biphasic increase in $[Ca^{2+}]_i$ that plateaued above baseline (e.g. Cell 3 in Figure 2.8Aiii,Biii), similar to the global response, others exhibited much faster initial transients that subsequently declined (e.g. Cells 1 & 6 in Figure 2.8Aiii,Biii). The secondary phase of the response was also oscillatory in a large proportion of cells (e.g. Cells 4 & 5 in Figure 2.8Aiii,Biii).

Close visual inspection of temporally-smoothed time-series images revealed that the Ca^{2+} responses in individual cells were apparently composed of either whole-cell increases in $[Ca^{2+}]_i$ or subcellular propagating Ca^{2+} waves (Figure 2.9). However, visualising and quantifying the dynamics of these Ca^{2+} signals was difficult due to the shear number of cells and the complexity of Ca^{2+} signals within the FOV. To enhance visualisation of Ca^{2+} activity, we employed image-processing techniques and, to enable quantification of Ca^{2+} signals we developed a semi-automated procedure for extracting and analysing individual cellular Ca^{2+} signals. Using these techniques, we analysed thousands of cells from over 50 arteries and confirmed the temporal heterogeneity of Ca^{2+} signalling in endothelial cells of intact and pressurised rat carotid arteries. However, for systematic presentation of our studies, the methods by which we analysed our GRIN images are presented in Chapter 3. Similarly, results obtained using our semi-automated analysis, including an in depth description of ACh-evoked endothelial Ca^{2+} signalling, are presented from Chapter 4 onwards.

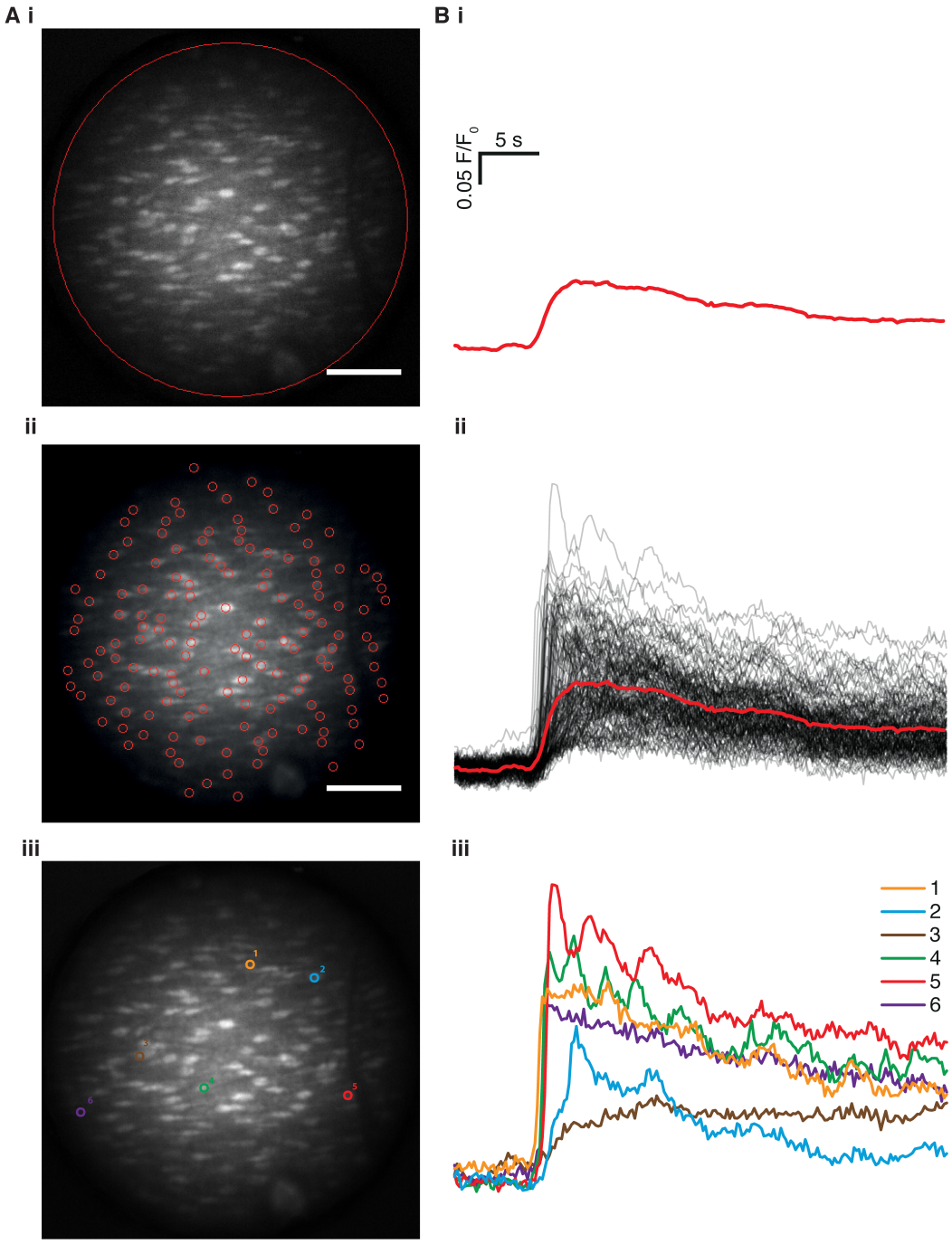

Figure 2.8 – ACh-evoked Ca^{2+} signals in pressurised rat carotid artery endothelial cells. (A) A single fluorescence image of OGB-1/AM loaded endothelial cells with ROIs encompassing (i) the entire FOV, (ii) 147 manually identified cells, and (iii) six selected cells. (B) Baseline corrected Ca^{2+} signals (F/F_0) from ROIs shown in A. All signals are plotted after application of 100 µM ACh. The red line in (ii) is the averaged Ca^{2+} signal of all identified cells. Data shown in Supplementary Video 1. Scale bars: 100 µm.

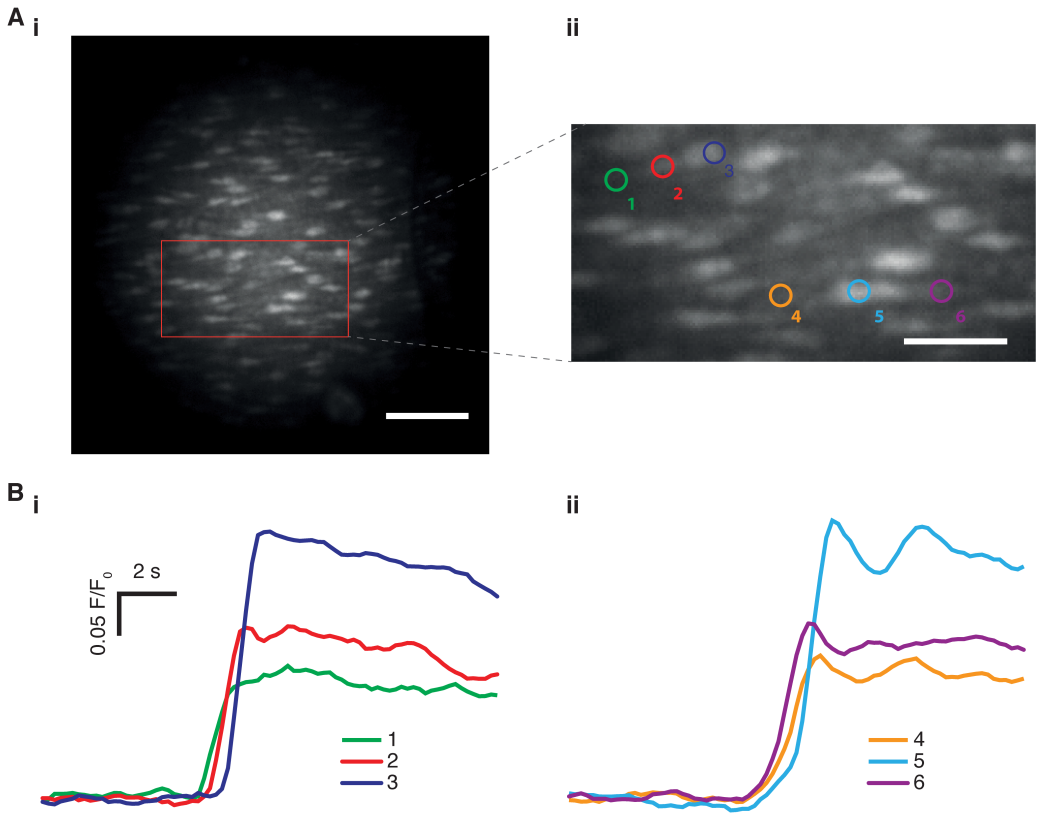

Figure 2.9 – Subcellular Ca^{2+} signals in pressurised rat carotid artery endothelial cells. (A) A single fluorescence image of OGB-1/AM loaded endothelial cells in an intact and pressurised artery. (i) Full FOV. Scale bar: 100 µm. (ii) Zoomed in region illustrated in i. Sets of three subcellular ROIs have been placed over the body of two distinct cells. Scale bar: 50 µm. (B) Subcellular Ca^{2+} (F/F_0) traces, in response to 100 µM ACh from regions shown in (Bii) used to illustrate the time-course of subcellular Ca^{2+} signals. (i) Time-course of subcellular Ca^{2+} signals in a single cell (ROIs 1-3 in Aii) illustrating the wave-like nature of Ca^{2+} rise that passed along the longitudinal axis of the cell. (ii) Time-course of subcellular Ca^{2+} signals in a single cell (ROIs 4-6 in Aii) illustrating that subcellular Ca^{2+} waves initiated at two opposing ends of a single cell annihilate on collision.

2.4 Discussion

We have introduced a novel method for wide-field fluorescence imaging of endothelial cells in intact blood vessels. The main feature of our approach is the use of a side-viewing GRIN microprobe – the cylindrical shape of the microprobe permits its placement within the artery lumen and allows unobstructed visualisation of the endothelium. Using our GRIN microprobe imaging system we have demonstrated that ACh-evoked Ca^{2+} dynamics can be recorded from hundreds of cells of large pressurised arteries (Figure 2.8; Supplementary Video 1), despite the curvature of the artery. Furthermore, in agreement with previous studies (233), we have demonstrated that the shortening of arteries upon excision results in a deformation of the endothelial cell layer (Figure 2.7). This latter finding underscores the importance of studying endothelial function in arteries subject to true physiological loading.

Our approach draws inspiration from an established tool used to study intact blood vessels – the pressure myograph (158). Using the pressure myography technique, arteries may be mounted on two opposing cannulae such that transluminal pressure and flow can be applied and blood vessels may be studied under physiological loading conditions. In our approach, only one end of an artery is mounted onto a cannula. The other end of the vessel is mounted directly onto a cylindrically shaped, side viewing GRIN microprobe (Figure 2.3). Thus, whilst the technique we employ is similar to pressure myography, it allows for unobstructed visualisation of the inner endothelial layer in the presence of transluminal pressure but the absence of luminal flow.

Previously, GRIN microendoscopes have been used in a wide variety of *in vivo* imaging applications, for example to permit *in vivo* imaging of the brain (212). Such probes typically utilise high (~0.5) NA GRIN lenses for high-resolution imaging. Due to manufacturing constrains, these high NA lenses are short in length (typically less than 5 mm (213)). In most applications, long probes are required to meet mechanical constraints posed by the depth of tissue under examination. Thus, high NA imaging lenses are attached in series to a weaker GRIN lens of lower NA (Figure 2.2). The GRIN probes are then coupled to a conventional microscope system.

Depending on the imaging modality and, where necessary, the illumination/scanning strategy, the relay lens is chosen to be either a quarter or half pitch (212). Additional length may be achieved by adding integer half-pitch lengths to the relay lens. Thus, high NA microendoscopic imaging is achievable, however the combination of lenses results in a FOV that is a fraction of the cross-sectional area of the lens itself.

A key element of the method described herein is the use of a single, whole pitch GRIN relay lens to reconjugate the image plane of detection optics along the length of the lens. This strategy ensures that the entire cross sectional area of the microprobe is accessible for imaging (230). The method, in combination with the use of a right-angle microprism, is particularly suited to fluorescence imaging of large populations of endothelial cells in intact, pressurised arteries, which are inaccessible to conventional microscopy. The low NA of our microprobe bestows a large enough DOF to retain good focus of the endothelium across the entire FOV, despite the curvature of the artery in its pressurised state. Furthermore, due to the absence of any biological tissue between the end of our probe and the endothelium, our optical excitation intensity is low. Previous studies have utilised high NA microscope objectives and optical sectioning microscopes (e.g. confocal) to image endothelial cells in intact arteries (135,168,169), from outside the artery. However, high NA objectives have a low DOF such that imaging of the endothelium is limited to a small number of cells on the curved endothelial surface. This can be partially overcome by implementing z-scanning strategies (233). However, light scattering by the artery wall necessitates long acquisition times and the use of significant optical excitation powers that preclude the recording of dynamic events and may induce tissue damage, respectively. Thus imaging the endothelium with sufficient signal-to-noise ratio to record Ca^{2+} signalling can only be achieved, with sufficiently low optical excitation densities and acquisition periods, in small diameter arteries.

We chose a 30.2 mm length, 0.5 mm diameter lens to provide adequate length to guide the optical path through the wall of the perfusion chamber and into arteries with a luminal diameter greater than 0.5 mm. To illuminate the entire FOV, we used the microprobe to project collimated laser illumination onto the endothelium (230). The intensity profile of the Gaussian beam we used results in a drop in illumination

intensity across the radius of the microprobe, an effect exacerbated due to vignetting by the GRIN lens. However, we were still able to visualise the endothelium across the entire FOV (Figure 2.7; Supplementary Video 1). Although the low NA of our system permits wide-field imaging of the endothelium despite its curvature, it also limits the attainable resolution. Nevertheless, the resolution of our imaging system is more than adequate (4.5 μm) to examine the endothelium with cellular resolution. Indeed, the system permits the analysis of both cellular (Figure 2.8) and subcellular (Figure 2.9) Ca^{2+} signals.

This study used preferential loading of the fluorescent chemical Ca^{2+} indicator, OGB-1/AM, to demonstrate that endothelial Ca^{2+} signalling can be simultaneously monitored in hundreds of endothelial cells from within an intact artery. We evoked endothelial Ca^{2+} activity using extraluminal application of ACh (100 μM). Our data point to the following conclusions. 1) ACh-evoked Ca^{2+} signals are heterogeneous across endothelial cells visualised in a single FOV. This observation is consistent with studies in endothelial cells of surgically opened aorta (123). 2) Ca^{2+} influx in smooth muscle cells did not contribute to the fluorescence signal. ACh has been shown to directly activate muscarinic receptors present only on endothelial cells (29). In agreement, the lack of fluorescence arising from smooth muscle cells in our images suggests that we may consider fluorescence signals recorded under these conditions as arising solely form endothelial cells.

Although a relatively high *extraluminal* concentration of ACh was required to activate the majority of endothelial cells, it is likely that the endothelium was not exposed to this concentration due to presence of an adventitial barrier to diffusion. In support, the potency of extraluminally applied ACh is reported to be 1/30 to 1/60 that of intraluminally applied ACh in the dog mesenteric artery (234), and 1/44 in the dog femoral artery (235). Additionally bradykinin is unable to evoke relaxant responses in isolated porcine coronary arteries when applied extraluminally, independent of enzymatic degradation and luminal pressure, but is able to evoke responses when applied intraluminally (236). This concept is further supported by observations of an adventitial barrier in rat tail arteries that prevents loading smooth muscle cells with

the calcium indicator Fura-2, and inhibits the action of noradrenaline, when these agents are applied extraluminally, but not intraluminally (237).

In summary, we have presented a novel method for imaging the endothelium in large, intact and pressurised blood vessels. The technique permits monitoring Ca^{2+} signalling in large populations of endothelial cells when the artery is mounted in a physiological configuration and at normal pressures, albeit in the absence of flow. Side-view GRIN imaging of the endothelium is straightforward and easy to implement and should broadly enable longitudinal studies of endothelial dysfunction, such as atherosclerosis or leukocyte and macrophage trafficking, in a most-physiological model. This would contrast with current experimental designs in which tissue specimens are taken from different animal cohorts at distinct time points, and would substantially reduce the number of animals needed, as a single animal could provide data at all time points. There already exists a large set of fluorescent markers for the study of blood vessel dysfunction, such as labels (both chemical indicators and those genetically encoded) for leukocytes and macrophages, reactive oxygen species, and mitochondria, and many of these will be readily combined with our endothelial imaging approach using GRIN lenses.

Chapter 3. Automated Calcium Signal Analysis

3.1 Introduction

Since the first recording of Ca^{2+} signals in live cells (238), many innovations have led to our understanding of the Ca^{2+} ion as a ubiquitous signalling molecule and as a comprehensive and versatile regulator of biological function (239). Such advances include the engineering of a large number of fluorescent probes, whose optical properties are carefully matched to Ca^{2+} concentration and kinetic changes in various subcellular regions (240–242). Improvements in the detection of signals from the fluorophores in both temporal and spatial resolution have also greatly facilitated understanding of Ca^{2+} control (243–246). Importantly, in the improvement of detection two-dimensional fluorescence imaging has established itself as a most powerful tool for assessing the dynamic interdependence of Ca^{2+} signals in large populations of cells, whether imaged in culture, in intact preparations or *in vivo*.

In early studies, global Ca^{2+} mobilisation, measured as a change in fluorescence intensity across entire fields of view, was quantified for analysis of large cell populations (79). Significantly, a reasonable Ca^{2+} response was obtained by averaging the signals from hundreds of cells. Whilst very valuable, this approach did not provide any insight into the behaviour of individual cells. Technical advances made the latter possible, with individual cellular signals analysed using linescan data generated from confocal laser scanning microscopy studies (245–247). This approach provided detailed information on the performance of individual cells and on the subcellular control of Ca^{2+}, but lacked an appreciation of communication among neighbouring cells. Due to performance increases in charge coupled device (CCD) cameras, high spatial and temporal resolution Ca^{2+} imaging of large cell populations is now possible and is an emerging technique, particularly in neuroscience (207) and increasingly in endothelial biology (167,179). The great strength of this approach is that subcellular Ca^{2+} changes can be quantified in tandem with information regarding communication between cells. However, this approach yields vast amounts of data that render the detection and analysis of Ca^{2+} events particularly challenging. Using our GRIN imaging system we are able to visualise up to 200 individual cells in an individual intact artery (Chapter 2). We desire to be able to perform longitudinal, paired experiments, in which the same artery is imaged at

discrete time points (e.g. concentration response experiments). Such an approach results in the generation of numerous data sets, and due to movement of cells (relaxation, contraction) cellular position may not be identical between experimental recordings. Thus any single artery may provide many separate data sets, each containing up to 200 individual cells, potentially leading to thousands of individual comparisons. To analyse our data quickly, consistently and reliably we require, as far as is possible, automated techniques.

Although several methods for analysing large-scale Ca^{2+} imaging data exist, suitable methods for signal extraction are most often not available. The usual method for assessing cellular Ca^{2+} activity is a multi-stage process: first, cellular boundaries are identified; secondly, regions of interest (ROIs) are drawn to outline individual cells, or more simply placed within an individual cell; finally individual signal parameters (e.g. peak levels, rise times) are calculated from the average fluorescence intensity traces of each ROI extracted from the raw data.

The use of cell outline as an ROI is most often applied to small-area, high magnification datasets, where additional, smaller ROIs may be placed over areas exhibiting fluctuations in fluorescence intensity, to analyse subcellular Ca^{2+} events. The latter approach to ROI placement is most often used in wide-area (low-magnification) time-lapse imaging experiments, where individual cell boundaries may be unclear but the appearance of distinct cell nuclei enables individual cells to be identified. Whilst a manual implementation of both ROI placement approaches and of signal extraction is feasible, the rate at which data can be analysed, even by a trained operator, usually limits its implementation to only a few cells per dataset. Additionally, manual placement may result in error due to erroneous placement of ROIs, and data loss due to the exclusion of low signal-to-noise ratio data. Thus, at best the full statistical power of the data may not be realised when using a manual ROI placement approach, and there is a real potential for false inferences to be drawn.

There are many well-documented tools for automated signal analysis of Ca^{2+} imaging data. However, most are limited to the analysis of confocal line scan images,

which restricts their use to single cells. Recently, several fully automated approaches to quantifying two-dimensional Ca^{2+} imaging data have been released (179,207,248), which enable a comprehensive evaluation of the diverse range of signalling events in large-scale Ca^{2+} imaging datasets. One approach combines principal component analysis and independent component analysis to separate signals from each individual cell. This approach works well for high signal-to-noise ratio spiking Ca^{2+} signals, but fails when too many cells (hundreds) are present or when signal-to-noise ratio decreases (207) or when the resonance of many cells correlates with a single causal component. The issue of cell number may be addressed by assigning ROIs, of a predetermined size and shape, based on a spatiotemporal analysis of Ca^{2+} spikes first isolated in both space and time (179), however optimum ROI placement is determined by the implementation of a running average algorithm. This technique designates overlapping ROIs as indicative of a singular event and subsequently calculates optimal placement of a single ROI. This technique is particularly useful for eliminating false-positives due to movement artefacts caused by the contraction of biological tissue or focal plane drift. However, there may be an increased occurrence of non-detected events as the overlap of ROIs of two or more spatially distinct but close signal origination sites will result in the detection of only one. Thus, the method relies heavily on the correct choice of size and shape of the ROIs and as such it has had particular use in analysing subcellular Ca^{2+} signals in high-magnification, high-resolution datasets.

The significance of studies, such as the two mentioned above, is that they standardise both the detection and the analysis of large-scale Ca^{2+} imaging experiments, and enable the analysis of how individual cellular Ca^{2+} events contribute to the aggregated response of a tissue. However, none adequately capture the Ca^{2+} signals in our large-scale endothelial imaging data. A truly discriminating ROI detection solution, that calculates the outline of individual cells from low magnification, large-scale time-series images, is required. Here, we describe a novel, largely automated routine that enables precise whole-cell Ca^{2+} signal extraction and analysis from our data and provides improved average measurements of the behaviour of the entire visualised network.

3.2 Methods

3.2.1 Large-scale Endothelial Ca^{2+} Imaging

Endothelial Ca^{2+} signalling was imaged as described in Chapter 2. Endothelial Ca^{2+} signalling was activated by direct application of 100 μM ACh, delivered with a handheld pipette.

3.2.2 Image Processing Cell-segmentation Algorithm

Individual endothelial cells were segmented using a custom, semi-automated image processing procedure, as illustrated in Figure 3.1. The image processing algorithm was developed using ImagePro Plus and FIJI (249). First, a 5-frame rolling average filter was applied to raw fluorescence image stacks (Figure 3.1A), to create a temporally smoothed copy of each frame (Figure 3.1B). Stacks illustrating active Ca^{2+} wavefront (Figure 3.1C) were then created, by sequential subtraction (SS) of the smoothed frames at 5 frame intervals, and were spatially smoothed by a single pass of a 3x3 pixel median filter (Figure 3.1D). Next, single-frame projections of the standard deviation (STDev) of intensity of the smoothed SS stacks were formed, to illustrate the total Ca^{2+} activity (i.e. all cells that experience changes in $[Ca^{2+}]_i$; Figure 3.1E). Due to vignetting of both the excitation and fluorescence light, fluorescence intensity was not uniform across the FOV. To normalise for this, we smoothed the STDev image with 10 passes of a large (25x25 pixel) mean filter and subtracted the resulting image (Figure 3.1F) from the original. This formed sharpened, background-corrected STDev images where individual cells could be clearly resolved (Figure 3.1G). After processing in this way, individual cell outlines were obtained by thresholding and then manually splitting joined cells (Figure 3.1H&I). Cell outlines were stored as .TXT files for subsequent signal extraction, processing and analysis. Except for the creation of STDev images (performed in FIJI) and for manually splitting joined cells, all processing was performed using batch-processing algorithms in ImagePro Plus.

3.2.3 Automated Extraction and Analysis of Fluorescence Ca^{2+} Signals

3.2.3.1 Averaged Cellular Ca^{2+} Fluorescence Extraction

Individual cellular fluorescence signals were extracted from raw image series using a set of custom Python scripts (Appendix A2). Raw image stacks (.TIF), corresponding cell outline files (plain text polygonal descriptions, .TXT) obtained using our semi-automated image-processing procedure, and individual experimental parameters (baseline/activity frame numbers) for each experiment were defined in a single script, *Data.py*. Execution of *Data.py* initiated a subroutine, *Process.py*, that extracted and saved, in .CSV format, the following from each dataset: 1) raw fluorescence signals, averaged over the area of each ROI; 2) baseline corrected fluorescence signals (F/F_0), calculated by dividing raw fluorescence signals by the average of the user defined baseline period defined in *Data.py*; and 3) differentiated baseline corrected fluorescence signals ($d(F/F_0)/dt$). To calculate parameters of individual F/F_0 signals, CSV files were further processed using another Python script, *Analyse.py*. For paired experimental analysis, individual datasets were grouped according to experiment in *Data.py*.

3.2.3.2 Ca^{2+} Signal Alignment

To provide a clear illustration of *total* and *averaged* Ca^{2+} activity, *Analyse.py* aligned individual F/F_0 traces with respect to their peak rate-of-change. Furthermore, *Analyse.py* automatically calculated baseline values of F/F_0, peak amplitudes and the time of peak rate-of-change for each signal. All data were stored in CSV format that were subsequently imported into Origin 9.1 for calculation of peak changes in fluorescence intensity ($\Delta F/F_0$), and for plotting using custom analysis scripts. For comparison of automatically extracted F/F_0 traces with those obtained using manual methods, raw, unaligned fluorescence signals were background corrected by dividing each signal by its average over the first 50 frames of acquisition.

The python analysis algorithm was developed using Python 2.7.3, making use of the Numpy (250) and Mat-plotlib modules. All extracted Ca^{2+} signal were batch processed using our Python algorithm (Appendix A2).

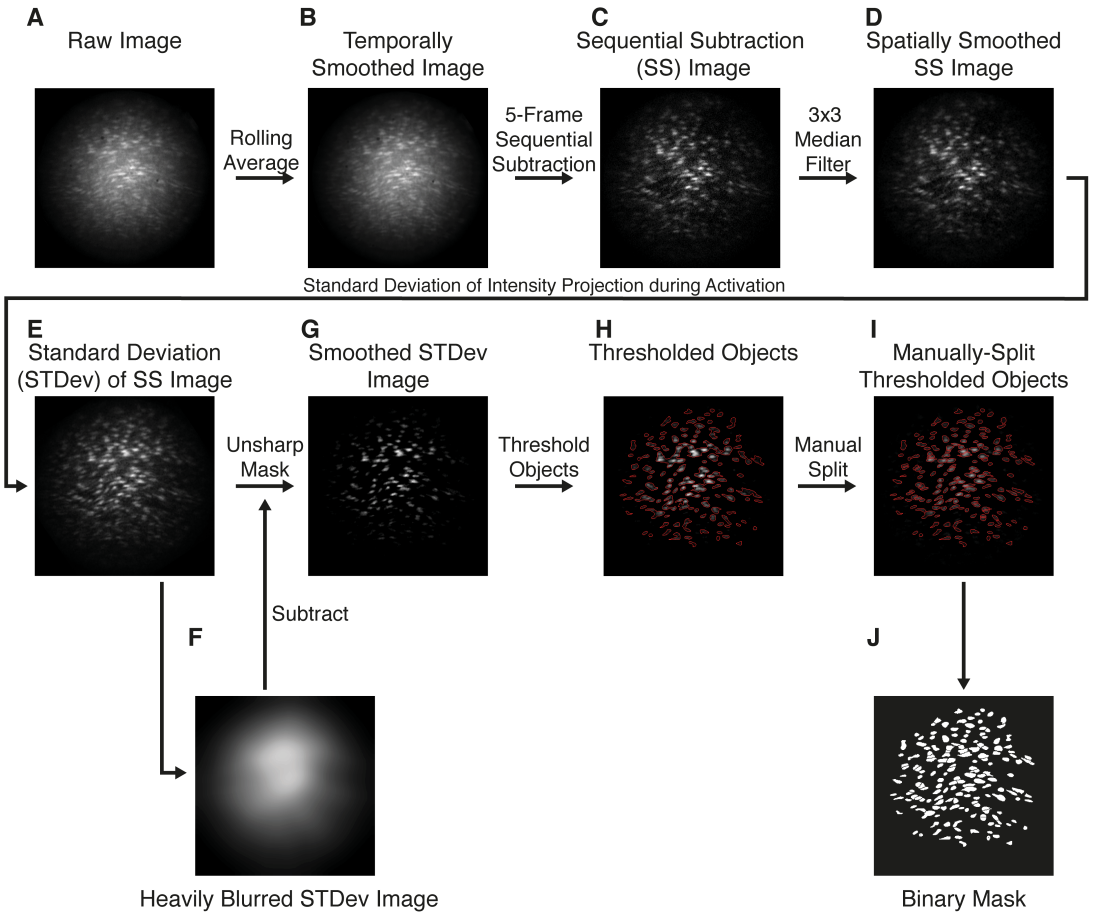

Figure 3.1 – Largely-automated segmentation of individual cells. (A) Raw GRIN microprobe image of rat carotid artery endothelial cells, loaded with OGB-1/AM, obtained from an intact, pressurised artery. (B) Temporally smoothed image. (C) 5-Frame sequential subtraction of (B), showing endothelial Ca^{2+} wave activity. (D) Noise was reduced by applying a 3x3 pixel median filter to (C). (E) Projection of the standard deviation of intensity of (D) during activation. (G) Cleaned image of (E), obtained by subtracting a heavily blurred (25x25 mean filter, 10 passes) copy (F) of (E) from (E) itself, followed by a single pass of a 3x3 median filter. (H) Cell outlines obtained by threshold segmentation shows that some cells are not split correctly. (I) Final cell outlines obtained by manually splitting objects in (H). (J) Binary image mask of individual cells.

3.2.4 Performance Evaluation of Other Approaches

3.2.4.1 Manual Processing of Ca^{2+} Image Data

Individual Ca^{2+} signals were extracted from raw image series manually, using ImagePro Plus. First, a 5-frame rolling average filter was applied to temporally smooth raw image series. Fluorescence traces for individual cells were then derived by visually identifying individual cells (which were either clearly distinguishable at baseline Ca^{2+}, or identified from fluctuations in fluorescence intensity), and circular ROIs were manually centred over individual cells. ROIs were then transferred to the raw image series, and individual traces were extracted using the *Track Objects* feature of ImagePro (intensity tracking of full 16-bit range) and stored as .CSV files. Signals were baseline corrected by dividing each signal by its average over the first 50 frames of acquisition.

3.2.4.2 Automated Processing of Ca^{2+} Image Data

To compare the performance of our procedure with another, commonly used, automated Ca^{2+} signal extraction and analysis algorithm, we implemented LC_Pro to extract Ca^{2+} signals from our data. LC_Pro is a plugin implemented in the ImageJ (or FIJI) platform that outputs .txt files containing baseline-corrected signals for each ROI, and is freely available to the research community. As LC_Pro only operates on 8-bit image series, we first down-sampled our images from 16-bit to 8-bit. In initial tests, we found that LC_Pro did not detect any events in the full range of our images, and so performed a linear contrast stretch on our images, such that 0.1% of pixels were saturated, prior to down sampling. This adjustment increased detection rates. LC_Pro does not provide files containing individual ROIs (of *a priori* user-defined size), thus the fidelity of its identification algorithm was unknown to us. As such, we modified the software to output individual ROIs. These file formats were incompatible with ImagePro Plus, and so ROIs were transferred onto the raw (16-bit) image series and individual traces, averaged over each ROI, extracted using the *Multi_Measure* feature of FIJI and stored as .CSV files. Signals were baseline corrected by dividing each signal by its average over the first 50 frames of acquisition.

3.3 Results

3.3.1 Evaluation of GRIN Ca^{2+} Data: Semi-automated vs. Manual

To determine whether our semi-automated technique for defining cellular ROIs provided a faithful representation of Ca^{2+} signals, we compared data it generated, from images obtained using our GRIN imaging system, to that obtained by manual methods described above. As can be seen (Figure 3.2A), the semi-automated procedure is superior to manual methods, even by a trained operator. Consistently, the semi-automated procedure identified more cells, particularly in the peripheral regions of our images that exhibit low contrast, due to vignetting. In addition, a single dataset was segmented into ~200 cells in approximately five minutes, whilst manual placement of the same number of circular ROIs often took longer than 30 minutes. In the case of identified cells, manual ROI placement yielded Ca^{2+} signals of slightly greater magnitude than our semi-automatically generated ROIs (Figure 3.2B,C), presumably as ROIs were manually placed over cell nuclei which exhibit a greater optical density than the rest of the cell. Plotting Ca^{2+} signals, generated using our semi-automated procedure, against corresponding, manually obtained Ca^{2+} signals illustrates the linear relationship that exists between signals obtained by the two methods (Figure 3.2C).

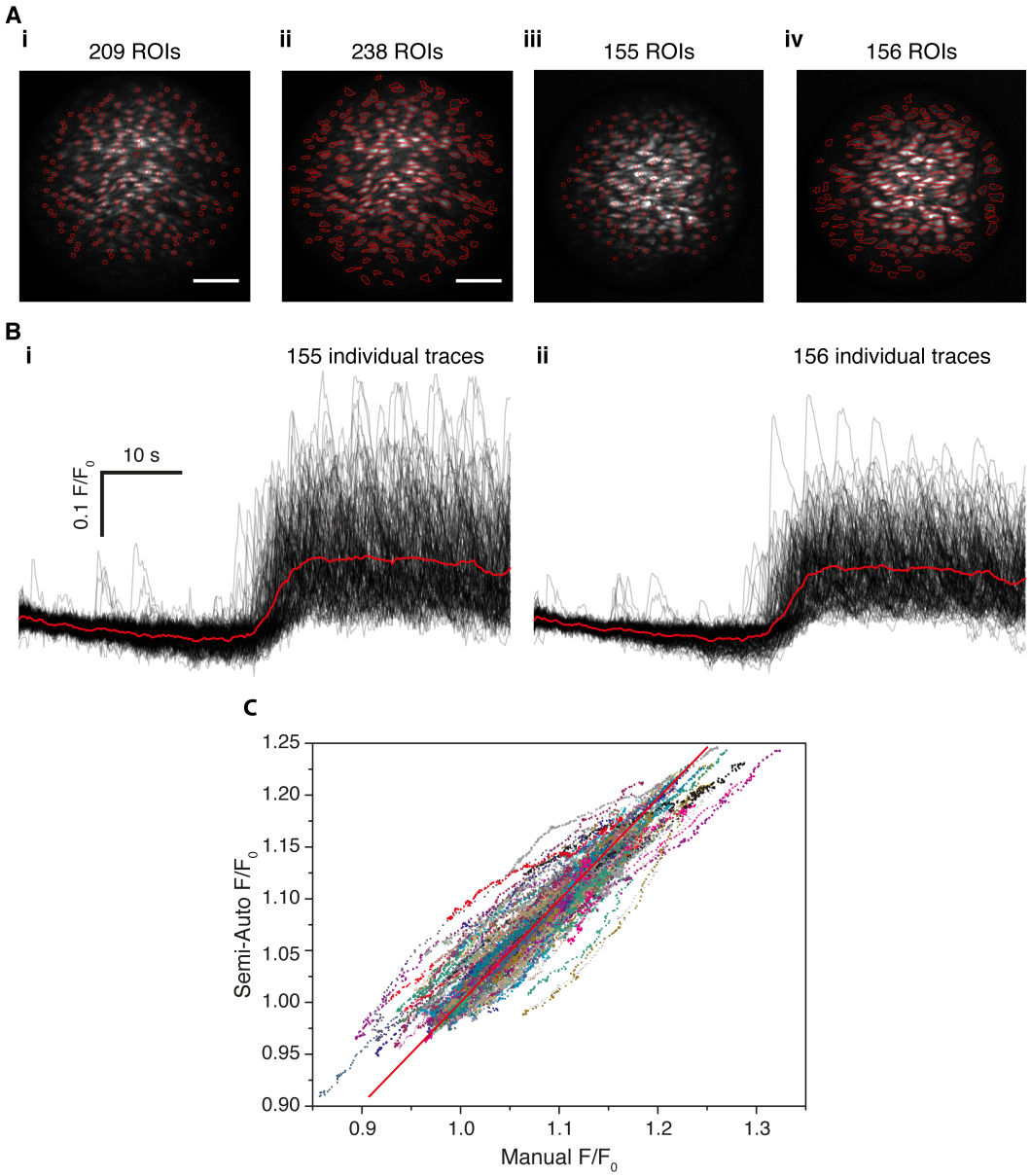

Figure 3.2 – Evaluation of signal extraction: semi-automated vs. manual. (A) Manually placed circular ROIs circumscribing cells (i,iii) and corresponding semi-automatically generated ROIs (ii, iv). Whilst manual ROIs were derived from temporally smoothed raw image series', for clarity all ROIs are overlaid on STDdev images. (B) Baseline corrected (F/F_0) Ca^{2+} signals obtained from manually placed (i) and semi-automatically placed (ii) ROIs shown in (Aiii) and (Aiv), respectively. (C) Individual F/F_0 Ca^{2+} signals, obtained from semi-automatically generated ROIs, plotted against those from corresponding manual ROIs. Data corresponds to that shown in (Aiii)/(Bi) and (Aiv)/(Bii). Each coloured dataset corresponds to a single Ca^{2+} signal. A linear best fit is overlaid in red. Note that the magnitude of the gradient is less than unity, as the semi-automatically generated ROIs encompass more of the cell periphery that manually placed ROIs, which are generally centred on the brighter nuclear region. Scale bars: 100 µm.

3.3.2 Evaluation of GRIN Ca^{2+} Data: Semi-automated vs. Automated

To evaluate our semi-automated technique for defining cellular ROIs against an established, fully automatic Ca^{2+} analysis algorithm, we compared data generated from images obtained using our GRIN imaging system, to that obtained by the ImageJ plugin LC_Pro (Section 3.2.4.2). In terms of speed, LC_Pro was significantly faster than our semi-automated procedure. However, in contrast to our method, which outlines cellular boundaries (Figure 3.3Ai) to extract high fidelity Ca^{2+} signals (Figure 3.3Bi; Section 3.3.1), LC_Pro uses circular ROIs, which do not reflect the true shape of the cell. As a result there were numerous errors in the number and placement of regions (Figure 3.3Ai,Aii) and erroneous Ca^{2+} signals (Figure 3.3Bii,Bii). Regardless of the diameter of the circular ROIs used, LC_Pro exhibited a high number of various errors (251): these included a high rate of non-detection, single ROIs consistently overlapping multiple cells, or ROIs placed in regions appearing to contain no identifiable cell. These errors were not restricted to the periphery of our images. Due to such poor performance, we did not compare signals generated by LC_Pro against our own procedure.

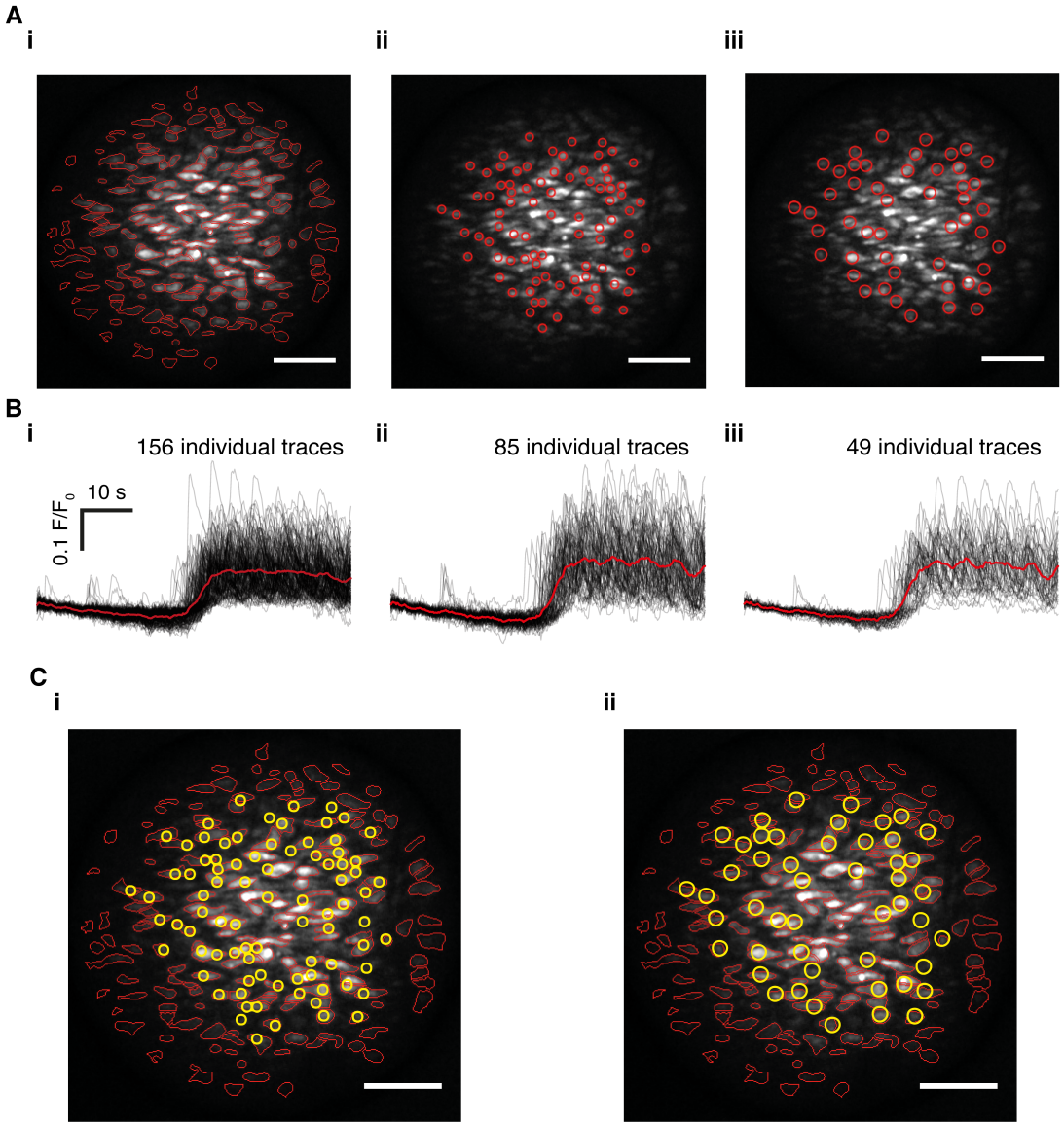

Figure 3.3 – Evaluation of signal extraction: semi-automated vs. automated. (A) STDev images with semi-automated cellular (i) and automatically generated (LC_Pro) circular ROIs of various diameters (ii, 10 pixels; iii, 15 pixels). (B) Baseline corrected (F/F_0) Ca^{2+} signals obtained from semi-automatically (i) and automatically placed (ii, 10 pixels; iii, 15 pixels) ROIs. (C) STDev images overlaid with semi-automatically generated ROIs (red) and automatically generated ROIs (yellow) using 10 pixel (i) and 15 pixel (ii) diameter circles. Data corresponds to that shown in (A) and (B). Note that LC_Pro ROI placement exhibits numerous errors, the severity of which depend on the choice of ROI diameter: (1) split, when two ROIs are assigned to a single cell; (2) merged, when one ROI is assigned to two or more reference cells; (3) spurious, when an ROI is assigned to a region where no cell is present; and (4) missing, when no ROI is assigned to a cell. Scale bars: 100 µm.

3.3.3 ACh-induced Ca^{2+} Activity

Analysis of semi-automatically derived, cellular Ca^{2+} signals revealed that ACh induces a significant elevation in individual endothelial cytoplasmic Ca^{2+} concentration ($[Ca^{2+}]_i$) that is followed by distinct oscillations (Figure 3.2B; Figure 3.3B; Figure 3.4Ai,ii left panels, grey lines). The total response of the entire cell complement was composed of a variable temporal spread of rises in $[Ca^{2+}]_i$, such that individual oscillations were lost when the fluorescence responses of all endothelial cells in the field-of-view were averaged. Rather than transient rises in Ca^{2+}, the average response exhibited a plateau (Figure 3.4Ai,ii left panels, red lines). The averages are reminiscent of responses obtained by photometry and whole field averaging (Figure 2.8A).

By aligning the $[Ca^{2+}]_i$ signals derived from each cell, with respect to the peak rate-of-change (i.e. activation; Figure 3.4Ai,ii middle panels) of individual signals, we were able to illustrate the *total* Ca^{2+} response with greater clarity (Figure 3.4Ai,ii right panels). Utilising the time of the peak rate-of-change of the differentiated fluorescence signals as a reference, we were able to extract data from individual traces. Figure 3.4B illustrates the mean peak F/F_0 values, mean basal F/F_0 values, and mean F/F_0 values after the peak (plateau value) for the two datasets illustrated in Figure 3.4A. As basal, peak and plateau fluorescence values are likely to vary between and during individual experiments, these values are unsuitable for direct comparison. As such, we calculate the peak change in fluorescence signals (Peak $\Delta F/F_0$; Figure 3.4C), which, in the case of a paired experiment, can be expressed relative to control.

3.3.4 Basal Ca^{2+} Activity

By creating STDev images from frames recorded prior to stimulation with ACh, we could extract signals only from cells that exhibited basal Ca^{2+} activity. Generally we were only able to detect spontaneous events that evolved into cell-wide waves. Example spontaneous Ca^{2+} signals are illustrated in Figure 3.5. Of the cells that exhibit basal Ca^{2+} activity in this dataset, two show repeat signalling whilst the remaining 4 cells only exhibit a single Ca^{2+} transient.

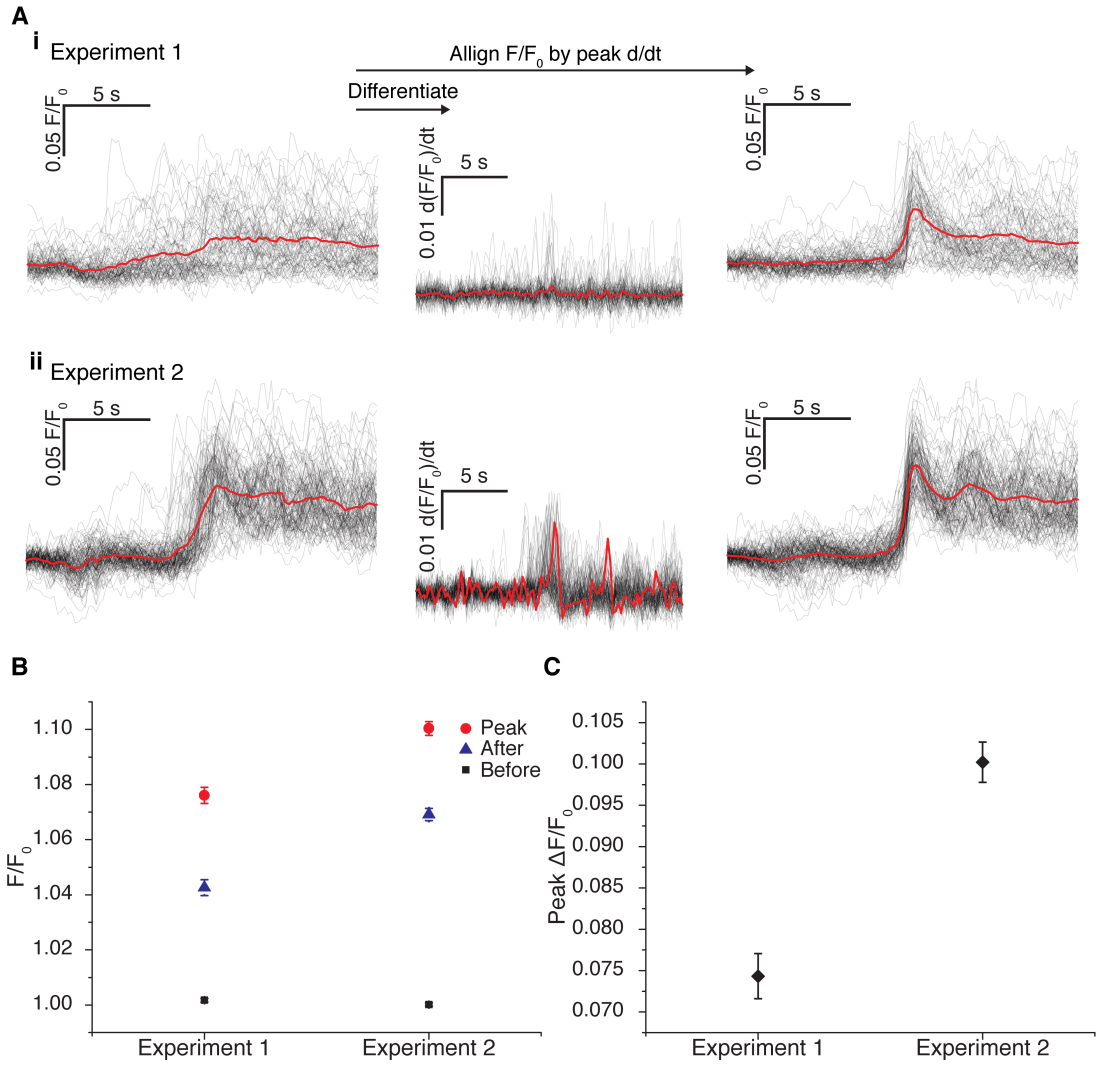

Figure 3.4 – Automatic data extraction from ACh-induced endothelial Ca^{2+} signals. (A) Automatically extracted, ACh-evoked, baseline corrected fluorescence Ca^{2+} signals (F/F_0, left panels) from two different experiments. Global mean data (thick red line) represents the data poorly. Ca^{2+} signals were differentiated (middle panels) and their time signatures were aligned with respect to the peak of the derivative, to synchronise the Ca^{2+} signals in each cell (right panels) and illustrate total Ca^{2+} activity (thick red line). (B) Averaged data automatically extracted from baseline corrected Ca^{2+} signals from the data shown in A. (C) Averaged peak change in Ca^{2+} signal ("before" F/F_0 value subtracted from the Peak F/F_0 value, for each signal) from the data shown in A and B.

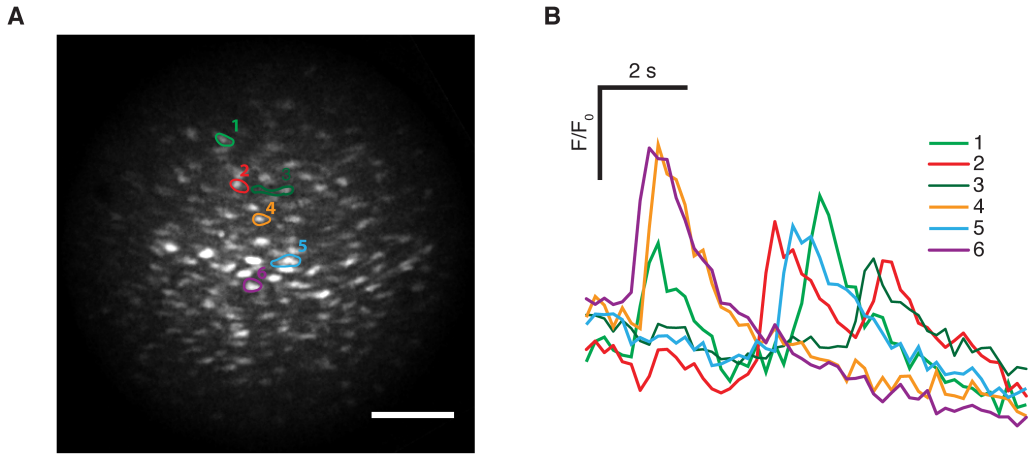

Figure 3.5 – Automatic data extraction from basal endothelial Ca^{2+} signals.

(A) ROIs highlighting cells exhibiting basal fluorescence Ca^{2+} activity, prior to ACh-evoked activity. Regions were semi-automatically generated from a 10 second period (50 frames) preceding ACh evoked activity, but are shown overlaid on a STDev image created using ACh-evoked activity. Scale bar: 100 µm (B) Individual Ca^{2+} signals of corresponding cells in A. Signals were baseline corrected by dividing raw fluorescence traces by the average of the full 10-second pre-stimulation period.

3.4 Discussion

With the development of technology enabling large-scale, two-dimensional microscopic imaging, data analysis has become increasingly challenging. There are no standardised techniques for processing data. Many research teams utilise labour intensive, time-consuming, manual routines for processing data. Others use semi-automated or fully automated software algorithms. Unfortunately, these procedures are not usually published for public use or they are designed for the requirements of very specific datasets. We addressed the issue of analysing fluorescence Ca^{2+} signals in images generated with our GRIN imaging system. The images are records of a large field-of-view that contain approximately 200 cells imaged at low-magnification – a number that makes manual processing of multiple datasets prohibitive. Thus, we developed a semi-automated procedure that extracts and analyses individual signals.

A key aspect of our approach, like other recently published algorithms (179,207,248,252) is using the activity of the cells themselves to facilitate their identification. However, raw or time-averaged fluorescence intensities were insufficient (manually or automatically) for cell identification - due to low contrast between neighbouring cells, and an uneven distribution of intensity across our images in both spatial and temporal dimensions. Therefore, we exploited the transient nature of endothelial Ca^{2+} signals to generate high contrast images of cells exhibiting Ca^{2+} activity (STDev image). Cell outlines were generated using sharpened images that were created by subtracting a heavily smoothed (25 × 25 mean filter, 20 passes) copy of the high contrast images from the original. In our procedure, the size of each ROI is slightly smaller than the cell itself and does not encompass the extremities of the elongated endothelial cells in an intact artery (135,168). The difference between the cell outline and the true shape of the cell is due to an unrecoverable loss of contrast towards the periphery of the cell. Nevertheless, the same is true for manually placed ROIs of set dimensions.

Although generation of the STDev image interrupts the flow of our otherwise automated image-processing procedure, it is the most important component as it generates images of sufficient quality to allow standard thresholding techniques to identify cellular boundaries, albeit with manual verification. Furthermore, this

procedure could be written into our ImagePro Plus macro enabling all except the final stage of our procedure to be automated. Following STDev generation is manual verification/correction of cell outlines. This is a significant step and improvement over other approaches. Remarkably, currently available automated routines do not provide a means for assessing the accuracy of ROI placement (179) or permit correction (179,207). By including the manual verification step, we ensure the fidelity of extracted signals.

A further important feature of our procedure, not shared by many previous techniques (179,207), is found in our approach to automatic post-processing of individual Ca^{2+} signals. Many other algorithms output individual signals, however, as the number of cells extends into the hundreds, appropriate visual representation is challenging as the unique properties of individual cells are usually lost when averaged (167). Additionally, most currently available algorithms output only aggregated data, rendering statistical analysis challenging. However in light of the heterogeneity of signals exhibited by our and other's data, it is important to be able to present data accordingly. By aligning Ca^{2+} signals with respect to their peak rate-of-change, aggregated Ca^{2+} responses were shown in a convenient and faithful manner and, by outputting the amplitude of individual signals at various time points, we are able to perform appropriate high power statistical analysis on our results.

Our analysis was specifically developed for fast processing and analysis of cell-wide (ACh-induced) Ca^{2+} transients in low magnification images obtained with our GRIN imaging system. Indeed, we demonstrated that the performance of our procedure exceeds that of a trained human operator and of an automated algorithm. Additionally, our procedure permits delineation of distinct Ca^{2+} activities, by adjusting the frames from which the STDev image is generated (i.e. pre-activation frames, activation frames, post-activation frames).

Our procedure should be broadly applicable to analysis of other Ca^{2+} imaging data. For example, in large-scale Ca^{2+} experiments on cultured cells. We also anticipate that our algorithm would be appropriate for the analysis of 'elementary' Ca^{2+} events that have been identified in endothelial cells (119,170) and numerous other cell types

(248,253) from high-resolution, high magnification image sequences. Additionally, our approach to defining cell outlines could be combined with the algorithm of Francis *et al.* (179) to ensure that fully automated, subcellular ROIs are positioned only within a given cell boundary.

Chapter 4. ACh-evoked Ca^{2+} Signalling in the Endothelium of Intact, Pressurised Arteries

4.1 Introduction

For proper functioning of the arterial system, vascular cells must act cooperatively with one another. The endothelium contributes substantially to this cooperative function by acting as a signal interpreter and relay system that ensure coordinated behaviour in the vascular system. To fulfil this role, endothelial cells produce chemical vasodilators that diffuse to control smooth muscle (SM) tone. Endothelial cells also have two additional properties that facilitate control of smooth muscle tone. First, endothelial cells are coupled to one another, via intercellular gap junctions (254,255), forming an electrically continuous, single-cell thick network that lines the entire inner surface of the vascular system. Second, heterocellular gap junctions (MEGJs) directly couple endothelial cells to smooth muscle cells (55,61,155). These homo- and heterocellular contacts allow endothelial cells to transmit localised electrical signals to remote regions (171,255) and to coordinate vasodilation by controlling smooth muscle hyperpolarisation (54,60,256), respectively. For example, localised application of ACh, may be translated into vasodilation upstream of the application site, at distances far beyond that which may be accounted for by diffusion of ACh, due to a spread of hyperpolarisation, in the opposite direction to flow, along the endothelium and into the smooth muscle layer (255,257).

Across the vascular tree, endothelial Ca^{2+} signalling critically regulates blood vessel function. Increases in endothelial $[Ca^{2+}]_i$, due to agonist-evoked activation and subsequent release of Ca^{2+} from the ER by IP_3Rs, may trigger the release of vasodilators or the spread of hyperpolarisation to smooth muscle cells. In addition to agonist-evoked responses, individual endothelial cells are capable of generating spontaneously occurring Ca^{2+} events, both in intact arteries (Figure 3.5) and in enzymatically dispersed native cells (258). On that basis, it is clear that individual endothelial cells may act as autonomous regulators of $[Ca^{2+}]_i$ and it follows that basal Ca^{2+} events may provide an impetus for an on going mechanism whereby individual endothelial cells may impact smooth muscle tone. Recently, studies examining Ca^{2+} in intact endothelial networks have provided evidence that spontaneously occurring (in the absence of agonist stimulation) subcellular spatiotemporal Ca^{2+} signals originate from distinct sites, and are modulated by G protein-coupled receptor

agonists, thus contributing to the endothelial response to vasoactive agonists (119,169,170,259–261). These IP_3-mediated Ca^{2+} signals, localised to discrete subcellular regions, and discernable in both *en face* preparations and pressurised arteries, have been shown to be a persistent mode of basal Ca^{2+} signalling that can be acutely altered by vasoactive agonists. Two findings, with respect to function, have given credence to a proposed physiological relevance of these events: 1) they predominantly occur close to, or within, MEGJs (119,170); 2) in response to agonists, these Ca^{2+} events evolve into cell-wide waves (168).

Although, endothelial cells may exhibit unstimulated spontaneous Ca^{2+} signals that occur independently of events occurring in neighbouring cells, and may display a heterogeneous $[Ca^{2+}]_i$ response to a number of agonists, endothelial cells act cooperatively within a tissue. Indeed, as an interconnected network of cells the endothelium enables output signals to be coordinated across large areas of tissue, and individual endothelial cells depend on input from other endothelial cells to generate a robust and coordinated response. Such a robust response is illustrated by the immediate vascular response to acute application of ACh: a pronounced elevation in *global* endothelial $[Ca^{2+}]_i$ that leads to marked vasodilation. The endothelium elicits vasodilation by governing the action of numerous Ca^{2+} -dependent pathways such as the generation of NO by endothelial NO synthase (eNOS) (30), the cyclooxygenase dependent generation of prostacyclin (44,45), and the activation of K^+ channels that result in membrane hyperpolarisation (31). However, whilst endothelial $[Ca^{2+}]_i$ is known to exert significant control over well-characterised effector pathways, a detailed understanding of the physiological control of endothelial $[Ca^{2+}]_i$ remains tenuous. This is particularly true with regards to the *self-regulated* engagement and tuning of endothelial Ca^{2+} responses across large endothelial networks.

Many studies utilising fluorescent chemical Ca^{2+} indicators have examined vasoactive agonist-evoked endothelial Ca^{2+} signalling in small populations of endothelial cells, visualised in pressurised resistance arteries, and in large populations, visualised in surgically opened and flattened arteries. These studies have demonstrated that although vasoactive agonists induce a global elevation in endothelial $[Ca^{2+}]$, the response of individual cells is spatiotemporally heterogeneous

(123,126,135,175,180,182). A fundamental limitation to studying heterogeneity in endothelial Ca^{2+} signals, in pressurised arteries, is the low number of endothelial cells that can be visualised with sufficient spatiotemporal resolution. *En face* preparations have demonstrated spatial heterogeneity in the responses of individual cells across large fields of endothelia (179,182,201,262). However, the extents to which the manipulation of arteries – to enable large numbers of endothelial cells to be visualised – and the loss of physiological parameters (e.g. pressure, mechanical forces) affect Ca^{2+} signalling are unknown.

Here, we use a side viewing GRIN microprobe imaging system (previously described in Chapter 2) and custom detection/analysis software (previously described in Chapter 3) to investigate the origin and transmission of cytosolic Ca^{2+} signals in large areas of endothelium in the intact and pressurised rat carotid artery. In an arrangement reminiscent of the structural hierarchy of neuronal networks, we demonstrate that spatially distinct clusters (ensembles) of endothelial cells appear to govern agonist-evoked Ca^{2+} signalling by triggering repeated IP_3-mediated Ca^{2+} waves that propagate to neighbouring cells, a feature of endothelial regulatory function missed in prior studies. Furthermore, we show that chemical activation of the endothelium causes a marked concentration-dependent increase in the amplitude of the response and in the number of cells recruited by initially responding (activator) ensembles. These observations suggest that for chemical (ACh) detection, signal processing in the endothelium is organised into clusters of functionally coupled cells that act as linked, relay elements of a communicating network.

4.2 Methods

4.2.1 Large-scale Endothelial Ca^{2+} Imaging

Endothelial Ca^{2+} signalling was imaged as described in Chapter 2. To assess endothelial function, arteries were stimulated, at 60 mmHg, by direct application of ACh (100 μM), delivered by a handheld pipette, at the start of each experiment to confirm endothelial viability and the stability of each preparation. In some experiments, arteries were activated with various concentrations of ACh, as indicated in the text. In other experiments, arteries were pre-treated with various pharmacological inhibitors, as indicated in the text, before activation with 100 μM ACh. In such experiments incubation was performed after the stability of the endothelial response was confirmed. Following each application of ACh and data acquisition period, the bath solution was immediately exchanged and the arteries were left for at least 20 minutes to re-equilibrate. The effects of different treatments on ACh-evoked Ca^{2+} activity were studied in paired experiments and expressed relative to control.

4.2.2 Semi-automated Analysis of Endothelial Ca^{2+} Signals

Endothelial (cellular) Ca^{2+} signalling was analysed as described in Chapter 3.

4.2.3 Visual Representation of Endothelial Ca^{2+} Signals

To facilitate visual inspection of endothelial Ca^{2+} signals a series of images were created to illustrate the active Ca^{2+} wavefronts, that is the forward difference of $[Ca^{2+}]_i$ changes (obtained by sequential subtraction) (244,263). For illustration in each figure, all images representing Ca^{2+} activity are composed of active Ca^{2+} wavefront (sequential subtraction) images superimposed, in green, onto greyscale images representing total Ca^{2+} activity (STDev images; see Chapter 3).

4.2.4 Solutions and Drugs

Solutions and drugs are as described in Chapter 2. In some experiments, the normal PSS was replaced with Ca^{2+}-free PSS, to elucidate the role of Ca^{2+} influx in the ACh-induced endothelial $[Ca^{2+}]_i$ response. In Ca^{2+}-free PSS, no Ca^{2+} was added and $MgCl_2$ (2 mM) and ethylene glycol tetraacetic acid (EGTA, 1 mM) were included. 2-aminoethoxydiphenyl borate (2-APB), cyclopiazonic acid (CPA), and 18β-

glycyrrhetinic acid (18α-GA) were dissolved in DMSO to 100 mM. Dissolution of 18α-GA was performed at 37°C. Ryanodine was dissolved in DMSO to 20 mM. Carbenoxolone (CBX), suramin and caffeine were dissolved in water. For experimentation, stock solutions were dissolved in physiological buffer to the concentrations indicated in the text such that the final concentration of DMSO, where present, was always less than or equal to 0.1%. Drugs were all obtained from Sigma.

4.2.5 Statistics

Summarised data are expressed as mean ± SEM. One-way ANOVA (with Tukey's post-hoc test as appropriate) was used for comparison. A p-value less that 0.05 was considered significant.

4.3 Results

4.3.1 ACh-evoked Ca^{2+} Signalling

In arteries pressurised to 60 mmHg, spontaneously occurring, whole-cell transient increases in Ca^{2+} occurred infrequently (< 0.97% of cells from 154 imaging experiments; see Figure 3.5). These spontaneous Ca^{2+} transients were not usually synchronised among cells and were restricted to particular cells. Activation of the endothelium by extraluminal ACh (100 μM, 60 mmHg) evoked rises in $[Ca^{2+}]_i$ in the majority of cells in the field (Figure 4.3). Despite activating the endothelium in arteries at resting diameter, the rise in $[Ca^{2+}]_i$ was often followed, approximately 30 seconds later, by a slight movement in endothelial cells as the vessel relaxed to ACh. The extent of this movement was always less than the width of a single endothelial cell, suggesting that the rat carotid artery exhibits a very low level of spontaneous smooth muscle tone. Nevertheless, analysis of endothelial Ca^{2+} signals was restricted to a period no greater than 30 seconds post ACh-induced activation; to avoid errors induced by movement of the cells.

The ACh-evoked response was composed of temporally distinct components. Initially, multiple large-scale Ca^{2+} waves would initiate and propagate across the field-of-view to activate the majority of visible endothelial cells. Most often, small spatial groupings of cells (ensembles), which were usually arranged in strips following the length of the artery, activated first Figure 4.1. When such activating ensembles were visualised, they appeared to initiate large-scale Ca^{2+} waves that would propagate across the field-of-view to activate the majority of visible endothelial cells (Figure 4.1**,** Figure 4.2A, Supplementary Videos 2&3). At times, these large-scale waves appeared to initiate outside the field-of-view (Figure 4.3). More than one large-scale wave could enter the field-of-view, occasionally in opposing directions, each travelling at a velocity of ~60 μm s^{-1}. These waves were similar to those seen travelling across, but originating within, the field-of-view. As these initial waves expanded, annihilation occurred on collision (Figure 2.9B and Figure 4.3) and complex spatiotemporal patterns of Ca^{2+} signalling developed (Figure 4.4, Supplementary Videos 2&3).

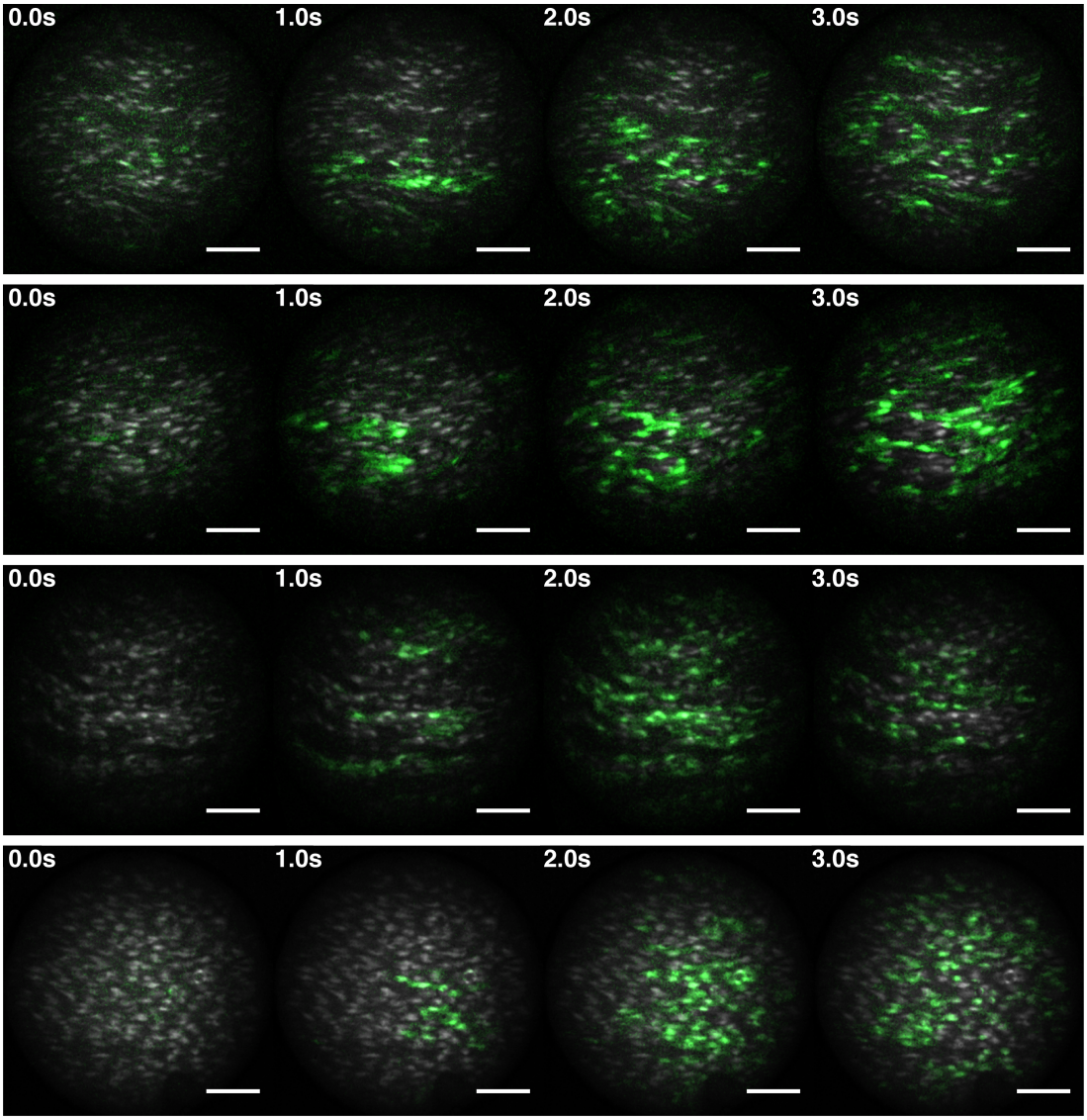

Figure 4.1 – Large-scale, ACh-evoked endothelial Ca^{2+} waves. Time-series fluorescence images of OGB-1/AM loaded endothelial cells showing propagation of large-scale, ACh-evoked (100 μM; bath application) Ca^{2+} waves that originate in distinct clusters of cells. Images are composed of instantaneous Ca^{2+} activity (green, Figure 3.1D) overlaid on standard deviation images (greyscale, Figure 3.1E), which are indicative of total Ca^{2+} activity. Scale bars: 100 μm.

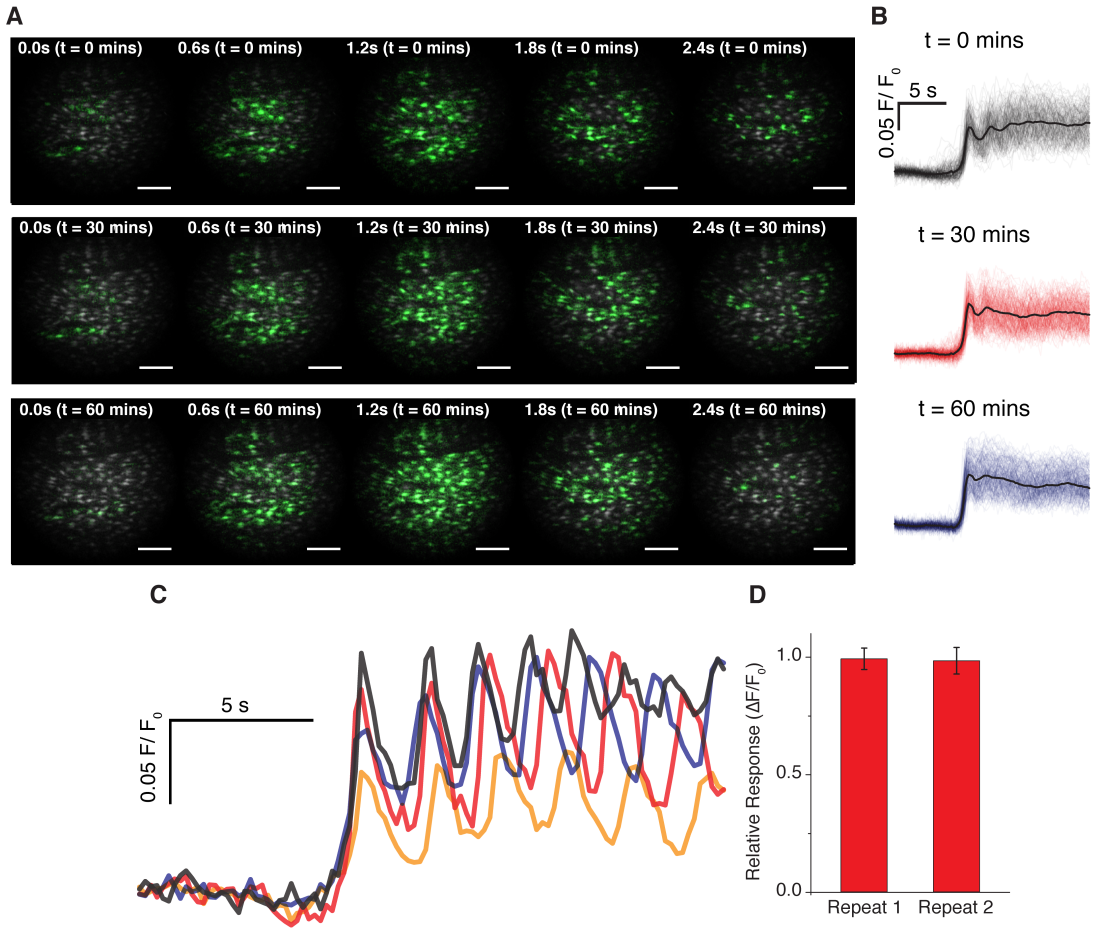

Figure 4.2 – Repeated activation of endothelial Ca^{2+} signalling. (A) Time-series fluorescence images of OGB-1/AM loaded endothelial cells showing approximately reproducible ACh-evoked Ca^{2+} signals (100 µM; bath application) in three repeat experiments in the same artery. Images are displayed as in Figure 4.1. Scale bars: 100 µm. (B) Semi-automatically extracted, time-aligned, and baseline-corrected ACh-evoked Ca^{2+} signals from data shown in A. The mean of the individual Ca^{2+} signals is overlaid as a thick black line. (C) Four individual Ca^{2+} signals from data shown in the top panel of A and B. Images correspond to data shown in Supplementary Video 4. (D) Summary data illustrating the stability of the average Ca^{2+} response activated by ACh (n = 5 ± SEM; normalised to control, first application, not shown). Successive ACh additions were separated by 20 minutes wash/reequilibration periods.

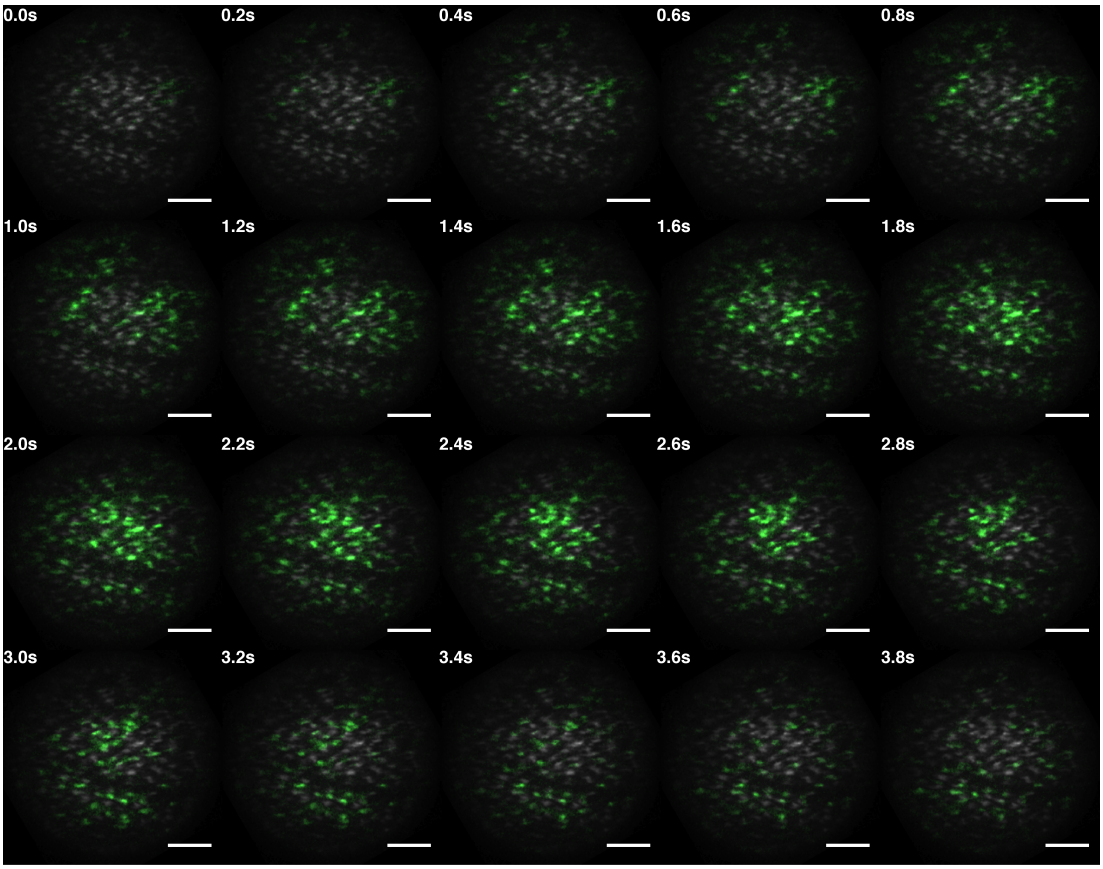

Figure 4.3 – Large-scale, ACh-evoked endothelial Ca^{2+} waves. Time-series fluorescence images of OGB-1/AM loaded endothelial cells showing propagation and subsequent collision and annihilation of large-scale, ACh-evoked (100 μM; bath application) Ca^{2+} waves that originate outwith the FOV. In this example, two waves originate at opposite sides of the field-of-view and travel towards the centre (longitudinal axis of artery is approximately horizontal). Images are displayed as in Figure 4.1. Scale bar: 100 μm.

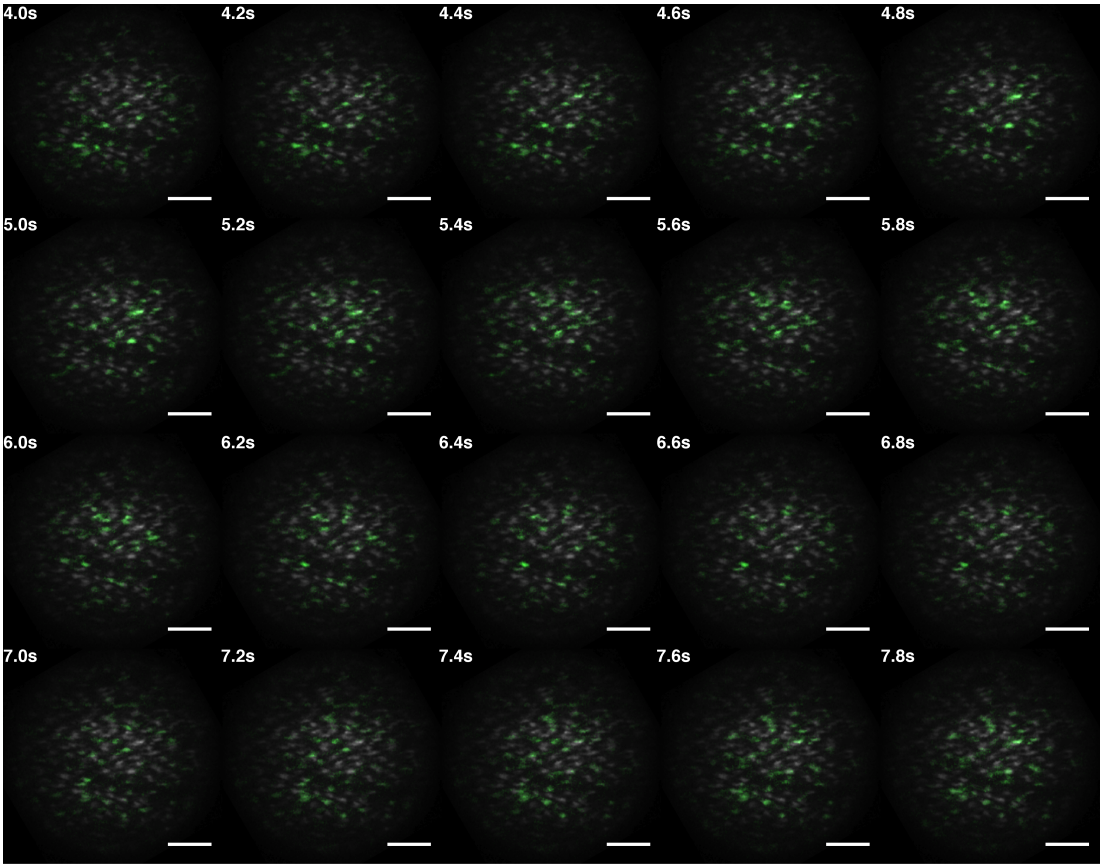

Figure 4.4 – Post ACh-activation endothelial Ca^{2+} waves. Time-series images of OGB-1/AM-loaded endothelial cells demonstrating complex Ca^{2+} signalling occurring after the collision and annihilation of initial ACh-evoked Ca^{2+} waves. Images are a continuation of the experiment shown in Figure 4.3, and are displayed in the same manner. Scale bar: 100 µm.

The pattern of initial wave progression, and the magnitude of Ca^{2+} signals were consistent on repeated activations by ACh (Figure 4.2A, Supplementary Video 4). Further analysis of a total of five time control experiments, showed there was not a significant difference in the peak magnitude of ACh-evoked Ca^{2+} signals following three ACh additions each separated by 20 minutes (Figure 4.2D), indicating the stability of the preparation.

Regardless of the spatial origin of the initial Ca^{2+} signal, complex oscillating Ca^{2+} signals occurred in the majority of cells following initiation by the large-scale Ca^{2+} wave(s). This is illustrated by the signals shown in Figure 4.2C and by the biphasic response of the mean aligned Ca^{2+} signals shown in Figure 4.2B. Due to the annihilation and collision of many Ca^{2+} waves, originating from distinct origination sites, the initial large-scale Ca^{2+} waves decoupled into multiple spatially-restricted events that were apparently desynchronised (as illustrated by the lack of oscillation visible in the mean Ca^{2+} signals shown in Figure 4.2B) at later times points. However, close inspection revealed small groupings of cells that appeared to remain linked via transmission of bi-directional Ca^{2+} waves (Figure 4.5). Because the entire preparation was exposed to a predefined ACh concentration instantaneously, these observations suggest that, for chemical (ACh) detection, signal processing in the endothelium is organised into a structural hierarchy where clusters of functionally coupled cells (Figure 4.1) act as linked, relay elements of a communicating network.

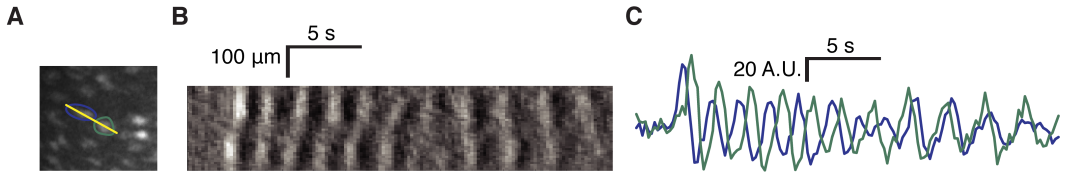

Figure 4.5 – Small-scale synchronous endothelial Ca^{2+} signalling activity. (A) Two endothelial cells exhibiting synchronous Ca^{2+} activity. (B) A kymograph (across yellow line in (A)) showing apparent bidirectional transmission of Ca^{2+} waves (rises in $[Ca^{2+}]_i$ are shown as lighter shades whilst declines are shown as darker shades) across two endothelial cells. (C) Plots of the derivate Ca^{2+} signal from the two cells (mean F/F_0 signal from two cells outlines in (A), differentiated with respect to time).

4.3.2 Regulation of ACh-evoked Endothelial Ca^{2+} Signalling

4.3.2.1 Effect of Extracellular Ca^{2+} on ACh-evoked Endothelial Ca^{2+} Signalling

Complex Ca^{2+} signals may result from the interaction of pathways that result in Ca^{2+} release from the ER, and pathways resulting in influx of Ca^{2+} from the extracellular space. To examine the role of Ca^{2+} influx in the ACh-evoked $[Ca^{2+}]_i$ response, arteries were exposed to Ca^{2+}-free PSS. ACh-evoked (100 µM) Ca^{2+} signalling persisted in the absence of extracellular Ca^{2+} (Figure 4.6A). Figure 4.6B demonstrates that neither the magnitude of the peak Ca^{2+} response nor the total number of cells responding to ACh were significantly different from control conditions (n = 4 animals).

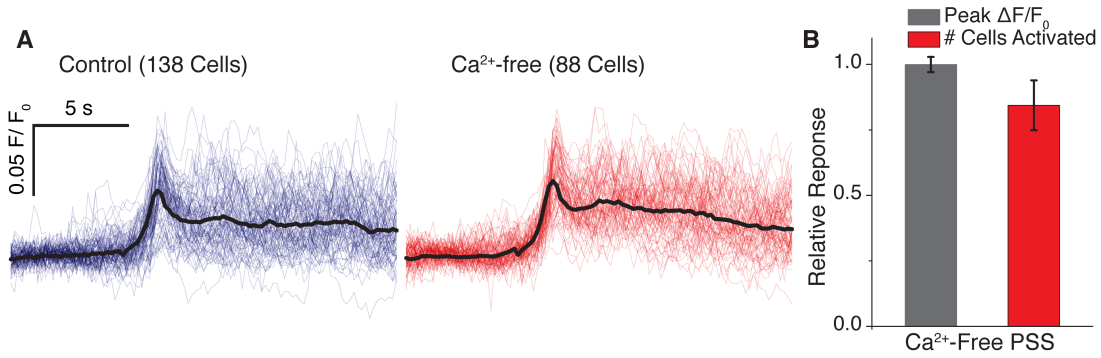

Figure 4.6 – Effect of extracellular Ca^{2+} on endothelial Ca^{2+} signalling. (A) Baseline-corrected and time-aligned ACh-evoked endothelial Ca^{2+} signals (F/F_0) obtained from the same artery before (left) and after (right) replacement of normal PSS with Ca^{2+}-free PSS (20 minutes equilibration). (B) Summary data showing the amplitude of the peak ACh-evoked (100 µM) response within each *activated* cell and the mean number of cells activated, in Ca^{2+}-free PSS. Data are presented as mean ± SEM (n = 4) normalised to control values (2 mM Ca^{2+}, 1; not shown), p <0.5 was considered significant.

4.3.2.2 Role of Intracellular Ca^{2+} Release Pathways in ACh-evoked Endothelial Ca^{2+} Signalling

IP_3Rs may be present in endothelial cells and contribute to ACh-evoked Ca^{2+} signalling. To examine the role of IP_3Rs in the ACh-evoked $[Ca^{2+}]_i$ response, arteries were incubated with the IP_3R inhibitor, 2-APB (100 µM), or the SERCA inhibitor, CPA (10 µM). As illustrated in Figure 4.7A, 2-APB significantly attenuated the ACh-evoked (100 µM) response. Both the number of endothelial cells responding to ACh, and the magnitude of responding cells were significantly reduced (n = 4 animals; Figure 4.7B). ACh-evoked Ca^{2+} signalling was completely abolished by CPA (n = 3 animals; Figure 4.7B).

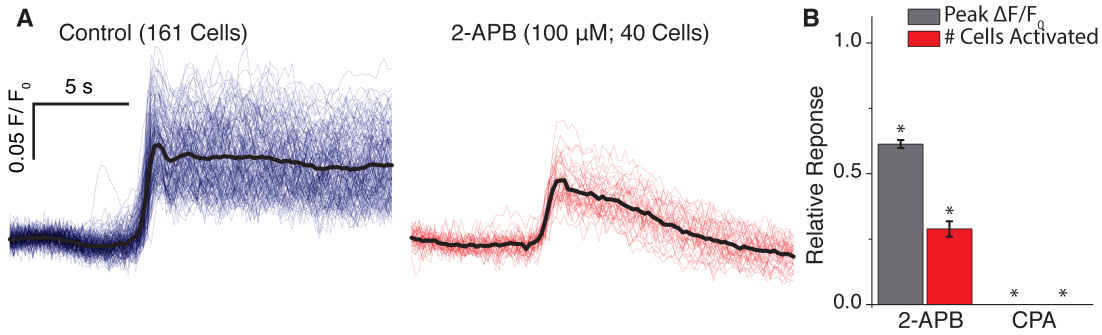

Figure 4.7 – Effect of IP_3R-mediated Ca^{2+} release on endothelial Ca^{2+} signalling. (A) Baseline-corrected and time-aligned ACh-evoked endothelial Ca^{2+} signals (F/F_0) obtained from the same artery before (left) and after (right) incubation with 2-APB (100 µM; 20 minutes equilibration). (B) Summary data showing the amplitude of the peak ACh-evoked (100 µM) response within each *activated* cell and the mean number of cells activated, in the presence of 2-APB (100 µM; n = 3) and CPA (10 µM; n = 3). Data are presented as mean ± SEM and normalised to control values (no treatment, 1; not shown), $p < 0.5$ was considered significant.

In some preparations, endothelial Ca^{2+} signalling may result from the activation of RyRs on the ER. To test the contribution of RyR to ACh-evoked (100 µM) endothelial Ca^{2+} signalling, arteries were incubated with the RyR inhibitor, ryanodine (10 µM), or stimulated with caffeine (10 mM). Representative Ca^{2+} (F/F_0) traces obtained from arteries incubated with RyR are shown in Figure 4.8A. In stark contrast to inhibitors of IP_3-mediated Ca^{2+} release, ryanodine had no significant effect on the peak magnitude of the ACh-evoked Ca^{2+} response or the number of cells responding to ACh (n = 3 animals; Figure 4.8B). ACh was applied two times in the presence of ryanodine, with no difference in response found (n = 3). Furthermore, application of caffeine, in the absence of ryanodine, failed to elicit a Ca^{2+} response (n = 3 animals; Figure 4.8B).

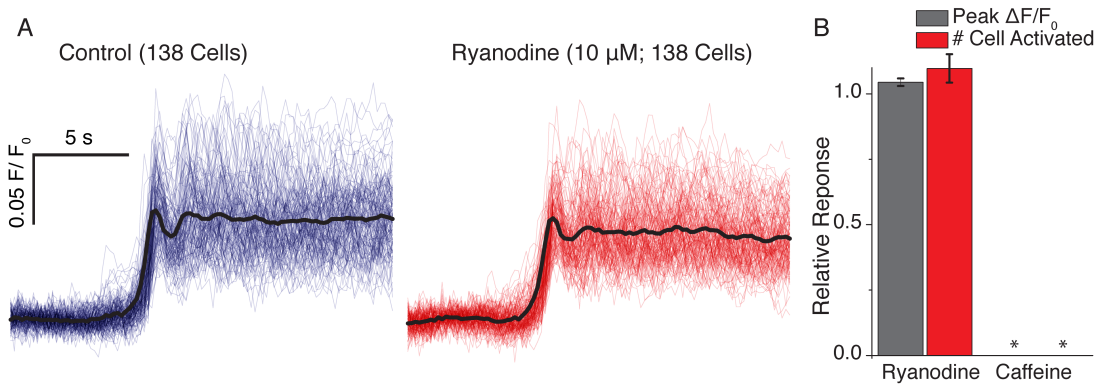

Figure 4.8 – Effect of RyR-mediated Ca^{2+} release on endothelial Ca^{2+} signalling. (A) Baseline-corrected and time-aligned ACh-evoked endothelial Ca^{2+} signals (F/F_0) obtained from the same artery before (left) and after (right) incubation with ryanodine (10 µM; 20 minutes equilibration). (B) Summary data showing the amplitude of the peak ACh-evoked (100 µM) response within each *activated* cell and the mean number of cells activated, in the presence of ryanodine (10 µM; n = 3) and the $[Ca^{2+}]_i$ response to caffeine (10 mM; n = 3). Data are presented as mean ± SEM and normalised to control values (no treatment, 1; not shown), $p < 0.5$ was considered significant.

In some cell types Ca^{2+} waves may propagate among cells by the sequential release of adenosine triphosphate (ATP). To test the contribution of ATP receptors to ACh-evoked (100 µM) endothelial Ca^{2+} signalling and wave progression, arteries were incubated with the purinergic ATP receptor inhibitor, suramin (100 µM). Representative Ca^{2+} (F/F_0) traces obtained from arteries incubated with suramin are shown in Figure 4.8A. Suramin had no significant effect on the peak magnitude of the ACh-evoked Ca^{2+} response, nor did it significantly alter the number of cells responding to ACh (n = 3 animals; Figure 4.8B).

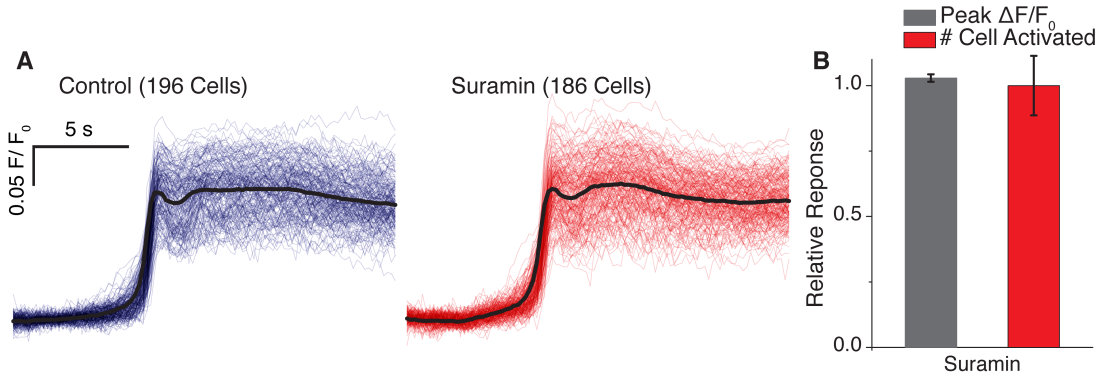

Figure 4.9 – Effect of ATP receptor blockade on endothelial Ca^{2+} signalling. (A) Baseline-corrected and time-aligned ACh-evoked endothelial Ca^{2+} signals (F/F_0) obtained from the same artery before (left) and after (right) incubation with suramin (100 µM; 20 minutes equilibration). (B) Summary data showing the amplitude of the peak ACh-evoked (100 µM) response within each *activated* cell and the mean number of cells activated, in the presence of suramin (100 µM; n = 3). Data are presented as mean ± SEM and normalised to control values (no treatment, 1; not shown), $p < 0.5$ was considered significant.

4.3.3 Inhibition of ACh-evoked Signalling with Gap Junction Blockers

To investigate whether ACh-evoked endothelial Ca^{2+} signalling occurs through intercellular gap junctions, we tested the effect of gap junction inhibition on the ACh-evoked response. Representative Ca^{2+} (F/F_0) traces for arteries pre-incubated with CBX (100 µM) are shown in Figure 4.10A. Both CBX and 18β-glycyrrhetinic acid (18β-GA, 100 µM) substantially reduced the mean magnitude of response to ACh (Figure 4.10B). However, the number of cells responding to ACh (Figure 4.10B) was not significantly reduced.

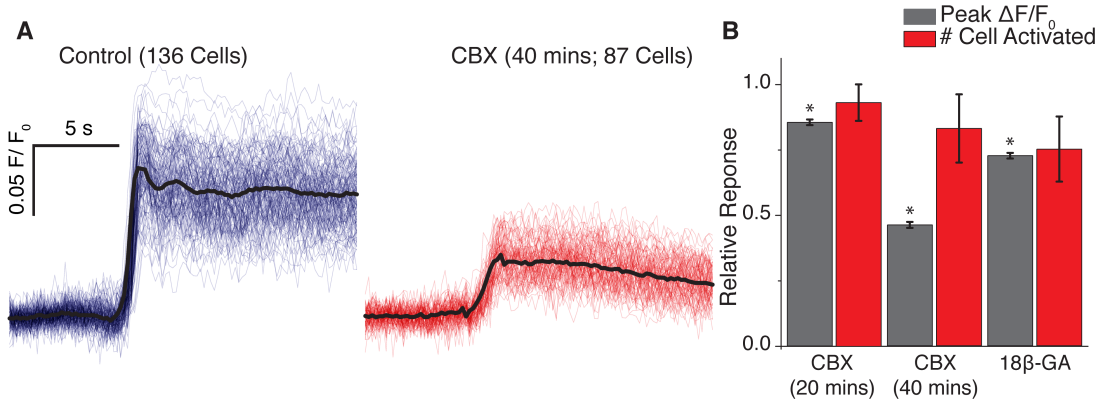

Figure 4.10 – Effect of gap junction inhibition on endothelial Ca^{2+} signalling. (A) Baseline-corrected and time-aligned ACh-evoked endothelial Ca^{2+} signals (F/F_0) obtained from the same artery before (left) and after (right) 40 minute incubation with CBX (100µM; 20 minutes equilibration). (B) Summary data showing the amplitude of the peak ACh-evoked (100 µM) response within each *activated* cell and the mean number of cells activated, in the presence of CBX for 20 and 40 minutes (100 µM; n = 3), and 18β-GA for 40 minutes. Data are presented as mean ± SEM and normalised to control values (no treatment, 1; not shown), $p < 0.5$ was considered significant.

Significantly, prolonged exposure to either 18β-GA (100 µM; 40 min; n =2; not shown) or CBX (100 µM; 60 min; n =2; not shown) resulted in a complete lack of response to ACh, and subsequently caused a slow increase in endothelial $[Ca^{2+}]_i$ that was followed by a decline to below resting values after approximately two hours (Figure 4.11). Time controls suggest that this was primarily an effect of the gap junction blockers.

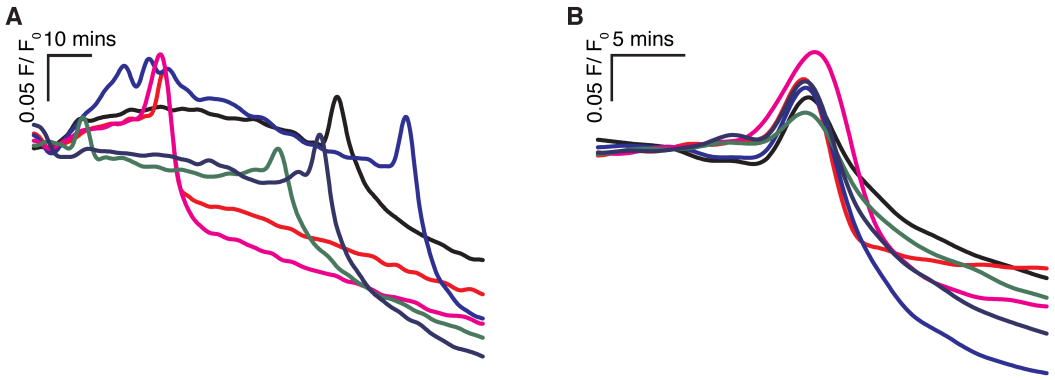

Figure 4.11 – Effect of gap junction inhibition on endothelial Ca^{2+} signalling. (A) Baseline-corrected (unaligned) endothelial Ca^{2+} signals (F/F_0) from six cells in an unstimulated artery incubated with 18β-GA (100 μM). Recordings are from a time-lapse experiment in which images were acquired at 10 second intervals, and start approximately 60 minutes after introduction of 18β-GA. (B) Time-aligned endothelial Ca^{2+} signals (F/F_0) shown in A. Raw Ca^{2+} signals have been aligned by the peak derivate Ca^{2+} signal, and baseline corrected using a 50 frame period prior to the peak. Signals in both panels have been temporally smoothed with a 10-point running average.

4.3.4 Concentration-dependence of ACh-evoked Endothelial Ca^{2+} Signalling

To explore how the organisation of IP_3-mediated endothelial Ca^{2+} activity may be mediated by the intensity of G protein-coupled (muscarinic) receptor activation, the endothelial Ca^{2+} response to pre-defined concentrations of ACh was examined. Three distinct features of the endothelial Ca^{2+} response to ACh were apparent (Figure 4.12,Figure 4.13): (1) there was a graded increase in the number of cells activated as the concentration of ACh increased (Figure 4.12A, Figure 4.13A); (2) the amplitude of the Ca^{2+} response within each cell, and the average of all activated cells, increased with ACh concentration (Figure 4.12B,C, Figure 4.13A); (3) the temporal spread of the response decreased with increasing ACh concentration (Figure 4.13B).

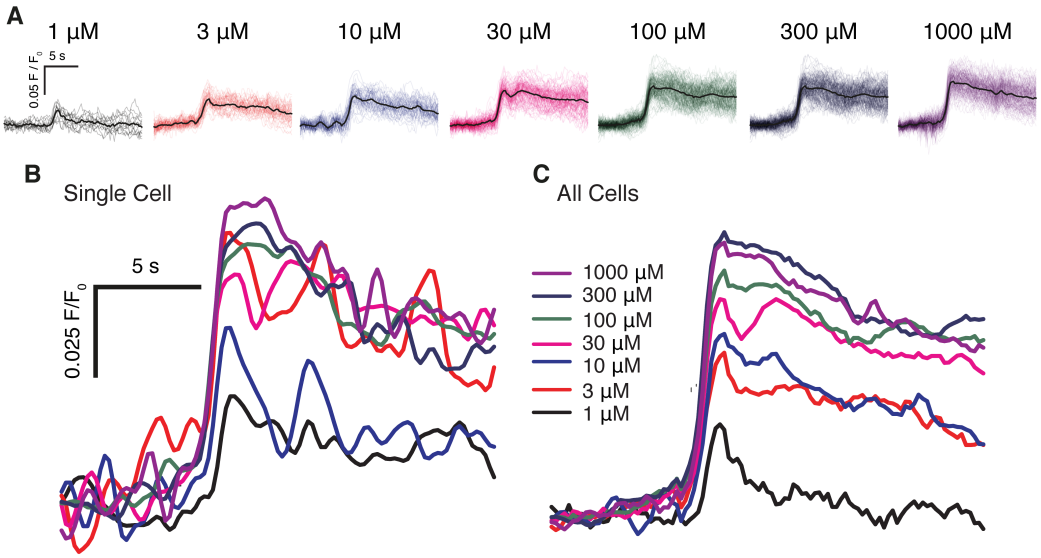

Figure 4.12 – Concentration-dependence of ACh-evoked Ca^{2+} signals. (A) Baseline corrected and time-aligned Ca^{2+} signals (with average overlaid in black) for a series of seven sequentially increasing applications of ACh in the same artery (B) Individual traces of the Ca^{2+} levels in a single endothelial cell (from (A)) upon activation with increasing ACh concentrations. Repetitive oscillations occur at some ACh concentrations (e.g. 3 µM). (C) Total endothelial Ca^{2+} activity (averages of (A)) for a single artery, upon repeated stimulation with increasing ACh concentrations. Ca^{2+} traces correspond to data shown in Supplementary Video 5.

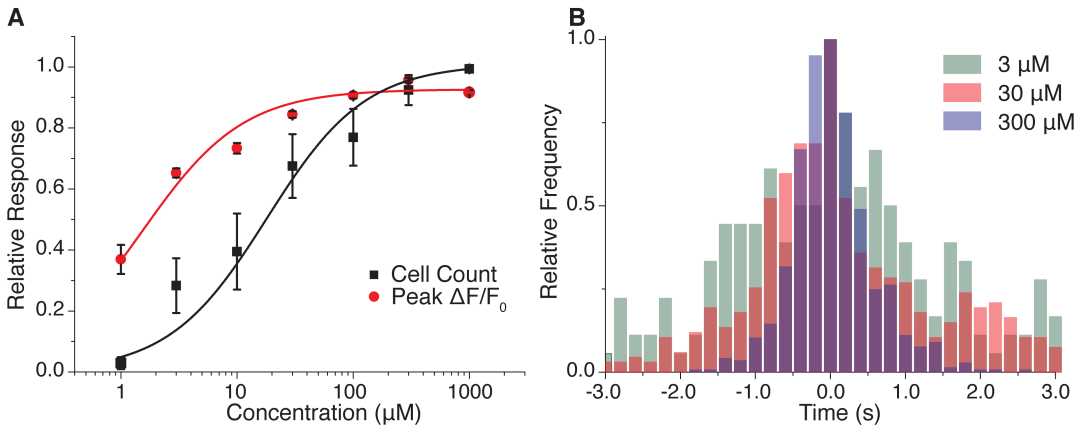

Figure 4.13 – Concentration-dependence of the ACh-evoked Ca^{2+} response. (A) Summary data illustrating the concentration dependence of the number of cells activated by ACh (black square) and the peak $\Delta F/F_0$ in cells activated by ACh (red circles; n ≥ 3 arteries ± SEM). All data normalised to peak response. (B) Normalised frequency distribution illustrating the temporal spread of time to activation for individual cells activated by three concentrations of ACh (3 μM, 30 μM, 300 μM; n = 6).

Close inspection of the active Ca^{2+} wavefronts (Figure 4.14, Supplementary Video 5) revealed further features of the ACh-evoked response. Low concentrations of ACh (e.g. 3 μM; Figure 4.14, top panel) induced an initial rise in endothelial $[Ca^{2+}]_i$ in only a small number of cells across the field-of-view. Subsequently, this rise in $[Ca^{2+}]_i$ would then spread to neighbouring cells in a wave-like fashion. This often resulted in (Ca^{2+}) activation occurring only within spatially distinct regions of endothelial cells across the field-of-view. These regions often appeared as strips of cells only one or two cells thick (similar to those seen in previous experiments using 100 μM; Figure 4.1). Interestingly, increasing concentrations of ACh caused an increasing number of cells to activate simultaneously, until all endothelial cells within the strips identified at lower concentrations activated near simultaneously (e.g. 30 μM; Figure 4.14, middle panel). The $[Ca^{2+}]_i$ rise would subsequently spread to further cells, which were not activated at low concentrations. This cumulative recruitment increased with ACh concentration.

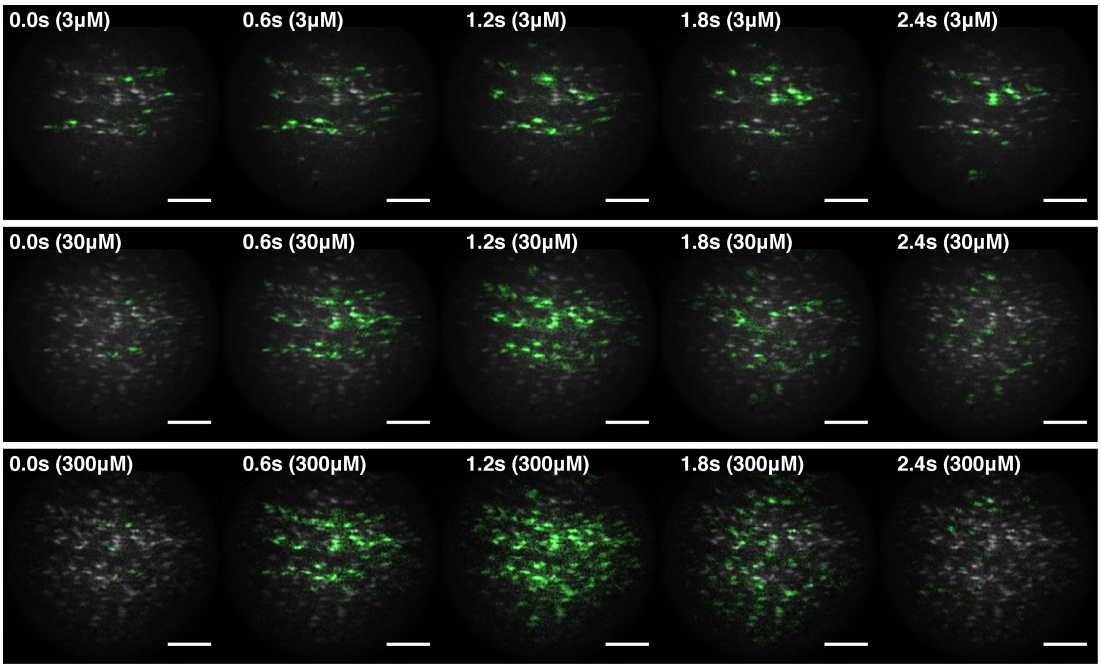

Figure 4.14 – Concentration-dependence of the ACh-evoked Ca^{2+} response. (A) Fluorescence images of OGB-1/AM loaded endothelial cells upon bath application of ACh, showing an increase in Ca^{2+} response and in the number of activated cells due to sequentially increasing bath concentration of ACh (3 μM, top; 30 μM, middle; 300 μM, bottom) from three repeat experiments in the same artery (20 min re-equilibration). Data from only three concentrations, of a complement of seven, are shown. Ca^{2+} signals (F/F_0) from a complete data set are shown in Figure 4.12. Images are displayed as in Figure 4.3; scale bar: 100 μm. Images correspond to data shown in Supplementary Video 5.

4.4 Discussion

In this study, endothelial responses to ACh were observed for a 30 second period in up to 200 cells (across a 0.5 mm diameter FOV) within each pressurised artery. In response to 100 μM ACh, an initial rise in endothelial $[Ca^{2+}]_i$ was observed in small groupings of cells, which was followed by Ca^{2+} wave progression that recruited neighbouring cells. Subsequently, complex patterns of Ca^{2+} activity emerged across the FOV due to the interaction of Ca^{2+} waves that appeared to arise from distinct sites. The complex activities across cells appeared to generate complex responses within endothelial cells. Accordingly, the response of individual endothelial cells was spatially and temporally heterogeneous across the field-of-view, in agreement with numerous other studies (123,126,167,175,201). However, whilst previous studies have reported differences in signalling events among cells (e.g. magnitude, time signature), the complex spatiotemporal relationships of $[Ca^{2+}]_i$ signalling among endothelial cell populations, particularly with regard to effects imparted by neighbouring cells has received little attention.

The $[Ca^{2+}]_i$ response, within individual cells, was assessed by measuring the peak change in the baseline-corrected fluorescence signal ($\Delta F/F_0$). Depletion of the ER Ca^{2+} concentration, using the SERCA inhibitor, CPA (10 μM), abolished all response to ACh, whilst inhibition of IP_3Rs, using 2-APB (100 μM), significantly reduced both the number of cells responding and the peak response within each responding cell. These results suggest that, in the absence of IP_3-mediated Ca^{2+} release from the ER, ACh fails to evoke Ca^{2+} wave initiation or propagation in rat carotid artery endothelial cells. Consistent with these findings, the ACh-evoked response (including the complex signalling that occurred due to wave propagation) persisted in the absence of extracellular Ca^{2+}. Furthermore, ryanodine (10 μM) did not alter the ACh-evoked Ca^{2+} rise, and caffeine (10 mM) failed to evoke a Ca^{2+} increase, suggesting RyR play a minor role in Ca^{2+} signalling in the endothelium. These findings are consistent with previous studies in pressurised resistance arteries (126,168) and in endothelial sheets (126) and tubes (167) isolated from resistance arteries, and strongly suggest that the nature of endothelial Ca^{2+} signals depend on

IP_3-mediated Ca^{2+} wave initiation and intracellular/intercellular signal propagation, in rat carotid endothelial cells.

Coordinated arterial function requires vascular cells to produce a concerted output (167,264). In the intact artery, coordinated endothelial signalling occurs because endothelial cells, which are in direct contact with each other, are interconnected. Each may be in contact with several other endothelial cells (167), such that they form a complex network lining the inner surface of the blood vessel. Endothelial cells may also be coupled to smooth muscle cells via heterocellular contact. This heterocellular coupling imparts an ability on the endothelium to induce a robust smooth muscle response (259), and allows Ca^{2+} signals originating in the smooth muscle layer to evoke or influence Ca^{2+} responses in the endothelium (169,170,176,264). Communication between vascular cells occurs through gap junction channels, intercellular connections that permit movement of charged ions and secondary messengers (265,266). These gap junction channels are formed by the coupling of connexons (also called hemi-channels) on adjacent cells. Connexons are hexameric complexes formed from individual connexin subunits that are robustly expressed on endothelial cells in various preparations, including the rat carotid artery (267–269).

Similar to findings in endothelial cells in arteries studied *ex vivo* (168) and *in vivo* (200,270) by conventional fluorescence microscopy, we report the occurrence of whole-cell Ca^{2+} waves in the absence of ACh stimulation, albeit at a very low frequency and in few cells. Although we did not investigate the nature of these spontaneous endothelial Ca^{2+} events, it is proposed that they are regulated, through gap junction channels, by smooth muscle cells (168). By uniformly exposing arteries to a pre-defined concentration of ACh (100 μM), in the presence of the gap junction inhibitors, CBX (100 μM) and 18β-GA (100 μM), we found that the magnitude of the endothelial Ca^{2+} response, in individual cells, was slightly reduced. Based on current perceptions regarding the regulation of endothelial Ca^{2+} signals by gap junctions (see above), a reduction in the number of cells responding to ACh in arteries exposed to gap junction blockers was anticipated but not observed. The action of these gap junction blockers is neither specific nor well defined (271,272). Indeed, the number of cells activated by ACh was only reduced when arteries were

exposed to the gap junction blockers for extended periods of times, which abolished the Ca^{2+} response. However, this only occurred after basal Ca^{2+} levels had been reduced following a transient increase in endothelial $[Ca^{2+}]_i$. These results suggest the blockers are altering cell function in ways unrelated to gap junctions.

Despite the confounding results of our studies using gap junction inhibitors, the existence of communication through endothelial gap junctions is indicated to in our studies of arteries exposed to increasing concentrations of ACh at discrete intervals. We found that low concentrations of ACh only activated small, spatially distinct groupings of endothelial cells, that we term activator ensembles. Increasing the concentration of ACh caused all cells within these regions to appear to activate almost simultaneously, and appeared to lead to the recruitment of additional cells via the spread of Ca^{2+}signals. The spread of Ca^{2+} waves, resulting in the recruitment of additional endothelial cells, is in agreement with the transfer of dyes through gap junction channels in native endothelial cells (256,273), suggesting a mechanism where the response of individual ensembles is translated into a signal that spans the macroscopic scale of the artery. Previous studies have demonstrated that only a small fraction of native murine aortic endothelial cells respond to a single concentration of ACh (182,262) and that a similar percentage of endothelial cells express muscarinic M3 receptors (262). Although not commented upon by the authors of these studies, it is interesting to note that close proximity (i.e. clustering) of endothelial cells exhibiting Ca^{2+} responses is apparent in their images (see Fig 2A (panels 5 & 6) in ref 262). Similarly, M3 receptor expression also appears in closely apposed cells (see Fig 3A & Fig 4A,B in ref 262).

Whilst Ca^{2+} waves appear to propagate among endothelial cells, such observations do not demonstrate causality (i.e. that a wave propagates between two cells instead of the two cells exhibiting independent Ca^{2+} waves). To demonstrate causality, further spatiotemporal analysis is required. In this regard, temporal latency between Ca2+ signals in neighbouring cells has recently been used as a quantitative measure of assessing intercellular endothelial Ca^{2+} signalling (167). Additionally, spatiotemporal cross-correlation analysis of frequencies may also be used to assess cross-level interdependence of Ca^{2+} signals in cell networks (207,274).

This study is the first to report the effects of the G protein-coupled receptor agonist, ACh, on endothelial $[Ca^{2+}]_i$ signalling in large, vital (rat carotid) arteries under physiological mechanical loading. Directly visualizing the endothelium in these arteries, using our GRIN imaging system (Chapter 2), has enabled us to characterise the response in large networked fields of endothelial cells in a pressurised artery. The major findings are (1) ACh-evoked $[Ca^{2+}]_i$ response is IP_3-mediated; (2) ACh-evoked $[Ca^{2+}]_i$ responses were heterogeneous across the populations of visualised cells; (3) endothelial cells appear to activate in discrete (activator) ensembles with specific, repeatable thresholds; (4) the number of cells exhibiting $[Ca^{2+}]_i$ responses due to ACh activation increased with ACh concentration, in a concentration-dependent manner, apparently due to the recruitment of additional endothelial cells by activator ensembles; (5) the magnitude of the peak ACh-evoked $[Ca^{2+}]_i$ response increased, in individual cells, with ACh, in a concentration-dependent manner.

These results suggest that endothelial cells within activator ensembles are primed with a small range of activation thresholds, perhaps due to differential expression of muscarinic M3 receptors. The combination of various activation thresholds, responses of variable amplitude, and plasticity in cell recruitment presumably maximises sensitivity to ACh over a wide concentration range whilst enabling signals to be relayed over a large dynamic range. The complex interaction of bioactive molecules with spatially distinct domains of effector cells, and the ability of cells to communicate with each over the whole endothelial surface suggests that non-excitable endothelial cells function cooperatively as an artery-lining, macroscopic excitable network.

Chapter 5. Pressure-Induced Suppression of ACh-evoked Ca^{2+} Signalling in the Endothelium of Intact, Pressurised Arteries

5.1 Introduction

The vascular endothelium is a single-cell thick layer that forms a complex and dynamic network regulating arterial tone (275), vascular permeability (146), angiogenesis (120), and smooth muscle proliferation (40,41,154). Such extensive control over the vascular system is conferred by the ability of the cellular network to detect and interpret multiple, simultaneously occurring hemodynamic signals, such as those derived from mechanical stimuli (hydrostatic pressure, luminal shear-stress, circumferential strain) and from various local blood borne signals (autocrine, paracrine, electrical signals and neurotransmitters). Ca^{2+} signalling is an orchestral component of endothelial function (119,167,168,175), however the exact mechanisms by which the endothelium receives, interprets, and responds to multiple simultaneously occurring hemodynamic stimuli, to converge on a physiological response lie beyond current understanding.

The detection and the transmission of signals by vascular endothelial cell networks have been studied in populations of endothelial cells in cell culture and in arteries that have been opened surgically. Experiments using these preparations indicate that mechanosensitive mechanisms may contribute to the endothelial response (e.g. ion channels, membrane receptors, cytoskeletal components, glycocalyx; (74,276)). Although the biological relevance of these mechanosensitive components seems plausible, the nature of any mechanosensor, and any integrated response, is unresolved. Several studies have shown that mechanical forces activate TRPV4 channels. For example, TRPV4 channels are activated by increases in stretch induced by cell suction (277) and by osmotic cell swelling (278). However, in other studies TRPV4 channels are not directly activated by either osmotic cell swelling (279) or stretch (280), suggesting that TRPV4 channels may be elemental relays of one or more as yet unidentified upstream signalling cascades (281), rather than direct mechanical force sensors.

The physiological response of the endothelial network critically depends on the complex, cylindrical, three-dimensional arrangement of vascular cells and their interaction with other cell types *in vivo*. For example, in many intact arteries, myogenic contraction occurs when the artery is subjected to circumferential stretch

by pressure increases. However, this contraction does not occur in arteries stretched, with equivalent forces, on wires (187). Although mechanical stimuli can and do produce responses localised to specific subcellular microdomains or ion channels/receptors (74,276), the *whole cell* may be required for physiological mechanotransduction to occur, as it is the whole cell that integrates many distinct environmental inputs to elicit a specific response (282).

In an effort to characterise the response of endothelial cells to vasoactive agonists, an imaging system that can visualise the endothelium of large, intact arteries was developed (Chapter 2). The imaging system (Figure 2.4) utilises a GRIN microprobe, that can be placed within the lumen of vessels to enable unobstructed visualisation of endothelial cells, loaded with fluorescent chemical Ca^{2+} indicators, in pressurised arteries. Utilising custom detection/analysis software (Chapter 3), agonist-evoked (ACh) Ca^{2+} signalling appeared to occur in a concentration-dependent manner, due to the preferential activation of endothelial cells within spatially restricted groups (activator ensembles; Chapter 4). The ACh-evoked Ca^{2+} signalling was dependent on the generation of IP_3 (Chapter 4). Because agonist-evoked and IP_3-dependent elevations in Ca^{2+} is known to produce various vasodilators (28,87,141), and because increased pressure is known to decrease agonist-evoked endothelial function (75,114,283), it is possible that modulation of IP_3-mediated Ca^{2+} release may provide a mechanism whereby mechanical forces may be transduced into physiological responses by the endothelium.

To investigate this hypothesis, pressure-dependent changes in endothelial cytosolic Ca^{2+} signals in larges areas of endothelium in the intact and pressurised rat carotid artery were investigated. Mechanical stimulation, due to increased transluminal pressure, distended the artery and suppressed IP_3-mediated Ca^{2+} signals. By modelling Ca^{2+} release, we show that pressure-induced changes in endothelial shape limit IP_3-mediated Ca^{2+} signalling by altering the geometry of the Ca^{2+} diffusive environment near IP_3 receptor (IP_3R) microdomains. We propose that geometric, microdomain-regulation of IP_3-mediated Ca^{2+} signalling explains macroscopic pressure-dependent endothelial-mechanosensing, without the need for a specific

mechanoreceptor, and provides a mechanism whereby the whole cell may modulate Ca^{2+}-dependent biological responses.

5.2 Methods

5.2.1 Large-scale Endothelial Ca^{2+} Imaging

Endothelial Ca^{2+} signalling was imaged as described in Chapter 2. To assess endothelial function, arteries were stimulated, at 60 mmHg, by direct application of ACh (100 μM), delivered by a handheld pipette, at the start of each experiment to confirm endothelial viability. In experiments where transmural pressure was increased from 60 mmHg to 110 mmHg to 160 mmHg, arteries were allowed to equilibrate at the experimental pressure for a period not less than 20 minutes before stimulation. In experiments where transmural pressure was decreased from 160 mmHg to 110 mmHg to 60 mmHg, arteries were pressurised to 160 mmHg following confirmation of endothelial viability at 60 mmHg, and allowed to equilibrate at the experimental pressure for a period not less than 20 minutes before stimulation. In other experiments, arteries were pre-treated with various pharmacological inhibitors and incubated for various times, as indicated in the text, before activation with 100 μM ACh. In such experiments incubation was performed after the stability of the endothelial responses were confirmed. Following each acquisition period, the bath solution was immediately exchanged and the arteries were left for at least 20 minutes to re-equilibrate. The effects of different treatments on ACh-evoked Ca^{2+} activity were studied in paired experiments and expressed relative to control.

5.2.2 Semi-automated Analysis of Endothelial Ca^{2+} Signals

Endothelial (cellular) Ca^{2+} signalling was analysed as described in Chapter 3.

5.2.3 Visual Representation of Endothelial Ca^{2+} Signals

Endothelial Ca^{2+} signals are represented graphically as described in Chapter 4.

5.2.4 Measurement of Artery Diameter

At the end of some experiments, we recorded the diameter of arteries as pressure was increased, in 5 mmHg increments, from 0 mmHg to 200 mmHg. For videomicroscopy-based diameter measurements, arteries were illuminated with bright field illumination, which was guided to a CCD camera mounted (Sony XC-77; Sony, Japan) mounted on the side-port of the inverted microscope on which our GRIN imaging system was mounted. Images were captured form the CCD camera

using Micromanager software (231), and a USB video capture device (Dazzle; Pinnacle Systems, USA) and stored on a computer for subsequent analysis. Artery diameter was measured using the Vessel Diameter plugin for ImageJ (159).

5.2.5 Histological Analysis

5.2.5.1 Fixation

In separate experiments, rat carotid arteries were fixed at pressure, as a precursor to histological examination. Arteries were mounted in a custom dual-cannula pressure myography chamber and length-adjusted to remove buckle at 160 mmHg. Following length adjustment, the lumenal physiological buffer was replaced with Zenker's fixative. Zenker's fixative was introduced to the lumen by releasing the artery pressure and perfusing the solution into the lumen. The orange colour of Zenker's solution enabled its visualisation, permitting determination of when the lumen was filled with fixative. Once the lumen was filled with fixative, the artery was sealed and the pressure was raised to 60 mmHg or 160 mmHg. Immediately following pressurisation, the extraluminal physiological buffer was removed from the bath and replaced with Zenker's solution. Arteries were left to fix for at least two hours - a time determined, in preliminarily experiments to be required to prevent a reduction in arterial dimensions upon removal of pressure. Following fixation, arteries were removed from the myography chamber, washed overnight in tap water and finally stored in 70% ethanol at 4^{o}C until use. Arteries were paired for analysis (i.e. two arteries from each animal were fixed at the two different pressures (60 mmHg and 160 mmHg).

5.2.5.2 Tissue Processing

Following fixation, arteries were dehydrated in alcohol series (70% ethanol, 4 hours, 4 changes; 95% ethanol, 2 hours, 2 changes; 100% ethanol, 2 hours, 4 changes), cleared (1:1 mixture of 100% ethanol, 1 hour; Histoclear, overnight, 4 changes), infiltrated and embedded (Paraffin Wax, 4 hours). Wax blocks were cut into 5 μm thick sections and mounted onto slides.

5.2.5.3 Staining

Slides were rehydrated in Histoclear (10 minutes, 1 change), then alcohol series (100% ethanol, 10 minutes, 1 change; 95% ethanol, 2 minutes; 70% ethanol, 2 minutes), before being washed in distilled water. Rehydrated slides were stained with Harris Hematoxylin solution (10 minutes), washed with warm running tap water (10 minutes) then Scotts tap water (1 minute), differentiated in acid alcohol (0.3%, 5 seconds), stained with Eosin (5 minutes), washed with warm running tap water (10 minutes), then dehydrated in alcohol series (70% ethanol, 2 minutes; 95% ethanol, 2 minutes; 100% ethanol, 10 minutes, 1 change), cleared in Histoclear (10 minutes, 1 change), before being mounted with Histoclear.

5.2.5.4 Assessment of Endothelial Nuclear Thickness

Stained artery cross-sections were imaged using a Leica DM LB2 microscope with a Leica DFC320 camera (Leica Microsystems, UK). The thickness of endothelial cell nuclei was measured using Image Pro Plus.

5.2.6 Solutions and Drugs

Solutions and drugs are as described in Chapter 2 and Chapter 4. RN1734 was dissolved in DMSO to 30 mM. For experimentation, the RN1734 stock solution was dissolved in physiological buffer to the concentration indicated in the text such that the final concentration of DMSO was 0.1%. Drugs were all obtained from Sigma. Histoclear and Histomount were obtained from Thermo Fisher (UK). Harris Haematoxylin, Scotts tap water and Eosin were obtained from and Sigma (UK). Zenker's fixative was obtained from Fisher Scientific.

5.2.7 Statistics

Statistics are as described in Chapter 4.

5.3 Results

5.3.1 Pressure Regulation of ACh-evoked Endothelial Ca^{2+} Signalling

To explore how IP_3-mediated (ACh-evoked) endothelial Ca^{2+} activity changed due to mechanical forces, we examined the endothelial Ca^{2+} response to ACh (100 μM) in individual arteries subject to step-wise increases in transmural pressure. As described in Chapter 4, when arteries were pressurised to 60 mmHg, ACh (100 μM) evoked rises in $[Ca^{2+}]_i$ in the majority of cells in the field (Figure 5.1, top panel; Supplementary Video 6) and complex spatiotemporal patterns of Ca^{2+} signalling developed. As intraluminal pressure was increased in steps (60 mmHg to 110 mmHg to 160 mmHg), ACh (100 μM) still evoked rises in $[Ca^{2+}]_i$ in the majority of cells in the field, but the response of individual cells was substantially reduced (Figure 5.1, middle and bottom panels; Supplementary Video 6). Semi-automatically extracted and aligned Ca^{2+} signals, shown in Figure 5.2, confirm the pressure-dependent reduction in the response of individual cells of a single artery.

Further analysis of the Ca^{2+} responses from eight arteries, confirmed the pressure dependent reduction in ACh-evoked endothelial Ca^{2+} signalling (totalling more than 800 cells visualised at each pressure; Figure 5.3A) and revealed two other distinct features of the endothelial Ca^{2+} response to ACh: (1) there was a decrease in the number of cells activated by ACh (100 μM) as pressure was increased (Figure 5.3B); (2) the temporal spread of the response decreased with increasing pressure (Figure 5.3C). As pressure was increased, vessel diameter also increased (Figure 5.3D), suggesting that the decrease in the number of cells visualised at increased pressures and the decrease in the temporal spread of Ca^{2+} responses may be geometric effects resulting from mechanical deformation (circumferential stretch) of the endothelial layer. The suppression of Ca^{2+} signals was reversed as pressure was decreased (Figure 5.4A-D), however control values of $\Delta F/F_0$ were not fully recovered (n = 1). Summarised data illustrates that decreasing pressure (160 mmHg to 110 mmHg to 60 mmHg) results in an increase in the endothelial Ca^{2+} response (Figure 5.4E).

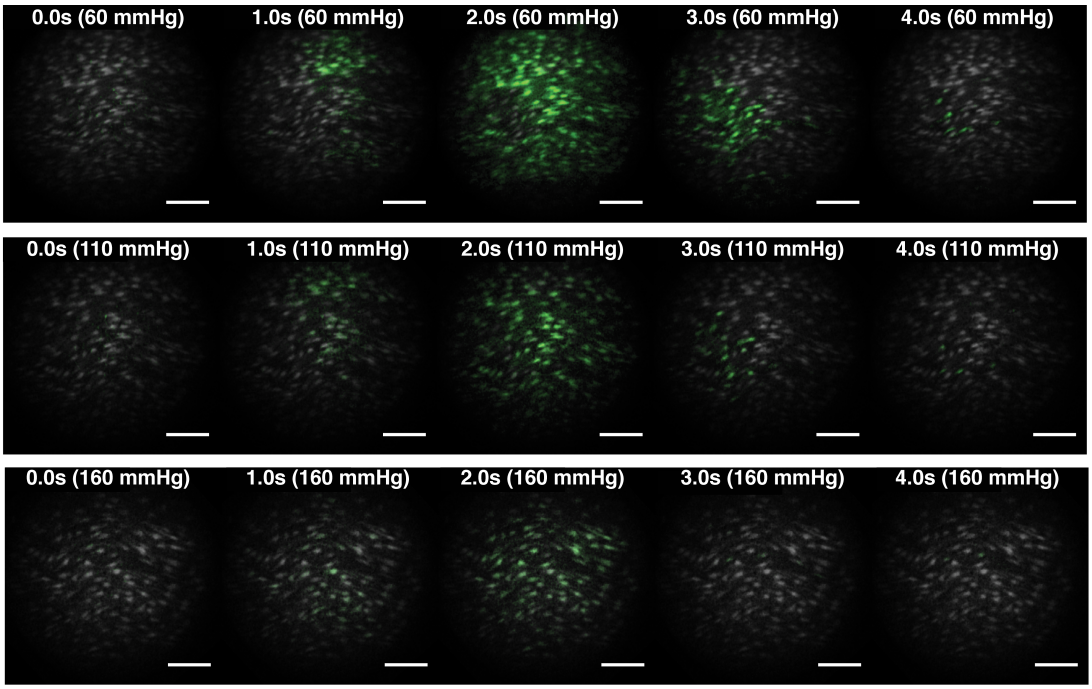

Figure 5.1 – Pressure-dependence of the ACh-evoked endothelial Ca^{2+} response. Fluorescence images of OGB-1/AM loaded endothelial cells upon bath application of ACh, showing an decrease in Ca^{2+} response in cells across the field-of-view as pressure is increased (60 mmHg, top; 110 mmHg, middle; 160 mmHg, bottom), from three sequential experiments in the same artery (20 min equilibration). Basal raw fluorescent intensity values decreased at increased pressures. Presumably this was due to photobleaching, and a decrease in the volume of Ca^{2+} indicator sampled due to stretch of the vessel. Ca^{2+} signals (F/F_0) from a complete data set are shown in Figure 5.2. Images are displayed as in Figure 4.3; scale bar: 100 μm. Images correspond to data shown in Supplementary Video 6.

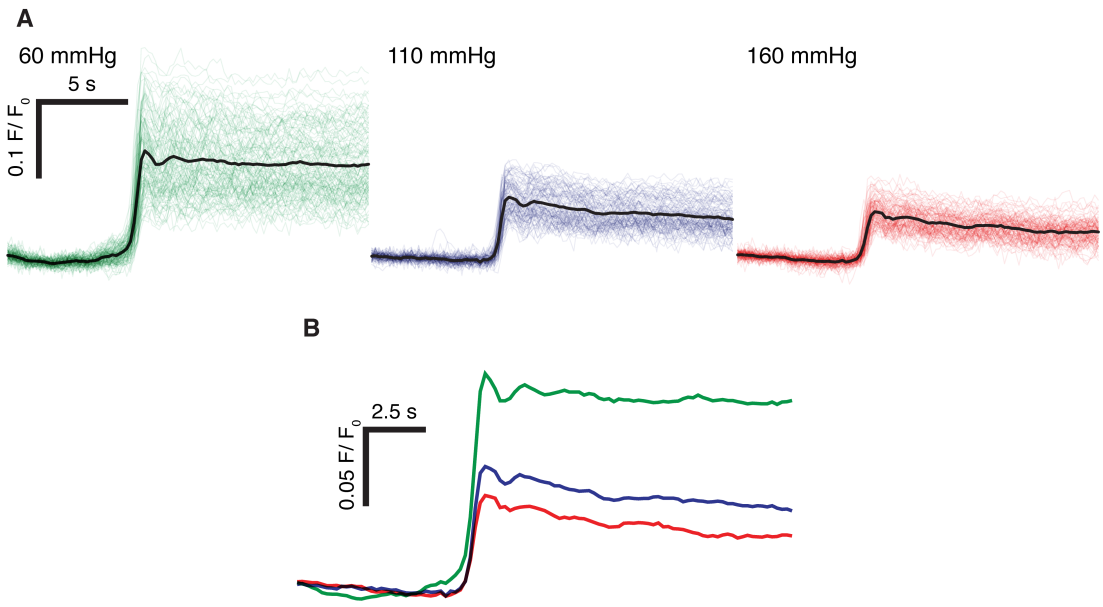

Figure 5.2 – Pressure-dependence of ACh-evoked Ca^{2+} signals. (A) Baseline corrected and time-aligned Ca^{2+} signals (with average overlaid in black) for a series of three sequential applications of ACh in the same artery at various pressures (60 mmHg, left; 110 mmHg, middle; 160 mmHg, right; 20 minutes equilibration) (B) Total endothelial Ca^{2+} activity (averages of (A)) for a single artery, upon repeated stimulation at increasing transluminal pressures. Ca^{2+} traces correspond to data shown in Supplementary Video 6.

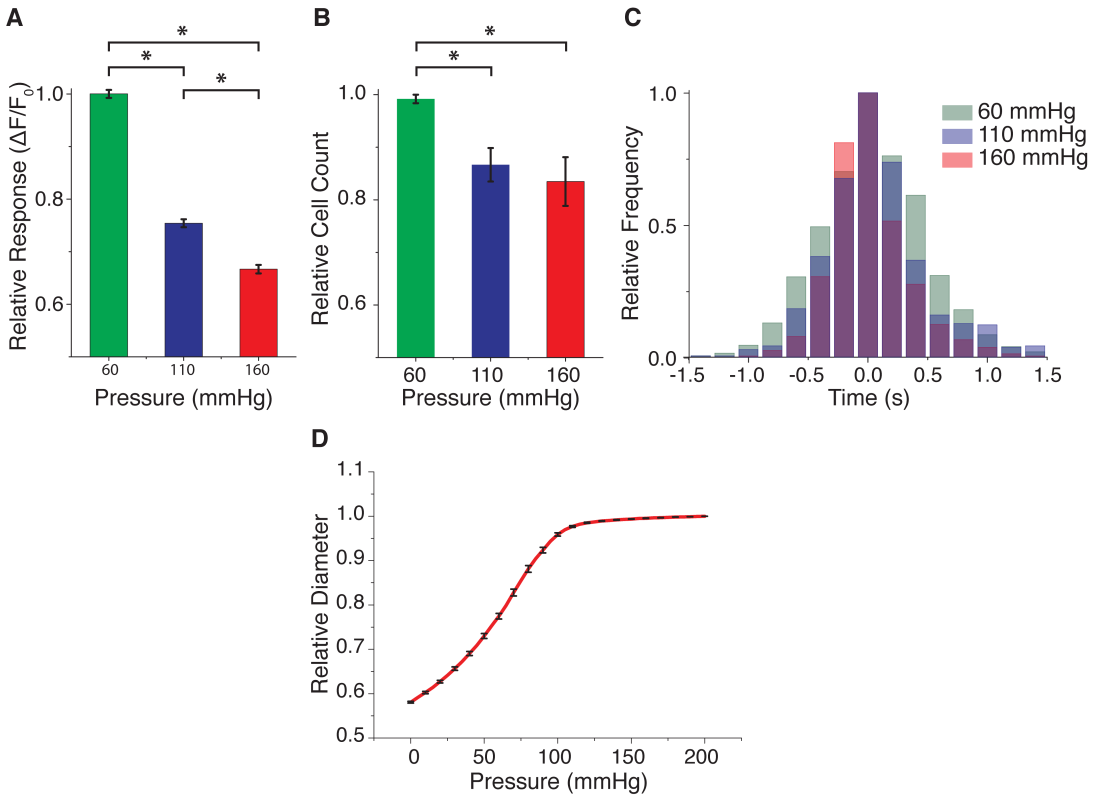

Figure 5.3 – Summarised pressure-dependence of ACh-evoked Ca^{2+} signals. (A) Summary data illustrating the pressure dependence of the number of cells activated by ACh (n = 8 ± SEM, normalised to 60 mmHg). (B) Summary data illustrating the pressure dependence of the number of cells responding to ACh (n = 8 ± SEM, normalised to 60 mmHg). (C) Normalised frequency distribution illustrating the temporal spread of time to activation for individual cells activated by ACh (100 μM) at 60 mmHg, 110 mmHg and 160 mmHg (n = 8 ± SEM). (D) Summary data illustrating a logistic change in vessel diameter as pressure is increased (from 0 - 200 mmHg; n = 3 ± SEM). Alternate error bars are omitted for clarity.

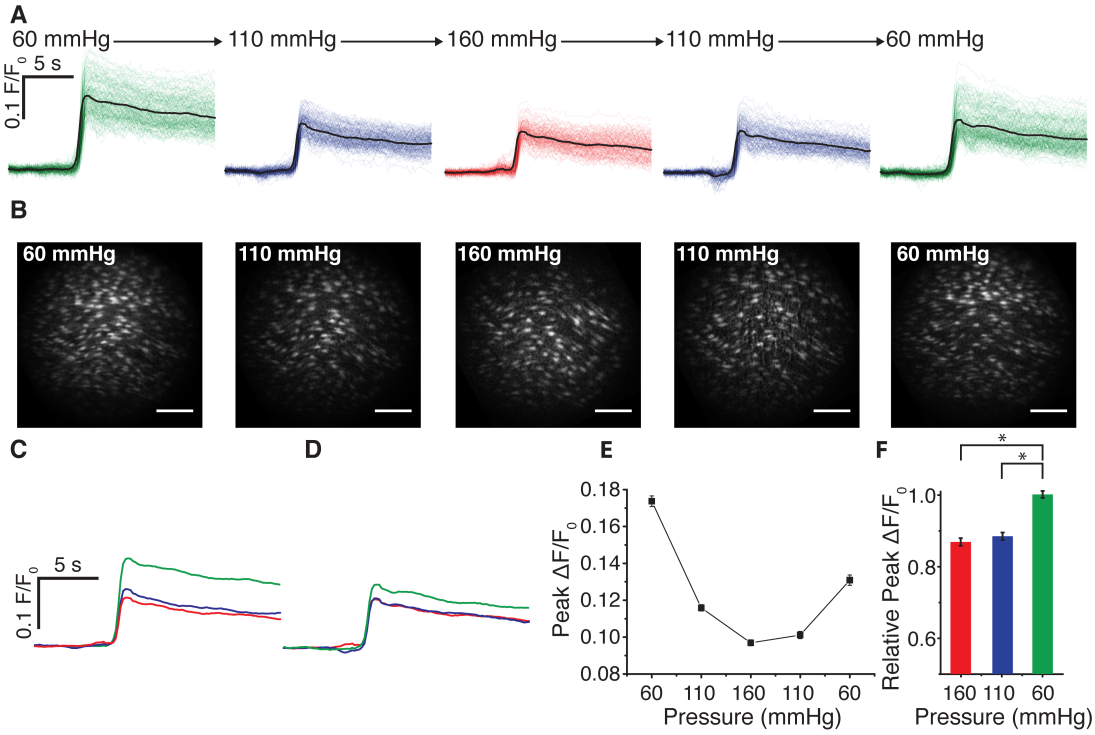

Figure 5.4 – Reversibility of endothelial Ca^{2+} signalling suppression by pressure. (A) Baseline corrected and aligned Ca^{2+} signals from ~200 cells (with average overlaid in black) obtained on ACh (100 µM bath concentration) over a series of increasing then decreasing pressure steps in the same artery. (B) Total endothelial Ca^{2+} activity (averages of (A)) for stepwise changes in intraluminal pressure. Scale bars 100 µm. (C) Averaged endothelial Ca^{2+} activity for stepwise increases (C) then decrease (D) in intraluminal pressure. (E) Peak changes in total Ca^{2+} activity ($\Delta F/F_0$) of data shown (A-D). (F) Summary data illustrating an increase in peak $\Delta F/F_0$, as pressure is reduced (n = 6 ± SEM, normalised to 60 mmHg).

5.3.2 Role of TRPV4 Channels in ACh-evoked Endothelial Ca^{2+} Signalling

It has been suggested that TRPV4 channels are involved in mediating pressure-dependent basal endothelial Ca^{2+} signalling (119,169) and in mediating ACh-evoked endothelial responses (119,261,284,285). To examine the role of TRPV4 channels in mediating the ACh-evoked $[Ca^{2+}]_i$ response in rat carotid arteries, the effect of the TRPV4 channel antagonist RN1734 was evaluated. Incubation with RN1734 (30 µM; 30 or 60 mins) significantly increased the number of cells activated by ACh (100 µM), and significantly increased the magnitude of the peak ACh-evoked Ca^{2+} response (n = 3 animals).

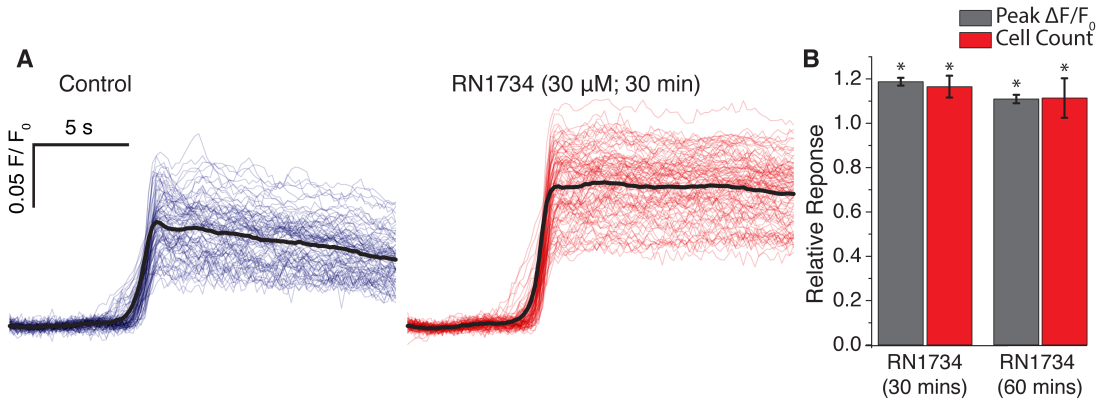

Figure 5.5 – Effect of TRPV4 antagonists on endothelial Ca^{2+} signalling. (A) Baseline-corrected and time-aligned ACh-evoked endothelial Ca^{2+} signals (F/F_0) obtained from the same artery before (left) and after (right) incubation with RN1734 (30 µM; 30 minutes equilibration). (B) Summary data showing the amplitude of the peak ACh-evoked (100 µM) response within each *activated* cell and the mean number of cells activated, in the presence of RN1734 for 30 and 60 minutes (30 µM; n = 3). Data are presented as mean ± SEM and normalised to control values (no treatment, 1; not shown), $p < 0.5$ was considered significant.

5.3.3 Effect of Transmural Pressure on Endothelial Cell Geometry

To further examine the effects of transmural pressure on endothelial cell geometry, the nuclear thickness of endothelial cells was measured from pressure fixed rat carotid arteries. The appearance of vessels fixed at 60 mmHg and 160 mmHg are shown in Figure 5.6A,B. The appearance of the endothelium depended on the pressure (i.e. diameter) at which vessels were fixed. Endothelial cells of vessels fixed at 60 mmHg exhibited round to oval nuclei (Figure 5.6A). By light microscopy, the

average height of endothelial cells at 60 mmHg was 2.73 µm (n = 13 cells from a single animal). In contrast, endothelial cells of vessels fixed at 160 mmHg displayed flattened, elongated cell nuclei (Figure 5.6B). Figure 5.6C illustrates that the average height of endothelial cells of vessels fixed at 160 mmHg was significantly less than those at 60 mmHg (1.55 µm; n = 21 cells from a single animal).

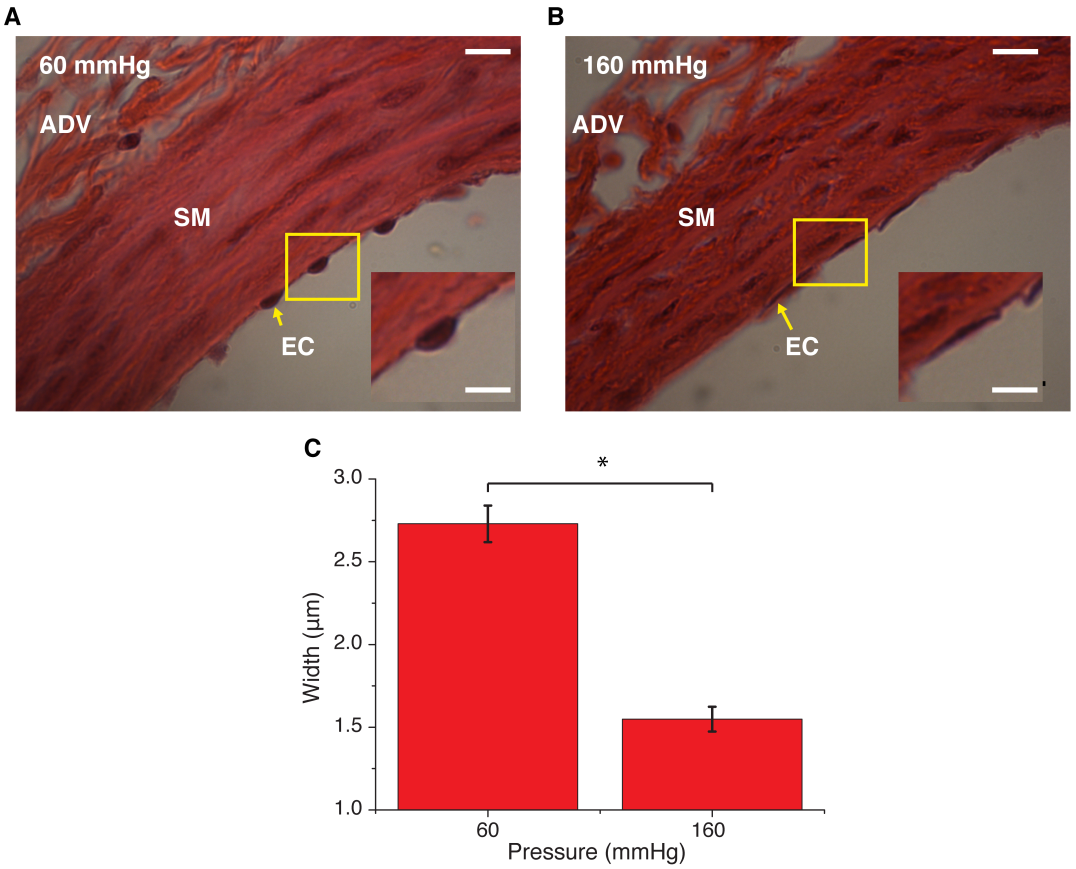

Figure 5.6 – Effect of transmural pressure on endothelial cell geometry. (A,B) Arteries fixed at 60mmHg (A) and 160 mmHg (B) and stained with Hematoxylin and eosin show the flattening of the endothelial cells (EC) at higher pressure. The insets (A,B) shows the corresponding yellow box expanded to illustrate the change in shape of single endothelial cells at each pressure. SM - smooth muscle and ADV - adventitia. Scale bars: main picture 10 µm, inset 5 µm. (C) Summary data showing the averaged endothelial cell thickness at 60 mmHg and 160 mmHg. Data are presented as mean ± SEM and normalised to control values (60 mmHg), $p \leq 0.5$ was considered significant.

5.3.4 Modelling Endoplasmic Reticulum Ca^{2+} Release from IP_3 Receptors

To explore how geometric changes of endothelial cells may modulate IP_3-mediated Ca^{2+} release at the scale of single or clustered IP_3R(s), which is below the limit of functional optical microscopy, we computationally simulated events at individual and clustered IP_3Rs (Appendix A3). The receptors were considered as existing on a planar interface between the ER and cytosol, with sufficient distance between the receptor(s) and the plasma membrane to negate edge effects.

As the diffusion of Ca^{2+} through IP_3Rs is passive, current through individual IP_3R channels is driven by diffusion and therefore depends on the concentration gradient between $[Ca^{2+}]_{ER}$, the ER Ca^{2+} concentration, and $[Ca^{2+}]_i$, the cytosolic Ca^{2+} concentration. A single open IP_3R acted as a point source of Ca^{2+}. Due to diffusion and cytosolic buffering, Ca^{2+} released from the single IP_3R equilibrated rapidly, resulting in a localised, quasi-static region of elevated $[Ca^{2+}]_i$ (microdomain; Figure 5.7A,B) around the channel. The Ca^{2+} concentration decreased sharply with distance from the IP_3R with a characteristic scale on the order of 100 nm (Figure 5.7B). Clustering of IP_3Rs resulted in a greater $[Ca^{2+}]_i$ in the vicinity of (open) IP_3R clusters than in the vicinity of isolated receptors (Figure 5.7A,B). Compared to a single IP_3R, the increased $[Ca^{2+}]_i$ reduced the local ion gradient between the store ($[Ca^{2+}]_{ER}$) and the cytosol at an IP_3R cluster, and concurrently reduced the entropic force driving Ca^{2+} release through the clustered channels (Figure 5.7D). In addition, the microdomain of each IP_3R merged into a larger, unified domain with a scale approaching the 500 nm thickness typical of endothelial cells.

In many cells (246,247,286), including endothelial cells (287) , IP_3Rs release Ca^{2+} into the cytosolic space between the ER and the cellular plasma membrane (PM). The proximity of the PM to IP_3Rs may create a restricted environment that limits the diffusion of Ca^{2+} away from IP_3Rs. Decreasing the IP_3R-PM spacing restricted Ca^{2+} diffusion such that $[Ca^{2+}]_i$ increased at the receptors (Figure 5.7A,C). Thus, a decreased IP_3R-PM spacing reduced the entropic force driving Ca^{2+} release (Figure 5.7D).

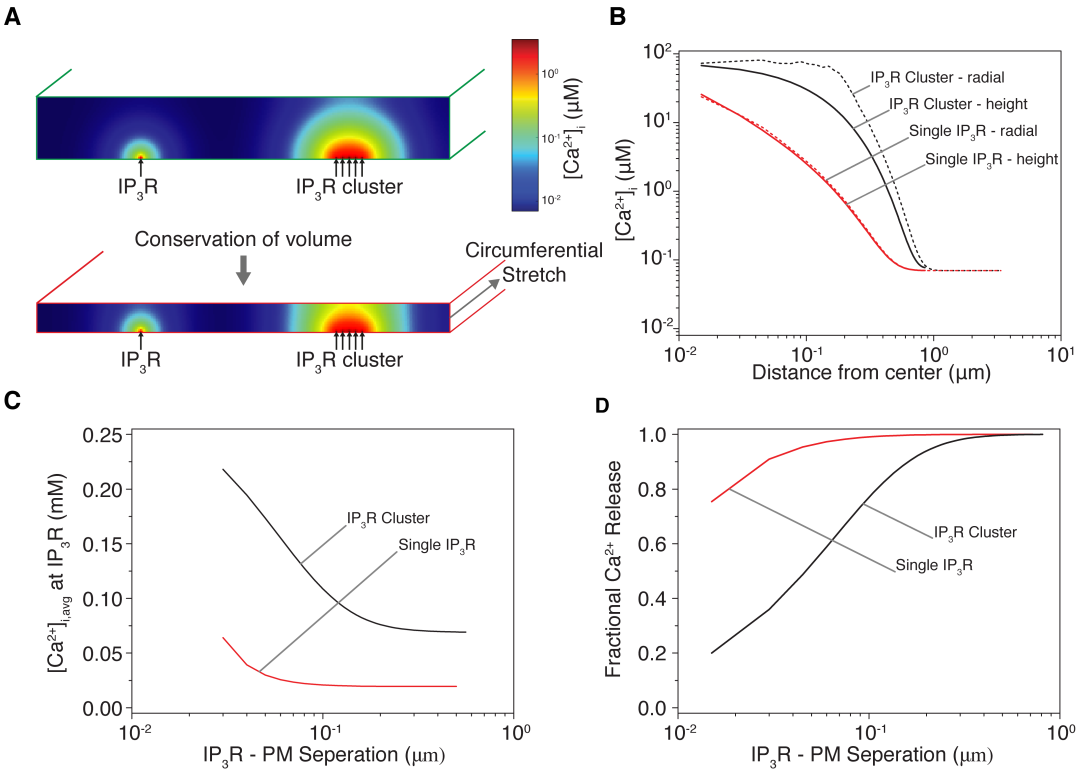

Figure 5.7 – Modelling endoplasmic reticulum Ca^{2+} release. (A) Cartoon illustrating the cytosolic Ca^{2+} distribution during Ca^{2+} release through a single IP_3R and a cluster of IP_3Rs as a cell (top, cell height: 0.57 μm) is stretched in the circumferential direction and thins to conserve volume (bottom, cell height: 0.27 μm). (B) Concentration profiles for $[Ca^{2+}]_c$ surrounding individual and clustered IP_3Rs shows that the microdomain of elevated $[Ca^{2+}]_c$ is significantly larger for clusters of receptors (C) The average $[Ca^{2+}]_c$ in the vicinity of IP_3Rs is sensitive to an increasing proximity between the ER and the plasma membrane (cell thinning), resulting in (D), a sensitivity of fractional Ca^{2+} release from internal stores that changes with receptor – plasma membrane distance (cell height) for single IP_3R and a cluster of IP_3Rs, with clusters having sensitivity over significantly larger cell heights, on the order of 500 nm.

5.4 Discussion

In this study, whether or not endothelial Ca^{2+} signalling is altered due to changes in transmural pressure was addressed. Whilst increased transmural pressure resulted in arterial distension, the focussing mechanism on our GRIN imaging system (Figure 2.4; Chapter 2), permitted tracking the endothelium and visualisation of Ca^{2+} signals in up to 200 cells at altered transmural pressures. The data shows that increased pressure suppresses, or conversely that decreased pressure enhances, agonist-evoked (ACh) endothelial Ca^{2+} signalling.

Many separate mechanisms present in endothelial cells have been proposed to act as sensors/transducers of mechanical forces (74,276,288). Rather than a single mechanism, multiple sensors and multiple transducers contribute to physiological mechanosensitive signalling (e.g. cytoskeletal elements, membrane receptors, glycocalyx, ion channels). Nevertheless, the majority of recent research into endothelial mechanotransduction has focussed on mechanosensitive ion channels, notably the Ca^{2+}-permeable TRPV4 channel (119,169,279,284,289). The functional importance of TRPV4 channels arises because they physiologically regulate endothelium-dependent vasodilatory responses. For example, studies have demonstrated that ACh-evoked vasodilator responses are markedly diminished in $TRPV4^{-/-}$ mice when compared to wild type mice (285,290), and that ACh-evoked Ca^{2+} signalling is impaired by TRPV4 channel blockade in wild type mice (261). Additionally, TRPV4-deficient mice exhibit impaired flow-mediated (mechanosensitive) endothelial responses in the carotid artery, when compared with their wild-type littermates (291), and shear-stress induced vasodilation in rat carotid arteries is inhibited by both the TRPV4 inhibitor, ruthenium red, and by buffering endothelial $[Ca^{2+}]_i$ (292). On the other hand, by studying isolated, intact arterioles under physiological transmural pressures using traditional microscopy, Dora *et al*. observed increased activation of spontaneous endothelial Ca^{2+} events at low transmural pressure due to TRPV4 channel activation (169).

In the present study, the hypothesis that increased ACh-evoked endothelial Ca^{2+} signalling, a precursor to agonist-evoked vasodilator responses, at low pressure is due to increased TRPV4 channel activation was investigated using the TRPV4

channel agonist, RN1734. RN1734 failed to decrease endothelial Ca^{2+} signal amplitude or the number of endothelial cells responding to ACh in rat carotid arteries pressurised to 60 mmHg. These data indicate that increases in agonist-evoked endothelial Ca^{2+} signalling by decreased pressure may not be mediated by the direct pressure-induced activation of TRPV4 channels. Indeed, normal ACh-induced dilation has been observed in the carotid artery of $TRPV4^{-/-}$ mice (293). Such contradictions, regarding TRPV4-mediated endothelial signalling, may be due to differences in the species of animal and the vascular bed studied, or to differences in the mechanisms of Ca^{2+} accumulation within the endothelium. For example, flow-mediated endothelial Ca^{2+} responses are primarily due to Ca^{2+} influx from the extracellular milieu, whilst agonist-evoked increases in $[Ca^{2+}]_i$ (as in the present study and (293)) are mainly the result of phospholipase C (PLC) activation and subsequent release of Ca^{2+} from the ER by IP_3Rs. Thus, mechanical stimuli may activate TRPV4 channels to different extents.

Several studies have demonstrated the release of Ca^{2+} from internal stores of endothelial cells upon stimulation with mechanical forces (e.g. cyclic strain (294)). Thus, it may be postulated that a pressure-induced decrease in endothelial Ca^{2+} signalling, as seen in the present study, may be explained by a decrease in the internal store Ca^{2+} content. However, many studies contradict this hypothesis. For example, whilst changes in pressure have been shown to elicit transient increases in endothelial $[Ca^{2+}]_i$, neither $PGF_{2\alpha}$ or α_2 adrenoceptor agonist-induced constriction of rat skeletal muscle arterioles (295) nor pressure-induced increases in arterial diameter in cerebral (296), uterine (297), or femoral (298) arteries have been shown to alter *sustained* levels of basal endothelial $[Ca^{2+}]_i$.

Morphological changes may modulate basal production and/or release of vasoactive factors, such as NO, from endothelial cells in intact arteries (114,299,300) and in cultured endothelial cell systems (e.g. due to changes in pressure; 222,227). Increases in the production of NO by eNOS is usually associated with an increase in endothelial $[Ca^{2+}]_i$ (35,92,135). Given the relationship between NO production and elevations in endothelial Ca^{2+}, it is puzzling that changes in endothelial cell morphology, due to concomitant changes in transmural pressure and arterial

diameter, do not modify basal endothelial $[Ca^{2+}]_i$ levels (135,295–297). Some explanation for the discrepancy was found when changes in local Ca^{2+}, rather than global Ca^{2+} changes, were studied. Local elementary endothelial Ca^{2+} events scale inversely with pressure in intact arteries (169). These exquisitely local events are not detected by global Ca^{2+} measures (119,167–170) and are now known to alter endothelium-dependent vasoactive pathways (119,169), such as NO production. Alternatively, it has been postulated that NO production/release may be modulated by Ca^{2+}-independent mechanisms (301–303). In contrast, it is generally accepted that the release of agonist-evoked (e.g. ACh) endothelial-dependent vasoactive factors is dependent on an increase in endothelial $[Ca^{2+}]_i$. Furthermore, in contrast to normotension, agonist-evoked endothelium-dependent vasoactive responses are attenuated in both animal models of hypertension (275,304–307) and in human hypertensive patients (308–310). Despite the significant literature on NO production by the endothelium, little is known about the pressure-dependent regulation of *agonist-evoked* endothelial Ca^{2+} signalling. Our study shows that increased pressure decreases ACh-evoked, IP_3-dependent Ca^{2+} signalling in the endothelium.

Previous electron microscopy studies have demonstrated substantial alterations in the 3-dimensional shape of individual endothelial cells of intact blood vessels held at different transluminal pressures (i.e. different arterial diameters) (311–314). These electron microscopy studies have revealed that the endothelial layer undergoes folding and the nuclear region becomes compressed. Our data show no folding of the endothelial layer in rat carotid arteries at the lowest pressure (60 mmHg) used in our study. However, increasing the pressure to 160 mmHg did result in compression of the nucleus, as endothelial cells were stretched to accommodate the increase in lumenal circumference. Presumably, intimal folds were absent from the endothelium of the rat carotid artery because the high elastin content bears the mechanical load in the circumferential direction. Intimal folding in micro-vessels has been proposed as a mechanism by which the intimal layer can accommodate increases in the lumen circumference (313). However, in larger arteries it has been proposed that intimal folding may be a fixation artefact (315) resulting from a decrease in diameter upon removal of transmural pressure after pressure fixation (316).

Elevated $[Ca^{2+}]_i$, in the immediate vicinity of a single open IP_3R, may be high enough to activate near-by IP_3Rs and result in regenerative Ca^{2+} wave propagation (317,318). In this process, IP_3R activity is exquisitely sensitive to clustering of IP_3Rs on the ER and the cytosolic space between the ER and membrane structures such as mitochondria and the plasma membrane (319–321). These features (clustering, cytosolic space) create a local diffusive environment (microdomain) in which Ca^{2+} and Ca^{2+} buffers regulate the activity of IP_3Rs and the release of Ca^{2+} from the ER due to the $[Ca^{2+}]_i$. We modelled the activity of single and clustered IP_3Rs and found that the geometry of the microdomain changes with the geometry of the cell (ER-PM distance). Circumferential stretch elongates endothelial cells around the artery, decreasing the cell height to maintain volume (322). A decreased ER-PM distance (as would be imposed by cellular compression) restricts Ca^{2+} diffusion away from the $IP_3R(s)$ and, in turn, increases the $[Ca^{2+}]_i$ at the receptor(s), and reduces the entropic force driving Ca^{2+} release from the ER (323). Thus, a mechanical force (circumferential stretch) can reduce Ca^{2+} release via IP_3R, in the absence of any force- or stretch-sensitive molecular machinery. The computational study by Hong *et al.* (324) provides evidence to support our simulation results. In this paper, store-operated Ca^{2+} entry (SOCE) was modelled in a cell of circular geometry, with the ER located in the centre of the cell, with good agreement between simulated and experimental results. They found that as the ER-PM distance was decreased, the $[Ca^{2+}]_i$ in the vicinity of SOCE channels increased dramatically due to a reduced space available for diffusion. However, they did not extend their simulation to study subsequent effects on Ca^{2+} release from the ER.

Our study is the first to report the effects of the intraluminal pressure on agonist-evoked (ACh) endothelial $[Ca^{2+}]_i$ signalling in intact (rat carotid) arteries. Directly visualizing the endothelium in these arteries, using our GRIN imaging system (Chapter 2), enabled the observation of reduced cellular Ca^{2+} signals when arteries are circumferentially stretched by increased transmural pressure. The reduced Ca^{2+} release explains the suppression of physiological responses at high transmural pressure (75,114,283). While mechanical activation of various ion channels may account for physiological responses (74,276) we propose the pressure-sensitive

response of individual cells may also arise from changes in the local diffusive environment surrounding IP_3R clusters, induced by geometric changes in cell shape. Many studies argue that hemodynamic forces are likely to affect first the function and then the structure of blood vessels. However, most studies overlook the fact that haemodynamic forces unavoidably alter the 3-dimensional structure of the cell. We postulate that the stretch-dependence of the IP_3R-mediated Ca^{2+} response to agonists is a direct consequence of mechanical forces rather than result of secondary mechanically activated molecular force transducers. Moreover, this hypothesis provides an additional explanation of the heterogeneity of Ca^{2+} responses in populations of endothelial cells (Chapter 4): not only can the expression of Ca^{2+} machinery differ among cells, but in cells expressing the same amount of channels the response would be a function of the individual cell geometry. Furthermore, our results suggest how hypertensive conditions limit the ability of cells to engage in Ca^{2+} signalling, offering insight into the associated degeneration of endothelial response (275,304–307).

Chapter 6. ACh-Evoked Ca^{2+} Signalling in the Endothelium of Intact, Pressurised Arteries from Aged Animals

6.1 Introduction

Aging is the summation of many, mostly invisible, but deleterious changes associated with altered structure and function of the cardiovascular system. The clinical effects of aging are powerfully demonstrated by the observations that the incidence and prevalence of clinical cardiovascular disease increase with advancing age (325), and that 30% of deaths worldwide are caused by cardiovascular disease (326), making cardiovascular disease the most common cause of death globally. Taken together, these facts raise the question of whether aging acts to intensify the effects of cardiovascular disease. However, before this question can be answered the effects of aging, in itself, must be understood.

There is general agreement that aging is associated with dramatic structural changes in the arterial wall (327–329). Of these, the most commonly reported changes are increases in arterial stiffness (reduction in elastic properties), luminal diameter, and wall thickness. The importance of such structural changes on arterial function has been highlighted by the fact that pulse wave velocity, the rate at which pressure waves induced by cardiac contraction travel down the arterial tree, which is correlated with arterial stiffness (330), is used as a predictor of cardiovascular mortality (331–333). However, whilst numerous clinical end-points, such as pulse wave velocity, have been established to assess cardiovascular risk and guide treatment intervention, the underlying mechanisms responsible for functional changes in the arterial wall remain unclear.

Changes in arterial structure increase tissue stresses and degrade vascular function. Among the cellular components of the vascular wall, endothelial cells may be the most predisposed to age-related stresses because, as a single layer that lines the inner surface of all blood vessels, they are impacted upon by numerous stressors such as blood-borne signalling molecules, electrical signals and mechanical forces. Indeed, because the endothelium acts as a signal-processing centre that detects, interprets and responds to multiple simultaneous messages to control vascular function, altered endothelial function is intimately linked to vascular disease (39,48,275,308,334,335). With advancing age, the ability of the endothelium to control vascular tone is attenuated in both human and animals models (336–339). Such impairment of

endothelial function is termed “endothelial dysfunction”, and is characterised by a decrease in the release of NO from the endothelium and thus a decrease in the relaxation of smooth muscle cells by endothelium-dependent vasoactive agonists, such as ACh (340–343). As an inhibitor of leukocyte adhesion (42), thrombosis (43) and smooth muscle cell proliferation (33,34,151), NO opposes structural alterations to blood vessels, in addition to regulating vascular tone (27,29,30,33). A decrease in the bioavailability of NO in ageing significantly contributes to the development of cardiovascular disease (335). Thus, endothelial dysfunction is a multifaceted disorder that contributes to and reinforces the changes that occur in vascular disease. Unfortunately, a detailed understanding of the physiological mechanisms that result in endothelial dysfunction has been hampered by the inaccessibility of the endothelium to conventional microscopic imaging techniques.

A rise in endothelial $[Ca^{2+}]_i$ is generally considered essential for the agonist-induced production of NO (35,92,135). Thus, it seems that an age-dependent reduction in the production and/or availability of NO may be causally related to altered endothelial Ca^{2+} signalling. However, to date only a limited number of studies have directly investigated the effects of aging on Ca^{2+} homeostasis in endothelial cells in intact artery preparations (183,344)**.** Prendergast *et al* (183,344) demonstrated that agonist-evoked (carbachol) endothelial Ca^{2+} signalling is unaltered with age in wild-type mice (344). However, in both of these studies arteries were surgically opened to expose the endothelium to microscopic investigation. This may result in alterations to the arterial response. Indeed, agonist-evoked responses of surgically opened arteries are diminished even when compared to ring preparations (345,346). Furthermore, responses in ring preparations are themselves diminished compared to those of intact arteries held under isobaric conditions in the pressure myograph (184,185,187,347–349). Whilst the effect of such surgical manipulation on endothelial Ca^{2+} signalling has not been studied directly, we have directly visualised pressure-mediated suppression of Ca^{2+} signals (Figure 5.3; Chapter 5), an effect attributed to arterial distension-induced changes in cellular geometry, and that can only be observed in pressurised arteries (Chapter 5).

Endothelial cells become thinner, and the lumenal diameter of arteries increase with advancing age (4,329,350). Given these observations, and results showing that Ca^{2+} signalling may be altered by the geometry of individual endothelial cells (Chapter 5), agonist-evoked (ACh) endothelial Ca^{2+} signalling may be differentially regulated in aged (versus control) vessels, subject to physiological mechanical loading. Additionally, because of geometric modulation of endothelial Ca^{2+} signals, advancing age may result in attenuation of the pressure-dependent suppression of endothelial Ca^{2+} signalling (Chapter 5), due to increased endothelial cell width (decreased cell height) and/or vessel stiffness in aged vessels.

To investigate this hypothesis, endothelial $[Ca^{2+}]_i$ signalling responses to ACh were investigated in intact and pressurised carotid arteries obtained from aged rats (18 months), visualised by GRIN fluorescence microscopy (Figure 2.4; Chapter 2), and compared to results from young rats (3 months). Concentration- and pressure-dependent responses data, and the frequency of ACh-induced oscillation (as a measure of the spatiotemporal characteristics of Ca^{2+} events (243)) were examined.

6.2 Methods

6.2.1 Animals & Tissue

Tissue was processed as described in Chapter 2. Studies were performed on young (approximately 10 week old) and old (approximately 72 week old), male Sprague-Dawley rats (250-350 *g*, young; 500 – 600 *g*, old), killed by overdose of pentobarbital sodium (Schedule 1 procedure; Animal (Scientific Procedures) Act 1986, UK).

6.2.2 Large-scale Endothelial Ca^{2+} Imaging

Endothelial Ca^{2+} signalling was imaged as described in Chapter 2, Chapter 4 and Chapter 5. Briefly, endothelial viability and stability was confirmed (at 60 mmHg) by application of ACh (100 μM) at the start of each experiment. In some experiments, arteries were activated with various concentrations of ACh, as indicated in the text. In other experiments arteries were stimulated at various transmural pressures. In these experiments, arteries were allowed to equilibrate at the experimental pressure for a period not less than 20 minutes before stimulation. Following each acquisition period, the bath solution was immediately exchanged and the arteries were left for at least 20 minutes to re-equilibrate. The effects of different pressures on ACh-evoked Ca^{2+} activity were studied in paired experiments and expressed relative to control (response at 60 mmHg). Data from young animals were pooled from data presented in Chapter 4 and Chapter 5.

6.2.3 Semi-automated Analysis of Endothelial Ca^{2+} Signals

Endothelial (cellular) Ca^{2+} signalling was analysed as described in Chapter 3.

6.2.4 Solutions and Drugs

Solutions and drugs are as described in Chapter 2 and Chapter 4.

6.2.5 Statistics

Summarised data are expressed as mean ± SEM, where *n* is number of animals. Concentration-dependent response data (averaged $\Delta F/F_0$, and the number of cells responding to ACh) were normalised to the maximum response. Curves were fitted to normalised concentration response data using Graphpad Prism 5. The maxima,

minima and Hill slope of the curves were constrained to unity, zero, and unity, respectively. Calculated curve-fit parameters (half maximal effective concentration; EC_{50}) are presented with 95% confidence intervals, and were compared statistically using the extra sum-of-squares F-test. Pressure data (peak $\Delta F/F_0$) were compared statistically using two-way ANOVA (with Tukey's post-hoc test as appropriate). Curves were fitted to normalised temporal distributions using Origin 9.1. The centre of curve and the peak were constrained to zero and unity, respectively. Calculated curve-fit parameters (full-width-half-maximum; FWHM) were compared statistically using the extra sum-of-squares F-test. To objectively analyse Ca^{2+} oscillations, peaks were identified mathematically from smoothed (4 point window fast Fourier filter) derivate Ca^{2+} traces ($d(F/F_0)/dt$), using the Peak Analyzer tool of Origin 9.1. Peaks were identified by local maxima. To exclude noise, peaks with a value less than 15% of the maximal amplitude were excluded. Oscillatory cells were defined as those exhibiting two or more peaks (initial ACh-induced peak plus at least one additional oscillation peak). The number of peaks occurring within a 20 second post ACh-activation period was calculated for each cell to determine cellular oscillation frequencies, and a one-way ANOVA was used for statistical comparison. All statistical analyses (except curve comparison; Origin 9.1) and two-way ANOVA (Minitab 17) were performed in SPSS, a p-value less that 0.05 was considered significant.

6.3 Results

6.3.1 Effect of Ageing on the Concentration-dependence of ACh-evoked Endothelial Ca^{2+} Signalling

The number of cells responding to ACh, and the amplitude of the ACh-evoked Ca^{2+} response, within individual endothelial cells of young animals, increases in a concentration-dependent manner (Chapter 4). To examine the effects of ageing on the ACh concentration dependence, the endothelial Ca^{2+} response to pre-defined concentrations of ACh was examined in arteries from old animals. Similar to the endothelial Ca^{2+} response in young animals (Figure 4.13A), there was a graded increase in (1) the number of cells activated as the concentration of ACh increased (Figure 6.1A), (2) the amplitude of the Ca^{2+} response within each cell, and (3) the average Ca^{2+} response of all cells activated by ACh (Figure 6.1). Notably, endothelial cells in arteries from old rats were significantly more sensitive to ACh stimulation than those from young arteries (EC_{50} values: 13.13 μM, 95% confidence interval [8.32, 20.73], young; 2.51 μM, 95% confidence interval [1.85, 3.42] old), yet the average peak change in baseline-corrected F/F_0 was unchanged (EC_{50} values: 2.49 μM, 95% confidence interval [1.52, 4.10], young; 2.01 μM, 95% confidence interval [0.89, 2.20], old).

6.3.2 Effect of Ageing on the Transmural Pressure-dependence of ACh-evoked Endothelial Ca^{2+} Signalling

ACh-evoked endothelial Ca^{2+} signalling is suppressed by increases in transmural pressure (Chapter 5). To examine the effects of ageing on the pressure-induced suppression, the endothelial Ca^{2+} response to ACh (100 μM) was examined in individual arteries, from old animals, subject to step-wise increases. Similar to the endothelial Ca^{2+} response in young animals (Figure 5.3 & Figure 6.2A), the endothelial Ca^{2+} response in arteries from old animals was significantly reduced as transmural pressure was increased (Figure 6.2B). However, the pressure-induced suppression (inhibition) of ACh-evoked endothelial Ca^{2+} signals was significantly reduced in arteries from old rats (greater than 300 cells from 3 rats; Figure 6.2C).

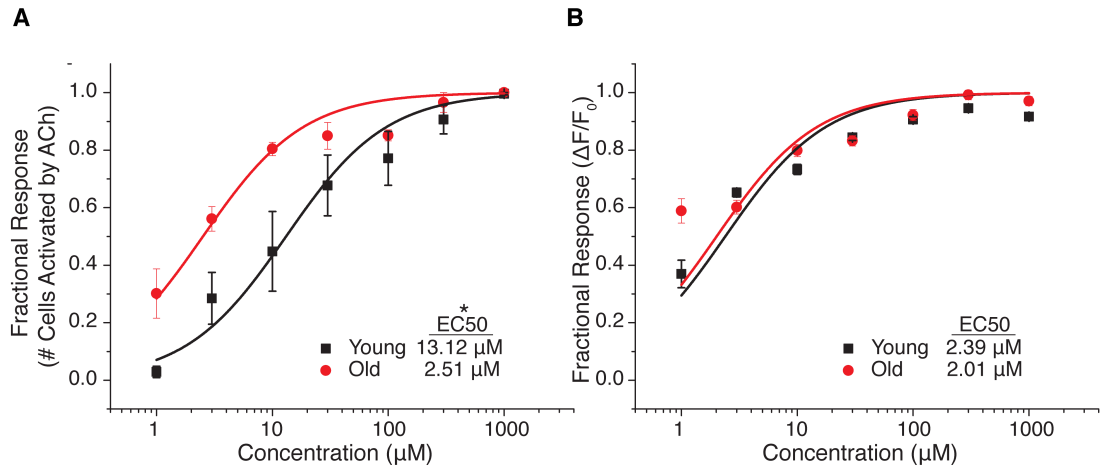

Figure 6.1 – Effect of age on the ACh-evoked endothelial Ca^{2+} response. (A) Summary data illustrating the concentration dependence of the number of cells activated by ACh in young (black square; n ≥ 3 arteries ± SEM) and old (red circles; n = 3 arteries, ± SEM) animals. (B) Summary data illustrating the concentration dependence of the peak $\Delta F/F_0$ in cells activated by ACh in young (black square; n ≥ 3 arteries ± SEM) and old (red circles; n = 3 arteries ± SEM) animals. All data normalised to peak response, $p < 0.05$ was considered significant.

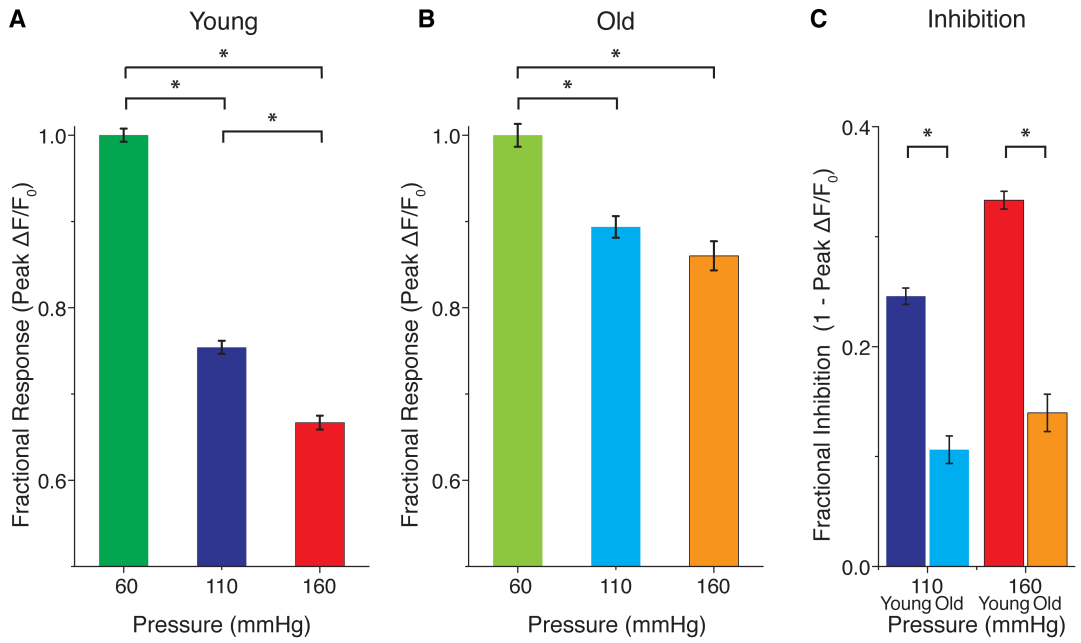

Figure 6.2 – Effect of age on suppression of endothelial Ca^{2+} signals by pressure. (A) Summary data illustrating the pressure dependence of the Ca^{2+} response (peak $\Delta F/F_0$) of cells activated by ACh in young rats (from Figure 5.3; n = 8 ± SEM, normalised to 60 mmHg). (B) (B) Summary data illustrating the pressure dependence of the Ca^{2+} response (peak $\Delta F/F_0$) number of cells activated by ACh in old rats (n = 3 ± SEM, normalised to 60 mmHg). (C) Summary data illustrating differential increase in the relative, pressure-induced inhibition of the Ca^{2+} response (1 – peak $\Delta F/F_0$) in young and old rats. $P < 0.05$ was considered significant.

Further analysis of the Ca^{2+} responses of arteries from aged rats (totalling more than 300 cells visualised at each pressure) revealed several changes in the response to increased pressure. First, that the number of cells activated by ACh (100 μM) remained unaltered as pressure was increased (Figure 6.3B), in contrast to the decrease seen in young rats (Figure 5.3B & Figure 6.3A). Secondly, similar to the response in young rats (Figure 5.3C & Figure 6.3C), the temporal spread of the Ca^{2+} responses decreased with increasing pressure (Figure 6.3D), but at each pressure the temporal spread was significantly larger than that in young animals (FWHM values: 0.89 ± 0.03 s, young 60 mmHg; 2.45 ± 0.16 s, old 60 mmHg; 0.68 ± 0.02 s, young 110 mmHg; 1.78 ± 0.09 s, old 110 mmHg; 0.59 ± 0.02 s, young 160 mmHg; 1.19 ± 0.02 s, old 160 mmHg).

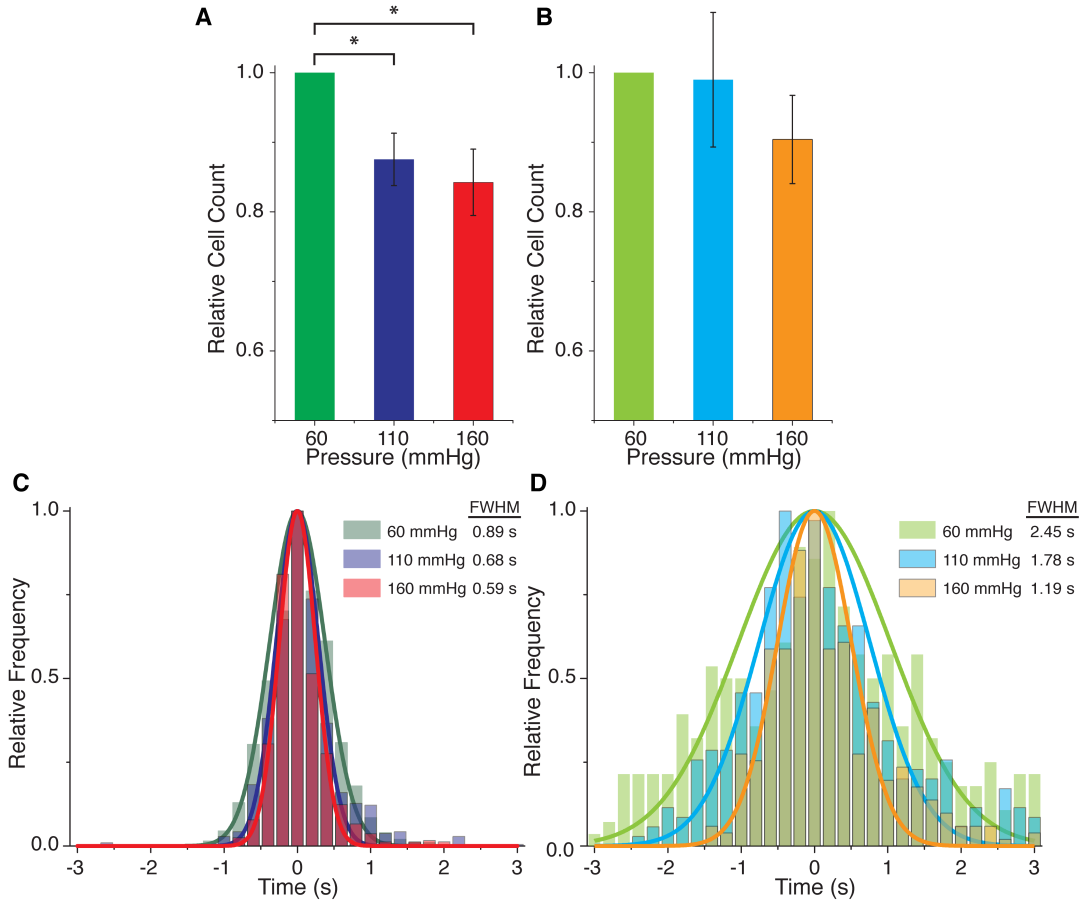

Figure 6.3 – Effect of age on the temporal spread of endothelial Ca^{2+} signals. (A) Summary data illustrating the pressure dependence of the number of cells responding to ACh (n = 8 ± SEM, normalised to 60 mmHg) in young rats. (B) Summary data illustrating the pressure dependence of the number of cells responding to ACh (n = 3± SEM, normalised to 60 mmHg) in old rats. (C) Normalised frequency distribution illustrating the temporal spread of time to activation for individual cells activated by ACh (100 µM) at 60 mmHg, 110 mmHg and 160 mmHg in young rats (n = 8). (D) Normalised frequency distribution illustrating the temporal spread of time to activation for individual cells activated by ACh (100 µM) at 60 mmHg, 110 mmHg and 160 mmHg in old rats (n = 3)

6.3.3 Effect of Ageing on the Oscillatory Nature of ACh-evoked Endothelial Ca^{2+} Signals

As described previously (Chapter 4), the ACh-evoked endothelial Ca^{2+} response was composed of an initial rise in $[Ca^{2+}]_i$ followed by oscillations that were superimposed on a sustained elevated plateau. Whilst the percentage of oscillating cells did not differ between young and old rats (Figure 6.4A; 99.5 ± 0.5%, n = 374 cells from 3 young animals; 93.7 ± 6.0, n = 362 cells from 3 old animals), the frequency of oscillations was significantly reduced in aged rats (Figure 6.4B; 0.27 ± 0.005 Hz, n = 372 cells from 3 young animals; 0.22 ± 0.003 Hz, n = 340 cells from 3 old animals).

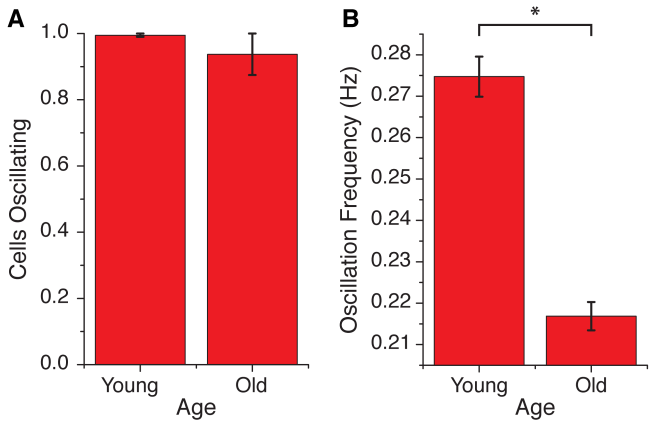

Figure 6.4 – Effect of age on ACh-evoked endothelial Ca^{2+} signal oscillations. (A) Summary data illustrating the number of cells exhibiting oscillatory ACh-evoked (100 μM) endothelial Ca^{2+} signals in young (n = 3 ± SEM) and old (n = 3 ± SEM) rats. (B) Summary data illustrating the frequency of ACh-evoked (100 μM) endothelial Ca^{2+} signals in young (n = 3 ± SEM) and old (n = 3 ± SEM) rats.

6.4 Discussion

Endothelial dysfunction has been demonstrated in aged animals (304,305,340) and in aged human studies *(309)*. However, the mechanisms responsible for an age-induced reduction in endothelium-dependent agonist-evoked vasodilation are poorly understood. Increased production of endothelium-derived contracting factors such as endothelin (351) and cyclooxygenase-dependent (e.g. prostaglandin H_2 and thromboxane A_2) (352), and decreased bioavailability of NO (340–343) are all thought to mediate an age-related decrease in endothelial vasodilation. Ca^{2+} signalling is a key regulator of endothelial function, and alterations in the control of Ca^{2+} critically contribute to the development of cardiovascular disease (353). However, the role of endothelial Ca^{2+} signalling in ageing has received little attention. Agonist-evoked (ACh) endothelium-dependent Ca^{2+} signals appear to originate in endothelial cells in spatially restricted regions (activator ensembles) and appear to propagate from these to neighbouring cells, dynamically recruiting and inducing a robust Ca^{2+} response (Chapter 4). The recruitment of cells and the magnitude of the Ca^{2+} response of individual responding cells increase in a concentration-dependent manner (Chapter 4). Furthermore, increased pressure suppresses agonist-evoked (ACh) endothelial Ca^{2+} signalling (Chapter 5). These Ca^{2+} signals are relayed to smooth muscle cells via the diffusion of NO, since endothelial Ca^{2+} signalling is a precursor to NO release. Because NO-mediated, endothelium-dependent vasodilation is impaired in aged animals and humans (336–339), we hypothesised that altered Ca^{2+} handling/regulation may occur in the aged endothelium. To address this question, we studied Ca^{2+} signalling in the endothelium in intact vessels (carotid arteries) of aged rats (18 month) subject to physiological pressures and mechanical loading.

In the present study, the sensitivity of endothelial cells to ACh was increased in aged rats (18 months) versus control rats (3 months), whilst the maximal Ca^{2+} response to ACh was unaltered with age (normalised to maximum response; Figure 6.1). Our use of an uncalibrated, single-wavelength chemical Ca^{2+} indicator prohibited comparison of absolute changes in $[Ca^{2+}]_i$ levels. Thus, whilst the magnitude of the Ca^{2+} response may differ among animals of different age relative to the maximum induced level,

we were unable to assess whether aging resulted in augmented basal or peak endothelial $[Ca^{2+}]_i$.

Although the mechanisms have not been explored, the increased sensitivity to ACh, in the absence of an increase in peak Ca^{2+} response, could be explained by a change in IP_3R expression. In mammalian cells, the IP_3R exists in three different isoforms, in order of decreasing sensitivity to IP_3: IP_3R-2, IP_3R-1, and IP_3R-3 (354,355). All three IP_3R isoforms exist in the intact rat vascular endothelium (356) and, in both cultured and freshly isolated endothelial cells, the expression pattern of the IP_3R isoforms is: IP_3R-3 > IP_3R-2 > IP_3R-1. Whilst IP_3R-1, IP_3R-2, and IP_3R-3 all appear to be localised to the nucleus of endothelial cells in intact vessels (356), IP_3R1 is also expressed in endothelial MEGJs (357). In murine cerebral arteries, an increased proportion of IP_3R-3 subtype expression, resulted in a decrease in IP_3 affinity without a change in the magnitude of agonist-evoked Ca^{2+} signalling (358,359). Thus, a proportional change in IP_3R expression could account for the increase in endothelial cell affinity to ACh seen in the present study and, in the case of IP_3R-2 upregulation within MEGJs, reductions in the myogenic response seen in ageing (360) due to increased spread of endothelium-dependent hyperpolarisation of smooth muscle cells (259). Further immunohistochemical analysis will be required to test this hypothesis.

A change in the expression and/or affinity of endothelial muscarinic receptors (i.e. ACh receptors) may also explain impairment of endothelial vasodilatory function in aging. However, no direct demonstration of altered expression of muscarinic receptors, or receptor defects, have been demonstrated in the endothelium (361). This hypothesis also contrasts with the results of the present study: namely that ageing increases endothelial cell sensitivity to ACh, which would require upregulation of muscarinic receptors which, in turn, would presumably increase relative peak Ca^{2+} signals. Furthermore, impaired endothelium-dependent vasodilation is found with non-muscarinic receptor agonists such as ATP, and ACh-induced hyperpolarisation of endothelial cells in intact murine endothelial tubes is maintained with age (362).

Altered Ca^{2+} signalling has been reported in both endothelial cells (344) and smooth muscle cells (336,363) in ageing. Such Ca^{2+} dysregulation may be the result of

altered Ca^{2+} handling by the ER. ER Ca^{2+} dysregulation may be the result of altered ER Ca^{2+} content, decreased Ca^{2+} release through IP_3Rs or increased cytosolic $[Ca^{2+}]_i$. For example, elevations in $[Ca^{2+}]_i$ in rat vascular smooth muscle cells (336,364) have been attributed to a decline in SERCA function (364,365). A common agreement is that most cells experience a decline in ER Ca^{2+} content (353,366). However, Ca^{2+} dysregulation occurs differently across vascular beds and tissues. For example, in contrast to observations in rat, basal $[Ca^{2+}]_i$ in freshly isolated murine mesenteric smooth muscle cells was not different, whilst SR storage was increased and SERCA function remained unaltered with age (363). The authors of these observations (363) suggest that abnormal vasoregulation present in these vessels may be the result of increased store-operated Ca^{2+} entry (SOCE). Further studies are required to ascertain if alterations in ER Ca^{2+} handling occurs in the endothelium.

In addition to age-related changes in the concentration response to ACh, inhibition of ACh-evoked endothelial Ca^{2+} signalling by increased pressure (Chapter 5) is significantly attenuated in arteries from aged rats (Figure 6.2). The pressure-mediated modulation of endothelial Ca^{2+} signals may be the result of geometric modulation of diffusive Ca^{2+} microdomains to limit the release of Ca^{2+} from the ER as endothelial cells thin, and the distance between the ER and the plasma membrane decreases (Chapter 5). Alterations in geometric modulation of endothelial Ca^{2+} signalling may be the direct result of changes in the mechanical properties of blood vessels that occur with age. Two mechanical properties are relevant: 1) thinning of the endothelial layer; and 2) an increase in arterial stiffness. Measurement from vessels fixed with (4,329,350) and without (367) pressure show that aging leads to thinning of the endothelium. Thinning is most often attributed to spreading of endothelial cells, to cover the increased lumenal surface as blood vessels grow (368). We suggest that such endothelial thinning may contribute to the decreased pressure-induced inhibition of ACh-evoked endothelial Ca^{2+} signalling seen in the present study. Thinning would result in reduction in the ER-PM distance in old versus young endothelial cells, thus an increased $[Ca^{2+}]_i$ in the vicinity of IP_3Rs, and a decrease in the relative inhibition of diffusive ER Ca^{2+} release. In support, there is an increased occurrence of apoptosis in the aged endothelium (334) and a decrease in endothelial

cell proliferation (334), providing the necessary conditions for a decrease in endothelial thickness. Additionally, age-related cardiovascular diseases, such as atherosclerosis, are also associated with cellular senescence *in vivo* (369), as well as the presence of greatly enlarged endothelial cells (370). Thus changes in endothelial cell geometry could partially explain decreased Ca^{2+} signalling in the atherosclerotic plaque-prone aortic arch, compared to the less plaque-prone thoracic aorta (344).

Increased arterial stiffness may also account for the reduction in pressure-induced inhibition of ACh-evoked endothelial Ca^{2+} signalling in ageing. Among others, the rat carotid artery experiences a reduction in percentage elastin content, and an increase in collagen content leading to arterial stiffening, with age (371). The conceptual model of arterial elasticity proposed by Roach and Burton describes the roles of these proteins in determining passive arterial mechanical properties (372). In this model, vascular wall stress at low pressure is borne by elastin. As pressure is increased, and arteries are circumferentially stretched, an increasing amount of stress is borne by collagen fibers as they gradually unfold. Thus, vessels become progressively stiffer with increasing pressure, a phenomenon that explains the nonlinear elasticity (logistic pressure-diameter curve, Figure 5.3D) of rat carotid arteries. In ageing, the increase in collagen-elastin ratio results in early recruitment of collagen fibrils during pressure increases, explaining the decrease in arterial distensibility in ageing (373). Indeed, there was a significant decrease in the number of endothelial cells responding to ACh as pressure was increased, whilst no significant difference was observed in the arteries of old rats (Figure 6.3A,B). This observation suggests that carotid arteries of old animals were stiffer than those of young rats. Given this observation, it is likely that endothelial cells of aged arteries would experience a lower percentage reduction in cell height upon increases in pressure, thus explaining the observed decrease in inhibition of ACh-evoked endothelial Ca^{2+} signalling as pressure was increased.

Whilst it is likely that either or both aforementioned hypotheses (endothelial cell thinning or increased vessel stiffness) may account for differences in Ca^{2+} signalling between young and old rats, we were unable to study changes in endothelial cell height due to the effects of circumferential stretch or pressure induced compression

independently. Further studies, isolating the effects of each possible mechanism, are required to elucidate the possible contributions of each.

Because the temporal properties of Ca^{2+} signals can affect cellular function, we addressed whether or not endothelial Ca^{2+} signalling dynamics are altered in ageing. To objectively analyse endothelial Ca^{2+} oscillations, an automated peak detection algorithm was used to identify repeating Ca^{2+} increases (oscillations) from derivate Ca^{2+} (F/F_0) signals. The frequency of ACh-induced Ca^{2+} oscillations was significantly lower in endothelial cells of aged compared to young rats (Figure 6.4B). All ACh-evoked Ca^{2+} signals automatically extracted from fluorescence images of endothelial cells in the carotid artery of young rats exhibited Ca^{2+} oscillations, and the percentage of ACh-evoked Ca^{2+} signals did not differ with age (Figure 6.4A). To the best of our knowledge, this is the first demonstration of age-related alterations in temporal signalling dynamics. However, other studies have demonstrated extensive endothelial Ca^{2+} oscillations in various arterial preparations of the rat (126,168,179,261). In a recent study, only a limited population of endothelial cells (1-2%) were reported to exhibit agonist-evoked Ca^{2+} oscillations (344). Such contradictory results are not uncommon in vascular studies, as illustrated by numerous investigations of age-associated modifications of endothelium-dependent vasodilation in animal models. For example, ageing has been shown to attenuate (339), have no effect on (338), and possibly augment (337) endothelial-dependent vasodilation. These results suggest that the effects of aging are complex and may depend on species, tissue, agonist, and complications arising from age-related pathologies in various animal models.

Our study is the first to report the effects of ageing on agonist-evoked (ACh) on endothelial $[Ca^{2+}]_i$ signalling in intact, pressurised (rat carotid) arteries. As rats have been shown to have a natural resistance to age-related pathophysiological conditions (374–378), directly visualizing the endothelium in arteries from both young (3 month) and old (18 month) rats has enabled the observation of alterations in endothelial Ca^{2+} signalling that may be attributed to the effects of ageing, *per se*, and not to age-related pathological disease. Endothelial cells from aged animals are more sensitive to chemical (ACh) activation, and have impaired pressure-induced

suppression of agonist-evoked Ca^{2+} signals. Altered endothelial Ca^{2+} signalling may explain the reduction in endothelium-dependent vasodilation (endothelial dysfunction) seen in aged animals and humans, and may be a consequence of alterations in the mechanical properties of vessels with age. However, whether age-related changes in endothelial Ca^{2+} regulation is the result of a process that degrades vascular function, or an adaptive process that occurs to normalise vascular responses remains unanswered.

Chapter 7. General Discussion

7.1 Summary of Principle Findings

The work presented in this thesis describes the design and application of a novel single-photon microendoscopic fluorescence imaging system, specifically designed to image the single-cell thick inner lining, the endothelium, of blood vessels. This thesis also describes functional vascular imaging experiments addressing the control of endothelial Ca^{2+} signalling, a key regulator of vascular function, in large populations of networked endothelial cells in intact vessels. Previously, microscopic access to such large populations of endothelial cells had only been possible by surgically opening blood vessels and laying them flat on the stage of a traditional microscope. The incorporation of a side-viewing GRIN microprobe into a myography chamber (Chapter 2), permits the study of endothelial function in vessels subject to physiological mechanical loading and transmural pressures.

The present results show that endothelial Ca^{2+} signals are heterogeneous and spatiotemporally complex. Because GRIN microendoscopic Ca^{2+} imaging of the endothelium enables sampling of network dynamics in up to 200 endothelial cells, objective and, as much as possible, automated analysis is required. Several research groups have developed fully-automated Ca^{2+} signal analysis algorithms for the analysis of cell networks (179,207,248). All of these approaches, however, suffer low fidelity in the identification of cells in our datasets. We therefore created a semi-automated, image-processing based procedure for identifying the boundaries of individual cells (Chapter 3). The process includes a manual verification step, to ensure accurate whole-cell signal extraction from our data. Like other algorithmic approaches to signal extraction, the approach utilises the activity of cells to assist in their identification (179,207,248,252) and therefore cannot identify inactive cells. However, the verification stage does permit manual identification of cells.

The temporal heterogeneity of Ca^{2+} is usually lost when averaged (167), thus appropriate visual representation is challenging. Therefore, a fully automated signal analysis algorithm that automatically extracts and aligns Ca^{2+} signals, with respect to the peak of their derivative, and outputs signal measurements was developed. By aligning Ca^{2+} signals with respect to their peak rate-of-change, total Ca^{2+} activity was displayed in a more convenient manner (Chapter 3, Appendix A2). This approach is

not limited to the identification and subsequent analysis of fluorescent Ca^{2+} signals but may be applied to any intensity-based measurement of two-dimensional imaging datasets, for example the fluorescence monitoring of endothelial NO labelled with diaminofluoresceins (379).

Analysis of fluorescent endothelial Ca^{2+} signals from intact and pressurised arteries revealed that chemical activation (ACh; 100 μM) evokes rises in $[Ca^{2+}]_i$ that are derived from IP_3-sensitive Ca^{2+} stores (Chapter 4). ACh-evoked endothelial Ca^{2+} signals appeared to originate in distinct activator cell ensembles, and expand across the distributed endothelial network to recruit cells in a concentration-dependent manner. The amplitude of the Ca^{2+} response within each cell is also concentration-dependant. Additionally, IP_3-evoked rises in $[Ca^{2+}]_i$ were modulated by transmural pressure (Chapter 5). The present data also shows that pressure rises result in arterial distension and flattening of endothelial cells, due to the combined effects of circumferential stretch and the normal force of pressure. By modelling IP_3-mediated Ca^{2+} release (Chapter 5, Appendix A3), endothelial shape changes were shown to alter the geometry of the Ca^{2+} diffusive environment near IP_3 receptor microdomains to limit IP_3-mediated Ca^{2+} signals as pressure increases. Taken together, these results suggest that endothelial cells within spatial domains of various threshold sensitivities provide a sensing and signalling system with high resolution and large dynamic range, and that geometric changes in cell shape modulate IP_3-mediated Ca^{2+} signalling, thus explaining macroscopic pressure-dependent, endothelial-mechanosensing without the action of a specific mechanoreceptor.

Finally, by studying the carotid artery endothelium of aged rats, a reduction in the pressure-mediated inhibition of ACh-evoked endothelial Ca^{2+} signals, and altered Ca^{2+} handling was found. These results represent the first recordings of differential endothelial Ca^{2+} signalling with ageing, in intact and pressurised arteries. It is likely that altered Ca^{2+} handling in the aged endothelium is a consequence of altered cellular geometry, and may explain age-related endothelial dysfunction.

7.2 Unresolved Issues and Future Work

7.2.1 GRIN Imaging of the Endothelium

Although *ex vivo* imaging of the endothelium in intact and pressurised arteries using our side-viewing GRIN imaging system has opened up new experimental possibilities, there are limitations. Vessel excision necessarily perturbs the balance of biochemical and mechanical forces that influence the reactivity of the blood vessel *in vivo*. Thus, whilst the loading and geometry of vessels can be accurately mimicked in *ex vivo* experiments, their loss and subsequent restoration during vessel preparation may influence vasoreactivity. Additionally the influence of most physiological influences of blood vessel function (blood flow, circulating hormones, etc.) are difficult, if not impossible, to imitate *ex vivo*. Thus, although measurements taken using GRIN imaging reflect the general function of the endothelium, they do not necessarily reflect the true *in vivo* action of endothelial cells, and special considerations should be taken when interpreting data.

Utilising low NA whole-pitch GRIN lenses permits imaging of the endothelium of large arteries in their natural curved geometry. Because a low NA translates to a large DOF, hundreds of naturally connected endothelial cells can be visualised despite the significant curvature of the pressurised vessels. However, low NA also results in low optical resolution and collection efficiency of fluorescence emission. Increasing the NA of the GRIN lens is essential to improve image quality and the ability to resolve fine features. As image brightness increases with the square of the NA, higher NA would also permit faster imaging. In the case of Ca^{2+} imaging, this may enable the spatial and temporal resolution of fast, low amplitude subcellular Ca^{2+} events (119,169,170).

In the present study, a long (30.2 mm) GRIN lens permitted the lens to pass through the wall of an arteriograph, guiding the optical path into pressurised arteries. Manufacturing constraints limit the NA of such long lenses. However, shorter whole-pitch lenses with considerably higher NA do exist. For example, an equivalent (0.5 mm diameter) 0.2 NA lens can be obtained from GRINTECH GmbH (Germany). Optimised for 488 nm light, the length of this lens is 12.2 mm. Therefore, with

simple modifications to the mechanical design of the arteriograph and lens coupling, an increase in NA greater than two-fold (more than four-fold increase in brightness for constant imaging conditions) may be achieved. Further increases in NA may be achieved with additional decreases in GRIN lens length. An increase in NA will result in a decrease in DOF (equation 2.7), and thus decrease the area of the curved artery surface that may be imaged. The NA at which this decrease in DOF will result in a reduction in FOV depends upon the imaging conditions and the radius of curvature of the artery (i.e. pressure). For example, for a GRIN lens with an increased NA of 0.2, the imaging system described in Chapter 2 could image the endothelium across the full 0.5 mm FOV only for arteries with diameters between 1.9 mm and 4.5 mm. For a smaller vessel diameter of 1 mm, the endothelium would only be in focus across a 357 μm diameter section of the full FOV. Additionally, the range of diameters across which the endothelium would be in focus and the example area in focus for a diameter of 1 mm would decrease with increasing magnification, as would be required to maintain diffraction limited imaging conditions. However, the area in focus may be increased by introducing optical aberrations (field curvature) into the imaging path of the detection optics. An alternative approach to increase NA, at the expense of a greatly reduced FOV, is the use of high NA compound GRIN lens probes, coupled with multiphoton microscopy (194,211).

The ability to monitor the endothelium in large, intact arteries exposed to flow would give significant insight into additional endothelial regulatory mechanisms. As an example, the effects of flow on endothelial Ca^{2+} signalling have, so far, only been studied in small resistance vessels (135), where the endothelium can be visualised through the artery wall, and in surgically opened arteries (201). The former approach is limited to the study of only a few endothelial cells, whilst the latter imposes unphysiological mechanical forces. Recently, minimally invasive, longitudinal imaging of the heart has been achieved using GRIN lenses (193). The study implemented a simple suction method for mechanical stabilisation of the beating heart. The method utilised a piece of latex tubing, connected to an outer cannula through which the GRIN lens was inserted. Such a modification to the system described herein would permit the study of large endothelial cell populations in

response to flow and pressure simultaneously (Figure 7.1A). By mounting the artery on an outer cannula, the GRIN microprobe may be free to rotate within the artery (as the artery would not be directly tied onto the GRIN lens), allowing 3-dimensional mapping of the endothelium (Figure 7.1B). Additionally, a GRIN probe with coaxial flow would allow for double-cannulation of arteries on GRIN microprobes. Such a system would permit simultaneous imaging of two areas of endothelium, either nearby or distal, and allow for the study of propagated endothelial Ca^{2+} waves (171) in large arteries.

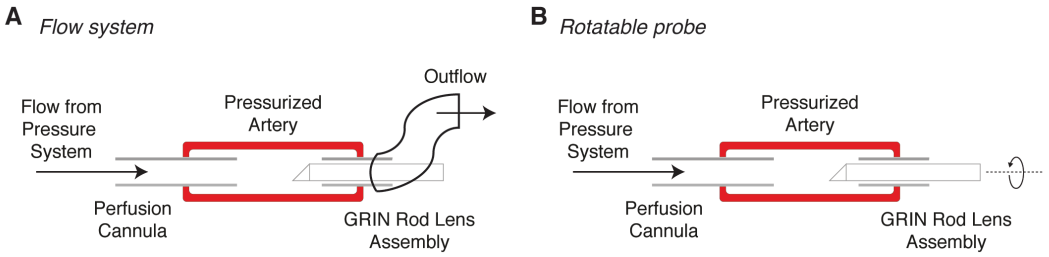

Figure 7.1 – Proposed alterations to endothelial GRIN imaging system. (A) Schematic of GRIN endothelial imaging with intraluminal flow enabled by inserting the GRIN lens inside an outer cannula through a piece of sealable tubing. (B) Schematic of rotatable GRIN imaging system. By mounting the artery on an outer cannula, the GRIN lens could be inserted into an artery and be free to rotate.

Additional capabilities that would expand the functionality of the GRIN imaging system include, but are not limited to the following: multi-wavelength fluorescence imaging; that would for example, enable concurrent monitoring of endothelial Ca^{2+} signalling with NO using diaminofluoresceins (379); a dedicated environmental chamber/incubator, that would allow organ culture and long-term studies of artery remodelling; a motor-driven focus system or tuneable liquid lens (345), to enable tracking of the endothelium during changes in diameter/pressure; full integration with a standard fluorescence microscope, to enable simultaneous imaging of the endothelium and smooth muscle. The endothelium of smaller arteries (~250 μm diameter) could also be imaged using smaller diameter GRIN lenses.

7.2.2 Endothelial Ca^{2+} Signalling

Our data, and that of others (119,123,126,170,183,344), demonstrate heterogeneity in the Ca^{2+} response of individual endothelial cells. Specifically, our data suggests that the spatial and temporal characteristics of the endothelial response changes due to alterations in the geometry of individual cells. We propose that differential spacing between the ER and the PM governs the diffusive release of agonist-induced Ca^{2+} release from the ER. High-resolution transmission electron microscopy of arteries fixed at various transmural pressures would confirm this hypothesis. In addition to heterogeneity among endothelial cells of individual vessels (Chapter 4), this effect may explain the pressure-induced reduction in the endothelial Ca^{2+} response (Chapter 5), and altered Ca^{2+} signalling in aging (Chapter 6). However, a multitude of Ca^{2+} signalling regulatory mechanisms exist and may contribute to the alterations in Ca^{2+} signalling. Specifically, altered ER Ca^{2+} handling (SERCA function, ER Ca^{2+} content) due to changes in pressure was not investigated in the present study. An investigation into the possibilities of altered ER Ca^{2+} handling would define the importance of our results. Additionally, altered expression of the receptors (e.g. IP_3 and muscarinic M3 receptors) involved in agonist-evoked Ca^{2+} signalling among individual endothelial cells and due to ageing may partially explain our results, and warrants immunohistochemical analysis of receptor expression.

7.3 Conclusion

The endothelium is a complex single-layer network of interconnected cells covering the entire inner surface of the vasculature. The control of endothelial Ca^{2+} signalling is an intriguing regulatory function with a well-established role in vascular, but its complexity is only beginning to emerge. The novel GRIN imaging system described in this work, developed specifically to image the endothelium from inside the lumen of intact and pressurised arteries, has enabled the identification of control mechanisms that remained elusive to traditional microscopic investigation. The new mechanisms governing the control of endothelial Ca^{2+} signalling that we have identified (namely the modulation of Ca^{2+} signals by cell shape) warrants further research, whilst the tools we have developed should provide novel insights into vascular control and pathophysiological conditions such as hypertension and

atherosclerosis. The approach described in this thesis offers the opportunity to investigate endothelial function in a physiological setting in ways not previously possible.

References

1. Harvey W, Leake CD. Exercitatio anatomica de motu cordis et sanguinis in animalibus. Springfield, Ill: Thomas; 1928. 272 p.

2. Cooper GM, Hausman RE. The Cell: A Molecular Approach. Sinauer Associates; 2013. 832 p.

3. González JM, Briones AM, Starcher B, Conde MV, Somoza B, Daly C, et al. Influence of elastin on rat small artery mechanical properties. Exp Physiol. 2005 Jul 1;90(4):463–8.

4. Alba C, Vidal L, Díaz F, Villena A, Vargas IP de. Ultrastructural and quantitative age-related changes in capillaries of the dorsal lateral geniculate nucleus. Brain Res Bull. 2004 Aug 30;64(2):145–53.

5. Mello JM de, Orsi AM, Padovani CR, Matheus SMM, Eleutério ML. Structure of the aortic wall in the guinea pig and rat. Braz J Morphol Sci. 2004 Mar;21(1):35–8.

6. Eckman DM, Stacey RB, Rowe R, D′Agostino R Jr, Kock ND, Sane DC, et al. Weekly Doxorubicin Increases Coronary Arteriolar Wall and Adventitial Thickness. PLoS ONE. 2013 Feb 21;8(2):e57554.

7. Webb RC. Smooth Muscle Contraction and Relaxation. Adv Physiol Educ. 2003 Dec 1;27(4):201–6.

8. Somlyo AP, Somlyo AV. Signal transduction and regulation in smooth muscle. Nature. 1994 Nov 17;372(6503):231–6.

9. Wray S, Burdyga T, Noble K. Calcium signalling in smooth muscle. Cell Calcium. 2005 Sep;38(3–4):397–407.

10. Yagi S, Becker PL, Fay FS. Relationship between force and Ca^{2+} concentration in smooth muscle as revealed by measurements on single cells. Proc Natl Acad Sci U S A. 1988 Jun;85(11):4109–13.

11. Somlyo AP, Somlyo AV. Ca^{2+} Sensitivity of Smooth Muscle and Nonmuscle Myosin II: Modulated by G Proteins, Kinases, and Myosin Phosphatase. Physiol Rev. 2003 Oct 1;83(4):1325–58.

12. Horowitz A, Menice CB, Laporte R, Morgan KG. Mechanisms of smooth muscle contraction. Physiol Rev. 1996 Oct 1;76(4):967–1003.

13. Jackson WF. Ion Channels and Vascular Tone. Hypertension. 2000 Jan 1;35(1):173–8.

14. Nelson MT, Patlak JB, Worley JF, Standen NB. Calcium channels, potassium channels, and voltage dependence of arterial smooth muscle tone. Am J Physiol - Cell Physiol. 1990 Jul 1;259(1):C3–18.

15. Chalmers S, Olson ML, MacMillan D, Rainbow RD, McCarron JG. Ion channels in smooth muscle: regulation by the sarcoplasmic reticulum and mitochondria. Cell Calcium. 2007 Nov;42(4-5):447–66.

16. Ross R, Glomset J, Harker L. Response to injury and atherogenesis. Am J Pathol. 1977 Mar;86(3):675–84.

17. Schwann T. Microscopical researches into the accordance in the structure and growth of animals and plants. Sydenham Society; 1847. 308 p.

18. Recklinghausen F v. Eine Methode, mikroskopische hohle und solide Gebilde von einander zu unterscheiden. Arch Für Pathol Anat Physiol Für Klin Med. 1860 May 1;19(3-4):451–451.

19. Recklinghausen F v. Die Lymphgefässe und ihre Beziehung zum Bidegewebe. August Hirschwald; 1862. 126 p.

20. Woodward JJ. Memoirs: Report on certain points connected with the Histology of Minute Blood-Vessels. Q J Microsc Sci. 1870 Oct 1;s2-10(40):380–93.

21. Heidenhain R. Versuche und Fragen zur Lehre von der Lymphbildung. Arch Für Gesamte Physiol Menschen Tiere. 1891 May 1;49(5-6):209–301.

22. Starling EH. On the Absorption of Fluids from the Connective Tissue Spaces. J Physiol. 1896 May 5;19(4):312–26.

23. Palade G. Fine Structure of Blood Capillaries. J Appl Phys. 1953;24(11):1424–1424.

24. Weibel ER, Palade GE. New Cytoplasmic Components in Arterial Endothelia. J Cell Biol. 1964 Oct 1;23(1):101–12.

25. Hibbs RG, Burch GE, Phillips JH. The fine structure of the small blood vessels of normal human dermis and subcutis. Am Heart J. 1958 Nov;56(5):662–70.

26. Simionescu M, Simionescu N, Palade GE. Segmental differentiations of cell junctions in the vascular endothelium. Arteries and veins. J Cell Biol. 1976 Mar 1;68(3):705–23.

27. Dale HH. The Action of Certain Esters and Ethers of Choline, and Their Relation to Muscarine. J Pharmacol Exp Ther. 1914 Nov 1;6(2):147–90.

28. Furchgott RF. The Pharmacology of Vascular Smooth Muscle. Pharmacol Rev. 1955 Jun 1;7(2):183–265.

29. Furchgott RF, Zawadzki JV. The obligatory role of endothelial cells in the relaxation of arterial smooth muscle by acetylcholine. Nature. 1980 Nov 27;288(5789):373–6.

30. Palmer RMJ, Ferrige AG, Moncada S. Nitric oxide release accounts for the biological activity of endothelium-derived relaxing factor. Nature. 1987 Jun 11;327(6122):524–6.

31. Bolton TB, Lang RJ, Takewaki T. Mechanisms of action of noradrenaline and carbachol on smooth muscle of guinea-pig anterior mesenteric artery. J Physiol. 1984 Jun 1;351(1):549–72.

32. Yanagisawa M, Kurihara H, Kimura S, Tomobe Y, Kobayashi M, Mitsui Y, et al. A novel potent vasoconstrictor peptide produced by vascular endothelial cells. Nature. 1988 Mar 31;332(6163):411–5.

33. Palmer RM, Ashton DS, Moncada S. Vascular endothelial cells synthesize nitric oxide from L-arginine. Nature. 1988 Jun 16;333(6174):664–6.

34. Rees DD, Palmer RM, Schulz R, Hodson HF, Moncada S. Characterization of three inhibitors of endothelial nitric oxide synthase in vitro and in vivo. Br J Pharmacol. 1990 Nov;101(3):746–52.

35. Schmidt HHHW, Pollock JS, Nakane M, Förstermann U, Murad F. Ca^{2+}/calmodulin-regulated nitric oxide synthases. Cell Calcium. 1992 Jun;13(6–7):427–34.

36. Rapoport RM, Murad F. Agonist-induced endothelium-dependent relaxation in rat thoracic aorta may be mediated through cGMP. Circ Res. 1983 Mar;52(3):352–7.

37. Carvajal JA, Germain AM, Huidobro-Toro JP, Weiner CP. Molecular mechanism of cGMP-mediated smooth muscle relaxation. J Cell Physiol. 2000 Sep 1;184(3):409–20.

38. Aisaka K, Gross SS, Griffith OW, Levi R. N^G-methylarginine, and inhibitor of endothelium-derived nitric oxide synthesis, is a potent pressor agent in the guinea pig: Does nitric oxide regulate blood pressure in vivo? Biochem Biophys Res Commun. 1989 Apr 28;160(2):881–6.

39. Huang PL, Huang Z, Mashimo H, Bloch KD, Moskowitz MA, Bevan JA, et al. Hypertension in mice lacking the gene for endothelial nitric oxide synthase. Nature. 1995 Sep 21;377(6546):239–42.

40. Scott-Burden T, Vanhoutte PM. The endothelium as a regulator of vascular smooth muscle proliferation. Circulation. 1993;87(5 SUPPL. V):V51–5.

41. Jeremy JY, Rowe D, Emsley AM, Newby AC. Nitric oxide and the proliferation of vascular smooth muscle cells. Cardiovasc Res. 1999 Aug 15;43(3):580–94.

42. Kubes P, Kanwar S, Niu XF, Gaboury JP. Nitric oxide synthesis inhibition induces leukocyte adhesion via superoxide and mast cells. FASEB J. 1993 Oct 1;7(13):1293–9.

43. Radomski MW, Palmer RM, Moncada S. An L-arginine/nitric oxide pathway present in human platelets regulates aggregation. Proc Natl Acad Sci. 1990 Jul 1;87(13):5193–7.

44. Moncada S. Eighth Gaddum Memorial Lecture. University of London Institute of Education, December 1980. Biological importance of prostacyclin. Br J Pharmacol. 1982 May;76(1):3–31.

45. Vane JR. Prostacyclin. J R Soc Med. 1983 Apr;76(4):245–9.

46. Rembold CM. Regulation of contraction and relaxation in arterial smooth muscle. Hypertension. 1992 Aug 1;20(2):129–37.

47. Morgado M, Cairrão E, Santos-Silva AJ, Verde I. Cyclic nucleotide-dependent relaxation pathways in vascular smooth muscle. Cell Mol Life Sci. 2012 Jan 1;69(2):247–66.

48. Kobayashi T, Tahara Y, Matsumoto M, Iguchi M, Sano H, Murayama T, et al. Roles of thromboxane A_2 and prostacyclin in the development of atherosclerosis in ApoE-deficient mice. J Clin Invest. 2004 Sep;114(6):784–94.

49. Arehart E, Stitham J, Asselbergs FW, Douville K, MacKenzie T, Fetalvero KM, et al. Acceleration of cardiovascular disease by a dysfunctional prostacyclin receptor mutation, potential implications for COX-2 inhibition. Circ Res. 2008 Apr 25;102(8):986–93.

50. Max M, Rossaint R. Inhaled prostacyclin in the treatment of pulmonary hypertension. Eur J Pediatr. 1999 Dec;158 Suppl 1:S23–6.

51. Haché M, Denault AY, Bélisle S, Couture P, Babin D, Tétrault F, et al. Inhaled prostacyclin (PGI_2) is an effective addition to the treatment of pulmonary hypertension and hypoxia in the operating room and intensive care unit. Can J Anaesth J Can Anesth. 2001 Oct;48(9):924–9.

52. Piaggesi A, Vallini V, Iacopi E, Tedeschi A, Scatena A, Goretti C, et al. Iloprost in the management of peripheral arterial disease in patients with diabetes mellitus. Minerva Cardioangiol. 2011 Feb;59(1):101–8.

53. Taylor SG, Weston AH. Endothelium-derived hyperpolarizing factor: a new endogenous inhibitor from the vascular endothelium. Trends Pharmacol Sci. 1988 Aug;9(8):272–4.

54. Garland JG, McPherson GA. Evidence that nitric oxide does not mediate the hyperpolarization and relaxation to acetylcholine in the rat small mesenteric artery. Br J Pharmacol. 1992 Feb;105(2):429–35.

55. Dora KA, Sandow SL, Gallagher NT, Takano H, Rummery NM, Hill CE, et al. Myoendothelial gap junctions may provide the pathway for EDHF in mouse mesenteric artery. J Vasc Res. 2003;40:480.

56. Taylor HJ, Chaytor AT, Evans WH, Griffith TM. Inhibition of the gap junctional component of endothelium-dependent relaxations in rabbit iliac artery by 18-α glycyrrhetinic acid. Br J Pharmacol. 1998 Sep 1;125(1):1–3.

57. Corriu C, Feletou M, Canet E, Vanhoutte PM. Endothelium-derived factors and hyperpolarization of the carotid artery of the guinea-pig. Br J Pharmacol. 1996 Nov;119(5):959–64.

58. Chen G, Suzuki H, Weston AH. Acetylcholine releases endothelium-derived hyperpolarizing factor and EDRF from rat blood vessels. Br J Pharmacol. 1988 Dec;95(4):1165–74.

59. Fisslthaler B, Popp R, Kiss L, Potente M, Harder DR, Fleming I, et al. Cytochrome P450 2C is an EDHF synthase in coronary arteries. Nature. 1999 Sep 30;401(6752):493–7.

60. Edwards G, Dora KA, Gardener MJ, Garland CJ, Weston AH. K_+ is an endothelium-derived hyperpolarizing factor in rat arteries. Nature. 1998 Nov 19;396(6708):269–72.

61. Kühberger E, Groschner K, Kukovetz WR, Brunner F. The role of myoendothelial cell contact in non-nitric oxide-, non-prostanoid-mediated endothelium-dependent relaxation of porcine coronary artery. Br J Pharmacol. 1994 Dec;113(4):1289–94.

62. Busse R, Edwards G, Félétou M, Fleming I, Vanhoutte PM, Weston AH. EDHF: bringing the concepts together. Trends Pharmacol Sci. 2002 Aug 1;23(8):374–80.

63. Spagnoli LG, Villaschi S, Neri L, Palmieri G. Gap junctions in myo-endothelial bridges of rabbit carotid arteries. Cell Mol Life Sci. 1982;38(1):124–5.

64. De Wit C, Boettcher M, Schmidt VJ. Signaling across myoendothelial gap junctions--fact or fiction? Cell Commun Adhes. 2008 Sep;15(3):231–45.

65. Moncada S, Gryglewski R, Bunting S, Vane JR. An enzyme isolated from arteries transforms prostaglandin endoperoxides to an unstable substance that inhibits platelet aggregation. Nature. 1976 Oct 21;263(5579):663–5.

66. Dusting GJ, Moncada S, Vane JR. Prostacyclin (PGI_2) is a weak contractor of coronary arteries of the pig. Eur J Pharmacol. 1977 Oct 1;45(3):301–4.

67. Félétou M, Köhler R, Vanhoutte PM. Endothelium-derived vasoactive factors and hypertension: possible roles in pathogenesis and as treatment targets. Curr Hypertens Rep. 2010 Aug;12(4):267–75.

68. Marsden PA, Danthuluri NR, Brenner BM, Ballermann BJ, Brock TA. Endothelin action on vascular smooth muscle involves inositol trisphosphate

and calcium mobilization. Biochem Biophys Res Commun. 1989 Jan 16;158(1):86–93.

69. Xuan YT, Whorton AR, Watkins WD. Inhibition by nicardipine of endothelin-mediated inositol phosphate formation and Ca^{2+} mobilization in smooth muscle cell. Biochem Biophys Res Commun. 1989 Apr 28;160(2):758–64.

70. Goto K, Kasuya Y, Matsuki N, Takuwa Y, Kurihara H, Ishikawa T, et al. Endothelin activates the dihydropyridine-sensitive, voltage-dependent Ca^{2+} channel in vascular smooth muscle. Proc Natl Acad Sci U S A. 1989 May;86(10):3915–8.

71. Kasuya Y, Takuwa Y, Yanagisawa M, Masaki T, Goto K. A pertussis toxin-sensitive mechanism of endothelin action in porcine coronary artery smooth muscle. Br J Pharmacol. 1992 Oct;107(2):456–62.

72. Kurihara Y, Kurihara H, Suzuki H, Kodama T, Maemura K, Nagai R, et al. Elevated blood pressure and craniofaclal abnormalities in mice deficient in endothelin-1. Nature. 1994 Apr 21;368(6473):703–10.

73. Motte S, McEntee K, Naeije R. Endothelin receptor antagonists. Pharmacol Ther. 2006 Jun;110(3):386–414.

74. Chien S. Mechanotransduction and endothelial cell homeostasis: the wisdom of the cell. Am J Physiol - Heart Circ Physiol. 2007 Mar 1;292(3):H1209–24.

75. Hishikawa K, Nakaki T, Suzuki H, Saruta T, Kato R. Transmural pressure inhibits nitric oxide release from human endothelial cells. Eur J Pharmacol. 1992 May 14;215(2-3):329–31.

76. Zhao Y, Flavahan S, Leung SWS, Xu A, Vanhoutte PM, Flavahan NA. Elevated Pressure Causes Endothelial Dysfunction in Mouse Carotid Arteries by Increasing Local Angiotensin Signaling. Am J Physiol - Heart Circ Physiol. 2014 Dec 5;ajpheart.00775.2014.

77. Weinbaum S, Tzeghai G, Ganatos P, Pfeffer R, Chien S. Effect of cell turnover and leaky junctions on arterial macromolecular transport. Am J Physiol. 1985 Jun;248(6 Pt 2):H945–60.

78. Ohtsuka A, Ando J, Korenaga R, Kamiya A, Toyamasorimachi N, Miyasaka M. The Effect of Flow on the Expression of Vascular Adhesion Molecule-1 by Cultured Mouse Endothelial Cells. Biochem Biophys Res Commun. 1993 May 28;193(1):303–10.

79. Ando J, Tsuboi H, Korenaga R, Takada Y, Toyama-Sorimachi N, Miyasaka M, et al. Shear stress inhibits adhesion of cultured mouse endothelial cells to lymphocytes by downregulating VCAM-1 expression. Am J Physiol - Cell Physiol. 1994 Sep 1;267(3):C679–87.

80. Gimbrone MA. Vascular Endothelium, Hemodynamic Forces, and Atherogenesis. Am J Pathol. 1999 Jul;155(1):1–5.

81. World CJ, Garin G, Berk BC. Vascular shear stress and activation of inflammatory genes. Curr Atheroscler Rep. 2006 May 1;8(3):240–4.

82. Katritsis D, Kaiktsis L, Chaniotis A, Pantos J, Efstathopoulos EP, Marmarelis V. Wall Shear Stress: Theoretical Considerations and Methods of Measurement. Prog Cardiovasc Dis. 2007 Mar;49(5):307–29.

83. Mazumdar J. Biofluid mechanics. Singapore: World scientific; 1998.

84. Tangelder GJ, Teirlinck HC, Slaaf DW, Reneman RS. Distribution of blood platelets flowing in arterioles. Am J Physiol. 1985 Mar;248(3 Pt 2):H318–23.

85. Chachisvilis M, Zhang Y-L, Frangos JA. G protein-coupled receptors sense fluid shear stress in endothelial cells. Proc Natl Acad Sci. 2006 Oct 17;103(42):15463–8.

86. Tzima E, Pozo MA del, Shattil SJ, Chien S, Schwartz MA. Activation of integrins in endothelial cells by fluid shear stress mediates Rho-dependent cytoskeletal alignment. EMBO J. 2001 Sep 3;20(17):4639–47.

87. Ranade SS, Qiu Z, Woo S-H, Hur SS, Murthy SE, Cahalan SM, et al. Piezo1, a mechanically activated ion channel, is required for vascular development in mice. Proc Natl Acad Sci U S A. 2014 Jul 15;111(28):10347–52.

88. Yamamoto K, Sokabe T, Matsumoto T, Yoshimura K, Shibata M, Ohura N, et al. Impaired flow-dependent control of vascular tone and remodeling in P2X4-deficient mice. Nat Med. 2006 Jan;12(1):133–7.

89. Tzima E, Irani-Tehrani M, Kiosses WB, Dejana E, Schultz DA, Engelhardt B, et al. A mechanosensory complex that mediates the endothelial cell response to fluid shear stress. Nature. 2005 Sep 15;437(7057):426–31.

90. Yamamoto K, Ando J. Endothelial cell and model membranes respond to shear stress by rapidly decreasing the order of their lipid phases. J Cell Sci. 2013 Mar 1;126(5):1227–34.

91. Florian JA, Kosky JR, Ainslie K, Pang Z, Dull RO, Tarbell JM. Heparan Sulfate Proteoglycan Is a Mechanosensor on Endothelial Cells. Circ Res. 2003 Nov 14;93(10):e136–42.

92. Kuchan MJ, Frangos JA. Role of calcium and calmodulin in flow-induced nitric oxide production in endothelial cells. Am J Physiol. 1994 Mar;266(3 Pt 1):C628–36.

93. Rubanyi GM, Romero JC, Vanhoutte PM. Flow-induced release of endothelium-derived relaxing factor. Am J Physiol. 1986 Jun;250(6 Pt 2):H1145–9.

94. Cooke JP, Rossitch E, Andon NA, Loscalzo J, Dzau VJ. Flow activates an endothelial potassium channel to release an endogenous nitrovasodilator. J Clin Invest. 1991 Nov;88(5):1663–71.

95. Joannides R, Haefeli WE, Linder L, Richard V, Bakkali EH, Thuillez C, et al. Nitric Oxide Is Responsible for Flow-Dependent Dilatation of Human Peripheral Conduit Arteries In Vivo. Circulation. 1995 Mar 1;91(5):1314–9.

96. Paniagua OA, Bryant MB, Panza JA. Role of Endothelial Nitric Oxide in Shear Stress–Induced Vasodilation of Human Microvasculature Diminished Activity in Hypertensive and Hypercholesterolemic Patients. Circulation. 2001 Apr 3;103(13):1752–8.

97. Fleming I, Fisslthaler B, Dixit M, Busse R. Role of PECAM-1 in the shear-stress-induced activation of Akt and the endothelial nitric oxide synthase (eNOS) in endothelial cells. J Cell Sci. 2005 Sep 15;118(Pt 18):4103–11.

98. Sampath R, Kukielka GL, Smith CW, Eskin SG, McIntire LV. Shear stress-mediated changes in the expression of leukocyte adhesion receptors on human umbilical vein endothelial cells in vitro. Ann Biomed Eng. 1995 Jun;23(3):247–56.

99. Diamond SL, Eskin SG, McIntire LV. Fluid flow stimulates tissue plasminogen activator secretion by cultured human endothelial cells. Science. 1989 Mar 17;243(4897):1483–5.

100. Davies PF. Flow-Mediated Endothelial Mechanotransduction. Physiol Rev. 1995 Jul;75(3):519–60.

101. Berk BC, Abe JI, Min W, Surapisitchat J, Yan C. Endothelial atheroprotective and anti-inflammatory mechanisms. Ann N Y Acad Sci. 2001 Dec;947:93–109; discussion 109–11.

102. Lehoux S, Tedgui A. Cellular mechanics and gene expression in blood vessels. J Biomech. 2003 May;36(5):631–43.

103. Caro CG, Fitz-Gerald JM, Schroter RC. Arterial Wall Shear and Distribution of Early Atheroma in Man. Nature. 1969 Sep 13;223(5211):1159–61.

104. Zhao S, Suciu A, Ziegler T, Moore JE, Bürki E, Meister JJ, et al. Synergistic effects of fluid shear stress and cyclic circumferential stretch on vascular endothelial cell morphology and cytoskeleton. Arterioscler Thromb Vasc Biol. 1995 Oct;15(10):1781–6.

105. Bayliss WM. On the local reactions of the arterial wall to changes of internal pressure. J Physiol. 1902 May 28;28(3):220–31.

106. Folkow B. Intravascular pressure as a factor regulating the tone of the small vessels. Acta Physiol Scand. 1949 Apr 14;17(4):289–310.

107. Folkow B. A study of the factors influencing the tone of denervated blood vessels perfused at various pressures. Acta Physiol Scand. 1952;27(2-3):99–117.

108. Acevedo A, Bowser S, Gerritsen M, Bizios R. Morphological and Proliferative Responses of Endothelial-Cells to Hydrostatic-Pressure - Role of Fibroblast Growth-Factor. J Cell Physiol. 1993 Dec;157(3):603–14.

109. Sumpio BE, Widmann MD, Ricotta J, Awolesi MA, Watase M. Increased ambient pressure stimulates proliferation and morphologic changes in cultured endothelial cells. J Cell Physiol. 1994 Jan;158(1):133–9.

110. Ohashi T, Sugaya Y, Sakamoto N, Sato M. Hydrostatic pressure influences morphology and expression of VE-cadherin of vascular endothelial cells. J Biomech. 2007;40(11):2399–405.

111. Schwartz EA, Bizios R, Gerritsen ME. Effects of sustained hydrostatic pressure on the expression of endothelial cell-leukocyte adhesion molecules. Pulmonary Edema. 1998.

112. Walpola PL, Gotlieb AI, Cybulsky MI, Langille BL. Expression of ICAM-1 and VCAM-1 and Monocyte Adherence in Arteries Exposed to Altered Shear Stress. Arterioscler Thromb Vasc Biol. 1995 Jan 1;15(1):2–10.

113. Huang A, Koller A. Both nitric oxide and prostaglandin-mediated responses are impaired in skeletal muscle arterioles of hypertensive rats. J Hypertens. 1996 Jul;14(7):887–95.

114. Huang A, Sun D, Kaley G, Koller A. Superoxide Released to High Intra-arteriolar Pressure Reduces Nitric Oxide–Mediated Shear Stress– and Agonist-Induced Dilations. Circ Res. 1998 Nov 2;83(9):960–5.

115. Jaffe EA, Hoyer LW, Nachman RL. Synthesis of Antihemophilic Factor Antigen by Cultured Human Endothelial Cells. J Clin Invest. 1973 Nov;52(11):2757–64.

116. Gimbrone MA, Cotran RS, Folkman J. Human Vascular Endothelial Cells in Culture. Growth and DNA Synthesis. J Cell Biol. 1974 Mar 1;60(3):673–84.

117. Tran QK, Watanabe H. Calcium signalling in the endothelium. Handb Exp Pharmacol. 2006;(176 Pt 1):145–87.

118. Behringer EJ, Segal. SS. Tuning electrical conduction along endothelial tubes of resistance arteries through Ca^{2+}-activated K^{+} channels. Circ Res. 2012 May 11;110(10):1311–21.

119. Sonkusare SK, Bonev AD, Ledoux J, Liedtke W, Kotlikoff MI, Heppner TJ, et al. Elementary Ca^{2+} Signals Through Endothelial TRPV4 Channels Regulate Vascular Function. Science. 2012 May 4;336(6081):597–601.

120. Kohn EC, Alessandro R, Spoonster J, Wersto RP, Liotta LA. Angiogenesis: role of calcium-mediated signal transduction. Proc Natl Acad Sci U S A. 1995 Feb 28;92(5):1307–11.

121. Huang AJ, Manning JE, Bandak TM, Ratau MC, Hanser KR, Silverstein SC. Endothelial cell cytosolic free calcium regulates neutrophil migration across monolayers of endothelial cells. J Cell Biol. 1993 Mar 15;120(6):1371–80.

122. Muller WA. Mechanisms of Transendothelial Migration of Leukocytes. Circ Res. 2009 Jul 31;105(3):223–30.

123. Huang T-Y, Chu T-F, Chen H-I, Jen CJ. Heterogeneity of $[Ca^{2+}]_i$ signaling in intact rat aortic endothelium. FASEB J. 2000 Apr 1;14(5):797–804.

124. Korenaga R, Ando J, Ohtsuka A, Sakuma I, Yang W, Toyo-oka T, et al. Close Correlation between Cytoplasmic Ca^{2+} Levels and Release of an Endothelium-Derived Relaxing Factor from Cultured Endothelial Cells. Cell Struct Funct. 1993;18(2):95–104.

125. Peach MJ, Loeb AL, Singer HA, Saye J. Endothelium-derived vascular relaxing factor. Hypertension. 1985 May 1;7(3 Pt 2):I94.

126. McSherry IN, Spitaler MM, Takano H, Dora KA. Endothelial cell Ca^{2+} increases are independent of membrane potential in pressurized rat mesenteric arteries. Cell Calcium. 2005 Jul;38(1):23–33.

127. Tracey WR, Peach MJ. Differential muscarinic receptor mRNA expression by freshly isolated and cultured bovine aortic endothelial cells. Circ Res. 1992 Feb 1;70(2):234–40.

128. Carter TD, Ogden D. Acetylcholine-stimulated changes of membrane potential and intracellular Ca^{2+} concentration recorded in endothelial cells in situ in the isolated rat aorta. Pflüg Arch. 1994 Oct 1;428(5-6):476–84.

129. Laskey RE, Adams DJ, Breemen C van. Cytosolic Ca^{2+} measurements in endothelium of rabbit cardiac valves using imaging fluorescence microscopy. Am J Physiol - Heart Circ Physiol. 1994 May 1;266(5):H2130–5.

130. Gordienko DV, Tsukahara H. Tetrodotoxin-blockable depolarization-activated Na^+ currents in a cultured endothelial cell line derived from rat interlobar arter and human umbilical vein. Pflüg Arch Eur J Physiol. 1994 Aug;428(1):91–3.

131. Gosling M, Harley SL, Turner RJ, Carey N, Powell JT. Human saphenous vein endothelial cells express a tetrodotoxin-resistant, voltage-gated sodium current. J Biol Chem. 1998 Aug 14;273(33):21084–90.

132. Walsh KB, Wolf MB, Fan J. Voltage-gated sodium channels in cardiac microvascular endothelial cells. Am J Physiol - Heart Circ Physiol. 1998 Feb 1;274(2):H506–12.

133. Traub O, Ishida T, Ishida M, Tupper JC, Berk BC. Shear Stress-mediated Extracellular Signal-regulated Kinase Activation Is Regulated by Sodium in Endothelial Cells. Potential Role for a Voltage-dependent Sodium Channel. J Biol Chem. 1999 Jul 16;274(29):20144–50.

134. Félétou M. Calcium Signaling in Vascular Cells and Cell-to-Cell Communications. The Endothelium, Part I: Multiple Functions of the Endothelial Cells -- Focus on Endothelium-Derived Vasoactive Mediators. New Jersey: Morgan & Claypool Life Sciences; 2011.

135. Falcone JC, Kuo L, Meininger GA. Endothelial cell calcium increases during flow-induced dilation in isolated arterioles. Am J Physiol - Heart Circ Physiol. 1993 Feb 1;264(2):H653–9.

136. Wood PG, Gillespie JI. Evidence for Mitochondrial Ca^{2+}-Induced Ca^{2+} Release in Permeabilised Endothelial Cells. Biochem Biophys Res Commun. 1998 May 19;246(2):543–8.

137. Tran Q-K, Ohashi K, Watanabe H. Calcium signalling in endothelial cells. Cardiovasc Res. 2000 Oct 1;48(1):13–22.

138. Ziegelstein RC, Spurgeon HA, Pili R, Passaniti A, Cheng L, Corda S, et al. A functional ryanodine-sensitive intracellular Ca^{2+} store is present in vascular endothelial cells. Circ Res. 1994 Jan;74(1):151–6.

139. Corda S, Spurgeon HA, Lakatta EG, Capogrossi MC, Ziegelstein RC. Endoplasmic Reticulum Ca^{2+} Depletion Unmasks a Caffeine-Induced Ca^{2+} Influx in Human Aortic Endothelial Cells. Circ Res. 1995 Nov 1;77(5):927–35.

140. Moccia F, Berra-Romani R, Tanzi F. Update on vascular endothelial Ca^{2+} signalling: A tale of ion channels, pumps and transporters. World J Biol Chem. 2012 Jul 26;3(7):127–58.

141. Bossu JL, Elhamdani A, Feltz A. Voltage-dependent calcium entry in confluent bovine capillary endothelial cells. FEBS Lett. 1992 Mar 16;299(3):239–42.

142. Bkaily G, d' OrlA(C)ans-Juste P, Naik R, PA(C)rodin J, Stankova J, Abdulnour E, et al. PAF activation of a voltage-gated R-type Ca^{2+} channel in human and canine aortic endothelial cells. Br J Pharmacol. 1993 Oct;110(2):519–20.

143. Lückhoff A, Busse R. Calcium influx into endothelial cells and formation of endothelium-derived relaxing factor is controlled by the membrane potential. Pflüg Arch Eur J Physiol. 1990 May;416(3):305–11.

144. Braunstein TH, Inoue R, Cribbs L, Oike M, Ito Y, Holstein-Rathlou N-H, et al. The role of L- and T-type calcium channels in local and remote calcium responses in rat mesenteric terminal arterioles. J Vasc Res. 2009;46(2):138–51.

145. Kuo IY, Ellis A, Seymour VAL, Sandow SL, Hill CE. Dihydropyridine-insensitive calcium currents contribute to function of small cerebral arteries. J Cereb Blood Flow Metab Off J Int Soc Cereb Blood Flow Metab. 2010 Jun;30(6):1226–39.

146. Hawkins BT, Egleton RD, Davis TP. Modulation of cerebral microvascular permeability by endothelial nicotinic acetylcholine receptors. Am J Physiol Heart Circ Physiol. 2005 Jul;289(1):H212–9.

147. Vulchanova L, Arvidsson U, Riedl M, Wang J, Buell G, Surprenant A, et al. Differential distribution of two ATP-gated channels (P_{2X} receptors) determined by immunocytochemistry. Proc Natl Acad Sci. 1996 Jul 23;93(15):8063–7.

148. Harrington LS, Mitchell JA. Novel role for P_{2X} receptor activation in endothelium-dependent vasodilation. Br J Pharmacol. 2004 Nov;143(5):611–7.

149. Berra-Romani R, Raqeeb A, Avelino-Cruz JE, Moccia F, Oldani A, Speroni F, et al. Ca^{2+} signaling in injured in situ endothelium of rat aorta. Cell Calcium. 2008 Sep;44(3):298–309.

150. Putney JW. A model for receptor-regulated calcium entry. Cell Calcium. 1986 Feb;7(1):1–12.

151. Heller S, O'Neil RG. Molecular Mechanisms of TRPV4 Gating. In: Liedtke WB, Heller S, editors. TRP Ion Channel Function in Sensory Transduction and Cellular Signaling Cascades. Boca Raton, Florida: CRC Press; 2007.

152. Árnadóttir J, Chalfie M. Eukaryotic Mechanosensitive Channels. Annu Rev Biophys. 2010;39(1):111–37.

153. Saunders KB, D'Amore PA. An in vitro model for cell-cell interactions. Vitro Cell Dev Biol J Tissue Cult Assoc. 1992 Aug;28A(7-8):521–8.

154. Fillinger MF, O'Connor SE, Wagner RJ, Cronenwett JL. The effect of endothelial cell coculture on smooth muscle cell proliferation. J Vasc Surg Off Publ Soc Vasc Surg Int Soc Cardiovasc Surg North Am Chapter. 1993 Jun;17(6):1058–67; discussion 1067–8.

155. Isakson BE, Duling BR. Heterocellular Contact at the Myoendothelial Junction Influences Gap Junction Organization. Circ Res. 2005 Jul 8;97(1):44–51.

156. Bevan JA, Osher JV. A direct method for recording tension changes in the wall of small blood vessels in vitro. Agents Actions. 1972;2(5):257–60.

157. Mulvany MJ, Halpern W. Mechanical properties of vascular smooth muscle cells in situ. Nature. 1976 Apr 15;260(5552):617–9.

158. Halpern W, Osol G, Coy GS. Mechanical behavior of pressurized in vitro prearteriolar vessels determined with a video system. Ann Biomed Eng. 1984;12(5):463–79.

159. Fischer MJM, Uchida S, Messlinger K. Measurement of meningeal blood vessel diameter in vivo with a plug-in for ImageJ. Microvasc Res. 2010 Sep;80(2):258–66.

160. Davis MJ. An Improved, Computer-based Method to Automatically Track Internal and External Diameter of Isolated Microvessels. Microcirculation. 2005 Jun 1;12(4):361–72.

161. Lu X, Kassab GS. Assessment of endothelial function of large, medium, and small vessels: a unified myograph. Am J Physiol - Heart Circ Physiol. 2011 Jan 1;300(1):H94–100.

162. Tsien RY, Rink TJ, Poenie M. Measurement of cytosolic free Ca^{2+} in individual small cells using fluorescence microscopy with dual excitation wavelengths. Cell Calcium. 1985 Apr;6(1-2):145–57.

163. Miyawaki A, Llopis J, Heim R, McCaffery JM, Adams JA, Ikura M, et al. Fluorescent indicators for Ca^{2+} based on green fluorescent proteins and calmodulin. Nature. 1997 Aug 28;388(6645):882–7.

164. Haughland RP. The Molecular Probes® Handbook. Ninth. Eugene, USA: Molecular Probes, Inc.; 2002.

165. Aoki H, Kobayashi S, Nishimura J, Yamamoto H, Kanaide H. Endothelin induces the Ca^{2+}-transient in endothelial cells in situ. Biochem Biophys Res Commun. 1991 Dec 31;181(3):1352–7.

166. Nishimura J, Aoki H, Chen X, Shikasho T, Kobayashi S, Kanaide I. Evidence for the presence of endothelin ET^{A} receptors in endothelial cells in situ on the aortic side of porcine aortic valve. Br J Pharmacol. 1995 Aug 1;115(8):1369–76.

167. Socha MJ, Domeier TL, Behringer EJ, Segal SS. Coordination of Intercellular Ca^{2+} Signaling in Endothelial Cell Tubes of Mouse Resistance Arteries. Microcirculation. 2012 Nov 1;19(8):757–70.

168. Kansui Y, Garland CJ, Dora KA. Enhanced spontaneous Ca^{2+} events in endothelial cells reflect signalling through myoendothelial gap junctions in pressurized mesenteric arteries. Cell Calcium. 2008 Aug;44(2):135–46.

169. Bagher P, Beleznai T, Kansui Y, Mitchell R, Garland CJ, Dora KA. Low intravascular pressure activates endothelial cell TRPV4 channels, local Ca^{2+} events, and IK_{Ca} channels, reducing arteriolar tone. Proc Natl Acad Sci. 2012 Oct 30;109(44):18174–9.

170. Ledoux J, Taylor MS, Bonev AD, Hannah RM, Solodushko V, Shui B, et al. Functional architecture of inositol 1,4,5-trisphosphate signaling in restricted spaces of myoendothelial projections. Proc Natl Acad Sci. 2008 Jul 15;105(28):9627–32.

171. Tallini YN, Brekke JF, Shui B, Doran R, Hwang S, Nakai J, et al. Propagated Endothelial Ca^{2+} Waves and Arteriolar Dilation In Vivo Measurements in Cx40BAC–GCaMP2 Transgenic Mice. Circ Res. 2007 Dec 7;101(12):1300–9.

172. Marchenko SM, Sage SO. Effects of shear stress on [Ca<sup>2+<sup>]$_i$ and membrane potential of vascular endothelium of intact rat blood vessels. Exp Physiol. 2000 Jan 1;85(1):43–8.

173. Kasai Y, Yamazawa T, Sakurai T, Taketani Y, Iino M. Endothelium-dependent frequency modulation of Ca^{2+} signalling in individual vascular smooth muscle cells of the rat. J Physiol. 1997 Oct 15;504(Pt 2):349–57.

174. Schuster A, Oishi H, Bény JL, Stergiopulos N, Meister JJ. Simultaneous arterial calcium dynamics and diameter measurements: application to myoendothelial communication. Am J Physiol - Heart Circ Physiol. 2001 Mar 1;280(3):H1088–96.

175. Falcone JC. Endothelial cell calcium and vascular control. Med Sci Sports Exerc. 1995 Aug;27(8):1165–9.

176. Dora KA, Doyle MP, Duling BR. Elevation of intracellular calcium in smooth muscle causes endothelial cell generation of NO in arterioles. Proc Natl Acad Sci. 1997 Jun 10;94(12):6529–34.

177. Bagher P, Davis MJ, Segal SS. Intravital macrozoom imaging and automated analysis of endothelial cell calcium signals coincident with arteriolar dilation in Cx40(BAC) -GCaMP2 transgenic mice. Microcirc N Y N 1994. 2011 May;18(4):331–8.

178. Nelson M, Ledoux J, Taylor M, Bonev A, Hannah R, Solodushko V, et al. Spinning Disk Confocal Microscopy of Calcium Signalling in Blood Vessel Walls. Microsc Anal Am Ed. 2010 Mar 1;24(2):5–8.

179. Francis M, Qian X, Charbel C, Ledoux J, Parker JC, Taylor MS. Automated region of interest analysis of dynamic Ca^{2+} signals in image sequences. Am J Physiol - Cell Physiol. 2012 Aug 1;303(3):C236–43.

180. Ohata H, Ujike Y, Momose K. Confocal imaging analysis of ATP-induced Ca^{2+} response in individual endothelial cells of the artery in situ. Am J Physiol. 1997 Jun;272(6 Pt 1):C1980–7.

181. Ohi Y, Takai N, Muraki K, Watanabe M, Imaizumi Y. Ca^{2+}-images of smooth muscle cells and endothelial cells in one confocal plane in femoral artery segments of the rat. Jpn J Pharmacol. 2001 May;86(1):106–13.

182. Marie I, Beny J-L. Calcium Imaging of Murine Thoracic Aorta Endothelium by Confocal Microscopy Reveals Inhomogeneous Distribution of Endothelial Cells Responding to Vasodilator Agents. J Vasc Res. 2002;39(3):260–7.

183. Prendergast C, Quayle J, Burdyga T, Wray S. Atherosclerosis affects calcium signalling in endothelial cells from apolipoprotein E knockout mice before plaque formation. Cell Calcium. 2014 Mar;55(3):146–54.

184. Vinall PE, Simeone FA. Whole mounted pressurized in vitro model for the study of cerebral arterial mechanics. Blood Vessels. 1987;24(1-2):51–62.

185. Halpern W, Kelley M. In vitro methodology for resistance arteries. Blood Vessels. 1991;28(1-3):245–51.

186. Marrelli SP. Selective measurement of endothelial or smooth muscle $[Ca^{2+}]_i$ in pressurized/perfused cerebral arteries with fura-2. J Neurosci Methods. 2000 Apr 15;97(2):145–55.

187. Dunn WR, Wellman GC, Bevan JA. Enhanced resistance artery sensitivity to agonists under isobaric compared with isometric conditions. Am J Physiol - Heart Circ Physiol. 1994 Jan 1;266(1):H147–55.

188. Nesbitt WS, Giuliano S, Kulkarni S, Dopheide SM, Harper IS, Jackson SP. Intercellular calcium communication regulates platelet aggregation and thrombus growth. J Cell Biol. 2003 Mar 31;160(7):1151–61.

189. Lorenzon P, Vecile E, Nardon E, Ferrero E, Harlan JM, Tedesco F, et al. Endothelial Cell E- and P-Selectin and Vascular Cell Adhesion Molecule-1 Function as Signaling Receptors. J Cell Biol. 1998 Sep 7;142(5):1381–91.

190. Zhang Q, Cao C, Mangano M, Zhang Z, Silldorff EP, Lee-Kwon W, et al. Descending vasa recta endothelium is an electrical syncytium. Am J Physiol - Regul Integr Comp Physiol. 2006 Dec 1;291(6):R1688–99.

191. Climent B, Zsiros E, Stankevicius E, de la Villa P, Panyi G, Simonsen U, et al. Intact rat superior mesenteric artery endothelium is an electrical syncytium and expresses strong inward rectifier K+ conductance. Biochem Biophys Res Commun. 2011 Jul 8;410(3):501–7.

192. Flusberg BA, Nimmerjahn A, Cocker ED, Mukamel EA, Barretto RPJ, Ko TH, et al. High-speed, miniaturized fluorescence microscopy in freely moving mice. Nat Methods. 2008;5(11):935–8.

193. Jung K, Kim P, Leuschner F, Gorbatov R, Kim JK, Ueno T, et al. Endoscopic Time-Lapse Imaging of Immune Cells in Infarcted Mouse Hearts. Circ Res. 2013 Feb 7;112(6):891–9.

194. Kim P, Chung E, Yamashita H, Hung KE, Mizoguchi A, Kucherlapati R, et al. In vivo wide-area cellular imaging by side-view endomicroscopy. Nat Methods. 2010 Mar 14;7(4):303–5.

195. Aird WC. Spatial and temporal dynamics of the endothelium. J Thromb Haemost. 2005 Jul 1;3(7):1392–406.

196. Nachman RL, Jaffe EA. Endothelial cell culture: beginnings of modern vascular biology. J Clin Invest. 2004 Oct;114(8):1037–40.

197. Mügge A, Peterson T, Harrison DG. Release of nitrogen oxides from cultured bovine aortic endothelial cells is not impaired by calcium channel antagonists. Circulation. 1991 Apr;83(4):1404–9.

198. Sun D, Nakao S, Xie F, Zandi S, Schering A, Hafezi-Moghadam A. Superior sensitivity of novel molecular imaging probe: simultaneously targeting two types of endothelial injury markers. FASEB J. 2010 May 1;24(5):1532–40.

199. Arrebola-Moreno AL, Laclaustra M, Kaski JC. Noninvasive Assessment of Endothelial Function in Clinical Practice. Rev Esp Cardiol Engl Ed. 2012 Jan;65(1):80–90.

200. Burdyga T, Shmygol A, Eisner DA, Wray S. A new technique for simultaneous and in situ measurements of Ca^{2+} signals in arteriolar smooth muscle and endothelial cells. Cell Calcium. 2003 Jul;34(1):27–33.

201. Huang T-Y, Chen H, Liu C-Y, Jen CJ. Endothelial $[Ca^{2+}]_i$ is an integrating signal for the vascular tone in rat aortae. BMC Physiol. 2001 Jun 20;1(1):5.

202. Long J, Junkin M, Wong PK, Hoying J, Deymier P. Calcium Wave Propagation in Networks of Endothelial Cells: Model-based Theoretical and Experimental Study. PLoS Comput Biol. 2012 Dec 27;8(12):e1002847.

203. Van Zandvoort M, Engels W, Douma K, Beckers L, oude Egbrink M, Daemen M, et al. Two-Photon Microscopy for Imaging of the (Atherosclerotic) Vascular Wall: A Proof of Concept Study. J Vasc Res. 2004;41(1):54–63.

204. Megens RTA, Oude Egbrink MGA, Cleutjens JPM, Kuijpers MJE, Schiffers PHM, Merkx M, et al. Imaging collagen in intact viable healthy and atherosclerotic arteries using fluorescently labeled CNA35 and two-photon laser scanning microscopy. Mol Imaging. 2007 Aug;6(4):247–60.

205. Megens RTA, oude Egbrink MGA, Merkx M, Slaaf DW, van Zandvoort MAMJ. Two-photon microscopy on vital carotid arteries: imaging the relationship between collagen and inflammatory cells in atherosclerotic plaques. J Biomed Opt. 2008 Aug;13(4):044022.

206. Winter PW, Shroff H. Faster fluorescence microscopy: advances in high speed biological imaging. Curr Opin Chem Biol. 2014 Jun;20:46–53.

207. Mukamel EA, Nimmerjahn A, Schnitzer MJ. Automated Analysis of Cellular Signals from Large-Scale Calcium Imaging Data. Neuron. 2009 Sep 24;63(6):747–60.

208. Oude Egbrink MGA, Engels W, Leenders PJA, Brunenberg EJL, Reesink KD, Janssen BJA, et al. In vivo high-resolution structural imaging of large arteries in

small rodents using two-photon laser scanning microscopy. J Biomed Opt. 2010 Jan 1;15(1):011108–011108.

209. Helmchen F, Denk W. Deep tissue two-photon microscopy. Nat Methods. 2005 Dec;2(12):932–40.

210. Wilt BA, Burns LD, Ho ETW, Ghosh KK, Mukamel EA, Schnitzer MJ. Advances in Light Microscopy for Neuroscience. Annu Rev Neurosci. 2009;32:435.

211. Jung JC, Schnitzer MJ. Multiphoton endoscopy. Opt Lett. 2003;28(11):902–4.

212. Jung JC, Mehta AD, Aksay E, Stepnoski R, Schnitzer MJ. In Vivo Mammalian Brain Imaging Using One- and Two-Photon Fluorescence Microendoscopy. J Neurophysiol. 2004 Nov 1;92(5):3121–33.

213. Barretto RPJ, Schnitzer MJ. In Vivo Optical Microendoscopy for Imaging Cells Lying Deep within Live Tissue. Cold Spring Harb Protoc. 2012 Oct 1;2012(10):pdb.top071464.

214. Rol P, Beck D, Fankhauser F, Niederer P. GRIN-endoscopy for laser treatment in ophthalmology. Klin Monatsblätter Für Augenheilkd. 1994 May;204(5):470–3.

215. Rector DM, Rogers RF, George JS. A focusing image probe for assessing neural activity in vivo. J Neurosci Methods. 1999 Sep 15;91(1-2):135–45.

216. Rector DM, Rogers RF, Schwaber JS, Harper RM, George JS. Scattered-light imaging in vivo tracks fast and slow processes of neurophysiological activation. Neuroimage. 2001;14(5):977–94.

217. Fisher JAN, Civillico EF, Contreras D, Yodh AG. In vivo fluorescence microscopy of neuronal activity in three dimensions by use of voltage-sensitive dyes. Opt Lett. 2004 Jan 1;29(1):71–3.

218. Kim JK, Lee WM, Kim P, Choi M, Jung K, Kim S, et al. Fabrication and operation of GRIN probes for in vivo fluorescence cellular imaging of internal organs in small animals. Nat Protoc. 2012 Aug;7(8):1456–69.

219. Barretto RPJ, Ko TH, Jung JC, Wang TJ, Capps G, Waters AC, et al. Time-lapse imaging of disease progression in deep brain areas using fluorescence microendoscopy. Nat Med. 2011;17(2):223–8.

220. Murayama M, Pérez-Garci E, Lüscher HR, Larkum ME. Fiberoptic system for recording dendritic calcium signals in layer 5 neocortical pyramidal cells in freely moving rats. J Neurophysiol. 2007;98(3):1791–805.

221. Murayama M, Larkum ME. In vivo dendritic calcium imaging with a fiberoptic periscope system. Nat Protoc. 2009 Oct;4(10):1551–9.

222. Kim JK, Vinarsky V, Wain J, Zhao R, Jung K, Choi J, et al. *In Vivo* Imaging of Tracheal Epithelial Cells in Mice during Airway Regeneration. Am J Respir Cell Mol Biol. 2012 Dec;47(6):864–8.

223. McLaughlin RA, Quirk BC, Curatolo A, Kirk RW, Scolaro L, Lorenser D, et al. Imaging of Breast Cancer With Optical Coherence Tomography Needle Probes: Feasibility and Initial Results. IEEE J Sel Top Quantum Electron. 2012 May;18(3):1184–91.

224. Pierscionek BK, Regini JW. The gradient index lens of the eye: An opto-biological synchrony. Prog Retin Eye Res. 2012 Jul;31(4):332–49.

225. Kita H, Uchida T. Light Focussing Glass Fiber And Rod. Proc SPIE 0021, Fiber Optics II: Applications and Technology. 1970. p. 117–24.

226. Uchida T, Furukawa M, Kitano I, Koizumi K, Matsumura H. Optical characteristics of a light-focusing fiber guide and its applications. IEEE J Quantum Electron. 1970 Oct;6(10):606–12.

227. Kita H, Kitano I, Uchida T, Furukawa M. Light-Focusing Glass Fibers and Rods. J Am Ceram Soc. 1971 Jul 1;54(7):321–6.

228. McNeillie FC, Thomson J, Ruddock IS. The imaging properties of gradient index optical fibres. Eur J Phys. 2004 Jul;25(4):479–87.

229. Li X, Yu W. Deep tissue microscopic imaging of the kidney with a gradient-index lens system. Opt Commun. 2008;281(7):1833–40.

230. Saunter CD, Semprini S, Buckley C, Mullins J, Girkin JM. Micro-endoscope for in vivo widefield high spatial resolution fluorescent imaging. Biomed Opt Express. 2012 Jun 1;3(6):1274–8.

231. Edelstein A, Amodaj N, Hoover K, Vale R, Stuurman N. Computer Control of Microscopes Using μManager. Current Protocols in Molecular Biology. 2010.

232. Ogilvie RW. Virtual Microscopy and Virtual Slides in Teaching, Diagnosis, and Research. CRC Press; 2005.

233. Megens RTA, Reitsma S, Schiffers PHM, Hilgers RHP, De Mey JGR, Slaaf DW, et al. Two-Photon Microscopy of Vital Murine Elastic and Muscular Arteries. J Vasc Res. 2007;44(2):87–98.

234. Toda N, Inoue S, Okunishi H, Okamura T. Intra- and extraluminally-applied acetylcholine on the vascular tone or the response to transmural stimulation in dog isolated mesenteric arteries. Naunyn Schmiedebergs Arch Pharmacol. 1990 Jan 1;341(1-2):30–6.

235. Toda N, Minami Y, Onoue H. Extraluminally applied acetylcholine and oxyhemoglobin on the release and action of EDRF. Eur J Pharmacol. 1988 Jun 22;151(1):123–6.

236. Tankó LB, Mikkelsen EO, Simonsen U. A new experimental approach in endothelium-dependent pharmacological investigations on isolated porcine coronary arteries mounted for impedance planimetry. Br J Pharmacol. 1999 Sep 1;128(1):165–73.

237. Tran NN, Spitzbarth E, Robert A, Giummelly P, Atkinson J, Capdeville-Atkinson C. Nitric oxide lowers the calcium sensitivity of tension in the rat tail artery. J Physiol. 1998;507(1):163–74.

238. Ridgway EB, Ashley CC. Calcium transients in single muscle fibers. Biochem Biophys Res Commun. 1967 Oct 16;29(2):229–34.

239. Berridge MJ. Inositol trisphosphate and calcium signalling. Nature. 1993 Jan 28;361(6410):315–25.

240. Grynkiewicz G, Poenie M, Tsien RY. A new generation of Ca^{2+} indicators with greatly improved fluorescence properties. J Biol Chem. 1985 Mar 25;260(6):3440–50.

241. Minta A, Kao JP, Tsien RY. Fluorescent indicators for cytosolic calcium based on rhodamine and fluorescein chromophores. J Biol Chem. 1989 May 15;264(14):8171–8.

242. Gee KR, Brown KA, Chen W-NU, Bishop-Stewart J, Gray D, Johnson I. Chemical and physiological characterization of fluo-4 Ca^{2+}-indicator dyes. Cell Calcium. 2000 Feb;27(2):97–106.

243. Berridge MJ. Calcium microdomains: Organization and function. Cell Calcium. 2006 Nov;40(5–6):405–12.

244. Lechleiter J, Girard S, Peralta E, Clapham D. Spiral calcium wave propagation and annihilation in Xenopus laevis oocytes. Science. 1991 Apr 5;252(5002):123–6.

245. Cheng H, Lederer WJ, Cannell MB. Calcium sparks: elementary events underlying excitation-contraction coupling in heart muscle. Science. 1993 Oct 29;262(5134):740–4.

246. Yao Y, Choi J, Parker I. Quantal puffs of intracellular Ca^{2+} evoked by inositol trisphosphate in Xenopus oocytes. J Physiol. 1995;482(3):533–53.

247. Bootman M, Niggli E, Berridge M, Lipp P. Imaging the hierarchical Ca^{2+} signalling system in HeLa cells. J Physiol. 1997;499(2):307–14.

248. Ellefsen KL, Settle B, Parker I, Smith IF. An algorithm for automated detection, localization and measurement of local calcium signals from camera-based imaging. Cell Calcium. 2014 Sep;56(3):147–56.

249. Schindelin J, Arganda-Carreras I, Frise E, Kaynig V, Longair M, Pietzsch T, et al. Fiji: an open-source platform for biological-image analysis. Nat Methods. 2012 Jul;9(7):676–82.

250. Van der Walt S, Colbert SC, Varoquaux G. The NumPy Array: A Structure for Efficient Numerical Computation. Comput Sci Eng. 2011 Mar;13(2):22–30.

251. Coelho LP, Shariff A, Murphy RF. Nuclear segmentation in microscope cell images: A hand-segmented dataset and comparison of algorithms. IEEE International Symposium on Biomedical Imaging: From Nano to Macro, 2009 ISBI '09. 2009. p. 518–21.

252. Ozden I, Lee HM, Sullivan MR, Wang SS-H. Identification and Clustering of Event Patterns From In Vivo Multiphoton Optical Recordings of Neuronal Ensembles. J Neurophysiol. 2008 Jul 1;100(1):495–503.

253. Niggli E, Shirokova N. A guide to sparkology: The taxonomy of elementary cellular Ca_{2+} signaling events. Cell Calcium. 2007 Oct;42(4–5):379–87.

254. Hill C, Rummery N, Hickey H, Sandow S. Heterogeneity In The Distribution Of Vascular Gap Junctions And Connexins: Implications For Function. Clin Exp Pharmacol Physiol. 2002 Jul 1;29(7):620–5.

255. Bagher P, Segal SS. Regulation of blood flow in the microcirculation: role of conducted vasodilation. Acta Physiol. 2011 Jul 1;202(3):271–84.

256. Cohen KD, Jackson WF. Membrane Hyperpolarization Is Not Required for Sustained Muscarinic Agonist-Induced Increases in Intracellular Ca^{2+} in Arteriolar Endothelial Cells. Microcirculation. 2005 Mar 1;12(2):169–82.

257. Dora KA, Xia J, Duling BR. Endothelial cell signaling during conducted vasomotor responses. Am J Physiol Heart Circ Physiol. 2003 Jul;285(1):H119–26.

258. Hüser J, Blatter LA. Elementary events of agonist-induced Ca^{2+} release in vascular endothelial cells. Am J Physiol - Cell Physiol. 1997 Nov 1;273(5):C1775–82.

259. Tran CHT, Taylor MS, Plane F, Nagaraja S, Tsoukias NM, Solodushko V, et al. Endothelial Ca^{2+} wavelets and the induction of myoendothelial feedback. Am J Physiol - Cell Physiol. 2012 Apr 15;302(8):C1226–42.

260. Qian X, Francis M, Solodushko V, Earley S, Taylor MS. Recruitment of Dynamic Endothelial Ca^{2+} Signals by the TRPA1 Channel Activator AITC in Rat Cerebral Arteries. Microcirc N Y N 1994. 2013 Feb;20(2):138–48.

261. Qian X, Francis M, Köhler R, Solodushko V, Lin M, Taylor MS. Positive Feedback Regulation of Agonist-Stimulated Endothelial Ca^{2+} Dynamics by

K_{Ca}3.1 Channels in Mouse Mesenteric Arteries. Arterioscler Thromb Vasc Biol. 2014 Jan 1;34(1):127–35.

262. Boittin F-X, Alonso F, Le Gal L, Allagnat F, Bény J-L, Haefliger J-A. Connexins and M3 Muscarinic Receptors Contribute to Heterogeneous Ca^{2+} Signaling in Mouse Aortic Endothelium. Cell Physiol Biochem. 2013;31(1):166–78.

263. McCarron JG, Chalmers S, MacMillan D, Olson ML. Agonist-evoked Ca^{2+} wave progression requires Ca^{2+} and IP_3. J Cell Physiol. 2010 Aug;224(2):334–44.

264. Yashiro Y, Duling BR. Integrated Ca^{2+} Signaling Between Smooth Muscle and Endothelium of Resistance Vessels. Circ Res. 2000 Nov 24;87(11):1048–54.

265. Sáez JC, Berthoud VM, Brañes MC, Martínez AD, Beyer EC. Plasma Membrane Channels Formed by Connexins: Their Regulation and Functions. Physiol Rev. 2003 Oct 1;83(4):1359–400.

266. Figueroa XF, Duling BR. Gap Junctions in the Control of Vascular Function. Antioxid Redox Signal. 2009 Feb;11(2):251–66.

267. Yeh H-I, Lupu F, Dupont E, Severs NJ. Upregulation of Connexin43 Gap Junctions Between Smooth Muscle Cells After Balloon Catheter Injury in the Rat Carotid Artery. Arterioscler Thromb Vasc Biol. 1997 Nov 1;17(11):3174–84.

268. Yeh H-I, Lai Y-J, Chang H-M, Ko Y-S, Severs NJ, Tsai C-H. Multiple Connexin Expression in Regenerating Arterial Endothelial Gap Junctions. Arterioscler Thromb Vasc Biol. 2000 Jul 1;20(7):1753–62.

269. Hong T, Hill CE. Restricted expression of the gap junctional protein connexin 43 in the arterial system of the rat. J Anat. 1998 May;192(Pt 4):583–93.

270. Duza T, Sarelius IH. Localized transient increases in endothelial cell Ca^{2+} in arterioles in situ: implications for coordination of vascular function. Am J Physiol - Heart Circ Physiol. 2004 Jun 1;286(6):H2322–31.

271. Behringer EJ, Socha MJ, Polo-Parada L, Segal SS. Electrical conduction along endothelial cell tubes from mouse feed arteries: confounding actions of glycyrrhetinic acid derivatives. Br J Pharmacol. 2012;166(2):774–87.

272. Connors BW. Tales of a Dirty Drug: Carbenoxolone, Gap Junctions, and Seizures. Epilepsy Curr. 2012;12(2):66–8.

273. Krüger O, Bény J-L, Chabaud F, Traub O, Theis M, Brix K, et al. Altered dye diffusion and upregulation of connexin37 in mouse aortic endothelium deficient in connexin40. J Vasc Res. 2002 Apr;39(2):160–72.

274. Jing D, Lu XL, Luo E, Sajda P, Leong PL, Guo XE. Spatiotemporal properties of intracellular calcium signaling in osteocytic and osteoblastic cell networks under fluid flow. Bone. 2013 Apr;53(2):531–40.

275. Lüscher TF, Raij L, Vanhoutte PM. Endothelium-dependent vascular responses in normotensive and hypertensive Dahl rats. Hypertension. 1987 Feb;9(2):157–63.

276. Deng Q, Huo Y, Luo J. Endothelial mechanosensors: the gatekeepers of vascular homeostasis and adaptation under mechanical stress. Sci China Life Sci. 2014 Aug 1;57(8):755–62.

277. Loukin S, Zhou X, Su Z, Saimi Y, Kung C. Wild-type and brachyolmia-causing mutant TRPV4 channels respond directly to stretch force. J Biol Chem. 2010 Aug 27;285(35):27176–81.

278. Alessandri-Haber N, Yeh JJ, Boyd AE, Parada CA, Chen X, Reichling DB, et al. Hypotonicity induces TRPV4-mediated nociception in rat. Neuron. 2003 Jul 31;39(3):497–511.

279. Vriens J, Owsianik G, Fisslthaler B, Suzuki M, Janssens A, Voets T, et al. Modulation of the Ca^{2+} permeable cation channel TRPV4 by cytochrome P450 epoxygenases in vascular endothelium. Circ Res. 2005 Oct 28;97(9):908–15.

280. Jian M-Y, King JA, Al-Mehdi A-B, Liedtke W, Townsley MI. High vascular pressure-induced lung injury requires P450 epoxygenase-dependent activation of TRPV4. Am J Respir Cell Mol Biol. 2008 Apr;38(4):386–92.

281. Yin J, Kuebler WM. Mechanotransduction by TRP channels: general concepts and specific role in the vasculature. Cell Biochem Biophys. 2010;56(1):1–18.

282. Ingber DE. Cellular mechanotransduction: putting all the pieces together again. FASEB J. 2006 May 1;20(7):811–27.

283. Ryan SM, Waack BJ, Weno BL, Heistad DD. Increases in pulse pressure impair acetylcholine-induced vascular relaxation. Am J Physiol. 1995 Jan;268(1 Pt 2):H359–63.

284. Sukumaran SV, Singh TU, Parida S, Narasimha Reddy CE, Thangamalai R, Kandasamy K, et al. TRPV4 channel activation leads to endothelium-dependent relaxation mediated by nitric oxide and endothelium-derived hyperpolarizing factor in rat pulmonary artery. Pharmacol Res. 2013 Dec;78:18–27.

285. Zhang DX, Mendoza SA, Bubolz AH, Mizuno A, Ge Z-D, Li R, et al. Transient Receptor Potential Vanilloid Type 4–Deficient Mice Exhibit Impaired Endothelium-Dependent Relaxation Induced by Acetylcholine In Vitro and In Vivo. Hypertension. 2009 Mar 1;53(3):532–8.

286. Sun XP, Callamaras N, Marchant JS, Parker I. A continuum of $InsP_3$-mediated elementary Ca^{2+} signalling events in Xenopus oocytes. J Physiol. 1998 May 15;509 (Pt 1):67–80.

287. Bourguignon LY, Iida N, Sobrin L, Bourguignon GJ. Identification of an IP_3 receptor in endothelial cells. J Cell Physiol. 1994 Apr;159(1):29–34.

288. Hill-Eubanks DC, Gonzales AL, Sonkusare SK, Nelson MT. Vascular TRP Channels: Performing Under Pressure and Going with the Flow. Physiology. 2014 Sep 1;29(5):343–60.

289. Adapala RK, Talasila PK, Bratz IN, Zhang DX, Suzuki M, Meszaros JG, et al. PKC_α mediates acetylcholine-induced activation of TRPV4-dependent calcium influx in endothelial cells. Am J Physiol - Heart Circ Physiol. 2011 Sep 1;301(3):H757–65.

290. Earley S, Pauyo T, Drapp R, Tavares MJ, Liedtke W, Brayden JE. TRPV4-dependent dilation of peripheral resistance arteries influences arterial pressure. Am J Physiol Heart Circ Physiol. 2009 Sep;297(3):H1096–102.

291. Loot AE, Popp R, Fisslthaler B, Vriens J, Nilius B, Fleming I. Role of cytochrome P450-dependent transient receptor potential V4 activation in flow-induced vasodilatation. Cardiovasc Res. 2008 Dec 1;80(3):445–52.

292. Köhler R, Heyken W-T, Heinau P, Schubert R, Si H, Kacik M, et al. Evidence for a Functional Role of Endothelial Transient Receptor Potential V4 in Shear Stress–Induced Vasodilatation. Arterioscler Thromb Vasc Biol. 2006 Jul 1;26(7):1495–502.

293. Hartmannsgruber V, Heyken W-T, Kacik M, Kaistha A, Grgic I, Harteneck C, et al. Arterial Response to Shear Stress Critically Depends on Endothelial TRPV4 Expression. PLoS ONE. 2007 Sep 5;2(9):e827.

294. Rosales OR, Isales CM, Barrett PQ, Brophy C, Sumpio BE. Exposure of endothelial cells to cyclic strain induces elevations of cytosolic Ca^{2+} concentration through mobilization of intracellular and extracellular pools. Biochem J. 1997 Sep 1;326(Pt 2):385–92.

295. Tuttle JL, Falcone JC. Nitric oxide release during α1-adrenoceptor-mediated constriction of arterioles. Am J Physiol - Heart Circ Physiol. 2001 Aug 1;281(2):H873–81.

296. Knot HJ, Nelson MT. Regulation of arterial diameter and wall $[Ca^{2+}]_i$ in cerebral arteries of rat by membrane potential and intravascular pressure. J Physiol. 1998 Apr 1;508(1):199–209.

297. Gokina NI, Goecks T. Upregulation of endothelial cell Ca^{2+} signaling contributes to pregnancy-enhanced vasodilation of rat uteroplacental arteries. Am J Physiol - Heart Circ Physiol. 2006 May 1;290(5):H2124–35.

298. Ungvari Z, Csiszar A, Huang A, Kaminski PM, Wolin MS, Koller A. High Pressure Induces Superoxide Production in Isolated Arteries Via Protein Kinase C–Dependent Activation of NAD(P)H Oxidase. Circulation. 2003 Sep 9;108(10):1253–8.

299. Sun D, Huang A, Recchia FA, Cui Y, Messina EJ, Koller A, et al. Nitric oxide-mediated arteriolar dilation after endothelial deformation. Am J Physiol - Heart Circ Physiol. 2001 Feb 1;280(2):H714–21.

300. Pittner J, Wolgast M, Casellas D, Persson AEG. Increased shear stress–released NO and decreased endothelial calcium in rat isolated perfused juxtamedullary nephrons. Kidney Int. 2005 Jan;67(1):227–36.

301. Oliver JA, Chase HS. Changes in luminal flow rate modulate basal and bradykinin-stimulated cell $[Ca^{2+}]_i$ in aortic endothelium. J Cell Physiol. 1992 Apr 1;151(1):37–40.

302. Fleming I, Bauersachs J, Busse R. Calcium-dependent and calcium-independent activation of the endothelial NO synthase. J Vasc Res. 1997 Jun;34(3):165–74.

303. Ignarro LJ. Nitric oxide as a unique signaling molecule in the vascular system: a historical overview. J Physiol Pharmacol Off J Pol Physiol Soc. 2002 Dec;53(4 Pt 1):503–14.

304. Konishi M, Su C. Role of endothelium in dilator responses of spontaneously hypertensive rat arteries. Hypertension. 1983 Dec;5(6):881–6.

305. Lüscher TF, Vanhoutte PM. Endothelium-dependent contractions to acetylcholine in the aorta of the spontaneously hypertensive rat. Hypertension. 1986 Apr;8(4):344–8.

306. Küng CF, Lüscher TF. Different Mechanisms of Endothelial Dysfunction With Aging and Hypertension in Rat Aorta. Hypertension. 1995 Feb 1;25(2):194–200.

307. Zhou MS, Nishida Y, Chen QH, Kosaka H. Endothelium-derived contracting factor in carotid artery of hypertensive Dahl rats. Hypertension. 1999 Jul;34(1):39–43.

308. Taddei S, Virdis A, Mattei P, Salvetti A. Vasodilation to acetylcholine in primary and secondary forms of human hypertension. Hypertension. 1993 Jun 1;21(6 Pt 2):929–33.

309. Taddei S, Virdis A, Mattei P, Ghiadoni L, Gennari A, Fasolo CB, et al. Aging and endothelial function in normotensive subjects and patients with essential hypertension. Circulation. 1995 Apr 1;91(7):1981–7.

310. Perticone F, Sciacqua A, Maio R, Perticone M, Maas R, Boger RH, et al. Asymmetric dimethylarginine, L-arginine, and endothelial dysfunction in essential hypertension. J Am Coll Cardiol. 2005 Aug 2;46(3):518–23.

311. Carlson EC, Burrows ME, Johnson PC. Electron microscopic studies of cat mesenteric arterioles: A structure-function analysis. Microvasc Res. 1982 Sep;24(2):123–41.

312. Walmsley JG, Gore RW, Dacey Jr. RG, Damon DN, Duling BR. Quantitative morphology of arterioles from the hamster cheek pouch related to mechanical analysis. Microvasc Res. 1982 Nov;24(3):249–71.

313. Greensmith JE, Duling BR. Morphology of the constricted arteriolar wall: physiological implications. Am J Physiol - Heart Circ Physiol. 1984 Nov 1;247(5):H687–98.

314. Sleek GE, Duling BR. Coordination of mural elements and myofilaments during arteriolar constriction. Circ Res. 1986 Dec 1;59(6):620–7.

315. Song SH, Roach MR. A morphological comparison of aortic elastin from five species as seen with the scanning electron microscope. Acta Anat (Basel). 1985;123(1):45–50.

316. Kratky RG, Lo DK, Roach MR. Quantitative Measurement of Fixation Rate and Dimension Changes in the Aldehyde/Pressure-Fixed Canine Carotid Artery. J Vasc Res. 1991;28(5):386–95.

317. Lechleiter JD, Clapham DE. Molecular mechanisms of intracellular calcium excitability in X. laevis oocytes. Cell. 1992 Apr 17;69(2):283–94.

318. Callamaras N, Marchant JS, Sun XP, Parker I. Activation and co-ordination of $InsP_3$-mediated elementary Ca^{2+} events during global Ca^{2+} signals in Xenopus oocytes. J Physiol. 1998 May 15;509 (Pt 1):81–91.

319. Rizzuto R, Pinton P, Carrington W, Fay FS, Fogarty KE, Lifshitz LM, et al. Close contacts with the endoplasmic reticulum as determinants of mitochondrial Ca^{2+} responses. Science. 1998 Jun 12;280(5370):1763–6.

320. Mazel T, Raymond R, Raymond-Stintz M, Jett S, Wilson BS. Stochastic Modeling of Calcium in 3D Geometry. Biophys J. 2009 Apr 3;96(5):1691–706.

321. Olson ML, Sandison ME, Chalmers S, McCarron JG. Microdomains of muscarinic acetylcholine and Ins(1,4,5)P_3 receptors create "Ins(1,4,5)P_3 junctions" and sites of Ca^{2+} wave initiation in smooth muscle. J Cell Sci. 2012 Nov 15;125(Pt 22):5315–28.

322. Girerd XJ, Acar C, Mourad JJ, Boutouyrie P, Safar ME, Laurent S. Incompressibility of the human arterial wall: an in vitro ultrasound study. J Hypertens Suppl Off J Int Soc Hypertens. 1992 Aug;10(6):S111–4.

323. Means S, Smith AJ, Shepherd J, Shadid J, Fowler J, Wojcikiewicz RJH, et al. Reaction Diffusion Modeling of Calcium Dynamics with Realistic ER Geometry. Biophys J. 2006 Jul 15;91(2):537–57.

324. Hong D, Jaron D, Buerk DG, Barbee KA. Transport-dependent calcium signaling in spatially segregated cellular caveolar domains. Am J Physiol - Cell Physiol. 2008 Mar 1;294(3):C856–66.

325. Go AS, Mozaffarian D, Roger VL, Benjamin EJ, Berry JD, Blaha MJ, et al. Heart Disease and Stroke Statistics—2014 Update A Report From the American Heart Association. Circulation. 2014 Jan 21;129(3):e28–292.

326. World Health Organization. Global status report on noncommunicable diseases 2010. Geneva: WHO; 2011.

327. Virmani R, Avolio AP, Mergner WJ, Robinowitz M, Herderick EE, Cornhill JF, et al. Effect of aging on aortic morphology in populations with high and low prevalence of hypertension and atherosclerosis. Comparison between occidental and Chinese communities. Am J Pathol. 1991 Nov;139(5):1119–29.

328. Nichols WW, O'Rourke MF, Vlachopoulos C. McDonald's Blood Flow in Arteries: Theoreticla, Experimental and Clinical Principles. Sixth. Boca Raton: CRC Press; 2011. 771 p.

329. Kalaria RN. Cerebral vessels in ageing and Alzheimer's disease. Pharmacol Ther. 1996;72(3):193–214.

330. Bramwell JC, Hill AV. The Velocity of the Pulse Wave in Man. Proc R Soc Lond Ser B Contain Pap Biol Character. 1922 Apr 1;93(652):298–306.

331. Vlachopoulos C, Aznaouridis K, Stefanadis C. Prediction of Cardiovascular Events and All-Cause Mortality With Arterial Stiffness: A Systematic Review and Meta-Analysis. J Am Coll Cardiol. 2010 Mar 30;55(13):1318–27.

332. Safar ME, Henry O, Meaume S. Aortic pulse wave velocity: an independent marker of cardiovascular risk. Am J Geriatr Cardiol. 2002 Oct;11(5):295–8.

333. Collaboration TRV for AS. Determinants of pulse wave velocity in healthy people and in the presence of cardiovascular risk factors: "establishing normal and reference values." Eur Heart J. 2010 Oct 1;31(19):2338–50.

334. Asai K, Kudej RK, Shen Y-T, Yang G-P, Takagi G, Kudej AB, et al. Peripheral Vascular Endothelial Dysfunction and Apoptosis in Old Monkeys. Arterioscler Thromb Vasc Biol. 2000 Jun 1;20(6):1493–9.

335. Naseem KM. The role of nitric oxide in cardiovascular diseases. Mol Aspects Med. 2005 Apr;26(1-2):33–65.

336. Matz RL, Sotomayor MA de, Schott C, Andriantsitohaina R. Preservation of vascular contraction during ageing: dual effect on calcium handling and sensitization. Br J Pharmacol. 2003 Mar;138(5):745–50.

337. Shipley RD, Muller-Delp JM. Aging decreases vasoconstrictor responses of coronary resistance arterioles through endothelium-dependent mechanisms. Cardiovasc Res. 2005 May 1;66(2):374–83.

338. Ishihata A, Ogaki T, Aita T, Katano Y. Role of prostaglandins in urotensin II-induced vasodilatation in the coronary arteries of aged rats. Eur J Pharmacol. 2005 Oct 31;523(1-3):119–26.

339. Ibarra M, López-Guerrero JJ, Mejía-Zepeda R, Villalobos-Molina R. Endothelium-Dependent Inhibition of the Contractile Response Is Decreased in Aorta from Aged and Spontaneously Hypertensive Rats. Arch Med Res. 2006 Apr;37(3):334–41.

340. Chou T-C, Yen M-H, Li C-Y, Ding Y-A. Alterations of Nitric Oxide Synthase Expression With Aging and Hypertension in Rats. Hypertension. 1998 Feb 1;31(2):643–8.

341. Perrier E, Fournet-Bourguignon M-P, Royere E, Molez S, Reure H, Lesage L, et al. Effect of uncoupling endothelial nitric oxide synthase on calcium homeostasis in aged porcine endothelial cells. Cardiovasc Res. 2009 Apr 1;82(1):133–42.

342. Yang Y-M, Huang A, Kaley G, Sun D. eNOS uncoupling and endothelial dysfunction in aged vessels. Am J Physiol - Heart Circ Physiol. 2009 Nov 1;297(5):H1829–36.

343. Puca AA, Carrizzo A, Ferrario A, Villa F, Vecchione C. Endothelial nitric oxide synthase, vascular integrity and human exceptional longevity. Immun Ageing. 2012 Nov 15;9(1):26.

344. Prendergast C, Quayle J, Burdyga T, Wray S. Atherosclerosis differentially affects calcium signalling in endothelial cells from aortic arch and thoracic aorta in Apolipoprotein E knockout mice. Physiol Rep. 2014 Oct 1;2(10):e12171.

345. Calderone V, Martinotti E, Scatizzi R, Pellegrini A, Breschi MC. A modified aortic multiple-ring preparation for functional studies. J Pharmacol Toxicol Methods. 1996 Jun;35(3):131–8.

346. Zonta F, Barbieri A, Reguzzoni M, Calligaro A. Quantitative changes in pharmacodynamic parameters of noradrenaline in different rat aorta preparation: influence of endogenous EDRF. J Auton Pharmacol. 1998 Jun 1;18(3):129–38.

347. Buus NH, VanBavel E, Mulvany MJ. Differences in sensitivity of rat mesenteric small arteries to agonists when studied as ring preparations or as cannulated preparations. Br J Pharmacol. 1994 Jun;112(2):579–87.

348. Schubert R, Wesselman JP, Nilsson H, Mulvany MJ. Noradrenaline-induced depolarization is smaller in isobaric compared to isometric preparations of rat mesenteric small arteries. Pflüg Arch Eur J Physiol. 1996 Mar;431(5):794–6.

349. Tankó LB, Simonsen U, Frøbert O, Gregersen H, Bagger JP, Mikkelsen EO. Vascular reactivity to nifedipine and Ca^{2+} in vitro: the role of preactivation, wall tension and geometry. Eur J Pharmacol. 2000 Jan 17;387(3):303–12.

350. Altschul R. Endothelium. Its development, morphology, function, and pathology. New York: The Macmillan Company; 1954.

351. Barton M. Aging and endothelin: Determinants of disease. Life Sci. In Press, Corrected Proof.

352. Tang EHC, Vanhoutte PM. Gene expression changes of prostanoid synthases in endothelial cells and prostanoid receptors in vascular smooth muscle cells caused by aging and hypertension. Physiol Genomics. 2008 Feb 1;32(3):409–18.

353. Puzianowska-Kuznicka M, Kuznicki J. The ER and ageing II: Calcium homeostasis. Ageing Res Rev. 2009 Jul;8(3):160–72.

354. Newton CL, Mignery GA, Südhof TC. Co-expression in vertebrate tissues and cell lines of multiple inositol 1,4,5-trisphosphate ($InsP_3$) receptors with distinct affinities for $InsP_3$. J Biol Chem. 1994 Nov 18;269(46):28613–9.

355. Miyakawa T, Maeda A, Yamazawa T, Hirose K, Kurosaki T, Iino M. Encoding of Ca^{2+} signals by differential expression of IP_3 receptor subtypes. EMBO J. 1999 Mar 1;18(5):1303–8.

356. Grayson TH, Haddock RE, Murray TP, Wojcikiewicz RJH, Hill CE. Inositol 1,4,5-trisphosphate receptor subtypes are differentially distributed between smooth muscle and endothelial layers of rat arteries. Cell Calcium. 2004 Dec;36(6):447–58.

357. Isakson BE. Localized expression of an $Ins(1,4,5)P_3$ receptor at the myoendothelial junction selectively regulates heterocellular Ca^{2+} communication. J Cell Sci. 2008 Nov 1;121(21):3664–73.

358. Georgeon-Chartier C, Menguy C, Prévot A, Morel J-L. Effect of aging on calcium signaling in C57Bl6J mouse cerebral arteries. Pflüg Arch - Eur J Physiol. 2013 Jun 1;465(6):829–38.

359. Morel JL, Fritz N, Lavie JL, Mironneau J. Crucial role of type 2 inositol 1,4,5-trisphosphate receptors for acetylcholine-induced Ca^{2+} oscillations in vascular myocytes. Arterioscler Thromb Vasc Biol. 2003 Sep 1;23(9):1567–75.

360. Gros R, Wert RV, You X, Thorin E, Husain M. Effects of age, gender, and blood pressure on myogenic responses of mesenteric arteries from C57BL/6 mice. Am J Physiol - Heart Circ Physiol. 2002 Jan 1;282(1):H380–8.

361. Matz RL, Schott C, Stoclet JC, Andriantsitohaina R. Age-related endothelial dysfunction with respect to nitric oxide, endothelium-derived hyperpolarizing factor and cyclooxygenase products. Physiol Res Acad Sci Bohemoslov. 2000;49(1):11–8.

362. Behringer EJ, Shaw RL, Westcott EB, Socha MJ, Segal SS. Aging Impairs Electrical Conduction Along Endothelium of Resistance Arteries Through Enhanced Ca^{2+}-Activated K^{+} Channel Activation. Arterioscler Thromb Vasc Biol. 2013 Aug 1;33(8):1892–901.

363. Goyal R, Angermann JE, Ostrovskaya O, Buchholz JN, Smith GD, Wilson SM. Enhanced capacitative calcium entry and sarcoplasmic-reticulum calcium storage capacity with advanced age in murine mesenteric arterial smooth muscle cells. Exp Gerontol. 2009 Mar;44(3):201–7.

364. Maloney JA, Wheeler-Clark ES. Reduction in sarcoplasmic reticulum Ca^{2+}-ATPase activity contributes to age-related changes in the calcium content and relaxation rate of rabbit aortic smooth muscle. J Hypertens. 1996 Jan;14(1):65–74.

365. Wray S, Burdyga T. Sarcoplasmic Reticulum Function in Smooth Muscle. Physiol Rev. 2010 Jan 1;90(1):113–78.

366. Decuypere JP, Monaco G, Missiaen L, De Smedt H, Parys JB, Bultynck G. IP_3 Receptors, Mitochondria, and Ca^{2+}. J Aging Res. 2011 Mar 8;2011:e920178.

367. Fornieri C, Quaglino D, Mori G. Role of the extracellular matrix in age-related modifications of the rat aorta. Ultrastructural, morphometric, and enzymatic evaluations. Arterioscler Thromb Vasc Biol. 1992 Sep 1;12(9):1008–16.

368. Keep RF, Jones HC. Cortical microvessels during brain development: A morphometric study in the rat. Microvasc Res. 1990 Nov;40(3):412–26.

369. Erusalimsky JD. Vascular endothelial senescence: from mechanisms to pathophysiology. J Appl Physiol. 2009 Jan 1;106(1):326–32.

370. Burrig KF. The endothelium of advanced arteriosclerotic plaques in humans. Arterioscler Thromb Vasc Biol. 1991 Nov 1;11(6):1678–89.

371. Cox RH. Effects of age on the mechanical properties of rat carotid artery. Am J Physiol - Heart Circ Physiol. 1977 Aug 1;233(2):H256–63.

372. Roach MR, Burton AC. The Reason for the Shape of the Distensibility Curves of Arteries. Can J Biochem Physiol. 1957 Aug 1;35(8):681–90.

373. Simon G, Danneman KJ. Dilation and reduced distensibility of rat carotid artery with aging. Clin Exp Hypertens N Y N 1993. 2005 Aug;27(6):459–66.

374. Fouda A-K, Atkinson J. Sensitivity to noradrenaline and electrical stimulation decreases with age in the rat tail artery. Naunyn Schmiedebergs Arch Pharmacol. 1986 Sep 1;334(1):37–9.

375. Gill TJ, Smith GJ, Wissler RW, Kunz HW. The rat as an experimental animal. Science. 1989 Jul 21;245(4915):269–76.

376. Lartaud I, Bray-des-Boscs L, Chillon JM, Atkinson J, Capdeville-Atkinson C. In vivo cerebrovascular reactivity in Wistar and Fischer 344 rat strains during aging. Am J Physiol - Heart Circ Physiol. 1993 Mar 1;264(3):H851–8.

377. Lartaud I, Makki T, Bray-des-Boscs L, Niederhoffer N, Atkinson J, Corman B, et al. Effect of chronic ANG I-converting enzyme inhibition on aging processes. IV. Cerebral blood flow regulation. Am J Physiol - Regul Integr Comp Physiol. 1994 Sep 1;267(3):R687–94.

378. Arribas SM, Vila E, McGrath JC. Impairment of Vasodilator Function in Basilar Arteries From Aged Rats. Stroke. 1997 Sep 1;28(9):1812–20.

379. Kojima H, Sakurai K, Kikuchi K, Kawahara S, Kirino Y, Nagoshi H, et al. Development of a fluorescent indicator for nitric oxide based on the fluorescein chromophore. Chem Pharm Bull (Tokyo). 1998 Feb;46(2):373–5.

380. Krupenkin T, Yang S, Mach P. Tunable liquid microlens. Appl Phys Lett. 2003 Jan 20;82(3):316–8.

381. Bortolozzi M, Lelli A, Mammano F. Calcium microdomains at presynaptic active zones of vertebrate hair cells unmasked by stochastic deconvolution. Cell Calcium. 2008 Aug;44(2):158–68.

382. Tu H, Wang Z, Nosyreva E, De Smedt H, Bezprozvanny I. Functional Characterization of Mammalian Inositol 1,4,5-Trisphosphate Receptor Isoforms. Biophys J. 2005 Jan 2;88(2):1046–55.

Appendices

A1 Supplementary Videos

Supplemetary videos are included in the enclosed CD.

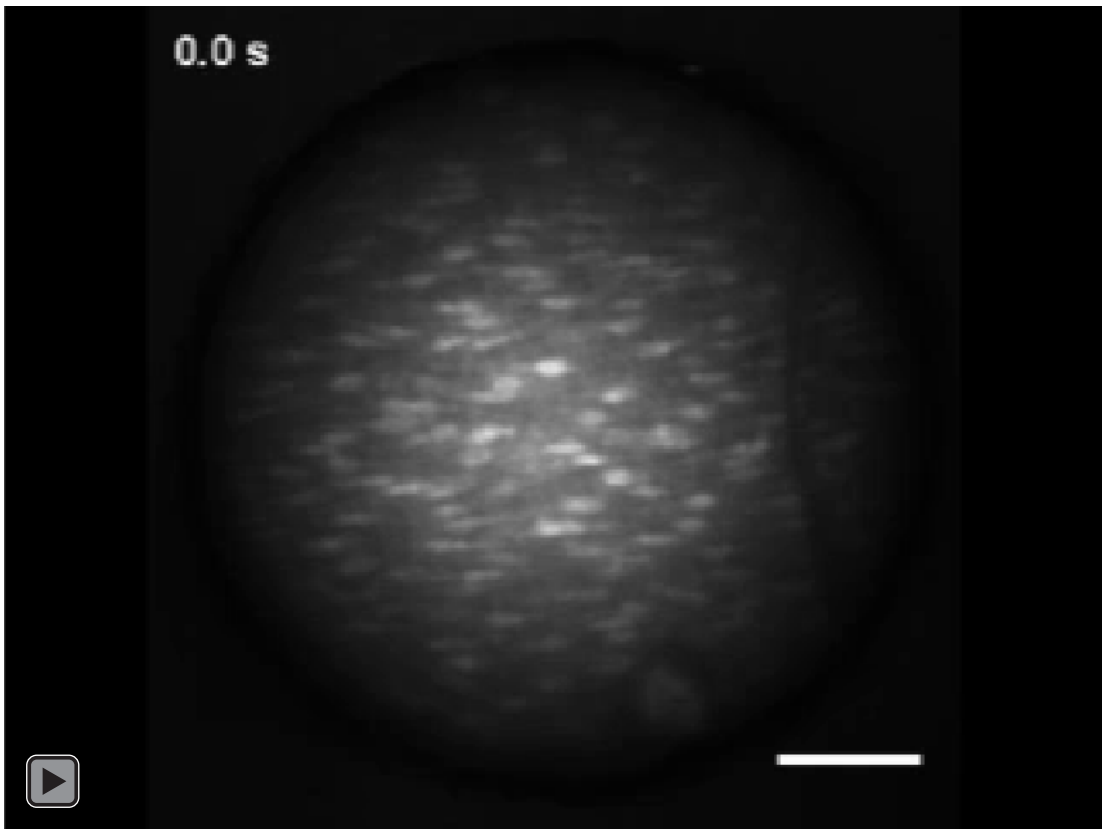

Supplementary Video 1 – ACh evoked Ca^{2+} signals in pressurised rat carotid artery endothelial cells. Activation of IP_3-mediated Ca^{2+} signals, by bath application of 100 μM ACh, in the endothelium of a rat carotid artery pressurized to 60 mmHg causes a rise in cytoplasmic Ca^{2+} concentration in the majority of cells across the field of view. Movie is composed of raw data to which a 5-frame rolling average has been applied, and has been contrast adjusted for visualisation. Data was acquired at 5 Hz and the scale bar corresponds to 100 μm.

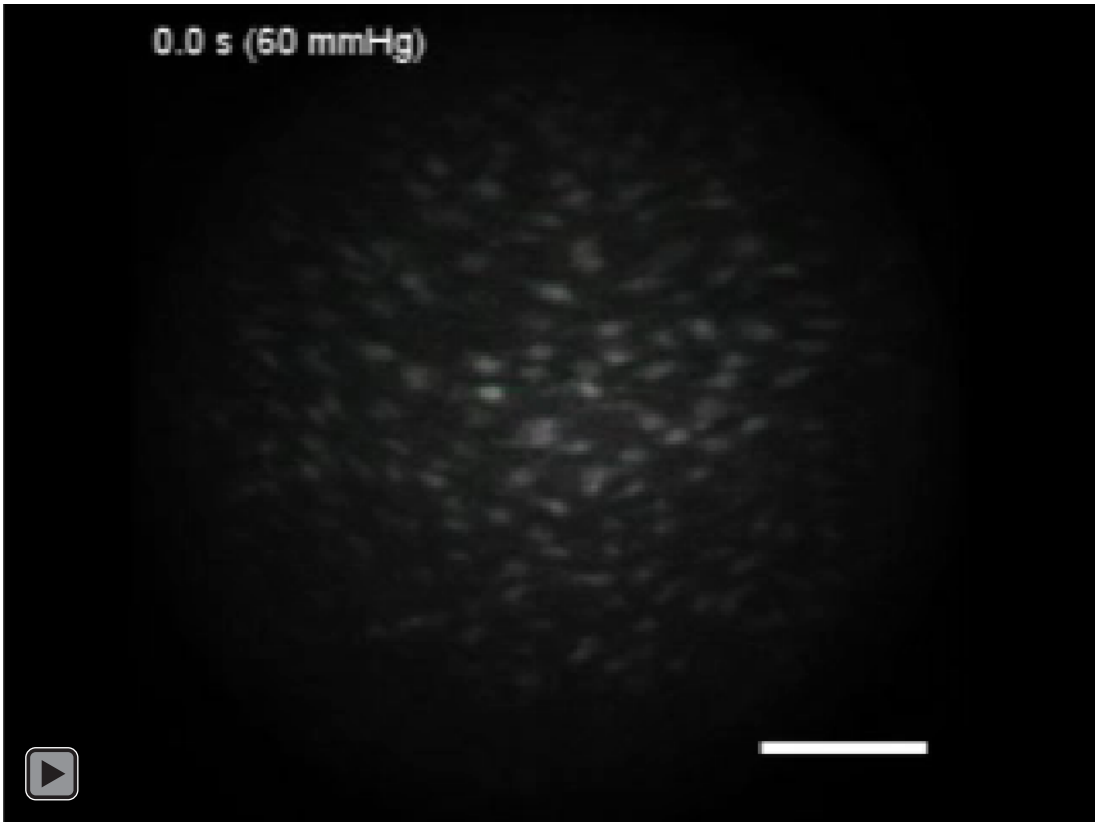

Supplementary Video 2 – Complexity of ACh-evoked endothelial Ca^{2+} signals in rat carotid artery endothelial cells (1). As ACh-evoked Ca^{2+} waves expand and collide between adjacent cells, complex spatiotemporal patterns of Ca^{2+} signaling developed. The movie is composed of a time series' of Ca^{2+} activity (green; 5-frame rolling average of raw data) overlaid on standard deviation images (STD) (grayscale; Panel E in Figure 3.1). Note that STD images only show cells that exhibit Ca^{2+} activity. Data was acquired at 5 Hz and the scale bar corresponds to 100 μm.

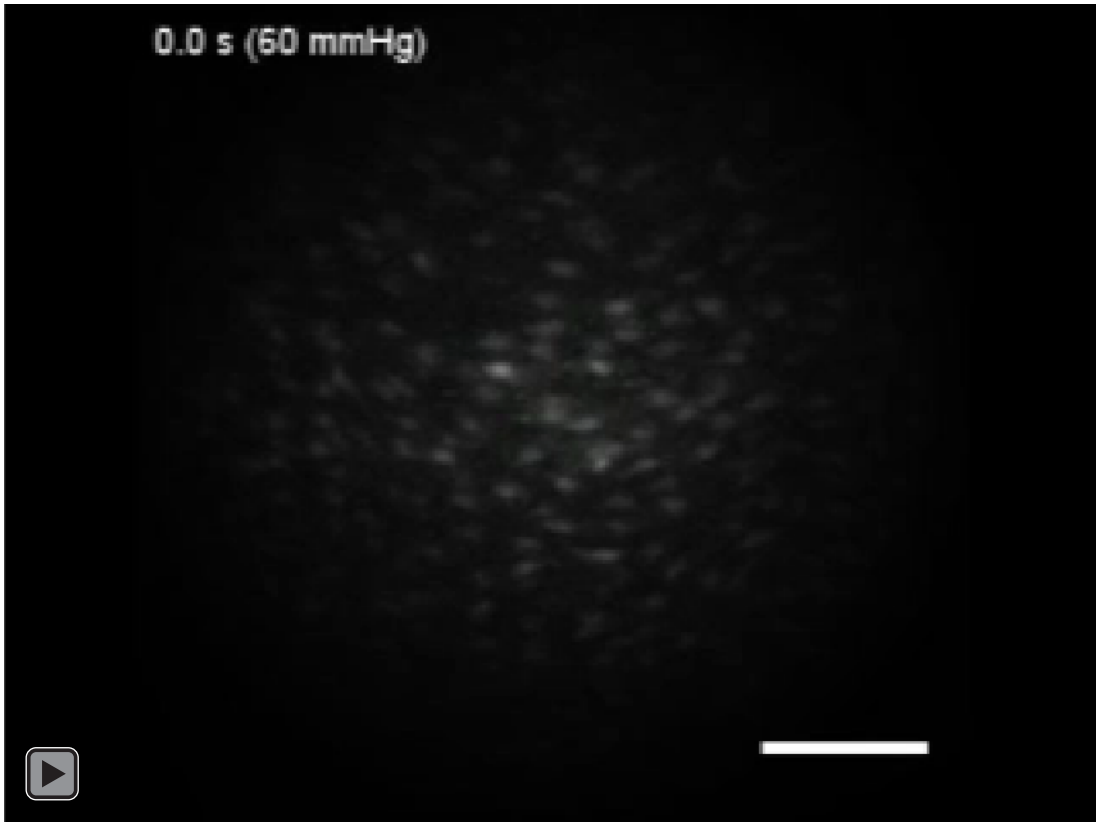

Supplementary Video 3 – Complexity of ACh-evoked endothelial Ca^{2+} signals in rat carotid artery endothelial cells (2). As ACh-evoked Ca^{2+} waves expand and collide between adjacent cells, complex spatiotemporal patterns of Ca^{2+} signaling develop. The movie is composed of a sequential subtraction of Ca^{2+} wave activity (green; green; Panel D in Figure 3.1), thus illustrating active Ca^{2+} wavefronts, overlaid on standard deviation images (STD) (grayscale; Panel E in Figure 3.1). Note that STD images only show cells that exhibit Ca^{2+} activity. Data was acquired at 5 Hz and the scale bar corresponds to 100 μm.

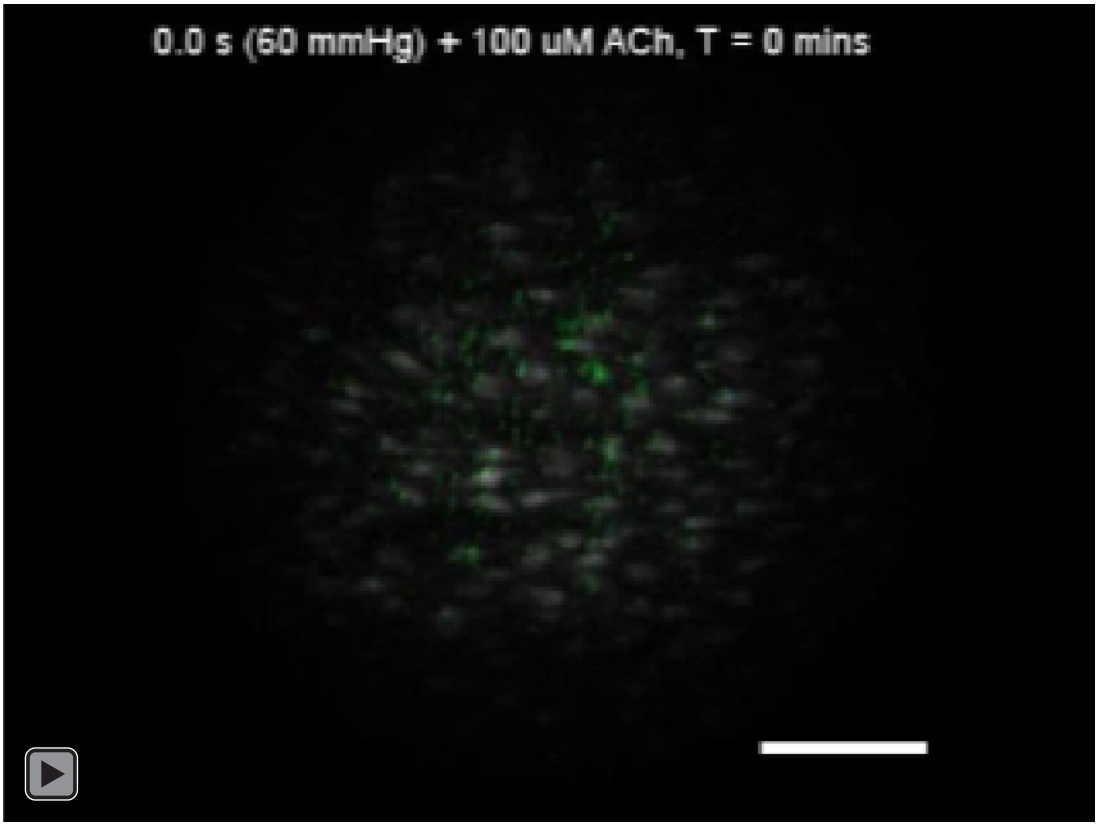

Supplementary Video 4 – Repeated activation of endothelial Ca^{2+} signalling. Repeated activation by bath application of 100 μM ACh produces reproducible patterns of Ca^{2+} activity. After each application of ACh, the bath solution was washed out with more than 20X the bath volume, and allowed to re-equilibrate for 20 minutes. The video corresponds to Ca^{2+} traces and time-series panels shown in Figure 4.2. The movie is composed of a time series of Ca^{2+} activity (green; Panel D in Figure 3.1) overlaid on standard deviation images (STDev) (grayscale; Panel E in Figure 3.1). Note that STDev images only show cells that exhibit Ca^{2+} activity. Data was acquired at 5 Hz and the scale bar corresponds to 100 μm.

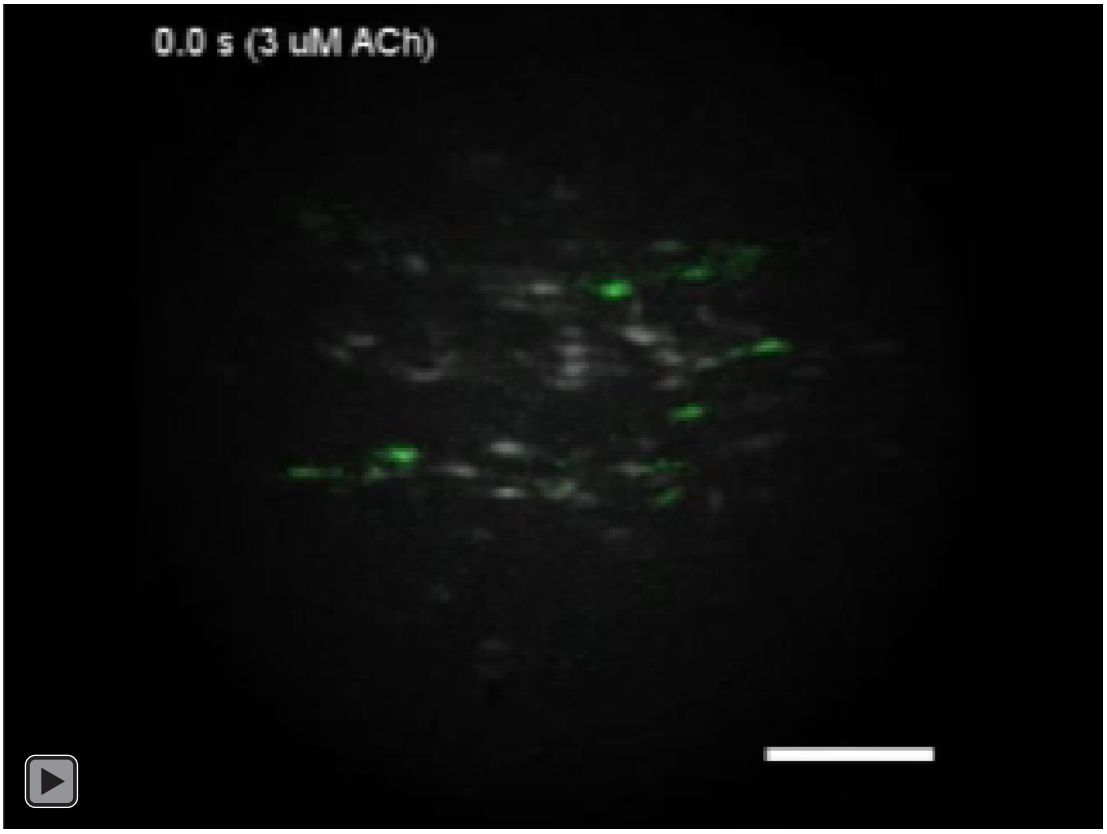

Supplementary Video 5 – Concentration-dependence of ACh-evoked endothelial Ca^{2+}signalling. As the concentration of ACh is increased (from 1 μM to 1 mM) in sequential activation of the same artery the number of cells activated and the magnitude of the Ca^{2+} response in each cell increases. After each ACh application, the bath solution was washed out with more than 20X the bath volume, and allowed to re-equilibrate for 20 minutes. The video corresponds to Ca^{2+} traces and time-series panels shown in **Figure 4.12** and **Figure 4.14**, respectively. The movie is composed of a time series' of Ca^{2+} wave activity (green; Panel D in **Figure 3.1**) overlaid on standard deviation images (STD) (grayscale; Panel E in **Figure 3.1**). Note that STD images only show cells that exhibit Ca^{2+} activity. Data was acquired at 5 Hz and the scale bar corresponds to 100 μm.

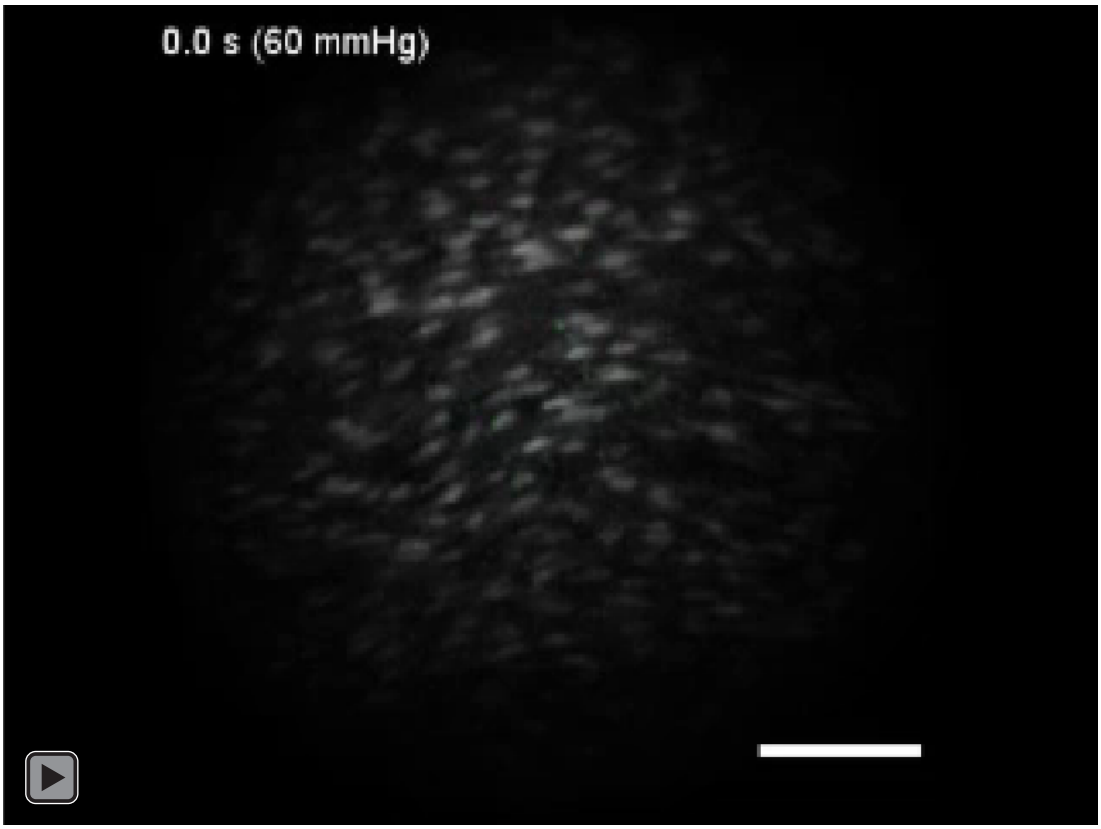

Supplementary Video 6 – Pressure-dependence of ACh-evoked endothelial Ca^{2+} signalling. IP_3-evoked Ca^{2+} signals (evoked by bath application of 100 μM ACh) are significantly attenuated as the artery transmural pressure is increased from 60 mmHg to 110 mmHg to 160 mmHg). That the initial burst of Ca^{2+} activity appears to occur faster at high pressure is an artifact caused by fewer cells in the field of view, due to distension of the artery and circumferential stretch of the endothelial cells. After each application of ACh, bath solution was washed out with more than 20X the bath volume, and allowed to re-equilibrate for 20 minutes. The movie corresponds to the time-series panels and Ca^{2+} traces illustrated in Figure 5.1 and Figure 5.2, respectively. The movie is composed of time series' of Ca^{2+} wave activity (green; Panel D in Figure 3.1) overlaid on standard deviation images (STD) (grayscale; Panel E in Figure 3.1). Note that STD images only show cells that exhibit Ca^{2+} activity. Data was acquired at 5 Hz and the scale bar corresponds to 100 μm.

A2 Python Scripts

Data.py – Stores file information, calls other scripts.

```
rom __future__ import division
import sys
import os

# FOR COMMENTS

PATH = '../' # dot dot slash means
parent folder
dataPath =  os.path.join(PATH,
'csvData')

nFramesToDifferntiateOver = 5

datasets = {}

#           key            image cube
regions                baseline
activity(for plot)   pressures

######## Aging Pressure Data
##################
datasets['0819_0101_03_1'] =
'20140819_01_01_03_1.tif',
'20140819_01_01_03_1.txt', (50, 100),
(100, 350),   60 #60
datasets['0819_0101_04_1'] =
'20140819_01_01_04_1.tif',
'20140819_01_01_04_1.txt', (50, 100),
(100, 350),   110 #110 repeat
datasets['0819_0101_05_1'] =
'20140819_01_01_05_1.tif',
'20140819_01_01_05_1.txt', (50, 100),
(100, 350),   160 #160
######## END OF Aging Pressure Data
##################

supersets = {}

############## Aging Pressure Data
####################
supersets['0819_01_Up'] =
'0819_0101_03_1', '0819_0101_04_1',
'0819_0101_05_1'
######### END OF Agin Pressure Data
#################

def get(key, disp=0):
    tifName, txtName, baseline,
activity, pressure = datasets[key]
    params = {}
    params['tifName'] =
os.path.join(PATH, tifName)
    params['txtName'] =
os.path.join(PATH, txtName)
    params['baseline'] = baseline
    params['activity'] = activity
    params['nddt'] =
nFramesToDifferntiateOver
    params['gfxPath'] =
os.path.join(os.path.join(PATH, 'gfx'),
key)
    params['dataPath'] = dataPath
    params['pressure'] = pressure
    if disp:
        print 'Saving graphics to:',
params['gfxPath']
    try:
        os.mkdir(params['gfxPath'])
    except OSError:
        pass
    return params

if __name__ == '__main__':
    for key in datasets.keys():
        print '-----------------------'
        print 'PROCESSING: %s' % key
        print '-----------------------'
        os.system('python
process.py %s' % key)
```

Process.py – Called by data.py, processes data

```
from __future__ import division
import sys
import os
import scipy.stats
import numpy
import pylab
import utils
import data as data

def plotname(txt):
    return
os.path.join(params['gfxPath'],
txt)+('_%s.png' % key)

def save(fname):
    fname = plotname(fname)
    print 'Saving', fname
    pylab.savefig(fname)

def savedata(grid, fname):
    grid = numpy.array(grid)
    assert grid.ndim == 2
    fname =
os.path.join(params['dataPath'],
'%s_%s.csv' % (key, fname))
    numpy.savetxt(fname, grid,
fmt='%.8e', delimiter=',')
# -------------------------------------
# Load data
# -------------------------------------
key = sys.argv[1]
params = data.get(key, disp=1)
frames =
utils.readFramesFromTif(params['tifName'
])
polys =
utils.readPolygonsFromTxt(params['txtNam
e'])
if len(polys) == 0:
    print '0 polygons in file:',
params['txtName']

assert len(polys) > 0 # we must have
polygons!!!
nz, ny, nx = frames.shape

# -------------------------------------
# PLOT: Global activity plot
# -------------------------------------
pylab.figure(figsize=(8,5))
sigma = frames.sum(axis=(1,2))
pylab.plot(sigma)
pylab.xlabel('Frame no.')
pylab.ylabel('Total signal')
save('Total signal')

# -------------------------------------
# PLOT: Pretty picture of regions etc.
# -------------------------------------
pylab.figure(figsize=(10,10))
f0, f1 = params['activity']
std =
pylab.std(frames[f0:f1]/frames[f0:f1].su
m(axis=0)**.5, axis=0)
pylab.imshow(std,
interpolation='nearest', origin='lower')
pylab.colorbar()
[pylab.plot(pg.points[:,0],
pg.points[:,1], color='black', lw=2) for
pg in polys]
nz, ny, nx = frames.shape
pylab.xlim(0, nx)
pylab.ylim(0, ny)
pylab.title('Pixel variation and region
masks')
save('img_ROIs')

# -------------------------------------
# Extract the polygons from the images
# -------------------------------------
signals = []
for pg in polys:
    pg.scanConvert()
    x0, x1 = pg.x0, pg.x1
    y0, y1 = pg.y0, pg.y1
    bb = pg.bounding_box
    cube = frames[:,y0:y1, x0:x1] * bb
    sigma = cube.sum(axis=(1,2)) #  Sum
over the XY dimensions
    signals.append(sigma)

assert len(signals) > 0 # we must have
signals!
signals = numpy.array(signals)
print 'Extracted %i signals' %
len(signals)

savedata(signals, 'signals_raw')

# -------------------------------------
# Baseline normalise the signals
# -------------------------------------
signalsBaselined = []
b0, b1 = params['baseline']
for sig in signals:
    sig = sig /
numpy.average(sig[b0:b1])
    signalsBaselined.append(sig)
savedata(signalsBaselined,
'signals_baselined')

# -------------------------------------
# PLOT: Baseline raw signals
# -------------------------------------
pylab.figure(figsize=(8,5))
pylab.title('Raw signal for each
region')
pylab.xlabel('Frame no.')
pylab.ylabel('Signal - ADUs')
for sig in signals:
    pylab.plot(sig)
save('signal_raw')

# -------------------------------------
# PLOT: Area normalised signals
# -------------------------------------
pylab.figure(figsize=(8,5))
pylab.title('Area normalised signal for
each region')
pylab.xlabel('Frame no.')
pylab.ylabel('Signal - ADUs')
for sig, pg in zip(signals, polys):

pylab.plot(sig/pg.bounding_box.sum())
save('signal_norm_by_area')

# -------------------------------------
# PLOT: Baseline normalised signals
# -------------------------------------
pylab.figure(figsize=(8,5))
```

```
pylab.title('Baseline normalised signal
for each region')
pylab.xlabel('Frame no.')
pylab.ylabel('Signal - ADUs')
for sig in signalsBaselined:
    pylab.plot(sig)
save('signal_norm_by_baseline')

# And again

pylab.figure(figsize=(8,5))
pylab.title('Baseline normalised signal
for each region')
pylab.xlabel('Frame no.')
pylab.ylabel('Signal - ADUs')
for sig in signalsBaselined:
    pylab.plot(sig, color='grey',
alpha=.4)
pylab.plot(numpy.average(signalsBaseline
d, axis=0), color='red')
pylab.ylim(0.95, 1.3)
save('signal_norm_by_baseline_1')

# --------------------------------------
# Differentiate the data
# --------------------------------------
ddtBaselined = [utils.diff(sig,
params['nddt']) for sig in
signalsBaselined]
savedata(ddtBaselined, 'ddtBaselined')

# --------------------------------------
# ddt line plot
# --------------------------------------
pylab.figure(figsize=(8,5))
pylab.title('Baseline normalised d/dt
for each region')
pylab.xlabel('Frame no.')
pylab.ylabel('d/dt - ADUs/frame')
for ddt in ddtBaselined:
    pylab.plot(ddt)
save('ddt_baseline_plot')

# --------------------------------------
# ddt heat plot
# --------------------------------------
pylab.figure(figsize=(12,6))
pylab.title('Baseline normalised d/dt
for each region')
pylab.xlabel('Frame no.')
pylab.ylabel('ROI')
pylab.imshow(ddtBaselined,
interpolation='nearest')
save('ddt_baseline_image')
# --------------------------------------
# ddt maximum shifted
# --------------------------------------

pylab.figure()
pylab.title('Peaks aligned and
normalised')
for sig in ddtBaselined:
    idx = sig.argmax()
    f0 = max((idx-50, 0))
    f1 = min((idx+50, len(sig)-1))
    x = numpy.arange(f0, f1) - idx
    sig = sig[f0:f1]
    #sig = sig / sig.max()
    pylab.plot(x, sig, alpha=.05)
pylab.ylim(-0.03, 0.03)
save('ddt_baseline_aligned')

# --------------------------------------
# ddy vertical offset plot
# --------------------------------------

pylab.figure(figsize=(6,5))
x0, x1 = params['activity']
voffset = [sig.max() - sig.min() for sig
in ddtBaselined]
voffset = sorted(voffset)
if len(voffset) > 10:
    voffset = voffset[5:-5]
voffset = 0.1 * numpy.average(voffset)
for i, sig in enumerate(ddtBaselined):
    pylab.plot(-0.25 + sig + i *
voffset)
pylab.xlim(x0, x1)
save(('ddt_baseline_offset'))

# --------------------------------------
# Time of peak onset plot
# --------------------------------------
img = numpy.zeros((ny, nx), 'f')

for sig, pg in zip(ddtBaselined, polys):
    f0, f1 = params['activity']
    mx = sig[f0:f1].argmax()
    x0, x1 = pg.x0, pg.x1
    y0, y1 = pg.y0, pg.y1
    bb = pg.bounding_box
    img[y0:y1, x0:x1] *= 1 - bb # Mask
out this shape
    img[y0:y1, x0:x1] += mx * bb
img[numpy.where(img==0)] = numpy.nan
pylab.figure(figsize=(10,10))
pylab.title('Frame no of max uptake')
pylab.imshow(img,
interpolation='nearest')
[pylab.plot(pg.points[:,0],
pg.points[:,1], color='black', lw=2) for
pg in polys]
nz, ny, nx = frames.shape
pylab.xlim(0, nx)
pylab.ylim(0, ny)
pylab.colorbar()
save('img_peaktime')

argmaxs = []
maxs = []
for sig in ddtBaselined:
    argmx = sig[f0:f1].argmax()
    mx = sig[f0:f1].max()
    argmaxs.append(argmx)
    maxs.append(mx)
pylab.figure()
pylab.xlabel('Peak frame #')
pylab.ylabel('Peakt ddt')
pylab.scatter(argmaxs, maxs)
save('pvp')
```

utils.py – Imported by process.py, processes data

```
# -*- coding: cp1252 -*-
from __future__ import division

import os

import numpy
import Image

import scipy

# THIS FILE COPYRIGHT (C) THE UNIVERSITY
OF DURHAM 2014
# THIS FILE IS NOT FOR RE-DISTRUBUTION.
ALL RIGHTS RESERVED

# EDIT AT YOUR OWN RISK

def readFramesFromTif(fname):
    img = Image.open(fname)
    nFrames = 0
    while 1:
        nFrames += 1
        try:
            img.seek(nFrames)
        except:
            nFrames -= 1
            break
    print 'Loading %i frames from %s' %
(nFrames, os.path.split(fname)[-1])
    nz = nFrames
    nx, ny = img.size
    frames = numpy.zeros((nz, ny, nx),
dtype=numpy.uint16)
    for i in range(nFrames):
        if (i%20) == 0: print '.',
        img.seek(i)
        dat =
numpy.fromstring(img.tostring(),
dtype=numpy.uint16)
        dat.shape =(ny, nx)
        #dat = dat.byteswap()
        frames[i] = dat
    print '\n',
    return frames

def readPolygonsFromTxt(fname):
    fp = open(fname)
    dat = fp.readlines()
    fp.close()
    polygons = []
    i = 0
    while i < len(dat):
        row = dat[i]
        if row[:9] == '# Points:':
            nPoints =
int(row.strip().split()[2])
            coords =
dat[i+1:i+1+nPoints]
            coords =
[line.strip().split() for line in
coords]
            coords = [[float(c) for c in
line] for line in coords]
            coords = numpy.array(coords)
            polygons.append(coords)
            i += nPoints
        i += 1
    polys = [Polygon(poly) for poly in
polygons]
    return polys

class Polygon(object):
    def __init__(self, points):
        self.points =
numpy.array(points, dtype=numpy.uint16)
        assert len(self.points.shape) ==
2
        assert self.points.shape[1] == 2
        self.converted = False

    def scanConvert(self):
        if self.converted:
            return self.bounding_box

        # Create blank array
        points = self.points
        xmin, xmax = points[:,0].min(),
points[:,0].max()
        ymin, ymax = points[:,1].min(),
points[:,1].max()
        bb_shape = (int(ymax-ymin)+1,
int(xmax-xmin)+1)
        bounding_box =
numpy.zeros(bb_shape, numpy.uint8)

        # Store out position in the
parent array
        self.x0, self.y0 = xmin, ymin
        self.x1, self.y1 = xmax+1,
ymax+1
        self.float_coords =
float(self.x0), float(self.y0),
float(self.x1), float(self.y1)
        # Make a wrapped list of all
points and find all inflexion points
        # i.e. both neighbouring points
above or both below
        wr = points.tolist()
        wr = [wr[-1]] + wr + [wr[0]]
        inflex_points = []
        for i in range(1, len(wr)-1):
            y0, y1, y2 = wr[i-1][1],
wr[i][1], wr[i+1][1]
            if (y1 < y0 and y1 < y2) or
(y1 > y0 and y1 > y2):

inflex_points.append(wr[i])
        # Make a list of lines to render
        npoints = len(points)
        lines = numpy.zeros((npoints,
4),dtype=numpy.uint16)
        lines[:,:2] = points
        lines[:-1,2:] = points[1:]
        lines[-1,2:] = points[0]
        # 1. Render all lines into
polygon
        for (x0, y0, x1, y1) in lines:
            if y0 > y1:
                y0, y1 = y1, y0
                x0, x1 = x1, x0
            if y1 == y0:
                # Horizontal lines
bugger the method up totally as they
cause us to pogo in and out of being
                # in the polygon on
every pixel - omitting them works fine
as the linew either side of it must
                # begin and end on the
same horizontal row
                # pixel
```

```
                if x1 < x0:
                    x0, x1 = x1, x0
                bounding_box[y0-ymin,x0-
xmin:x1-xmin+1] = 2 # Special signal
that we're in an extended line
            else:
                x1, x0, y1, y0 =
float(x1), float(x0), float(y1),
float(y0)
                # Above conversions are
due to lines being uint16 numpy scalars
                grad = (x1-x0) / (y1-y0)
                y0, y1 = int(y0),
int(y1)
                for iy in range(y0,
y1+1):
                    ix = int(.5 + x0 +
grad * (iy-y0) )
                    bounding_box[iy-
ymin, ix-xmin] = 1
        for (x,y) in inflex_points:
            bounding_box[y-ymin,x-xmin]
= 2
        if 0:
            self.bounding_box =
bounding_box
            return bounding_box
        # Now scan across every row of
the image filling between pixels in the
lines
        # using an odd condition to cope
with concave shapes.
        for iy in range(bb_shape[0]):
            in_poly = False
            for ix in
range(bb_shape[1]):
                if in_poly == False and
bounding_box[iy,ix] == 1:
                    x0 = ix
                    in_poly = True
                elif in_poly == True and
bounding_box[iy,ix] == 1:

bounding_box[iy,x0:ix] = 2
                    in_poly = False#
        # Reset inflex points to 1
        bounding_box = (bounding_box >
0).astype(numpy.uint8)
        self.bounding_box = bounding_box
        self.converted = True
        return bounding_box

    def Area(self):
        if not self.converted:
            self.ScanConvert()
        area =
numpy.sum(self.bounding_box.astype(numar
ray.Int16))
        return area

    def CoM(self, overlay = False, img =
[]):
        if not self.converted:
            self.ScanConvert()
        image = self.bounding_box
        if overlay:
            image =
img[self.y0:self.y1,self.x0:self.x1] *
image
        # Calculate the centre of mass
of our shape
        centroid, bg = com(image, bg =
0)
        centroid += (self.x0, self.y0)
        return centroid

def diff(sig, n):
    x = numpy.arange(2*n+1)
    ddt = []
    for i in range(n, len(sig)-n):
        y = sig[i-n:i+n+1]
        grad, intercept, r_value,
p_value, std_err =
scipy.stats.linregress(x, y)
        ddt.append(grad)
    ddt = numpy.array(ddt)
    return ddt
```

index.py – Imported by process.py, processes data

```
from __future__ import division

import data as data

ssets = sorted(data.supersets.keys())

fp = open('../index.html', 'w')
fp.write('<html><body>')
fp.write('<table border=3>\n')
for key in ssets:
    N = len(data.supersets[key])
    # Data set name
    fp.write('<tr><td>\n')
    fp.write('<h1>%s</h1>\n' % key)
    fp.write('</td></tr>\n')
    # Summary graphic
    fp.write('<tr><td>\n')
    fp.write('<img
src="gfx/superset_%s_all_per_cell.png"
height="450">\n' % key)
    # Result
    fp.write('<img
src="gfx/superset_summary_%s.png"
height="450">\n' % key)
    fp.write('</td></tr>\n')
    # Line scans
    fp.write('<tr><td>\n')
    subkeys = data.supersets[key]
    subkeys = sorted(subkeys, key=lambda
sk:data.get(sk)['pressure'])
    for k1 in subkeys:
        fp.write('<img
src="gfx/%s/ddt_baseline_image_%s.png"
height=220>' % (k1, k1))
    fp.write('</td></tr>\n')

fp.write('</table>')

fp.write('</html></body>')
```

analyse.py – Batch analyses grouped data

```
# -*- coding: utf-8 -*
# <nbformat>3.0</nbformat>
# <codecell>

from __future__ import division
import numpy
import data as data
import os
import pylab
import sys

superset = sys.argv[1]
keys = data.supersets[superset]
MASTER_TITLE = superset

keys = sorted(keys, key=lambda
k:data.get(k)['pressure'])
pres = [data.get(k)['pressure'] for k in
keys]
pres = numpy.array(pres)
presdict = {k:p for (k,p) in zip(keys,
pres)}

## DO NOT EDIT:  LOAD DATA
def csvPath(key, what):
    return os.path.join(data.dataPath,
'%s_%s.csv' % (key, what))
signals_baselined = {key:
numpy.loadtxt(csvPath(key,
'signals_baselined'), delimiter=',') for
key in keys}
ddt_baselined = {key:
numpy.loadtxt(csvPath(key,
'ddtBaselined'), delimiter=',') for key
in keys}

# Colours by pressure
cdict = {}
cdict[60] = 'blue'
cdict[110] = 'green'
cdict[160] = 'red'

# Re-index by dataset key
cdict = {k:cdict[presdict[k]] for k in
keys}

def analyse_signal_set(signals, ddts,
hz, suptitle, savename=None):
    # Take a series of signals and plot
some stuff
    # Plot each dataset - normalised and
ddt.

    n = len(keys)
    fig = pylab.figure(figsize=(16, 8))
    # Create two rows of subplots with
linked y-axes
    plots = []
    for iy in range(2):
        oy = 1 + iy * (n+1); # y offset
        for i in range(1, n):
            print 2, n, oy+i
        axs =  [fig.add_subplot(2, n+1,
oy),]
        axs += [fig.add_subplot(2, n+1,
oy+i, sharey=axs[0]) for i in range(1,
n+1)]
        plots.append(axs)
    ix = 0
    pylab.suptitle('%s: %s' %
(MASTER_TITLE, suptitle), fontsize=18)
    # Find global minima and maxima
    mnact, mxact = [], []
    mnddt, mxddt = [], []
    # Plot the individual signals for
each cell
    for ik, key in enumerate(keys):
        n =
data.nFramesToDifferntiateOver
        plot = plots[0][ik]
        ident =  presdict[key]
        if type(ident) in (int, float):
            ident = 'pres=%immHg' %
ident
        plot.set_title('Signal, %s' %
ident)
        [plot.plot(numpy.arange(len(s)),
s, alpha=0.1, color=cdict[key]) for s in
signals[key]]
        plot = plots[1][ik]
        plot.set_title('Baseline normed
d/dt')
        [plot.plot(n +
numpy.arange(len(s)), s, alpha=0.1,
color=cdict[key]) for s in ddts[key]]

    # Now plot averages vs pressure

    for key in keys:
        plot = plots[0][-1]
        signal =
numpy.average(signals[key], axis=0)
        ident = presdict[key]
        if type(ident) in (int, float):
            ident = 'pres=%immHg' %
ident

        plot.plot(signal, label=ident,
color=cdict[key])
        plot = plots[1][-1]
        ddt = numpy.average(ddts[key],
axis=0)
        plot.plot(ddt, label=ident,
color=cdict[key])
    plots[0][-1].set_title('Signal
averaged over cells')
    plots[1][-1].set_title('d/dt
averaged over cells')
    pylab.legend()
    if not savename:
        return
    imgPath = os.path.join('../gfx',
savename+'.png')
    pylab.savefig(imgPath)
    for key in keys:
        csvPath =
os.path.join('../csvData/',
'%s_%s_signals.csv' % (savename, key))
        numpy.savetxt(csvPath,
numpy.transpose(signals[key]),
fmt='%.8f',  delimiter=',')
        csvPath =
os.path.join('../csvData/',
'%s_%s_ddts.csv' % (savename, key))
        numpy.savetxt(csvPath,
numpy.transpose(ddts[key]), fmt='%.8f',
delimiter=',')
```

```
# Totally unaligned

# analyse_signal_set(signals_baselined,
ddt_baselined, 5, 'Unaligned data')

# Align to global ddt
siga = {}
ddta = {}
centers = {}

for key in keys:
    params = data.get(key)
    i0, i1 = params['activity']
    ddts = ddt_baselined[key]
    avgddt = numpy.average(ddts, axis=0)
    idx = numpy.argmax(avgddt[i0:i1]) +
i0
    nFramesPad1 = 30 # ten seconds
    nFramesPad2 = 120 # ten seconds
    siga[key] =
signals_baselined[key][:, idx-
nFramesPad1:idx+nFramesPad2]
    ddta[key] = ddt_baselined[key][:,
idx-nFramesPad1:idx+nFramesPad2]
    centers[key] = idx

analyse_signal_set(siga, ddta, 5,
'Aligned globally per data set',
savename='superset_%s_aligned_per_datase
t' % MASTER_TITLE)

# ---------------------------------------
# Align per trace
siga = {}
ddta = {}
for key in keys:
    # Only search near the primary event
    params = data.get(key)
    i0, i1 = params['activity']
    idxGlobal =
numpy.argmax(avgddt[i0:i1]) + i0

     #idxGlobal = centers[key]
    search = 30
    keep1 = 30
    keep2 = 60
    i0, i1 = idxGlobal - search,
idxGlobal + search
    ddts = ddt_baselined[key]
    sigs = signals_baselined[key]
    siga[key] = []
    ddta[key] = []
    for i, ddt in enumerate(ddts):
        idx = i0 +
numpy.argmax(ddt[i0:i1])
        siga[key].append(sigs[i][idx-
keep1:idx+keep2])
        ddta[key].append(ddts[i][idx-
keep1:idx+keep2])

# analyse_signal_set(siga, ddta, 5,
'Algined per cell')

# Now re-normaise each signal
# Align per trace
siga = {}
ddta = {}
timeshifts = {}
for key in keys:
    # Only search near the primary event
    idxGlobal = centers[key]
    search = 30
    keep1 = 30
    keep2 = 60
    i0, i1 = idxGlobal - search,
idxGlobal + search
    ddts = ddt_baselined[key]
    sigs = signals_baselined[key]
    siga[key] = []
    ddta[key] = []
    timeshifts[key] = []
    for i, ddt in enumerate(ddts):
        idx = i0 +
numpy.argmax(ddt[i0:i1])
        timeshifts[key].append(idx)
        sig = sigs[i][idx-
keep1:idx+keep2]
        ddt = ddts[i][idx-
keep1:idx+keep2]
        # Find the baseline
        baseline =
numpy.average(sig[:20])
        siga[key].append(sig/baseline)
       ddta[key].append(ddt/baseline)

# Analyse the time-shifts
nMax = max(len(shifts) for shifts in
timeshifts.values())
grid = numpy.zeros((1+nMax, len(keys)),
'f')
try:
    grid[0,:] = [presdict[key] for key
in keys]
except ValueError:
    print 'WARNING: UNABLE TO STORE ROW
HEADERS IN SHIFTS.CSV'

x = numpy.arange(-10, 10)
pylab.figure()
print grid

for i, key in enumerate(keys):
    print grid
    # Pack away for saving
    shifts = timeshifts[key]
    grid[1:1+len(shifts), i] = shifts
    # Plot it
    shifts = numpy.array(shifts) -
round(numpy.average(shifts))
    y = [(shifts == val).sum() for val
in x]
    y = numpy.array(y)
    y = y / len(shifts)
    ident = presdict[key]
    if type(ident) in (int, float):
        ident = 'pres=%immHg' % ident
    pylab.plot(x, y, label='%s - n=%i' %
(ident, len(shifts)), color=cdict[key])
    pylab.bar(x-0.5, y, width=0.9,
color=cdict[key], alpha=.05)
    pylab.title('Distribution of timing
jitter on peak ddt')
    pylab.legend()
pylab.xlabel('Shift - frames')
pylab.ylabel('Relative Frequency')
numpy.savetxt('../csvData/superset_shift
s_%s.csv' % superset, grid, fmt='%.1f',
delimiter=',')
pylab.savefig('../gfx/superset_shifts_%s
.png' % superset)
analyse_signal_set(siga, ddta, 5,
'Algined per cell, normalised to per-
cell peak ddt',
savename='superset_%s_aligned_per_cell'
% MASTER_TITLE)
```

```
# Now plot before, after etc for each
signal

befores = [] # Storage for value and
standard devisations
afters  = []
peaks   = []
ddtmxs  = []
for key in keys:
    siga[key] = numpy.array(siga[key])
    ddta[key] = numpy.array(ddta[key])
    # Find maximmum value of each signal
and each ddt and average of each before
and after
    pks = numpy.max(siga[key], axis=1)
    dts = numpy.max(ddta[key], axis=1)
    print siga[key].shape, '<<<'
    b = numpy.average(siga[key][:,
15:25], axis=1) # WARNING + TODO!  HARD
CODED TIMECODES
    a = numpy.average(siga[key][:,
35:45], axis=1) # WARNING + TODO!  HARD
CODED TIMECODES
    befores.append((numpy.average(b),
numpy.std(b)/numpy.sqrt(len(siga))))
    afters.append ((numpy.average(a),
numpy.std(a)/numpy.sqrt(len(siga))))
    peaks.append  ((numpy.average(pks),
numpy.std(pks)/numpy.sqrt(len(pks))))
    ddtmxs.append ((numpy.average(dts),
numpy.std(dts)/numpy.sqrt(len(dts))))

befores = numpy.array(befores)
afters = numpy.array(afters)
peaks = numpy.array(peaks)
ddtmxs = numpy.array(ddtmxs)

bad = sum(type(p) not in (int, float)
for p in pres)
if bad:
    x = numpy.arange(len(pres))
else:
    x = pres
# SAVE TO DISK
# -------------------------------------
# Data on each type
headers = 'sigBefore', 'sigPeak',
'sigAfter', 'ddtPeak', 'ddtMaxFrame'
nData = len(headers) # before, during,
after, peak ddt, ddt shift
fp =
open('../csvData/superset_info_%s.csv' %
superset, 'w')
# Header with pressures
[fp.write('%s' % key + nData*',') for
key in keys]
fp.write('\n')
[[fp.write('%s,' % h) for h in headers]
for k in keys]
fp.write('\n')
ncellsmax = max(len(sig) for sig in
siga.values())
grid = numpy.zeros((ncellsmax,
nData*len(keys)), 'f')

for i, key in enumerate(keys):
    sig = numpy.array(siga[key])
    ddt = numpy.array(ddta[key])
    print sig.shape
    data0 = numpy.average(sig[:, 15:25],
axis=1) # WARNING + TODO!  HARD CODED
TIMECODES
    print data0.shape
    data1 = numpy.max(sig, axis=1)
    data2 = numpy.average(sig[:, 35:45],
axis=1) # WARNING + TODO!  HARD CODED
TIMECODES
    data3 = numpy.max(ddt, axis=1)
    data4 = numpy.argmax(ddt, axis=1)
    n = len(sig)
    grid[:n, i*nData+0] = data0
    grid[:n, i*nData+1] = data1
    grid[:n, i*nData+2] = data2
    grid[:n, i*nData+3] = data3
    grid[:n, i*nData+4] = data4

fmt = '%.7f,' * grid.shape[1] + '\n'
for row in grid:
    txt = fmt % tuple(row)
    fp.write(txt)
fp.close()

pylab.figure(figsize=(6,9))
pylab.suptitle('Superset - %s' %
MASTER_TITLE)
pylab.subplot(211)
pylab.title('Baseline normalised signals
at...')
pylab.errorbar(x , befores[:,0],
yerr=befores[:,1] , label='Before',
fmt=None, alpha=.5, lw=4,
ecolor='black')
pylab.errorbar(x , afters [:,0],
yerr=afters [:,1] , label='After',
fmt=None, alpha=.5, lw=4,
ecolor='orange')
pylab.errorbar(x , peaks  [:,0],
yerr=peaks  [:,1] , label='Peak',
fmt=None, alpha=.5, lw=4, ecolor='red')
pylab.plot(x , befores[:,0],
color='black')
pylab.plot(x , afters [:,0],
color='yellow')
pylab.plot(x , peaks  [:,0],
color='red')
pylab.ylabel('Normalised signal')
pylab.legend()
if bad:
    pylab.xticks(x, pres)
    pylab.xlim(-1, len(x))
else:
    pylab.xlim(min(pres)-40,
max(pres)+40)

pylab.subplot(212)
pylab.title('Baseline normalised d/dt at
peak')
pylab.errorbar(x , ddtmxs[:,0],
yerr=ddtmxs[:,1], alpha=.5, lw=.5,
color='red')
pylab.plot(x , ddtmxs[:,0], color='red')
pylab.xlabel('mmHg')
pylab.ylabel('Normalised signal /
frame')
if bad:
    pylab.xticks(x, pres)
    pylab.xlim(-1, len(x))
else:
    pylab.xlim(min(pres)-40,
max(pres)+40)
pylab.savefig(os.path.join('../gfx',
'superset_summary_%s.png' % superset))
pylab.show()
```

A3 IP_3R Ca^{2+} Release Model

Model Description

We developed a model to study the flow of free Ca^{2+} from the endoplasmic reticulum into the cytosol, and the ions subsequent diffusion and rapid buffering in the microdomain surrounding either an individual IP_3R or a cluster of IP_3Rs. This model was used to examine the effects of changes in cell dimension. We represent the cytosolic concentrations of ionic Ca^{2+}, buffer and buffered Ca^{2+} with $C_{Ca,cyt}$, $C_{B,cyt}$ and $C_{CaB,cyt}$ respectively. The partial differential equation governing the concentration, C_s, of a species, s, in our model was:

$$\frac{\partial C_s}{\partial t} = D_s \nabla^2 C_s + \phi_s + J_s \qquad \textbf{(A3.1)}$$

where C_s is the concentration, D_s is the diffusion coefficient, ϕ_s is the source term derived from chemical reactions and J_s is the source term resulting from trans-membrane flux, which we took as zero for all species except Ca^{2+}, for which it comprises IP_3R-mediated Ca^{2+} currents.

Buffering

We employed the first order mass action reaction kinetic

$$\phi_{Ca,cyt} = -K_{on} . C_{Ca,cyt} C_{B,cyt} + K_{off} C_{CaB,cyt} \qquad \textbf{(A3.2)}$$

$$\phi_{B,cyt} = \phi_{CaB,cyt} = -\phi_{Ca,cyt} \qquad \textbf{(A3.3)}$$

where K_{on} and K_{off} are the rate constants for the buffer.

Trans-membrane flux

Ca^{2+} pumps (SERCAs) and membrane (plasma and ER) leakage currents are typically continuous, low magnitude processes that function to maintain specific concentrations of Ca^{2+} in the cytosol (typically <100 nM) and the ER (typically >0.5 mM) in the long term (Supplementary Table 1). This is in contrast to IP_3Rs, which are reported to open for durations of between 2 ms and 20 ms, with a transient current that is far higher than those of the aforementioned long-term processes. We therefore omitted the slow acting sources and sinks, as their effects over the brief temporal and spatial scales of an individual microdomain, with which we are concerned, are limited. The transport of Ca^{2+} from the ER to the cytosol, through an open IP_3R, is a purely diffusive process, and is therefore driven in linear proportion to the ionic concentration gradient between the two partitions. Therefore individual IP_3R are represented by the source term:

$$J_s = \alpha J_0 \frac{C_{Ca,er} - C_{Ca,cyt}}{C_{Ca,er}} \quad \textbf{(A3.4)}$$

where $C_{Ca,er}$ is the concentration of Ca^{2+} in the ER, taken as a constant, J_0 is the experimentally measured maximal ion current of an isolated IP_3R and α is a conversion factor from a current (in moles per second) to a molar concentration for the voxel to which the current is applied.

Computation

Equation A3.1 was solved for a regular voxel grid in Cartesian space (Supplementary Table 1) using a first order finite difference solver. A sufficiently large volume was used such that edge effects are negligible, with the condition being that $C_{Ca,cyt}$ did not exceed a level 1% above baseline at the edges (excluding the edge containing the IP_3Rs), except where we intentionally simulated compressed cells. *The Courant-Freidcrichs-Lewy* condition:

$$\frac{2D_s dt}{dx^2} < 1 \quad \textbf{(A3.5)}$$

was obeyed for each species, where *dt* is the simulation time-step and *dx* is the linear size of a voxel. Simulation was conducted using bespoke C code employing Intel AVX-2 vector extensions. The Python language was used to process and analyse simulation results.

Boundary conditions

Our model was initialised with homogeneous Ca^{2+} and buffer concentrations as given in Supplementary Table 1, with $C_{CaB,cyt}$ being initialised to equilibrium values. A zero flux boundary condition was applied to the edges of the cuboidal simulation volume.

Simulation verification

Our simulation code was compared with analytical expressions for simplified test cases of 3D diffusion from a point source and for the microdomain profile of an isolated Ca^{2+} source in a strongly buffered environment.

Analytical diffusion

Equation A3.6 gives the analytical form of the concentration profile for a slug of mass, *M*, released at position $r = 0$ and time $t = 0$, where *r* is scalar radius from the origin.

$$C(r,t) = \frac{M}{(4D\pi t)^{3/2}} \exp\left(-\frac{r^2}{4Dt}\right) \quad \textbf{(A3.6)}$$

The Ca^{2+} diffusion component of our simulation was initialised with a volume of 1.68 μm on a side, with Ca^{2+} parameters as per Supplementary Table 1, and with zero Ca^{2+} concentration except in the central voxel, which was set to 1 molar. Supplementary Figure 1A,C illustrates the good agreement between our simulation and the analytical case.

Analytical microdomain profile

An analytical solution for the equilibrium concentration profile, at distance r from an isolated source of constant current J_{Ca} in an isotropic, exists for an inexhaustible buffer that only forward binds:

$$c(r) = c_\infty + \frac{J_{Ca}}{2\pi D_{ca}} \frac{e^{-r/\lambda}}{r} \qquad \textbf{(A3.7)}$$

where c_∞ is the Ca^{2+} concentration far from the source – that is the equilibrium level, $\gamma = (D\tau)^{0.5}$ is a space constant and $\tau = 1/(K_{on}B)$ is the mean capture time of the buffer, of concentration B. Our simulation was configured to match, as well as possible, this analytical case. Specifically parameters from Supplementary Table 1 were used to simulate a single source, with the following modifications: K_{Off} was set to zero (forward binding only), $\phi_{B,cyt}$ from equation A3.2 was set to zero (inexhaustible buffer) and the concentration gradient was removed from equation A3.3 (constant current source). As a consequence of these changes any background Ca^{2+} was rapidly depleted in this model, so c_∞ was also set to zero to facilitate direct comparison. After running the model, the total quantity of free (unbuffered) cytosolic Ca^{2+} was examined (Supplementary Figure 1B). This level rose rapidly, stabilizing to equilibrium in ~0.1ms. A comparison of A3.6 and the concentration profile of the model, once equilibrium is reached, is shown in Supplementary Figure 1C. The responses were very similar, with the effect of quantised voxel sizes limiting the model concentration at small r and edge effects raising the concentration at high r.

Simulation Parameters

Parameters for the simulation were chosen to be physiologically relevant, and are given in Supplementary Table 1 along with references.

Grid and Solver			**Reference / notes**
Voxel Scale	dx	0.015 μm	
Solver timestep	dt	0.120 μs	
Courant-Freidcrchs-Lewy condition[Ca^{2+}]	$2Ddtdx^{-2}$ Must be < 1	0.23	Evaluated for Ca^{2+} as most diffusive.
Cytosolic Ca^{2+}			
Equilibrium concentration	C_{inf}	70 nM	(123,323,381)
Diffusion coefficient	$D_{Ca,cyt}$	220 $\mu m^2 s^{-1}$	(323)
Cytosolic buffer - Parvalbumin			
Diffusion coefficient	$D_{B,cyt}$	90 $\mu m^2 s^{-1}$	(381)
Diffusion coefficient	$D_{CaB,\ cyt}$	90 $\mu m^2 s^{-1}$	*As for buffer*
Forward binding constant	K_{on}	18.5 $\mu M^{-1} s^{-1}$	(381)
Backward binding constant	K_{off}	0.95 s^{-1}	(381)
IP_3R			
ER Ca^{2+}concentration	$C_{Ca,er}$	0.25 mM	(323)
Maximum channel current	J_0	$3.3x10^{-19}$ mol s^{-1}	(323,382)

Supplementary Table 1 – Numerical parameters used in reaction diffusion simulations

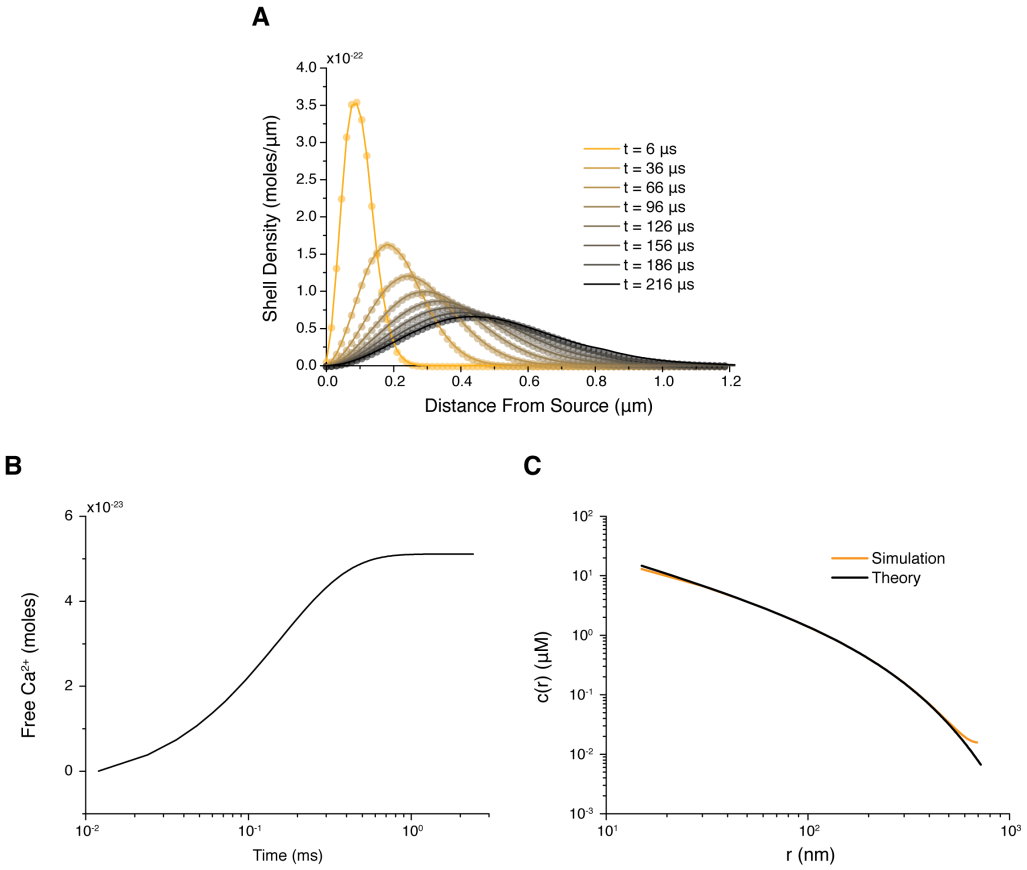

Supplementary Figure 1 (A) Radial density shows good agreement with our simulation (circles) and the analytical test case (lines) for a slug of mass released at the origin. (B) Free Ca^{2+} concentration at an IP_3R as a function of time from receptor opening. The total cytosolic Ca^{2+} rises immediately after IP_3R opening then plateaus as the current flowing through IP_3R and cytosolic Ca^{2+} buffering reaches equilibrium (~0.1ms). (C) Ca^{2+} concentration as a function of radial distance from IP_3Rs. When equilibrated, the Ca^{2+} profile may be approximated by an analytical case (yellow line), which compares accurately to an examination of our simulation (black line).

A4 Research Output

Wilson C, Saunter CD, Girkin JM, McCarron JG. Age-related changes in endothelial Ca2+ signalling revealed by imaging from inside arteries at normal physiological pressures. 1st Scottish Microscopy Group and Microscopy Society of Ireland Symposium. Glasgow, UK; 2014. *Poster Presentation*

Wilson C, Saunter CD, Girkin JM, McCarron JG. Endothelial mechanosensing via IP3-mediated Ca2+ signalling in rat carotid arteries. Proc Physiol Soc 31, C68. London, UK; 2014. *Selected Talk / Physiological Society Travel Award*

Wilson C, Saunter CD, Girkin JM, McCarron JG. Endothelial mechanosensing visualised from inside intact, pressurised arteries. Early Career Physiologists Symposium 2014. London, UK; 2014. *Selected Talk/Best Oral Presentation Winner*

Wilson C, Saunter CD, Zagnoni M, Girkin JM, McCarron JG. Visualizing the endothelium from inside intact arteries at physiological pressures reveals pulsatile linear, circular and spiral Ca2+ waves (668.1). FASEB J. 2014 Apr 1;28(1 Supplement):668.1. *Microcirculatory Society (MCS) President's Symposium Selected Talk / Poster*

Wilson C, Saunter CD, Girkin JM, McCarron JG. IP3-Mediated Endothelial Mechanosensitivity Revealed by a Novel Imaging System. Stress and Signaling in the Vascular Endothelium. Durham, UK; 2014. *Invited Talk*

Wilson C, Saunter CD, Girkin JM, McCarron JG. Novel methodology to simultaneously image endothelial and smooth muscle function in pressurized arteries. The FASEB Journal. 2013 Apr 9;27(1_MeetingAbstracts):901.12. *Poster Presentation*

Wilson C, Saunter CD, Girkin JM, McCarron JG. Inside and OutL Novel Methodology for Measuring Blood Vessel Function. Biophysics at All Scales. British Biophysical Society Biennial Meeting. Durham, UK; 2012. *Poster Presentation*